Supersymmetry Searches in Dilepton Final States with the ATLAS Experiment

von

Matthias Lungwitz

geb. in Bonn

Dissertation
zur Erlangung des Grades

Doktor der Naturwissenschaften

vorgelegt dem

Fachbereich Physik, Mathematik und Informatik
der
Johannes Gutenberg-Universität Mainz

Mainz im Juni 2013

1. Berichterstatter: [In der elektronischen Fassung aus Datenschutzgründen entfernt.]
2. Berichterstatter: [In der elektronischen Fassung aus Datenschutzgründen entfernt.]
mündliche Prüfung: 09.01.2014
Dissertation an der Universität Mainz (D77)

Abstract

One of the main goals of the ATLAS experiment at the Large Hadron Collider (LHC) at CERN in Geneva is the search for new physics beyond the Standard Model. In 2011, proton-proton collisions were performed at the LHC at a center of mass energy of 7 TeV and an integrated luminosity of 4.7 fb^{-1} was recorded. This dataset can be tested for one of the most promising theories beyond limits achieved thus far: supersymmetry. Final states in supersymmetry events at the LHC contain highly energetic jets and sizeable missing transverse energy. The additional requirement of events with highly energetic leptons simplifies the control of the backgrounds. This work presents results of a search for supersymmetry in the inclusive dilepton channel. Special emphasis is put on the search within the Gauge-Mediated Symmetry Breaking (GMSB) scenario in which the supersymmetry breaking is mediated via gauge fields. Statistically independent Control Regions for the dominant Standard Model backgrounds as well as Signal Regions for a discovery of a possible supersymmetry signal are defined and optimized. A simultaneous fit of the background normalizations in the Control Regions via the profile likelihood method allows for a precise prediction of the backgrounds in the Signal Regions and thus increases the sensitivity to several supersymmetry models. Systematic uncertainties on the background prediction are constrained via the jet multiplicity distribution in the Control Regions driven by data. The observed data are consistent with the Standard Model expectation. New limits within the GMSB and the minimal Supergravity (mSUGRA) scenario as well as for several simplified supersymmetry models are set or extended.

Kurzfassung

Eines der wesentlichen Ziele des ATLAS-Experiments am Large Hadron Collider (LHC) am CERN in Genf ist die Suche nach neuer Physik jenseits des Standardmodells. Im Jahr 2011 wurden dazu am LHC Proton-Proton-Kollisionen bei einer Schwerpunktsenergie von 7 TeV durchgeführt und eine integrierte Luminosität von 4.7 fb^{-1} aufgezeichnet. Die gewonnenen Daten ermöglichen es, eine der vielversprechendsten Theorien jenseits bisher erreichter Grenzen zu testen: Die Supersymmetrie. Endzustände in Supersymmetrie-Ereignissen am LHC sind gekennzeichnet durch hochenergetische Jets und erhebliche fehlende Transversalenergie. Die zusätzliche Forderung nach Ereignissen mit hochenergetischen Leptonen vereinfacht das Kontrollieren der Untergründe. Die Arbeit präsentiert Ergebnisse zur Suche nach Supersymmetrie im inklusiven Dilepton-Kanal. Ein besonderer Schwerpunkt liegt dabei auf der Suche innerhalb des Gauge-Mediated Symmetry Breaking (GMSB)-Szenarios, in dem die Supersymmetrie-Brechung durch Eichfelder vermittelt wird. Statistisch unabhängige Kontrollregionen für die dominanten Standardmodell-Untergründe sowie Signalregionen zum Nachweis eines möglichen Supersymmetrie-Signals werden definiert und optimiert. Die simultane Anpassung der Normierungen der Standardmodell-Untergründe in den Kontrollregionen mit Hilfe der "profile likelihood"-Methode ermöglicht eine präzise Vorhersage der Untergrunderwartung in den Signalregionen und steigert die Sensitivität der Analyse auf verschiedene Supersymmetrie-Modelle. Systematische Fehler auf die Untergrundvorhersage werden dabei mit Hilfe der Jet-Multiplizitätsverteilung in den Kontrollregionen datenbasiert eingeschränkt. Die beobachteten Daten stimmen gut mit der Standardmodell-Untergrunderwartung überein. Neue Grenzen innerhalb des GMSB- und minimal Supergravity (mSUGRA)-Szenarios sowie für verschiedene vereinfachte Supersymmetrie-Modelle werden gesetzt oder erweitert.

Contents

1. Introduction

The Standard Model of Particle Physics is one of the most successful scientific models in the world. It describes all known elementary particles and their corresponding interactions[1] within the framework of a relativistic quantum field theory to a very high precision. Among its many accomplishments are the prediction of the existence and the mass of the W boson (discovered 1983 with the UA1 and UA2 Experiments [1–3]) and the top quark (discovered 1995 at the Tevatron [4, 5]). During completion of this thesis there are now even tantalizing hints that a Standard Model-like Higgs boson has been discovered (see chapter 2.4), though the measurement of its properties (spin & CP state as well as production and decay modes) still needs to be completed for a full confirmation. Overall, the Standard Model is able to accommodate for all experimental precision measurements in an excellent way as shown in Figure 1.

Nevertheless there are a number of open issues that cannot be answered within the Standard Model itself: The large number of free parameters which cannot be predicted theoretically (18 different masses, couplings etc.), the origin of the number of particle families and their observed mass pattern, the missing incorporation of the gravitational interaction, the source of matter-antimatter-asymmetry in the universe, the hierarchy problem (cf. chapter 3.4) and the nature of dark matter

[1] Apart from gravity.

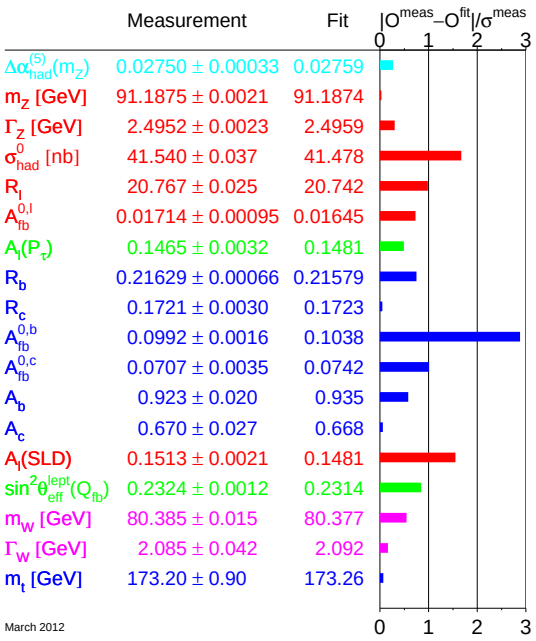

Figure 1: Pull distribution for the Standard Model fit to various electroweak precision data [6], for a detailed discussion cf. [7].

and dark energy (cf. chapter 3.3). The answers to all these open questions must lie beyond the Standard Model, and correspondingly various extensions have been proposed and studied for a long time. One of the most promising and most analyzed extensions is the concept of Supersymmetry (SUSY) and the corresponding Minimal Supersymmetric Standard Model (MSSM). SUSY postulates a new symmetry between fermions and bosons, and in the MSSM each Standard Model particle receives a new supersymmetric partner. Furthermore, the Higgs sector needs to be extended by another Higgs doublet and corresponding superpartners (cf. chapter 3.2). This extension of the Standard Model solves a number of problems in a very elegant way (cf. chapter 3.4).

Despite of being theoretically appealing, supersymmetry has not yet been observed experimentally (cf. chapter 3.6). The search for supersymmetry is therefore one of the main reasons for the construction and operation of the Large Hadron Collider (LHC) at CERN in Geneva and the two general purpose detectors ATLAS and CMS [8–13]. With a design center of mass energy of 14 TeV it is possible to probe the physics beyond the Standard Model in proton-proton collisions on energy scales that have not been reached in a laboratory before.

The aim of this thesis is the search for supersymmetry in final states with at least two leptons[2] at the ATLAS experiment. In 2011 the LHC provided proton-proton collisions at a center of mass energy of 7 TeV with a total integrated luminosity of 4.7 fb^{-1} recorded with the ATLAS detector. This dataset will be probed for hints of supersymmetry as a continuation of previous work on simulation [14] and smaller datasets [15–18]. For this purpose, a simultaneous fit to multiple regions of phase space is set up in order to constrain the Standard Model backgrounds and to enhance the sensitivity to different signal models. The results obtained in the context of this thesis have been published by ATLAS [19].

The thesis will be organized as follows: After a brief introduction of the Standard Model in chapter 2, the concept of Supersymmetry will be described in chapter 3. The properties of the dilepton final state with respect to signal and background processes are described in chapter 4. Chapter 5 contains a description of the LHC and the ATLAS detector that is used to reconstruct and identify the collision results as described in chapter 6. The description of the analysis itself starts in chapter 7, where special emphasis is placed on the background estimation and the systematic uncertainties in chapters 8 and 9. Finally, the simulatenous fit to Signal and Control Regions as the core of the analysis is discussed in chapter 10. The corresponding results are contained in chapter 11 and their interpretation is given in chapter 12. Chapter 13 summarizes the work of thesis and gives an outlook to possible further updates in the future.

[2] In the scope of this work 'leptons' usually denotes electrons and muons including those from τ-lepton decays.

2. The Standard Model of Particle Physics

2.1. Overview

The Standard Model of Particle Physics is a relativistic quantum field theory, and as such its fundamental building blocks are quantized fields of space-time exhibiting well-defined transformation properties under Lorentz group transformations of special relativity. Interactions are a consequence of the local gauge invariance under the gauge group $SU(3)_{\text{Color}} \otimes SU(2)_{\text{Left}} \otimes U(1)_{\text{Hypercharge}}$. The strong interaction is described by quantum chromodynamics (QCD), while electromagnetic and weak interactions are unified within the electroweak theory. It has been shown [20] that the Standard Model is a renormalizable field theory ensuring that all physical observables are finite. The following brief summary of the Standard Model is based on [21]. More detailed descriptions can for example be found in [22–24].

2.2. Particles and Forces

The field content of the Standard Model is divided into twelve spin-1/2 fields which belong to the fundamental representation of the gauge group and therefore form the building blocks of matter. In addition there are twelve vector-like gauge fields of spin 1 in the adjoint representation which mediate the gauge interactions as force carriers. Finally there is the scalar Higgs boson as a consequence of electroweak symmetry breaking and the Higgs mechanism as described in chapter 2.3. The twelve fermions and their corresponding antiparticles are further divided into six quarks which carry color charge and therefore interact via the strong interaction and six leptons which only participate in electroweak interactions. Both quarks and leptons can be be arranged into three generations of particles with identical quantum numbers, but different masses. Table 1 gives an overview over the fermions in the Standard Model where the left-handed and the right-handed components of the fields are separated as required by the chiral nature of the Standard Model[3].

Name	Generations			$SU(3)_C$, $SU(2)_L$, $U(1)_Y$
Quarks	$\begin{pmatrix} u^i \\ d^i \end{pmatrix}_L$	$\begin{pmatrix} c^i \\ s^i \end{pmatrix}_L$	$\begin{pmatrix} t^i \\ b^i \end{pmatrix}_L$	$(\mathbf{3}, \mathbf{2}, 1/3)$
	u^i_R	c^i_R	t^i_R	$\left(\overline{\mathbf{3}}, \mathbf{1}, 4/3\right)$
	d^i_R	s^i_R	b^i_R	$\left(\overline{\mathbf{3}}, \mathbf{1}, -2/3\right)$
Leptons	$\begin{pmatrix} \nu_e \\ e \end{pmatrix}_L$	$\begin{pmatrix} \nu_\mu \\ \mu \end{pmatrix}_L$	$\begin{pmatrix} \nu_\tau \\ \tau \end{pmatrix}_L$	$(\mathbf{1}, \mathbf{2}, -1)$
	e_R	μ_R	τ_R	$(\mathbf{1}, \mathbf{1}, -2)$

Table 1: The fermionic sector of the Standard Model. The Index $i = 1, 2, 3$ represents the three color eigenstates while the last column lists the corresponding representations of SU(3) and SU(2) as well as the weak hypercharge.

[3]The Standard Model treats neutrinos as massless dirac fields. Extensions including the mass differences observed through neutrino oscillations [25] and from cosmology [26] are possible [27, 28]. Furthermore, the possibility of the neutrinos being Majorana particles is investigated [29].

Name		Representation	Gauge group
Gluons	G^a_μ	$(\mathbf{8},\mathbf{1},0)$	$SU(3)_C$
Vector bosons	W^i_μ	$(\mathbf{1},\mathbf{3},0)$	$SU(2)_L$
Abelian boson	B_μ	$(\mathbf{1},\mathbf{1},0)$	$U(1)_Y$

Table 2: The gauge fields of the Standard Model with the corresponding representations of SU(3) and SU(2), the weak hypercharge and the corresponding gauge group.

The gauge bosons of the Standard Model are formed by the eight gluons that mediate the strong interaction, the photon γ and the three vector bosons W^+, W^- and Z^0 of the electroweak interactions. The physical mass eigenstates of the electroweak bosons are related to the gauge eigenstates W^i_μ and B_μ via a rotation by the Weinberg angle $\sin^2\theta_W \approx 0.23$ [30] after electroweak symmetry breaking:

$$W^\pm = (W^1 \pm W^2)/\sqrt{2} \tag{1}$$
$$A = B\cos\theta_W + W^3\sin\theta_W \tag{2}$$
$$Z^0 = -B\sin\theta_W + W^3\cos\theta_W \tag{3}$$

The multiplet structure of the gauge bosons is shown again in Table 2.

The Higgs sector of the Standard Model consists of one doublet of scalar Higgs fields:

$$H = \begin{pmatrix} H^+ \\ H^0 \end{pmatrix} \text{ with representations } (\mathbf{1},\mathbf{2},-1)\,.$$

2.3. Electroweak Symmetry Breaking and the Higgs Mechanism

Explicit mass terms for the electroweak gauge bosons in the Lagrangian of the Standard Model violate the invariance under local $SU(2)_L$ transformations. Therefore another mechanism is necessary to explain the physical masses[4] of the $W^\pm$ and Z^0 bosons which are measured to be $M_{W^\pm} = 80.385 \pm 0.015$ GeV [31, 32] and $M_{Z^0} = 91.1876 \pm 0.0021$ GeV [7]. An elegant solution is provided by the Higgs mechanism: By postulating a Higgs potential

$$V(\phi) = \mu^2 H^\dagger H + \lambda\left(H^\dagger H\right)^2 \tag{4}$$

with $\lambda > 0$, $\mu^2 < 0$ and correspondingly a non-vanishing vacuum expectation value

$$\langle H\rangle = \begin{pmatrix} 0 \\ \upsilon \end{pmatrix} \qquad \upsilon = m/\sqrt{\lambda} \tag{5}$$

with Higgs mass m and Higgs coupling λ, the gauge group of the Standard Model is broken spontaneously:

$$SU(3)_C \otimes SU(2)_L \otimes U(1)_Y \Rightarrow SU(3)_C \otimes U(1)_{EM} \tag{6}$$

[4]Natural units are used throughout this thesis setting $c = \hbar = 1$ and omitting c and $\hbar$ from corresponding expressions.

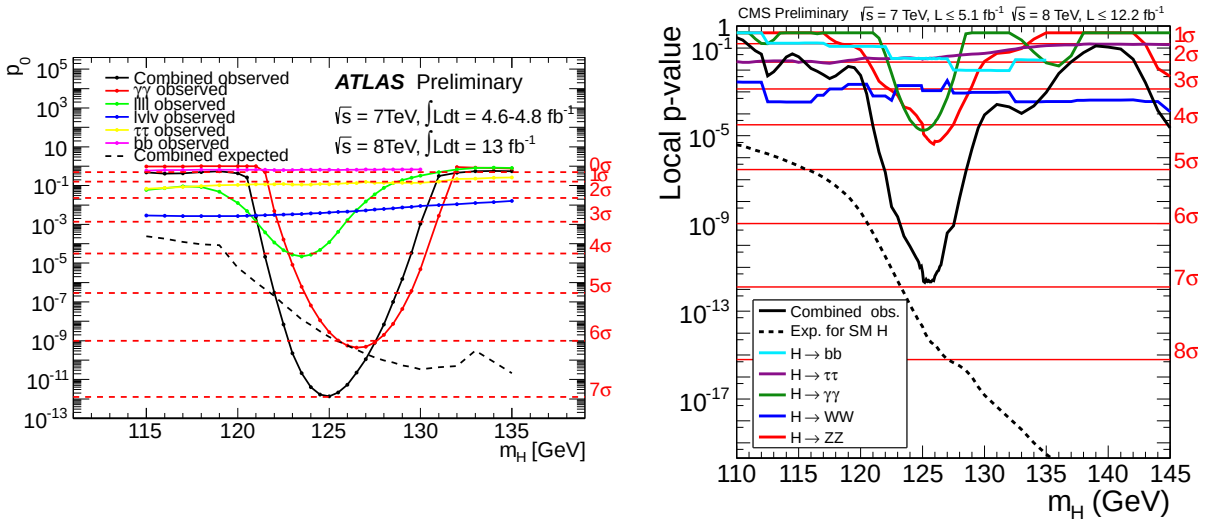

Figure 2: Measurements of the local probability p_0 for the background-only hypothesis as a function of m_h for various individual channels in searches for the Standard Model Higgs boson at ATLAS (left) and CMS (right) [37, 38].

The spontaneous symmetry-breaking creates scalar Nambu-Goldstone bosons which generate masses for the weak gauge bosons:

$$M_W = \frac{1}{\sqrt{2}} g v, \quad M_Z = M_W / \cos\theta_W \tag{7}$$

with the weak coupling constant g while the photon remains massless. The remaining neutral Goldstone boson is called the Higgs boson. Its mass term $m_h^2 = 2v^2\lambda$ is a free parameter within the Standard Model. In addition to the generation of weak boson masses in a gauge-invariant and renormalizable way, also the matter fields obtain masses via Yukawa-interactions without introducing explicit mass terms which would violate $SU(2)_L$.

2.4. Discovery of a Higgs-like Resonance

On 4th July 2012 the ATLAS and CMS collaborations announced the discovery of a new Higgs-like particle with a mass of approximately 125 GeV [33, 34]. By now, a signal has been established in several search channels, leading to a combined statistical significance of $\approx 7\sigma$ per experiment as shown in Figure 2 and a mass measurement of $125.5 \pm 0.2(\text{stat})^{+0.5}_{-0.6}(\text{sys})$ GeV [35] at ATLAS and $125.7 \pm 0.3(\text{stat}) \pm 0.3(\text{sys})$ GeV [36] at CMS.

The measurements of the particle's properties are ongoing. Figure 3 shows the current status of the signal strength measurement $\mu = \sigma_{obs}/\sigma_{SM}$ in the two experiments. Most channels are consistent with the Standard Model prediction, while the observed signal strength for the $h \to \gamma\gamma$ process deviates from unity at ATLAS[5].

With respect to the couplings and the CP eigenstate, several studies are ongoing [37–39]. Currently results are consistent with the properties predicted by the Standard Model, though a final

[5] Furthermore, a certain tension in the measurement of the particle's mass is observed at ATLAS that is not resolved yet [37].

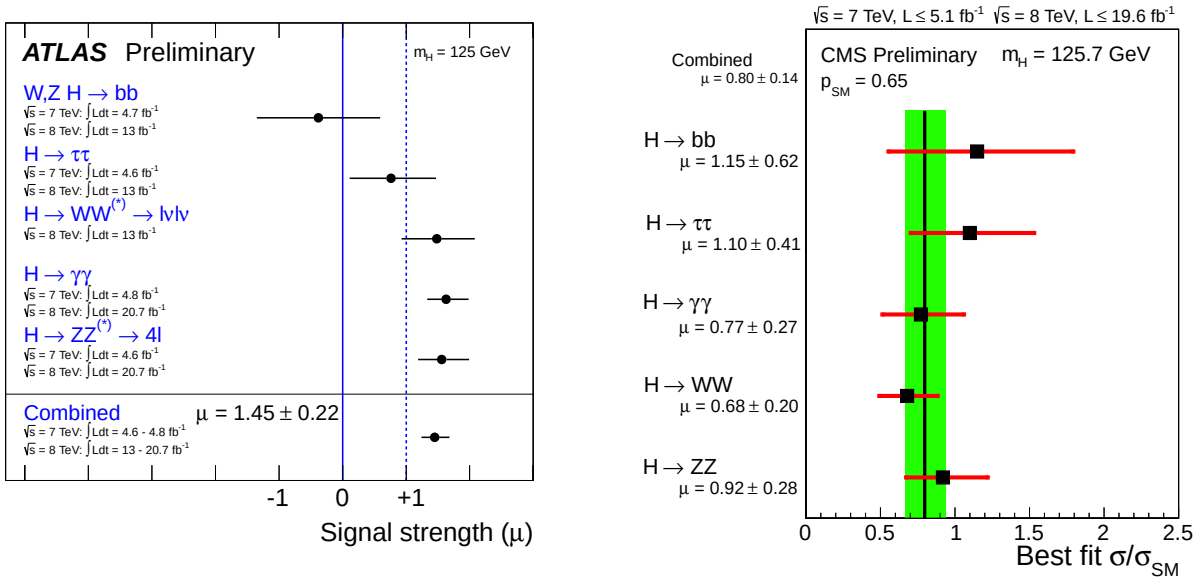

Figure 3: Measurements of the signal strength parameter μ for several channels and for their combination in searches for the Standard Model Higgs boson at ATLAS (left, assuming $m_h = 125$ GeV) and CMS (right, assuming $m_h = 125.7$ GeV) [35, 36].

confirmation might have to wait for the next data-taking period[6].

After having introduced the Standard Model of Particle Physics and its current experimental status, an introduction to supersymmetry will be given in the following chapter 3 solving several of the shortcomings of the Standard Model (see chapter 3.4).

[6] A measurement of the Higgs-selfcoupling will only be possible with a significantly larger dataset [40].

3. Supersymmetry

3.1. Overview

As described in the previous chapter 2, the Standard Model of Particle Physics is a renormalizable gauge theory and as such a consistent description of nature, while possibly being incomplete. However, a nontrivial extension within the framework of relativistic quantum field theories (apart from extending the gauge group) is prohibited by the *Coleman-Mandula theorem* [41, 42] which states that the symmetry group of a nontrivially interacting quantum field theory has to be a direct product of the Poincaré group and the internal gauge group. The only possible exception is supersymmetry: As shown by Haag, Łopuszański and Sohnius [43], a nontrivial extension of the Poincaré algebra is possible by using anticommutating spin-1/2 generators Q_α to define the supersymmetry algebra

$$\{Q_a, Q_{\dot{b}}^\dagger\} = (\sigma^\mu)_{a\dot{b}} P^\mu \tag{8}$$

$$\{Q_a, Q_{\dot{b}}\} = \{Q_a^\dagger, Q_{\dot{b}}^\dagger\} = 0 \tag{9}$$

$$[P^\mu, Q_{\dot{a}}] = \left[P^\mu, Q_{\dot{a}}^\dagger\right] = 0 \tag{10}$$

where P^μ is the momentum generator of spacetime translations, $\sigma^\mu = (1, \sigma^i)$ with the Pauli matrices σ^i and using two-component Weyl fermion notation. The generator Q_a transforms a bosonic state into a fermionic state and vice versa. Such related states are called *superpartners* that form the irreducible representations of the supersymmetry algebra denoted as *supermultipletts*. If supersymmetry was present in nature, therefore the maximal possible symmetry would be realized.

3.2. The Minimal Supersymmetric Standard Model

Supersymmetry [44–52] postulates the existence of additional superpartners for each Standard Model particle as it is impossible to impose invariance under supersymmetry transformations using only Standard Model particles. In the Minimal Supersymmetric Standard Model (MSSM) [53–57], exactly one additional particle is introduced per bosonic and per fermionic degree of freedom in the Standard Model[7]. The superpartners of the fermions are denoted as *sfermions* residing in the chiral supermultipletts as shown in Table 3.

For the bosonic particles of the Standard Model, the suffix *ino* is appended for the supersymmetric partners in the vector supermultipletts as presented in Table 4. The combined set of all the supersymmetric partners is usually referred to as sparticles.

In contrast to the Standard Model, it is necessary to add a second complex Higgs doublet and the corresponding superpartners in order to give mass to both up- and down-type quarks via Yukawa couplings and to avoid anomaly traces [61].

As in the Standard Model, the gauge eigenstates W^0 and B^0 mix to the mass eigenstates Z^0 and γ after electroweak symmetry breaking. In contrast now three electrically neutral and two charged Higgs bosons are predicted. These are correspondingly denoted as h^0, H^0, A^0, H^+ and H^- where A^0 is a pseudo-scalar and the other four are scalar bosons.

[7] Further extensions such as the Next-to-Minimal Standard Model (NMSSM) [58, 59] which solves the μ-Problem [60] by adding an additional gauge singlet field are possible as well.

Name		Spin 0	Spin 1/2	$SU(3)_C$, $SU(2)_L$, $U(1)_Y$
Squarks, Quarks	Q	$(\widetilde{u}_L \;\; \widetilde{d}_L)$	$(u_L \;\; d_L)$	$(\mathbf{3}, \mathbf{2}, \frac{1}{6})$
(×3 generations)	$\overline{u}$	$\widetilde{u}^*_R$	$u^\dagger_R$	$(\overline{\mathbf{3}}, \mathbf{1}, -\frac{2}{3})$
	$\overline{d}$	$\widetilde{d}^*_R$	$d^\dagger_R$	$(\overline{\mathbf{3}}, \mathbf{1}, \frac{1}{3})$
Sleptons, Leptons	L	$(\widetilde{\nu} \;\; \widetilde{e}_L)$	$(\nu \;\; e_L)$	$(\mathbf{1}, \mathbf{2}, -\frac{1}{2})$
(×3 generations)	$\overline{e}$	$\widetilde{e}^*_R$	$e^\dagger_R$	$(\mathbf{1}, \mathbf{1}, 1)$
Higgs, Higgsinos	H_u	$(H^+_u \;\; H^0_u)$	$(\widetilde{H}^+_u \;\; \widetilde{H}^0_u)$	$(\mathbf{1}, \mathbf{2}, +\frac{1}{2})$
	H_d	$(H^0_d \;\; H^-_d)$	$(\widetilde{H}^0_d \;\; \widetilde{H}^-_d)$	$(\mathbf{1}, \mathbf{2}, -\frac{1}{2})$

Table 3: Chiral supermultipletts in the MSSM (modified after [61]). The chirality index L, R is added for the squarks and sleptons for clarity despite of them being scalar particles.

Name	Spin 1/2	Spin 1	$SU(3)_C$, $SU(2)_L$, $U(1)_Y$
Gluino, Gluon	$\widetilde{g}$	g	$(\mathbf{8}, \mathbf{1}, 0)$
Winos, W bosons	$\widetilde{W}^\pm \;\; \widetilde{W}^0$	$W^\pm \;\; W^0$	$(\mathbf{1}, \mathbf{3}, 0)$
Bino, B boson	$\widetilde{B}^0$	B^0	$(\mathbf{1}, \mathbf{1}, 0)$

Table 4: Gauge supermultipletts in the MSSM (modified after [61]).

Furthermore, also the supersymmetric partners of the electroweak gauge bosons possess the same quantum numbers as the higgsinos which leads to a corresponding mixing between the neutral particles to the four *neutralinos* $\tilde{\chi}^0_{1,2,3,4}$ and between the charged gauginos and higgsinos to the four *charginos* $\tilde{\chi}^\pm_{1,2}$ (ordered ascending by mass).

Similarly to the mixing in the gaugino sector, also the gauge eigenstates of the superpartners of the left- and right-handed fermions can mix due to electroweak symmetry breaking. While this mixing is small for the first two families, it can have a significant size for stop, sbottom and stau depending on $\tan\beta$. The corresponding mass eigenstates are denoted as $\tilde{f}_{1,2}$.

In addition to these superpartners of the Standard Model particles, the breaking of local supersymmetry will lead to the prediction of a spin-2 graviton G and its spin-3/2 superpartner, the gravitino $\tilde{G}$ as further discussed in chapter 3.5.

3.3. R-Parity

Besides the above description of the MSSM, regularly another discrete Z_2 symmetry called *R-Parity* is introduced:

$$P_{\mathrm{R}} = (-1)^{3B-L+2S} \tag{11}$$

with Baryon number B, Lepton number L and Spin S for a given particle. Imposing this additional symmetry prevents B- and L-violating terms in the *superpotential* of the supersymmetry Lagrangian which determines the scalar interactions as well as the fermion masses and Yukawa couplings. Therefore, interactions that would lead to proton decays (similar to $SU(5)$ *Grand Unified Theory*

(GUT) models [62]) are forbidden as required by experimental data [63]. As all Standard Model particles have $P_R = 1$ and all the supersymmetric partners have $P_R = -1$, there has to be an even number of supersymmetry particles at each interaction vertex. As a consequence the lightest supersymmetric particle (LSP) is stable.

The assumption of R-parity conservation leads to very important experimental consequences. If the LSP interacts only weakly[8], it can be an interesting candidate for dark matter as will be discussed in chapter 3.4.5. Furthermore it will not interact within particle physics detectors and therefore lead to signatures involving missing energy as further discussed in chapter 4.

Although there are possible supersymmetry scenarios involving R-parity violation where the corresponding interactions are assumed to be sufficiently small (RPV supersymmetry, see e.g. [64] or [65]), R-parity conservation will be assumed for the rest of this work.

3.4. Motivation for Supersymmetry

While no supersymmetric partner of any of the Standard Model particles has been observed so far, there are a number of reasons why supersymmetry is one of the best motivated extensions of the Standard Model and therefore has been searched for extensively since the early 80s (see chapter 3.6).

3.4.1. Unification of Interactions

A very fundamental problem of modern physics is the missing unification between general relativity as the description of gravity and the Standard Model of Particle Physics describing the strong and electroweak interactions. The graviton as a hypothetical force carrier of the gravitational interaction has to be a massless spin-2 particle [66] and therefore cannot be in the same representation of the Poincaré algebra as the other gauge bosons. However, local supersymmetry can include the spin-2 graviton and its spin-3/2 superpartner, the gravitino, and connects the supersymmetry transformations to the coordinate transformations which form the basis of general relativity within the theory of *supergravity* [67, 68].

3.4.2. Unification of Coupling Constants

In quantum field theories coupling constants are scale dependent quantities. This scale dependence (*running*) is described by the renormalization group equations (RGEs) and the corresponding beta functions. For any GUT that unites strong and electroweak interactions, it is necessary that there exists an energy scale at which the corresponding coupling constants are of the same size. In the MSSM as the simplest supersymmetric extension of the Standard Model (see chapter 3.2) the coupling constants of the strong, weak and electromagnetic interaction unify at a scale $M_{GUT} \approx 10^{16}$ GeV as shown in Figure 4.

[8] Otherwise the model would be ruled out experimentally.

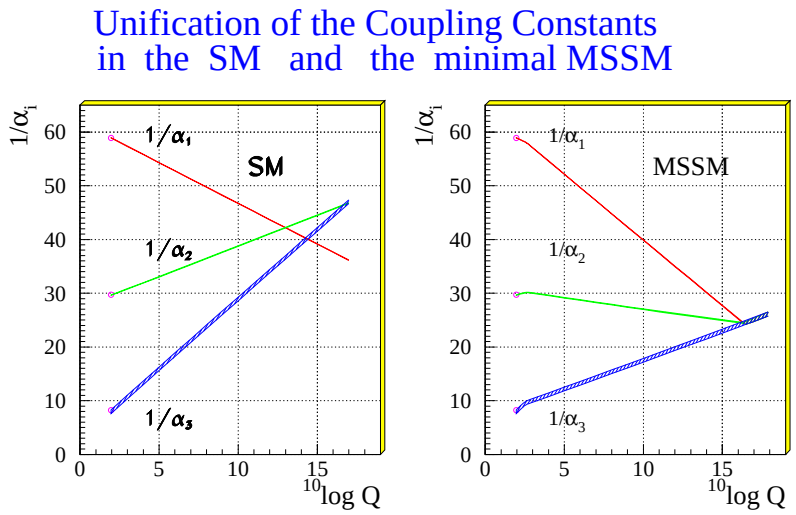

Figure 4: Scale dependence of the couplings in the Standard Model (left) and in the MSSM (right) [21].

3.4.3. The Hierarchy Problem

One of the most profound problems in theoretical high energy physics is the so called hierarchy problem: The Planck scale $M_{pl} = \sqrt{\frac{\hbar c}{G}} \approx 10^{19}$ GeV where quantum gravity effects become relevant and the electroweak scale $v = \sqrt{G_F \sqrt{2}} \approx 246$ GeV differ by many orders of magnitude which seems unnatural from a theoretical point of view. Furthermore, propagators in quantum field theories receive radiative corrections due to loop diagrams. While the gauge bosons and fermions of the Standard Model are protected against such corrections via gauge and chiral symmetries[9], this is not the case for the scalar Higgs field. As such, the Higgs boson mass receives quadratic corrections depending on the cutoff Λ of the theory [61]:

$$\delta m^2 \simeq \frac{g^2}{16\pi^2}\Lambda^2 \tag{12}$$

Therefore a large amount of finetuning of the coupling constants is necessary to sustain the hierarchy of the two scales.

In supersymmetry however the additional superpartners contribute with the same loop corrections resulting in an exact cancellation. As boson and fermion loop diagrams differ by a relative factor of (-1), when the corresponding dimensionless couplings to the Higgs field fulfill

$$\lambda_f^2 = \lambda_s \tag{13}$$

for each fermion f and scalar particle s in the same supermultiplett, the contributions cancel as illustrated in figure 5. This cancellation is an intrinsic property of supersymmetry which is valid to all orders in perturbation theory [57, 69–71].

[9] Here, only logarithmically divergent terms occur.

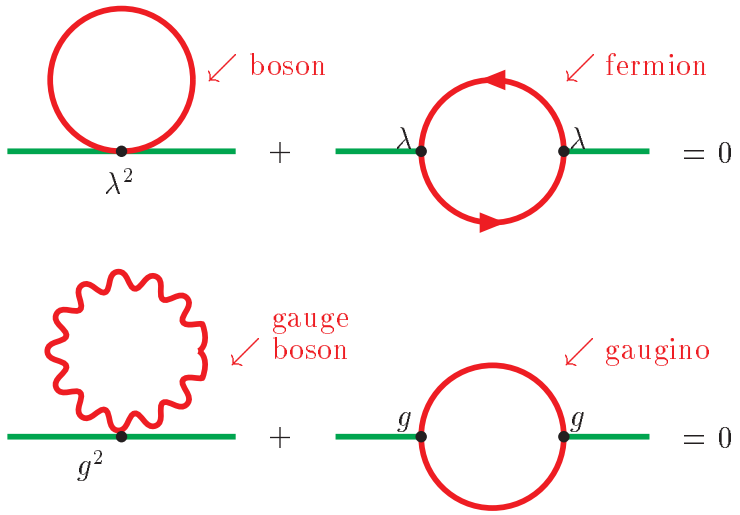

Figure 5: Cancellation of quadratically divergent loop correction to the Higgs boson propagator due to superpartners [21].

3.4.4. Light Higgs Boson

In the Standard Model, the Higgs boson mass is a free parameter that is only bounded by some generic arguments as shown in Figure 6. In contrast, within supersymmetry the mass of the lightest Higgs boson h^0 is directly related to the mass of the Z^0 boson [73, 74]:

$$m_{h^0} < |cos2\beta| m_{Z^0} \tag{14}$$

at tree level. Taking into account the significant quantum corrections (especially from top-stop

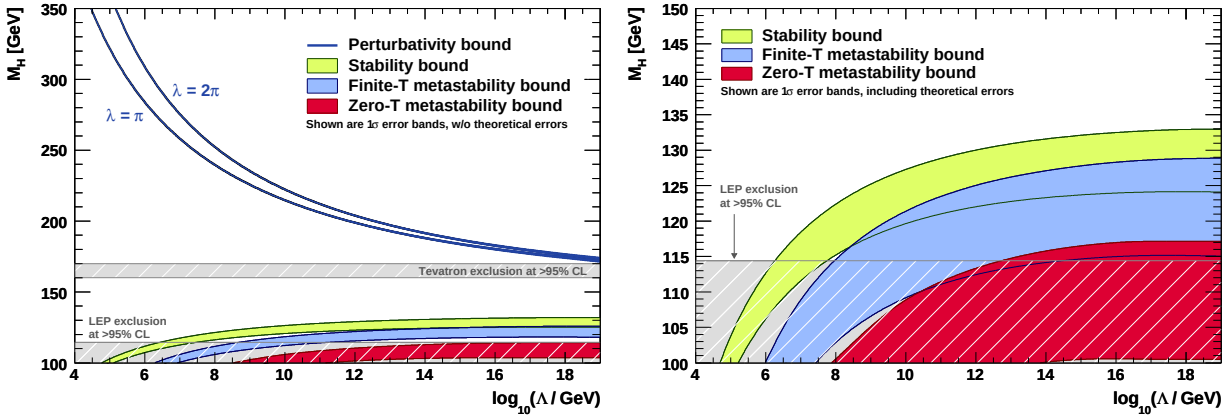

Figure 6: The scale Λ at which the two-loop RGEs drive the quartic SM Higgs coupling non-perturbative, and the scale Λ at which the RGEs create an instability in the electroweak vacuum ($\lambda < 0$) [72].

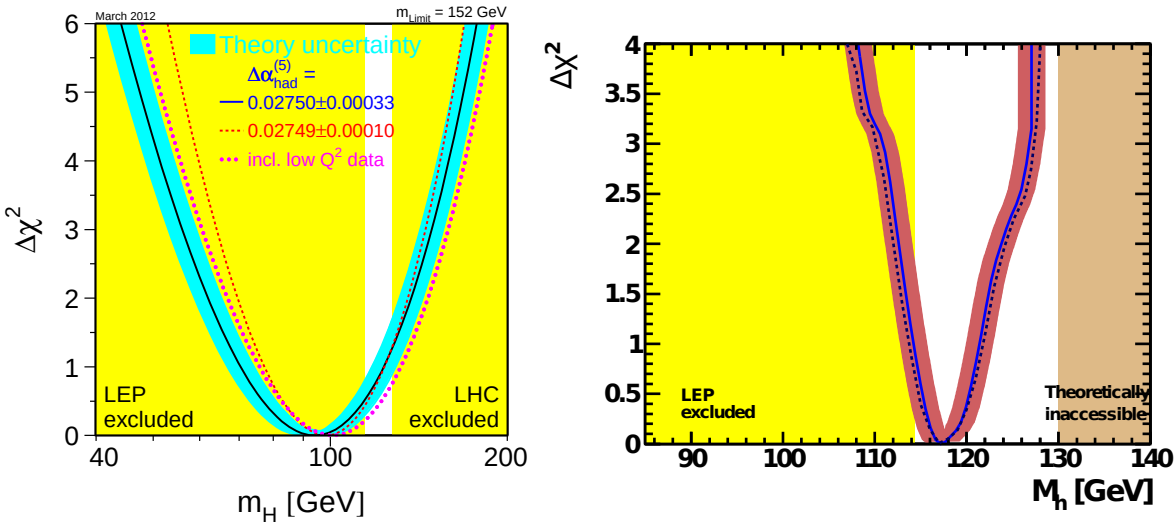

Figure 7: The one-dimensional $\Delta\chi^2$ functions for M_h in the SM (left) and the CMSSM (right) from fits to electroweak precision data [6, 75].

loops), this bound is softened to [61]

$$m_{h^0} \leq 135 \text{ GeV} \tag{15}$$

Such a bound is in good agreement with the indirect predictions on the Higgs boson mass from electroweak precision data as shown in figure 7.

The potential discovery of a Standard Model-like Higgs boson with a mass of approximately 125 GeV [33, 34] leads to some tension for certain models of supersymmetry breaking, though the amount of fine-tuning is limited as long as the masses and the mixing between $\tilde{t}_1$ and $\tilde{t}_2$, the supersymmetric partners of the top quark, is sufficiently large [76, 77]. While the question of Higgs-aware supersymmetry searches will become important in the future [78–82], it will not be considered in more detail in the following as the corresponding results were only obtained during completion of this work.

3.4.5. Dark Matter

An essential question in modern astroparticle physics is the nature of dark matter as observed via various effects such as the rotational speeds of galaxies [83], gravitational lensing effects like the Bullet cluster shown in Fig. 8 left or the large scale structure of the universe [84] as inferred from the WMAP measurements depicted in Fig 8 right.

While there might be other possible explanations for some of the observed effects[10], the simplest explanation for most of the observations is that dark matter is *cold*, i.e. moves slowly compared to

[10]Such as Modified Newtonian Dynamics (MOND) [89].

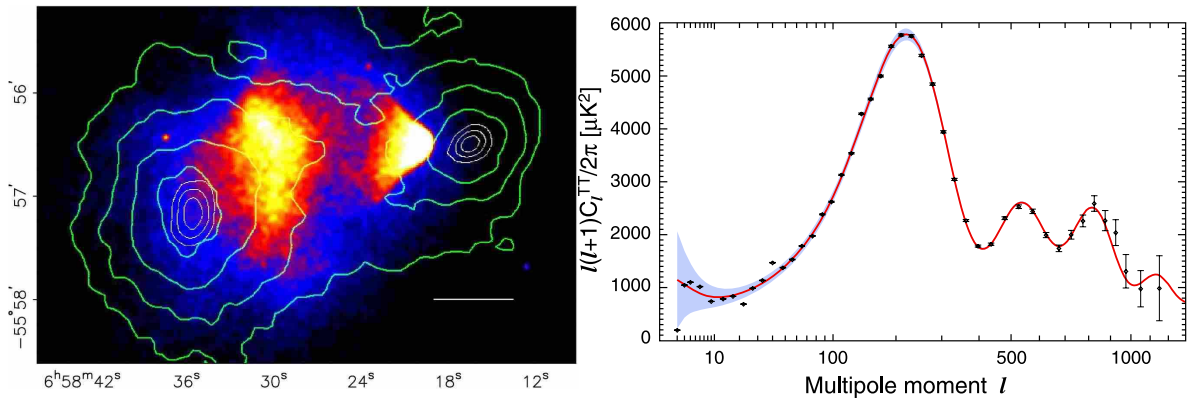

Figure 8: Left: The merging cluster 1E0657–558 ("Bullet cluster") [85]. The green contours correspond to the mass distribution reconstructed from gravitational lensing, while the color gradient shows the observed plasma masses in the X-ray spectrum. Right: The temperature power spectrum obtained by WMAP (black data) compared to the fit in the ΛCDM model (red curve) [26, 86–88].

the speed of light and is composed of at least one not yet observed non-baryonic, weakly interacting particle that can either be a massive WIMP (weakly interacting massive particle) [90] or the hypothetical axion postulated to solve the strong CP problem in quantum chromodynamics [91, 92].

A lot of effort is ongoing in order to detect dark matter WIMPs directly in experiments such as XENON [93, 94] or CDMS and EDELWEISS [95]. No clear indication of a signal has been identified so far[11].

Within supersymmetry, the LSP is stable if R-parity is conserved (see chapter 3.3). As such, it provides an interesting candidate for dark matter consistent with cosmological observations [99, 100].

3.5. Supersymmetry Breaking

All particles within a given supermultiplett share their quantum numbers for all operators commutating with the supersymmetry generators. This holds for the generator of translations

$$[P^\mu, Q_{\dot{a}}] = \left[P^\mu, Q^\dagger_{\dot{a}}\right] = 0 \tag{16}$$

and as such, $Q_{\dot{a}}$ also commutates with the mass operator $P^2 = M^2$:

$$\left[M^2, Q_{\dot{a}}\right] = \left[M^2, Q^\dagger_{\dot{a}}\right] = 0 \tag{17}$$

Therefore Standard Model particles and their superpartners are required to have the same mass and should have been found experimentally. Thus supersymmetry has to be broken.

Several supersymmetry breaking mechanisms have been studied having in common that supersymmetry breaking is assumed to be *spontaneous* and *soft* in order to keep solving the hierarchy problem and to prevent quadratic divergencies. Exactly analogous to the electroweak symmetry breaking described in chapter 2.3, spontaneous supersymmetry breaking requires a Lagrangian density invariant under supersymmetry transformations, but a non-vanishing vacuum expectation value which breaks supersymmetry. In this case, the so called F- and D-components of the superfields (see

[11] There is however an ongoing discussion regarding results obtained by DAMA/LIBRA [96, 97] and CoGeNT [98].

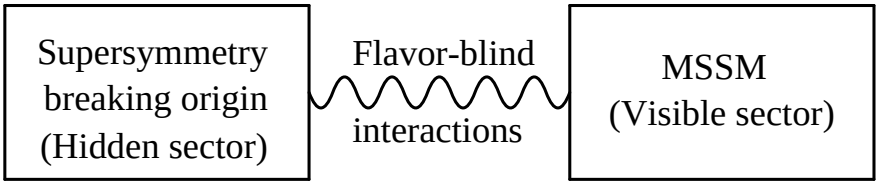

Figure 9: Sketch of the mediation of supersymmetry breaking between hidden and visible sector [61].

e.g. [61]) describing the fields of a supermultiplett take on this role. Correspondingly the various breaking mechanisms can generally be classified in D-term (Fayet-Iliopoulos, [101]) and F-term (O'Raifeartaigh, [102]) breaking.

As it is impossible to break supersymmetry without violating gauge invariance, the breaking needs to happen via additional fields in a *hidden sector* which is disjoint from the *visible sector*, i.e. the MSSM. The breaking of supersymmetry in this hidden sector is communicated to the visible sector via flavor-blind interactions with *messenger* fields as shown in figure 9.

There are quite a few possibilities regarding the nature of the additional messenger fields and the corresponding interactions leading to different predictions for the masses of the sparticles [103], for example:

- Mediation via gravity (SUGRA)
- Mediation via gauge fields (GMSB)
- Mediation via anomalies (AMSB)
- Mediation via gauginos
- Mirage-mediation

In the most general formulation of supersymmetry breaking, many new parameters (up to 105 [61]) have to be introduced to describe all possible supersymmetry breaking terms in the Lagrangian as a priori there is no knowledge on the nature of this breaking mechanism. Common for all of these scenarios listed above is the goal to reduce the amount of additional parameters.

In the following, only the first two types of supersymmetry breaking will be studied in more detail, further details on the various breaking scenarios can be found in [21] or [61]. It should be noticed that the necessity of supersymmetry breaking and the inclusion of an invisible sector certainly diminishes the predictive power of supersymmetry as it removes the unambigousness of unbroken supersymmetry (in terms of couplings and interactions) and the many new parameters have no direct connection to the Standard Model.

3.5.1. Gravity Mediation and mSUGRA

One possibility for the mediation of supersymmetry breaking from the hidden to the visible sector is via the gravitational interaction. *Supergravity* requires supersymmetry to be a local symmetry and provides a connection to the coordinate transformations of general relativity. Furthermore, the spin-3/2 gravitino is introduced as the superpartner of the spin-2 graviton which takes on the role as the "gauge" particle of local supersymmetry transformations and acquires a mass via the

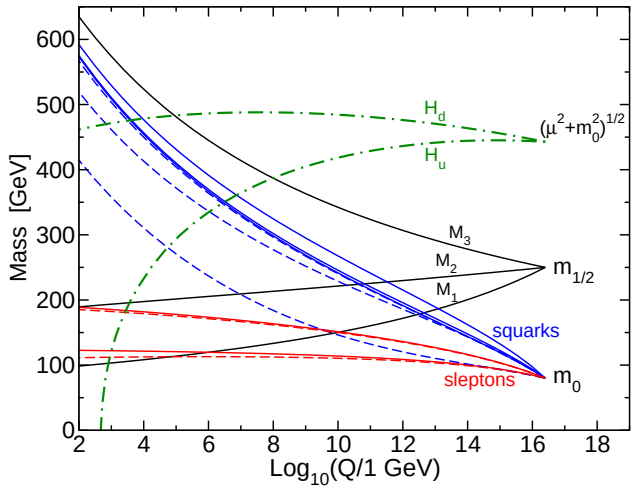

Figure 10: Scale dependence of the scalar and gaugino mass parameters for an examplary mSUGRA model [61].

super-Higgs mechanism in analogy of electroweak symmetry breaking[12]. While this mass $m_{3/2}$ of the gravitino is comparable to the masses of the other sparticles it only interacts gravitationally and therefore will not be of relevance in the following[13]. As a quantum theory description for gravity could not be found so far, there is no complete model describing the breaking in detail and one has to rely on an effective approach.

Assuming maximal universality for the supersymmetry breaking parameters as well as unification of the mass parameters and couplings at the GUT scale, only the following parameters are necessary for a complete prediction of the mass spectrum and the phenomenology of the corresponding *minimal supergravity* (mSUGRA) scenario [104–112]:

- m_0, the universal scalar mass
- $m_{1/2}$, the universal gaugino mass
- A_0, the universal trilinear coupling parameter
- $\tan\beta$, the ratio of the vacuum expectation values for the two Higgs doublets
- sign μ, the sign of the Higgsino mass parameter

Choosing values for these five parameters at the GUT scale determines the complete mass spectrum at the electroweak scale using the renormalization group equations as shown in figure 10.

This drastic reduction of the number of free parameters allows for performing analyses within mSUGRA by fixing parameters and studying hyperplanes in e.g. m_0 and $m_{1/2}$ as further discussed in chapter 4.4.

[12] Here, the analogon to the Nambu-Goldstone boson is a fermionic goldstino.
[13] In SUGRA scenarios, a gravitino LSP would have severe cosmological implications and is therefore disfavoured.

3.5.2. Gauge Mediation and GMSB

In constrast to the gravity-mediated supersymmetry breaking scenario above, in *gauge-mediated supersymmetry breaking* (GMSB) the mediation between hidden and visible sector takes place through ordinary gauge interactions via *messenger* particles. In the minimal GMSB scenario [113–119], these messenger fields form a complete representation of $SU(5)$ which preserves the unification property of the gauge couplings[14]. The masses of the gauginos are radiatively generated at one-loop level, while sfermion masses require two loops as both gauge and messanger fields are necessary [123]. In this mimimal model, six parameters describe the complete mass spectrum and the resulting phenomenology:

- Λ, the scale of supersymmetry breaking
- M_{mes}, the mass scale of the messenger fields
- N_5, the number of equivalent messenger fields
- C_{grav}, the scale of the gravitational coupling
- $\tan\beta$, the ratio of the vacuum expectation values for the two Higgs doublets
- sign μ, the sign of the Higgsino mass parameter

Λ is one of the most relevant parameters for the phenomenology of the model as it sets the overall mass scale on which all sparticles in the MSSM depend on linearly. The messenger mass scale M_{mes} has to be larger than the supersymmetry breaking scale Λ to avoid color and charge breaking in the messenger sector and somewhat smaller than the Planck scale to avoid gravity-induced flavor problems. N_5 also has a direct impact on the masses of the superpartners: The gaugino masses scale with N_5 while the sfermion masses scale with $\sqrt{\mathrm{N}_5}$. As in other scenarios $\tan\beta$ has important consequences on the mass differences and branching ratios between the first, second and the third family while sign μ impacts e.g. the stop mixing. Finally C_{grav} determines the lifetime of the next-to-lightest supersymmetric particle (NLSP).

The most distinctive feature of GSMB is the predicition of a gravitino LSP having important consequences on the resulting decay signatures and also cosmological implications. The GMSB model will be further analyzed in chapter 4.3.

3.6. Experimental Status

Until today no sparticle has been discovered. Before the start of the LHC, the most stringent limits on supersymmetry have been set by the LEP and Tevatron experiments[15]. Searches have been carried out in many different final states including jets, leptons, photons and missing energy[16]. It is very difficult to derive global limits on parameters of the MSSM due to the complexity introduced by supersymmetry breaking. Therefore usually certain breaking scenarios or Simplified Models are assumed in order to constrain the relevant parameter space. Consequently, limits on masses of sparticles can strongly depend on the underlying assumptions. As such e.g. the 95% C.L. limit on

[14] Further generalizations denoted as Generalized Gauge Mediation (GGM) are possible [120–122].

[15] LEP was the predecessor of the LHC at CERN, colliding electrons and postrons at up to $\sqrt{s} = 209$ GeV. The Tevatron was a proton-antiproton collider at the Fermilab near Chicago that operated at $\sqrt{s} = 1.96$ TeV.

[16] Particles interacting only weakly such as neutrinos or the LSP leave detectors without interactions causing an imbalance in the total energy sum of a collision.

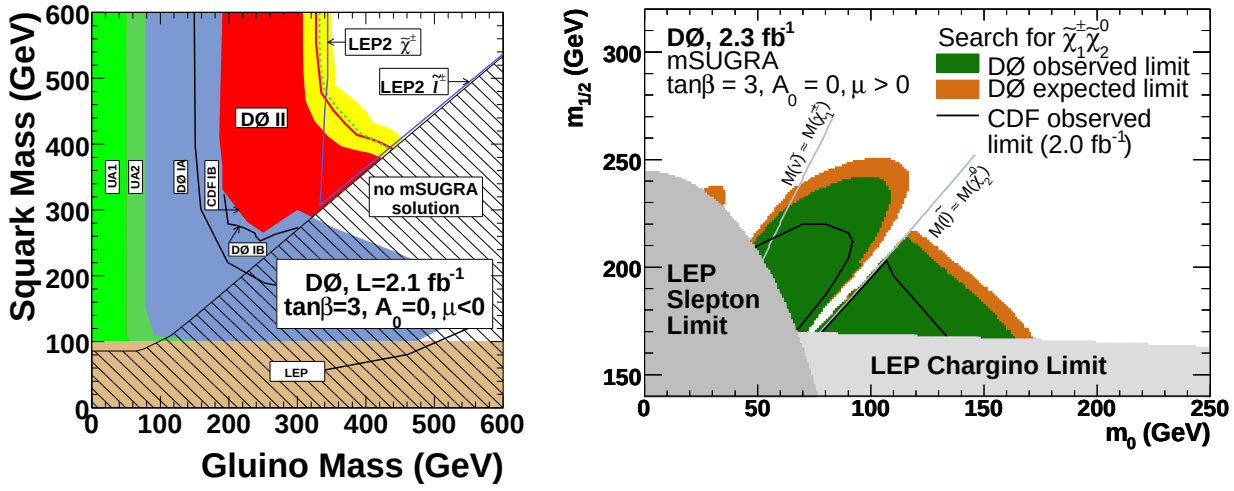

Figure 11: Left: 95% C.L. exclusion limit in the $m_{\tilde{g}}$-$m_{\tilde{q}}$ plane of a search in the Jets+E_T^{miss} channel by the DØ experiment compared to results from CDF and LEP [126]. Right: 95% C.L. exclusion limits in the m_0-$m_{1/2}$ plane from searches at LEP, DØ and CDF[127]. Both Limits are are obtained within the mSUGRA scenario.

the mass of the lightest neutralino in the general MSSM from direct searches at collider experiments currently excludes values below 46 GeV [124], while within the mSUGRA scenario assuming $A_0 = 0$ and $\mu > 0$ the $\tilde{\chi}_1^0$ mass limit is at 59 GeV [125].

Examples for exclusion limits on supersymmetry models before the start of the LHC are shown in figure 11. Figure 11 left shows the limits obtained from the interpretation of a search in the jets+E_T^{miss} channel by the DØ experiment within the mSUGRA scenario. The red area is excluded under the most conservative assumption on the production cross sections of squarks and gluinos while the red (dashed green) lines are the exclusion contours assuming nominal cross section values. Figure 11 right shows similar interpretations of searches for charginos and neutralinos in three lepton final states at CDF and DØ, where the actual model parameters m_0 and $m_{1/2}$ are used for setting the limit.

Similar to the exclusion limit in the mSUGRA scenario, Figure 12 shows results from the LEP and Tevatron experiments interpreted within the GMSB scenario. These results are based on searches requring two acoplanar photons and missing energy or two isolated leptons and missing energy. Assuming a massless LSP, the LEP experiments have excluded $\tilde{e}_R$ masses of up to 99.9 GeV, $\tilde{\mu}_R$ masses of up to 94.9 GeV as well as $\tilde{\tau}_1$ masses of up to 86.6 GeV [128]. Furthermore, the OPAL experiment at LEP has performed a detailed interpretation of several analyses within the GMSB scenario [129]. For a messenger scale $M_{mes} = 250$ TeV and $N_5 = 3$ messenger fields, mass scales Λ below 26 TeV are excluded.

Apart from direct searches at collider experiments, it is also possible to derive a prediction for masses in the MSSM using indirect constraints from electroweak precision data. As shown in Figure 13 both the mass of the top quark and of the W boson depend on the masses of the other particles in the MSSM and in the Standard Model, and as such a precision measurement of these masses (black contour) allows for a comparison to theoretical predictions and to fits assuming either only the Standard Model (blue contour) or different supersymmetry models (red/magenta contours).

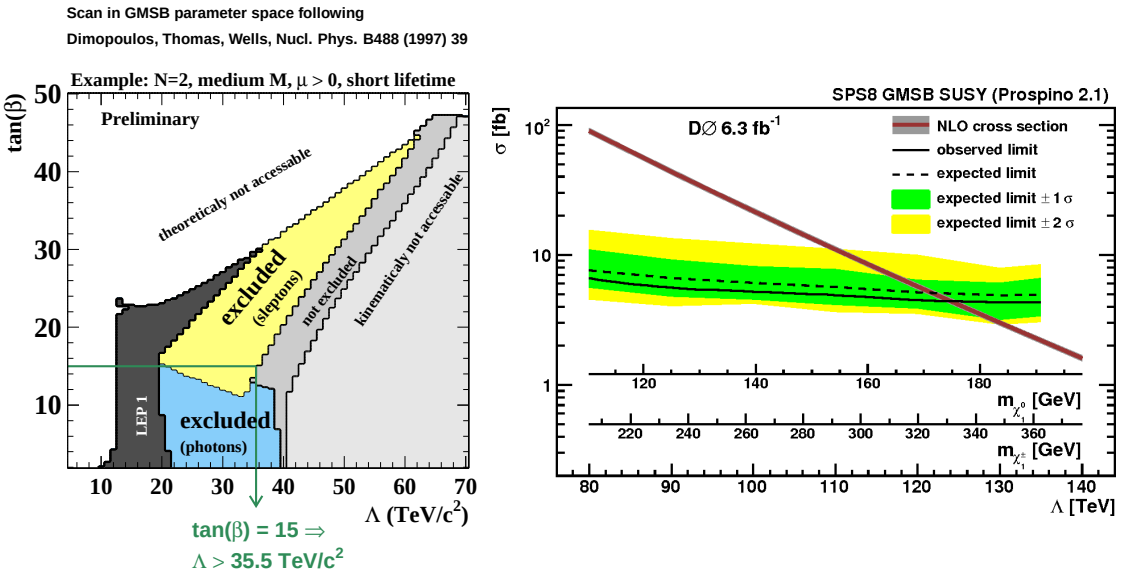

Figure 12: Left: 95% C.L. exclusion limits in the $\Lambda - \tan\beta$ plane combining searches for sleptons (yellow) and acoplanar photons (blue) at LEP [130]. Right: 95% C.L. exclusion limit on cross section times branching ratio as a function of Λ and the corresponding chargino and neutralino mass within the GMSB scenario obtained from acoplanar diphoton searches by the DØ experiment [131].

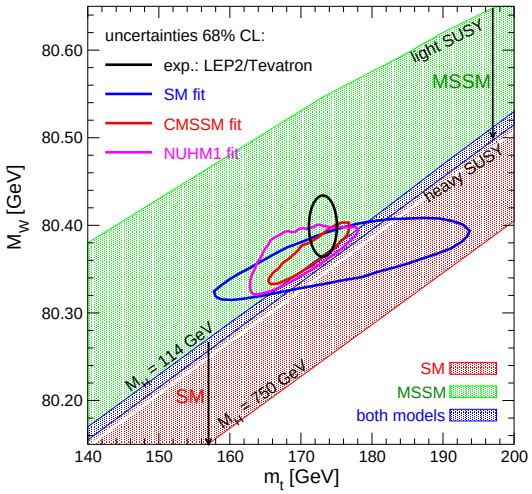

Figure 13: Prediction of m_W in the MSSM and in the Standard Model as a function of m_t and a comparison to current experimental data and fits to electroweak precision measurements [135].

Further indirect constraints can be derived from flavor physics measurements such as $B_s \longrightarrow \mu\mu$ [132] and $b \longrightarrow s\gamma$ [133, 134].

In the following chapter 4, the phenomenology specific to supersymmetry searches in the dilepton final state will be discussed, before explaining in chapter 5 how it is possible to test models of supersymmetry on unprecedented energy scales with the proton collisions provided by the LHC using the ATLAS detector to detect and reconstruct the collision events.

4. Supersymmetry in the Dilepton Final State

This thesis focusses on the search for supersymmetry in the proton-proton collisions provided by the Large Hadron Collider (LHC) which will be described in chapter 5. For this purpose, the dileptonic final state with the signature

$$\text{n jets} + \geq 2 \text{ leptons} + E_T^{\text{miss}}$$

will be analyzed. In the following the relevant supersymmetric production and decay modes leading to this signature will be discussed and compared to the background expectation from Standard Model processes motivating the dilepton final state as a search channel.

4.1. Production Processes

As discussed in chapter 3, the gauge couplings of the sparticles are identical to the couplings of their Standard Model partners. If the center of mass energy is sufficiently large, production processes via the strong interaction will therefore dominate in the proton-proton collisions of the LHC. Both pair production of squarks and gluinos as well as the production of one squark and gluino each is possible as shown exemplarily in Figure 14.

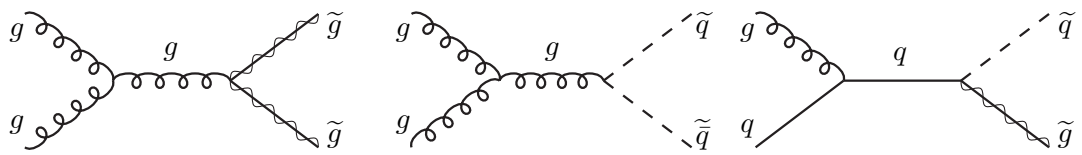

Figure 14: Feynman diagrams for gluino and squark production via gluon-gluon- and gluon-quark–fusion [61]. t- and u-channel diagrams are possible as well.

At hadron colliders such as the LHC, the partons as the fundamentally interacting particles are confined within hadrons. The interaction cross sections of partons $\hat{\sigma}_{ij}$ and of protons σ_{pp} are related via the factorization theorem [136]:

$$\sigma_{pp}(\sqrt{s}) = \sum_{i,j=q,\bar{q},g} \int dx_i dx_j f_i(x_i, \mu_F^2) f_j(x_j, \mu_F^2) \cdot \hat{\sigma}_{ij}(\sqrt{\hat{s}}, x_i, x_j, \mu_R^2) \tag{18}$$

Here, $\hat{\sigma}_{ij}$ denotes the parton-parton cross section, evaluated at a center of mass energy $\sqrt{\hat{s}}$ and a renormalization scale μ_R which is necessarily introduced in the finite order calculations of the perturbative expansion. The parton distribution functions (PDFs) [137–139] $f_i(x_i, \mu_F^2)$ describe the probability of finding a parton i within the proton with fraction x_i of the total proton momentum, evaluated at a factorization scale μ_F that separates the calculation via perturbative QCD from the non-perturbative regime.

The individual cross sections for the supersymmetric production processes depend on the sparticle masses as well as on the center of mass energy. For the proton-proton collisions at $\sqrt{s} = 7$ TeV discussed in this thesis, gluon-fusion induced production processes play a major role as the gluon parton distribution functions and correspondingly the parton luminosities for gluon-gluon production dominate [140].

In addition to the production of sparticles via the strong interaction, also electroweak production of charginos, neutralinos and sleptons is possible. These production mechanisms become especially relevant if the production of strongly interacting particles is suppressed by the PDFs due to high squark or gluino masses. While this thesis focusses mainly on the strong production modes, ATLAS has conducted searches for direct production of charginos and neutralinos [141] as well as sleptons [142].

4.2. Decay Modes

Being the gauge boson of the strong interaction gluons only couple to quarks (and other gluons). Correspondingly, gluinos can only decay into a (real or virtual) squark and a quark. Depending on the mass difference between squarks and gluinos, squarks either decay into a quark and a gaugino or into a quark and a gluino, provided that the gluino is sufficiently light. In such a case, the gluino decays in a three-body decay via a virtual squark leading to additional jets in the final state and longer decay chains.

In the supersymmetry breaking models considered in this work, squarks and gluinos are heavier than the lightest charginos and neutralinos[17]. Therefore (real or virtual) squarks decay in cascade decays via electroweak processes to the LSP, possibly involving additional gauginos or sleptons. The details of such decay chains depend on the mass spectrum and the gaugino mixing predicted by the model and can lead to significant differences with respect to the branching ratios as discussed in the following.

Depending on the mass spectrum, heavier gauginos usually decay via two-body decays into lighter gauginos or sleptons and sneutrinos, accompanied by corresponding Standard Model particles:

- $\tilde{\chi}_i^0 \to Z\tilde{\chi}_j^0, \mathrm{W}\tilde{\chi}_i^\pm, h^0\tilde{\chi}_j^0, \ell\tilde{\ell}, \nu\tilde{\nu}$
- $\tilde{\chi}_i^\pm \to W\tilde{\chi}_j^0, Z\tilde{\chi}_j^0, h^0\tilde{\chi}_j^\pm, \ell\tilde{\nu}, \nu\tilde{\ell}$

If the gaugino two-body decays are kinematically forbidden, three-body decays into two fermions via off-shell gauge bosons take place. Furthermore depending on the field content of the gauginos, i.e. the size of the bino, wino and higgsino components, certain decays are favoured. Similarly, sleptons and sneutrinos can decay into the corresponding lepton or neutrino and a gaugino in two-body decays, depending on the mass hierarchy. If the gravitino is the LSP (as realized in GMSB scenarios), decay chains of gauginos and sleptons end in gravitino final states as discussed in the following chapter.

4.3. GMSB

GMSB predicts that the lightest supersymmetric particle is the gravitino with a mass of a few eV which escapes the detection and thus leads to missing energy E^{miss}. With the gravitino having a tiny mass, the nature of the next heavier sparticle, the NLSP, has important consequences on the phenomenology of this scenario. For the interpretation of the results of this work within the

[17] Otherwise the LSP would be a charged particle or the squark decay via virtual gauginos could lead to a significant squark lifetime.

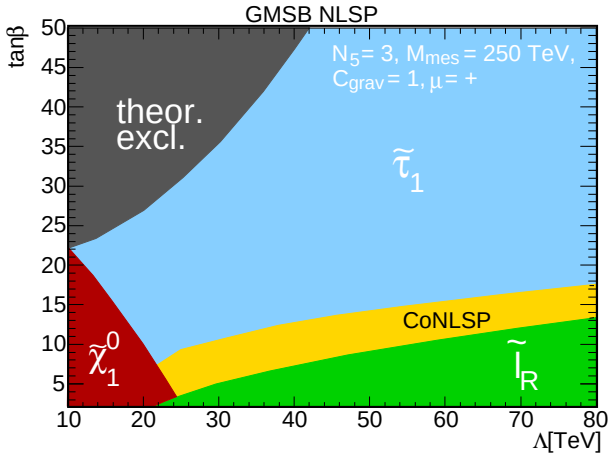

Figure 15: NLSP type in the Λ-tan β plane in the GMSB scenario [18]. In the region denoted as CoNLSP the mass difference between $\tilde{\tau}_1$ and $\tilde{\ell}_R$ is smaller than the tau mass. The upper left corner is excluded as it would lead to tachyonic states.

minimal GMSB scenario, the following parameters are fixed

- $M_{mes} = 250$ TeV
- $N_5 = 3$
- $C_{grav} = 1$
- sign $\mu = +$

and Λ and tan β will be varied as shown in Figure 15.

This choice of parameters is driven by the necessity to further restrict the parameter space to a two-dimensional hyperplane to allow for a meaningful interpretation. For $N_5 = 1$, the NLSP is either the lightest neutralino (small tan β) or the lightest stau (larger tan β), while for $N_5 \geq 2$ also slepton NLSPs are possible leading to leptonic final states. Existing limits from LEP, especially OPAL [129], and previous studies by ATLAS [143] lead to the parameter choice above as a benchmark scenario.

With this choice of parameters, typical resulting mass spectra are shown in Figure 16. As a general property of the investigated hyperplane, the squarks and gluinos have a much larger mass than the gauginos and the sleptons. As the gluino is heavier than the squarks, gluinos decay via real squarks. Furthermore squark production processes provide a larger contribution to the total cross sections.

The squarks usually decay directly to the lightest neutralino which subsequently decays via the NLSP to the Gravitino. Depending on the nature of the NLSP, the following signatures arise:

- $\tilde{\chi}_1^0 \rightarrow \gamma\tilde{G} \Longrightarrow$ Diphoton final states
- $\tilde{\chi}_1^0 \rightarrow \tilde{\tau}_1^{\pm}\tau^{\mp} \rightarrow \tau^{\pm}\tau^{\mp}\tilde{G} \Longrightarrow$ tau final states
- $\tilde{\chi}_1^0 \rightarrow \tilde{\ell}_R^{\pm}\ell^{\mp} \rightarrow \ell^{\pm}\ell^{\mp}\tilde{G} \Longrightarrow$ leptonic final states

These decays can take place at both legs of the Feynman diagram, and as such final states with up to four leptons are possible as depicted in Figure 17. Additionally it can be seen that final states with opposite-sign same-flavor lepton pairs will have a large branching ratio, motivating a corresponding selection.

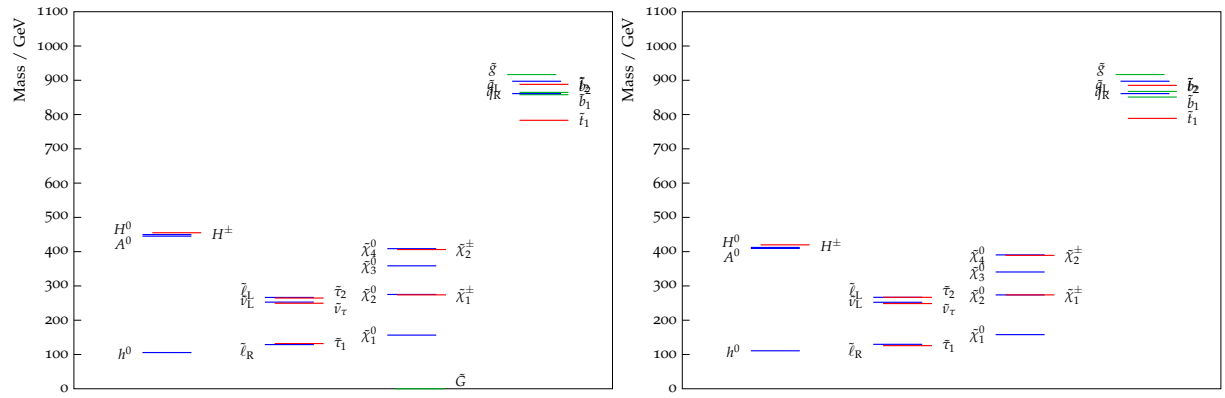

Figure 16: Mass spectra for $\Lambda = 40$ TeV and $\tan\beta = 5$ (left, $\tilde{e}_R/\tilde{\mu}_R$ NLSP) and $\tan\beta = 15$ (right, $\tilde{\tau}_1$ NLSP) (using [144]).

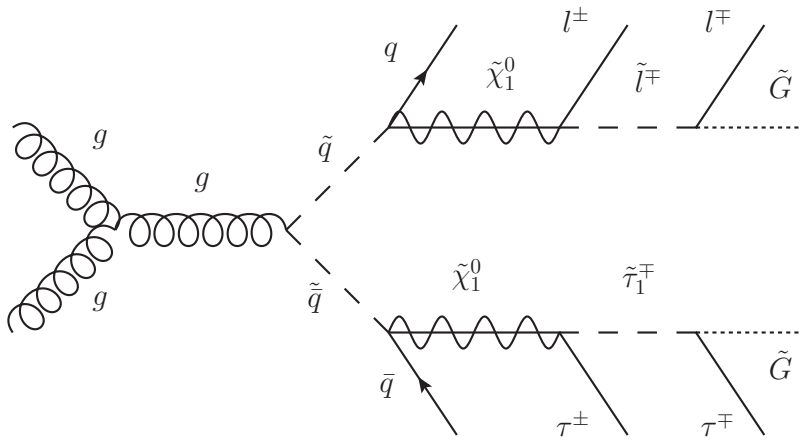

Figure 17: Representative Feynman diagram in the slepton NLSP region of the GMSB model for squark pair production followed by decays via neutralinos and sleptons to the gravitino leading to a multilepton+jets+E_T^{miss} final state (using [145]).

For larger values of $\tan\beta$, the $\tilde{\tau}_1$ becomes lighter than the right-handed selectron and smuon. Correspondingly, the branching ratios of the $\tilde{\chi}_1^0$ decays change as depicted in Figure 18. Therefore the sensitivity of the analysis is reduced in the stau-NLSP region, though leptonic final states are possible as the neutralino to slepton branching ratio does not vanish completely and the sleptons decay via staus in a three-body decay as shown in Figure 19. Furthermore, the possible presence of leptonic τ decays leads to leptonic final states as well.

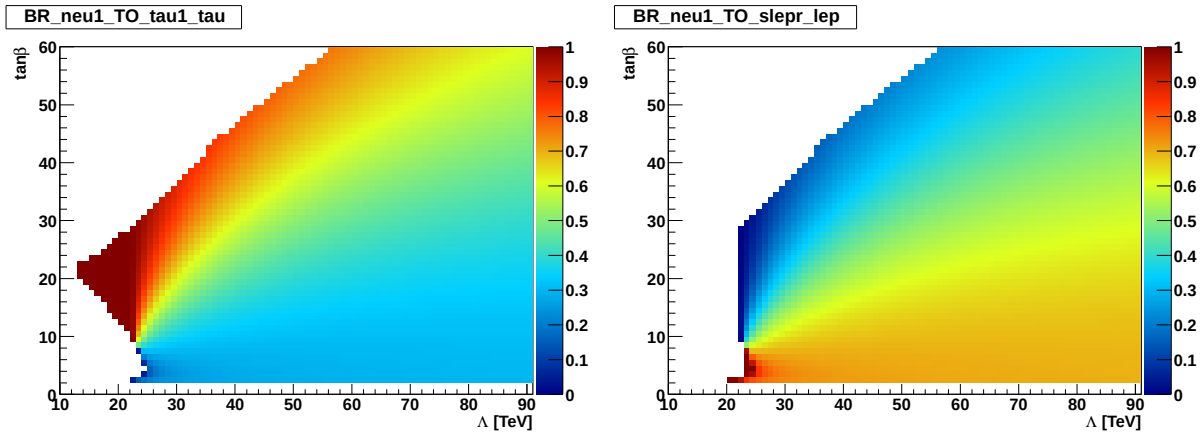

Figure 18: Branching Ratio of $\tilde{\chi}_1^0$ to $\tilde{\tau}_1\tau$ (left) and to $\tilde{\ell}_R\ell$ (right) as a function of Λ and $\tan\beta$.

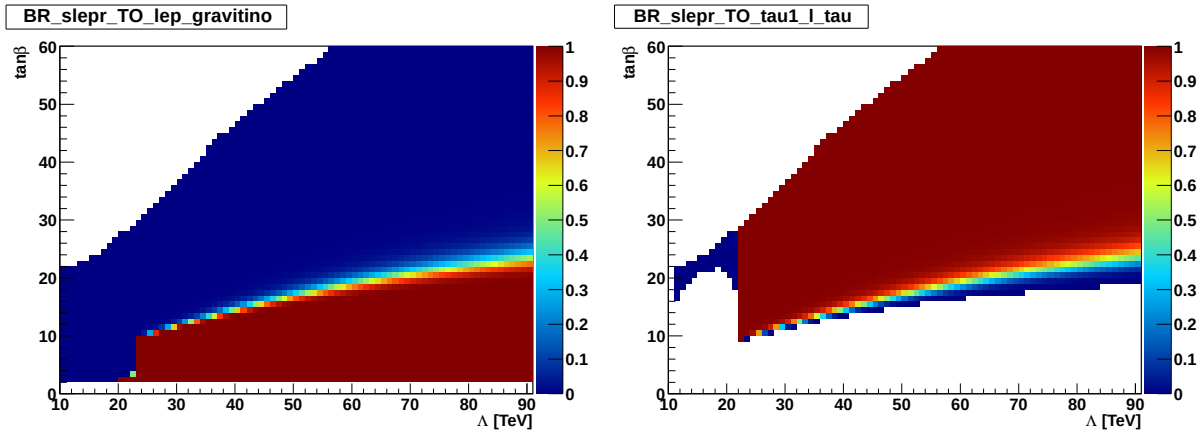

Figure 19: Branching Ratio of $\tilde{\ell}_R$ to $\tilde{G}\ell$ (left) and to $\tilde{\tau}_1\tau\ell$ (right) as a function of Λ and $\tan\beta$.

The differences between the slepton and the stau NLSP region do not only change the sensitivity of this analysis due to the branching ratios into leptonic final states, but also have important consequences on the kinematical properties of the signal. For example the transverse momentum of the lepton (which in general is relatively large due to the large mass splittings between $\tilde{\chi}_1^0$, $\tilde{\ell}_R^{\pm}$ and $\tilde{G}$) is significantly smaller in the stau NLSP than in the slepton NLSP region as shown in Figure 20, as the lepton originates either from the three-body gaugino decay or from leptonic tau decays.

The hierarchies in the mass spectra shown in Figure 16 are quite generic for the investigated hyperplane because the masses of the sparticles scale with Λ as discussed in chapter 3.5.2. This dependence has a direct impact on the cross section which is shown in Figure 21. The cross sections are calculated to next-to-leading order in the strong coupling constant, adding the resummation of soft gluon emission at next-to-leading-logarithmic accuracy (NLO+NLL) [146–150]. For the

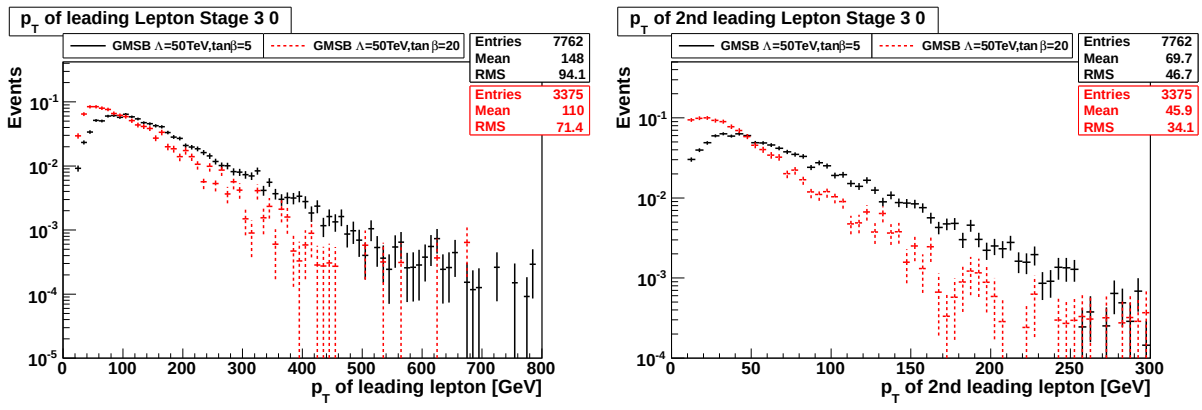

Figure 20: Transverse momentum of the leading (left) and second leading lepton (right) for the GMSB signals with $\Lambda = 50$ TeV and $\tan\beta = 5$ (black, $\tilde{\ell}_R^{\pm}$ NLSP) or $\tan\beta = 20$ (dashed red, $\tilde{\tau}_1$ NLSP) after a dileptonic preselection normalized to unity.

electroweak production modes, PROSPINO 2.1 [146, 151–153] is used. Additional details on the cross section prediction can be found in [154] and will be further discussed in chapter 9.3.

Apart from the dependence of the total cross section on Λ, the relative contributions of the different production processes to the total cross section change as a function of Λ and $\tan\beta$ as shown in figures 22. For low values of Λ, either $\tilde{q}\tilde{q}$ or $\tilde{q}\tilde{g}$ production provides the largest contribution, while for large values of Λ above 40-50 TeV electroweak production dominates, as the cross section for strong production processes falls faster than σ_{EW}.

Consequently less signal events will be produced increasing the value of the parameter Λ. However, the decrease of the cross section is partially compensated by the fact that the total energy in the events also scales with Λ, simplifying the suppression of Standard Model backgrounds. This property is depicted in Figure 23 using the effective mass

$$m_{eff} = \sum_{i=0}^{N_{jets}} \mathrm{p}_{T,i} + \sum_{j=0}^{N_{leptons}} \mathrm{p}_{T,j} + E_T^{\mathrm{miss}}$$

On the one hand, the division of the signal into strong production processes (broad peak at higher m_{eff} values) and electroweak production processes (peak at lower m_{eff} values) it is clearly visible in Figure 23. This separation occurs as strong production processes lead to more and typically harder jets in the final states. As σ_{strong} falls more rapidly with Λ than σ_{EW}, the mean of the m_{eff} distribution is larger for the models with smaller Λ. On the other hand, the contribution of the distribution from strong production processes is shifted to higher values for higher Λ, as the corresponding sparticles have a larger mass. This property will be further used in the signal region optimization in chapter 7.7.

Eventually the GMSB scenario is attractive both from a theoretical and an experimental point of view. In addition to the inclusive dilepton analysis studied in this thesis, also analyses using tau-based final states provide complementary sensitivity [155–157]. Furthermore, a dedicated multi-lepton analysis could further enhance the sensitivity [158].

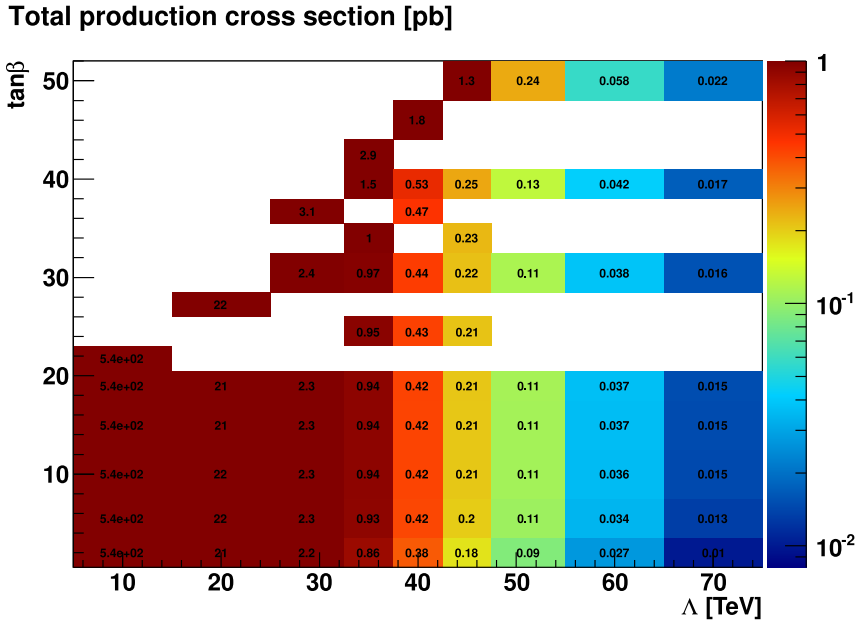

Figure 21: Total production cross section in the GMSB model as a function of Λ and $\tan\beta$. The entries in the plane correspond to the simulated grid discussed in chapter 7.5.

4.4. mSUGRA

In a similar approach to the GMSB scenario discussed in the previous chapter, a two-dimensional hyperplane in the mSUGRA parameter space is investigated. For this purpose, the following parameters are fixed:

- $\tan\beta = 10$
- $A_0 = 0$
- sign $\mu = +$

The chosen parameter values are motivated from indirect fits and from direct constraints in the Higgs sector [159–162][18].

In constrast to the GMSB model, the sleptons are significantly heavier in the mSUGRA scenario as shown in Figure 24. Thus the main source for leptons is the decay of charginos and neutralinos into the lightest neutralino being the LSP via real or virtual W and Z bosons. As such the branching ratios into a dileptonic final state are suppressed compared to the decay via sleptons due to the twofold requirement of heavier gauginos in the decay chain followed by leptonic gauge boson decays: Due to the smaller phase space, the branching ratio of squarks into heavier gauginos is considerably smaller than the direct decay into the LSP, and the small leptonic branching ratios of W and Z bosons further limit the probability of a dilepton final state. Furthermore, the transverse momenta of the leptons are smaller than in the GMSB model, especially if the intermediate W and Z bosons are virtual due to too small gaugino mass differences.

[18] This set of parameters is chosen as a common benchmark scenario between the ATLAS and CMS experiments, though it is now disfavoured by the recent Higgs boson discovery.

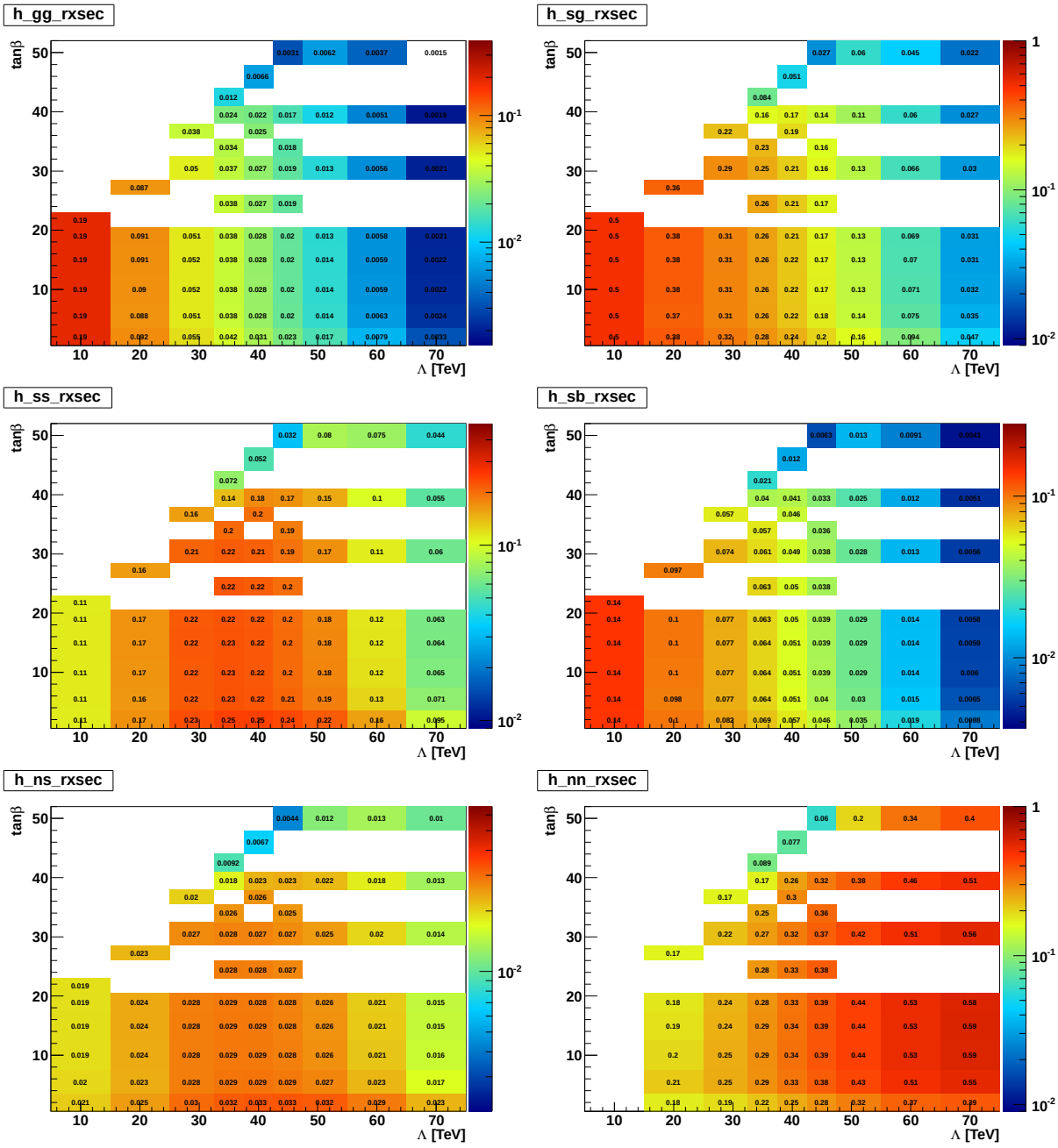

Figure 22: Relative contribution to the total production cross section for gluino-gluino (top left), gluino-squark (top right), squark-squark (middle left), squark-antisquark (middle right), squark–gaugino (bottom left) and gaugino-pair production (bottom right) as a function of Λ and $\tan\beta$. It should be noted that the z-axis range is different for the different plots.

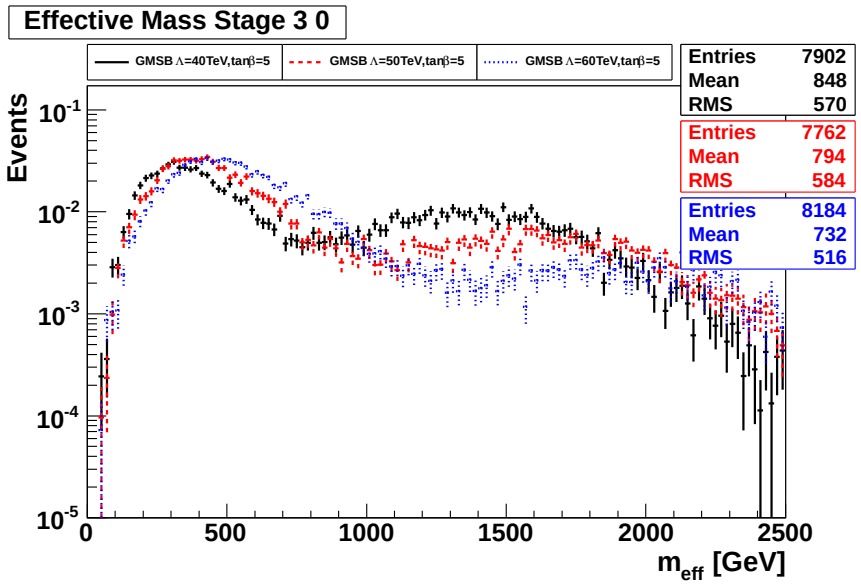

Figure 23: Distribution of effective mass for GMSB signal models with $\tan\beta = 5$ and $\Lambda = 40, 50, 60$ TeV after a dileptonic preselection normalized to unity.

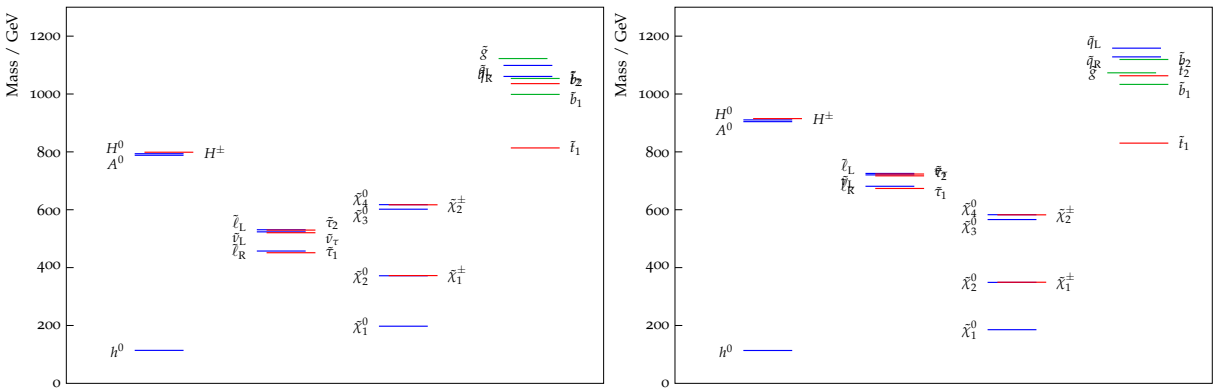

Figure 24: Mass spectra for $(m_0, m_{1/2}) = (420\text{ GeV}, 480\text{ GeV})$ (left, 2-body region) and for $(m_0, m_{1/2}) = (660\text{ GeV}, 450\text{ GeV})$ (right, 3-body region) (using [144]).

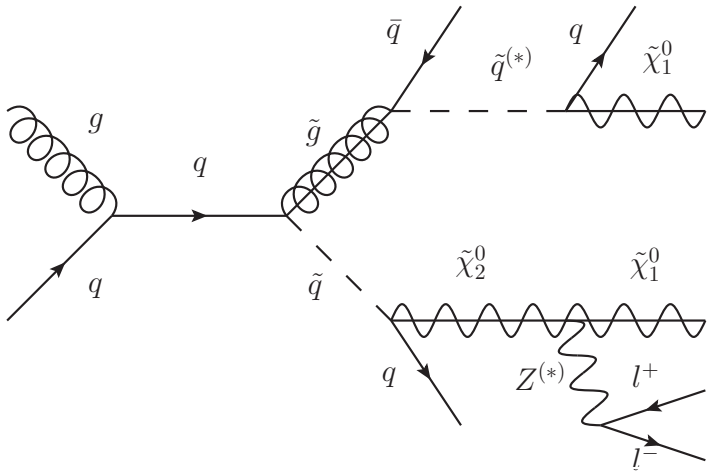

Figure 25: Representative Feynman diagram for the production of a squark and a gluino in the mSUGRA model resulting in a dilepton final state via the decay of a $\tilde{\chi}_2^0$ (using [145]).

Another difference to GMSB is that the gluino is not always heavier than the squark as also visible in Figure 24. This is due to the fact that the squark masses depend on both m_0 and $m_{1/2}$ while the gluino mass only depends on $m_{1/2}$. As a consequence, the $m_0 - m_{1/2}$ hyperplane is separated into a region where the gluinos decay via two-body decays ($m_0 \ll m_{1/2}$) and a region where three-body decays of the gluinos via virtual squarks take place ($m_0 \gg m_{1/2}$). A typical resulting Feynman diagram leading to a dileptonic final state is shown in Figure 25, alternatively also the decay via two charginos leads to the same signature[19]. Additional details on the properties of the investigated mSUGRA model with respect to the dilepton final state can be found in [14], while information on the cross sections is contained in [163].

From the description above it can be expected that the sensitivity of this dilepton analysis is not as large as in a zero- or one-lepton analysis. Nevertheless it provides complementarity on a common benchmark scenario.

4.5. Simplified Models

In addition to the investigation of specific supersymmetry breaking models, a phenomenological approach using *Simplified Models* [164, 165] is possible. In this effective bottom-up approach only specific Feynman diagrams of the MSSM and the corresponding event topologies are investigated. As such, Simplified Models provide no fundamental description of the breaking mechanism of supersymmetry. In contrast to GMSB and mSUGRA these models provide a simple and direct interpretation that can be re-cast into other theoretical frameworks [166].

Several Simplified Models are considered assuming pair production of either squarks or gluinos followed by decays via one or two intermediate sparticles into the LSP which is assumed to be the lightest neutralino. In the *one-step* case, the following decay chains are investigated:

- $\tilde{g} \to q\overline{q}'\tilde{\chi}_1^{\pm} \to q\overline{q}'W^{\pm}\tilde{\chi}_1^0$
- $\tilde{q}_L \to q'\tilde{\chi}_1^{\pm} \to q'W^{\pm}\tilde{\chi}_1^0$

[19] In this case, also same-sign lepton pairs are possible due to gluinos being Majorana particles.

using only left-handed squarks of the first and second generation and assuming wino-like charginos. The W boson can be real or virtual and Standard Model branching ratios are assumed. To investigate two-dimensional slices of the relevant mass parameter space, two different scenarios are defined using the compression parameter

$$x = (m_{\tilde{\chi}_1^\pm} - m_{\tilde{\chi}_1^0})/(m_{heavy} - m_{\tilde{\chi}_1^0})$$

with m_{heavy} being the mass of the squark or the gluino respectively. In one set of models, $x = 1/2$ is fixed while m_{heavy} and $m_{\tilde{\chi}_1^0}$ are varied. Alternatively, $m_{\tilde{\chi}_1^0}$ is set to 60 GeV while m_{heavy} and x are scanned. An example diagram is shown in Figure 26 top left.

Similarly, *two-step* Simplified Models are defined, assuming again pair production of gluinos or squarks. In contrast to the one-step case, two intermediate sparticles are inserted into the decay chain. Three different decay chains are investigated. In the first model the squarks or gluinos both decay via a chargino, which then decays either via a left-handed slepton or a left-handed sneutrino as shown in Figure 26 top right. Equal branching ratios to all generations of sleptons and sneutrinos are assumed. In the second type of two-step models, one chargino is replaced by the second lightest neutralino which decays either into a left-handed slepton and the corresponding lepton or into a sneutrino-neutrino pair as depicted in Figure 26 bottom left. Again equal branching ratios into all three generations of sleptons and sneutrinos are assumed. In the third class of models, again decays of the colored sparticles into two charginos are assumed, but no intermediate sleptons are present in the decay chain. The charginos instead decay into the second lightest neutralino and a (real or virtual) W boson. The $\tilde{\chi}_2^0$ then decays via (real or virtual) Z bosons to the LSP as shown in Figure 26 bottom right.

In all three sets of two-step Simplified Models, the masses of the squarks or gluinos and the LSP are varied, while the masses of the intermediate particles are fixed using similar compression parameters as in the one-step case. In the first two models involving sleptons, the $\tilde{\chi}_1^\pm$ and the $\tilde{\chi}_2^0$ have equal masses fixing $x = 1/2$. Furthermore the slepton and sneutrino masses are also assumed to be equal and halfway between the chargino/neutralino and the LSP mass. In the third model involving W- and Z bosons, the mass of the secondary $\tilde{\chi}_2^0$ replacing the sleptons/sneutrinos is set halfway between the chargino and the LSP mass correspondingly.

In all the investigated Simplified Models, the other superpartners are decoupled by setting their corresponding masses to 4.5 TeV. Additional information on the generated models, such as the corresponding cross sections, is contained in [163].

4.6. Background Processes

In order to search for the previously discussed supersymmetry models, it is necessary to identify the corresponding signal among the Standard Model background processes. Figure 27 shows the cross sections for Standard Model processes at hadron colliders. In general, the requirement of at least two isolated leptons with high transverse momentum effectively suppresses many of the Standard Model backgrounds, especially the dominant di- and multijet QCD events.

Dileptonic final states at hadron colliders are possible via different Standard Model processes. The most important one for this analysis is the dileptonic decay mode of top-antitop pair production as shown in Figure 28 left.

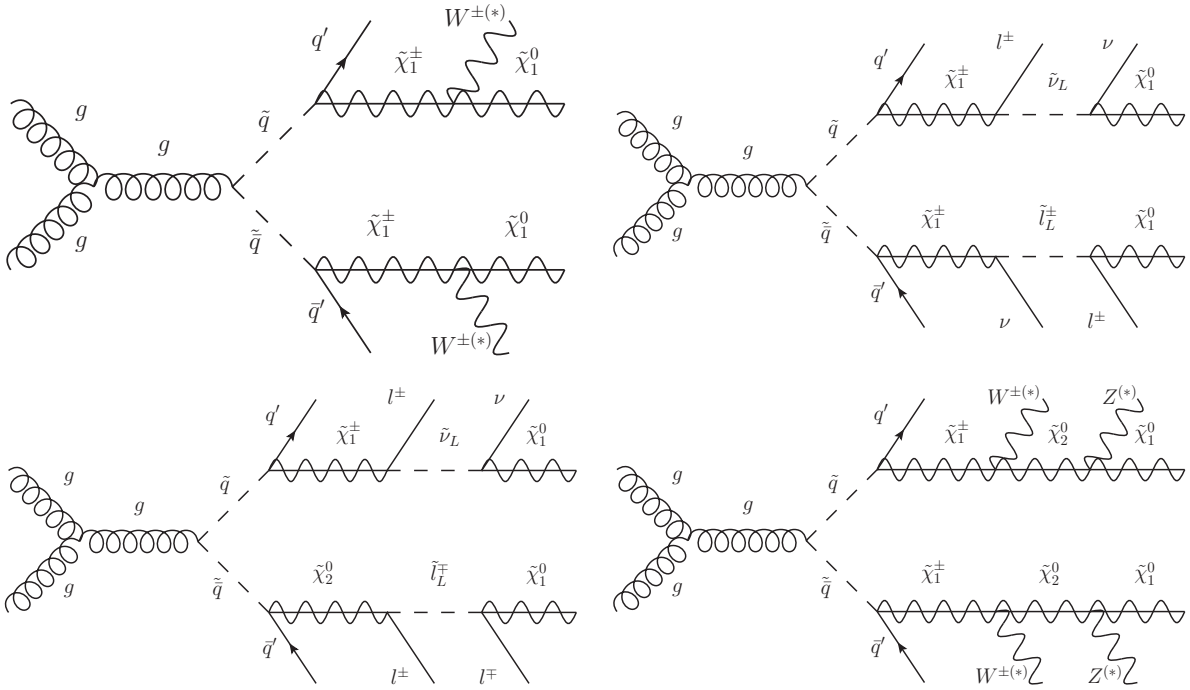

Figure 26: Representative diagrams for different Simplified Models: One-step decay via charginos (top left), two-step decay via sleptons (top right), two-step decay via neutralinos and sleptons (bottom left) and two-step decay via neutralinos and W/Z bosons (using [145]). Similar diagrams using gluino pair production are investigated as well.

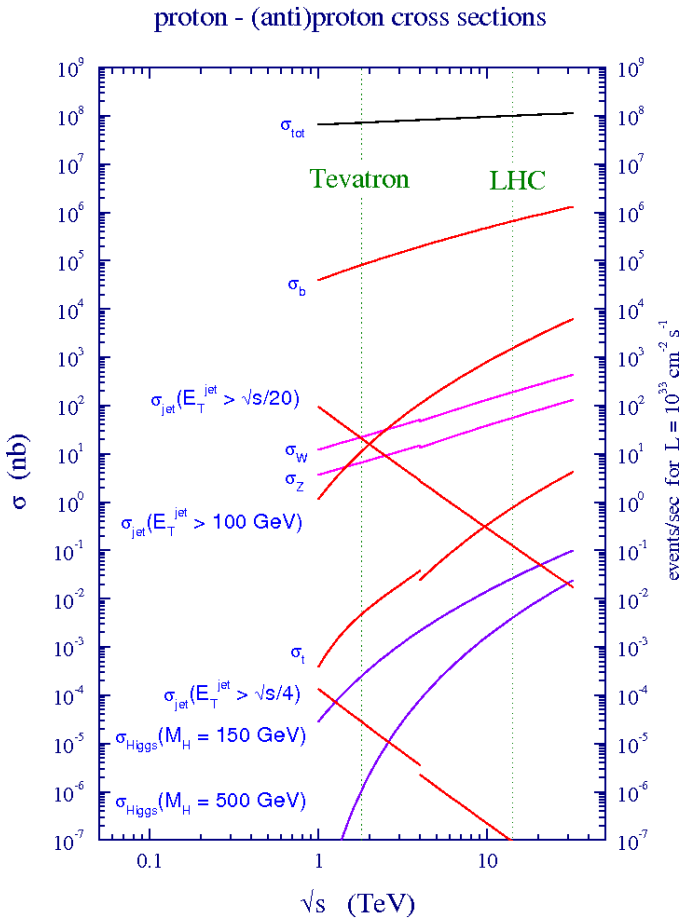

Figure 27: Standard Model cross sections at Tevatron and LHC [167] as a function of $\sqrt{s}$. The transition from $p\bar{p}$ to pp results in a small discontinuity of the curves at 4 TeV.

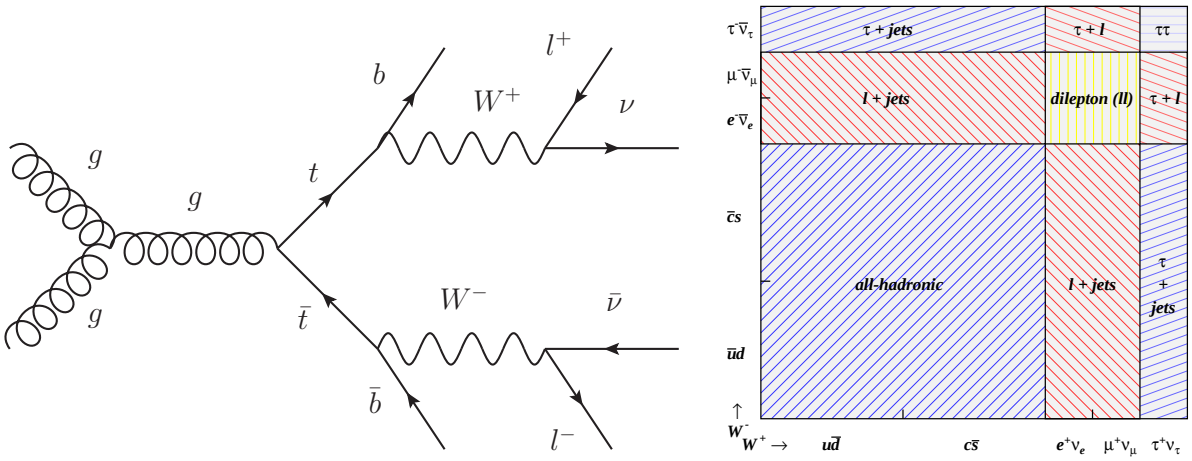

Figure 28: Left: Feynman diagram for dileptonic $t\bar{t}$ production (using [145]). Right: Branching ratios of the W bosons in the $t\bar{t}$ decay chain [168].

This process leads to final states containing two b-jets, two leptons of opposite sign and two neutrinos which leave the detector undetected and lead to E_T^{miss}. Additional jets can be produced via initial or final state radiation further mimicking the signal process. All three flavor combinations (ee,$e\mu$ and $\mu\mu$) are possible. The dileptonic decay of the top-antitop pair is suppressed compared to the semi-leptonic and fullhadronic decays as shown in Figure 28 right.

Another important possibility for a dileptonic final state is the decay of a Z boson into an electron positron or a muon antimuon pair as shown in Figure 29. While this process provides no intrinsic E_T^{miss}, the presence of additional jets from initial state radiation can lead to significant amounts of E_T^{miss} due to resolution effects and mismeasurement as further discussed in chapter 7. To a lesser extend, also the Z boson decay into a tau pair is important as dileptonic final states are possible when both taus decay leptonically, leading to intrinsic E_T^{miss} due to the additional neutrinos in the final state.

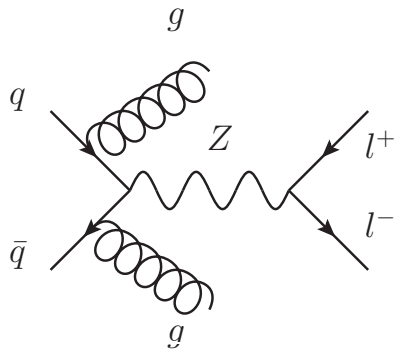

Figure 29: Feynman diagram for s-channel Z+jets production with two initial state gluon emissions (using [145]).

Further relevant background processes include the production of a single top quark (especially in the Wt channel) or the diboson production of a WW, WZ or ZZ pair. These processes are suppressed due to their smaller cross section, lower jet multiplicity and/or less E_T^{miss}.

Reducible backgrounds where one or both leptons are misidentified can arise from W+jet production or from QCD processes, as the corrosponding cross sections are large. The W+jet background also has intrinsic E_T^{miss} and is as such highly relevant for analyses involving a single lepton. In the context of this dilepton analysis, only a small impact due to these reducible backgrounds is expected.

5. The Large Hadron Collider and the ATLAS Experiment

With a design center of mass energy of 14 TeV and a target instantaneous luminosity of 10^{34} cm^{-2} s^{-1}, the Large Hadron Collider (LHC) at CERN provides proton-proton collisions at the highest energies reached at accelerator facilities in the world. Detecting the results of these collisions with the ATLAS detector allows for testing the Standard Model on unprecedented scales and for searching for the production and decay of sparticles as discussed in chapter 4.

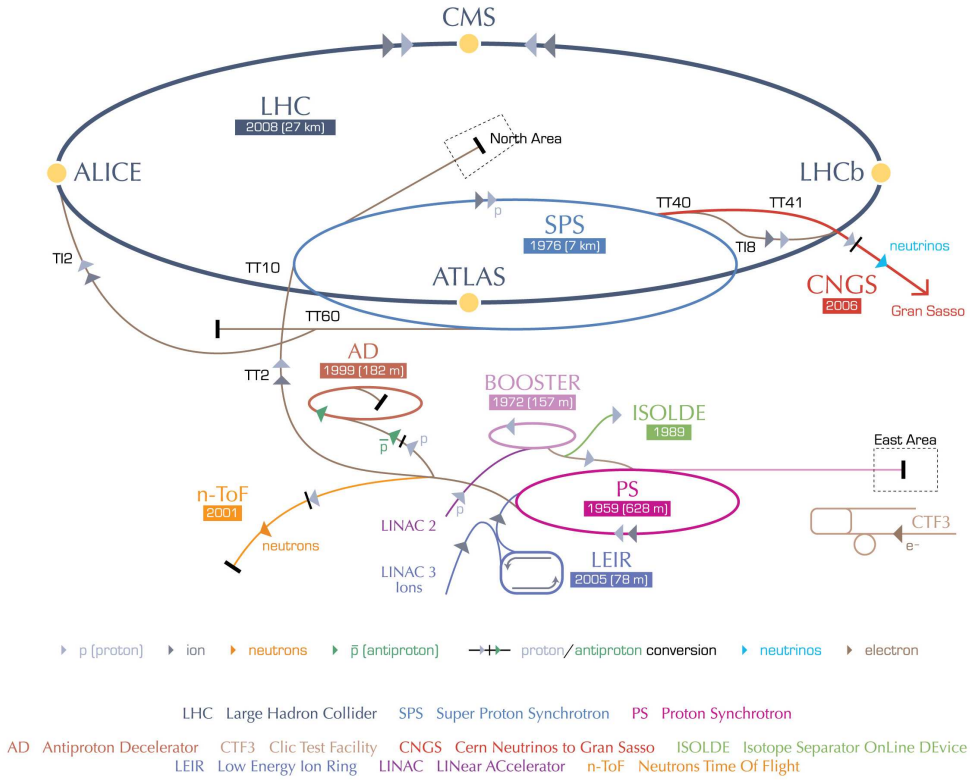

Figure 30: Overview over layout of the CERN accellerator complex including the Large Hadron Collider and the four main experiments [169].

5.1. The Large Hadron Collider

The LHC was constructed in the circular tunnel of its predecessor LEP (Large Electron Positron collider) after a long period of planning [170–172]. The tunnel has a circumference of 27 km and is located on average 100 m below ground level near Geneva under the swiss-french border. The LHC ring is formed by approximately 8000 dipole, quadrupole, sextupole and octupole magnets for focussing, stabilization and to keep the beams on a circular orbit. Both beam pipes are contained within one common yoke and cryostat forming the world's largest superconducting site using liquid helium for cooling the magnets to 1.9 K. The circular arcs of the ring are interspersed with eight long straight sections (LSS) that contain further instrumentation (collimation systems, radio frequency system, beam extraction) and of which four sections are used to form the interaction points around which the main experiments ATLAS, CMS, LHCb and ALICE are constructed. Before being filled

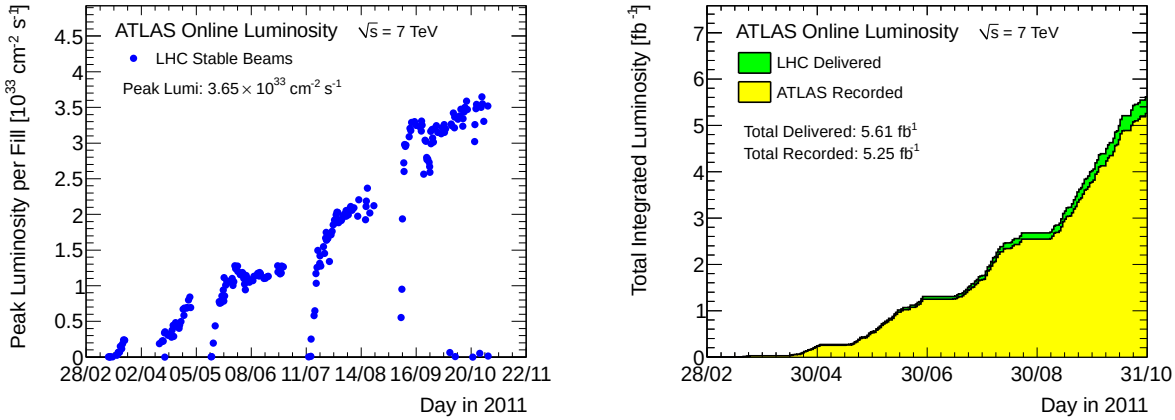

Figure 31: Left: Peak Luminosity per day in 2011 [176]. Right: Integrated luminosity recorded by ATLAS in 2011 [176].

into the LHC, the protons are accellerated via linear accellerators, the Proton Synchrotron (PS) and the Super Proton Synchrotron (SPS) to an injection energy of 450 GeV per beam. The protons are grouped in well-defined *bunches* which are[20] further arranged to *bunch trains* in order to reduce the fill time and to allow for easier increases in luminosity. The original design bunch spacing is 25 ns corresponding to a revolution frequency of 40 MHz using up to 2808 bunches in total. An overview over the LHC accellerator complex is show in Figure 30.

17 days after the first test beams successfully circulated in the LHC ring on August 2^{nd} 2008, a failure in a weld joint occurred leading to quenching magnets (i.e. loss of superconductivity) and an accidental release of 600 MJ stored in one sector of LHC dipole magnets [173]. After a shutdown of 14 months for reparation and installation of further protection systems [174], first collisions took place in november 2009 followed by the first regular data taking period in 2010 which provided an integrated luminosity of 35 pb^{-1} of proton-proton collisions at a center of mass energy of 7 TeV. Instantaneous luminosities of up to 2×10^{32} cm^{-2} s^{-1} were reached in 2010 operating at a bunch spacing of 50 ns.

In 2011, higher luminosities of up to 3.6×10^{33} cm^{-2} s^{-1} were achieved by using up to 1380 bunches consisting of 1.45×10^{11} protons each and due to smaller beam cross sections at interaction points. Further information on the commissioning of the LHC and the first periods of operation can be found in [175]. The total integrated luminosity of 4.7 fb^{-1} of proton-proton collisions at 7 TeV which were recorded in 2011 will form the main dataset of this thesis. Figure 31 shows the evolution of the peak luminosity (left) and the integrated luminosity (right) as recorded by ATLAS in 2011.

In 2012 the center of mass energy was raised slightly to 8 TeV, however the corresponding dataset will not be used within this work. Further upgrades of the LHC and its experiments are planned for the shutdown in 2013-2014, after which the beam energies will be raised to 6.5-7 TeV with instantaneous luminosities above 10^{34} cm^{-2} s^{-1} being planned [177]. Additional upgrades are forseen for the shutdown in 2018 [178] and to the High Luminosity LHC with instantaneous luminosities above 10^{35} cm^{-2} s^{-1} for 2021 [179] to enhance the physics potential even further [180].

[20] since September 2010

5.2. The ATLAS Detector

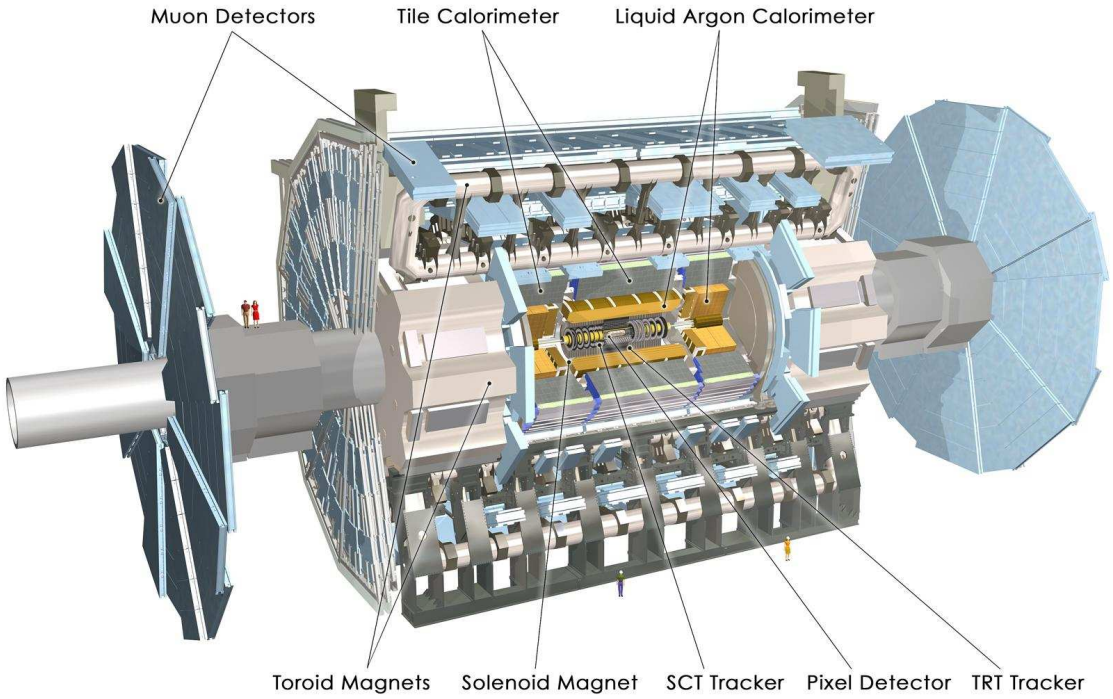

Figure 32: Cut-away view of the ATLAS detector and its components [181].

The ATLAS[21] detector is one of the two general purpose detectors at the LHC with a total size of 46 m x 26 m x 26 m. The detector design was driven by the goal of covering a broad physics spectrum with emphasis on the discovery of the Higgs boson and searches for new physics beyond the Standard Model.

The detector consists of the inner detector for tracking and vertexing, electromagnetic and hadronic calorimeters and a muon spectrometer as shown in Figure 32. The inner detector is contained within a superconducting solenoid magnet providing a magnetic field of 2 T to allow for momentum measurements of electrically charged particles. In addition, a toroidal magnetic field for the measurement of muon momenta is provided by large superconducting air-core magnets outside of the calorimeters.

The combination of position sensitive subdetectors, magnets and calorimeters is necessary in order to identify and measure the kinematical properties of the particles produced in the proton-proton collisions. Especially for the determination of missing transverse energy E_T^{miss} in the event (see chapter 5.2.1 and 6.7), it is important that the detectors cover as much of the 4π solid angle as possible. Details on the design and expected performance of ATLAS described in the following can be found in [182] and [183].

[21] **A** **T**oroidal **L**HC **A**pparatu**S**.

5.2.1. The ATLAS Coordinate System

In the following, the coordinate system used by ATLAS will be introduced. The primary interaction vertex is chosen as the origin of the coordinate system. The beam axis within the detector defines the z-axis while the x-y plane is transversal to the beam with the x-axis pointing towards the center of the LHC ring and the y-axis pointing towards the surface. In spherical coordinates ϕ denotes the azimuthal angle in the x-y plane and θ is the polar angle to the z-axis. The pseudorapidity η is defined via θ as

$$\eta = -\ln\tan(\theta/2) \tag{19}$$

as a good approximation of the rapidity $y = \frac{1}{2}\ln\frac{E+p_z}{E-p_z}$ for $E \gg m$. The rapidity is a useful quantity at hadron colliders as distances Δy are Lorentz invariant quantities and therefore the unknown Lorentz boost of the parton-parton center of mass system along the z-axis does not affect Δy. Correspondingly angular distances are expressed via

$$\Delta R = \sqrt{\Delta\phi^2 + \Delta\eta^2} \tag{20}$$

As the initial boost of the parton-parton system along the z-axis is unknown at hadron colliders, mainly the transverse momentum

$$p_T = \sqrt{p_x^2 + p_y^2} \tag{21}$$

and the missing transverse energy (see chapter 6.7)

$$E_T^{\text{miss}} = \sqrt{(E_x^{\text{miss}})^2 + (E_y^{\text{miss}})^2} \tag{22}$$

with

$$E_{x(y)}^{\text{miss}} = E_{x(y)}^{\text{miss,calorimeter}} + E_{x(y)}^{\text{miss,muon system}} \tag{23}$$

are used to describe the kinematical properties of an event.

5.2.2. The Inner Detector

The inner detector shown in Figure 33 consists of three different detectors for tracking and vertexing and is surrounded by the superconducting solenoid magnet.

The innermost component is the Pixel Detector consisting of pixel modules arranged in three concentric layers around the beampipe and three additional disks on either side. The pixel modules consist of silicon sensors and the corresponding front-end readout electronics providing in total approximately 80 million readout channels (pixels) of 50×400 μm^2 each. This high granularity is crucial for providing the necessary spatial resolution for vertex and track reconstruction in a high *pileup* environment [184]: The high instantaneous luminosity of the LHC leads to multiple interactions per bunch crossing as shown in Figure 34 which also impacts the reconstruction and performance of physics objects (chapter 6). Being close to the beampipe, providing sufficient radiation hardness and fault-tolerant logics while keeping a low material budget has been one of the main challenges in the design and the development of the Pixel Detector.

Similar to the Pixel Detector, the Semi-Conductor Tracker (SCT) is built of longer silicon microstrip detectors of 80 $\mu\text{m} \times 12$ cm arranged in four double-layers. Covering a larger area the SCT provides the main part of the ATLAS tracking system.

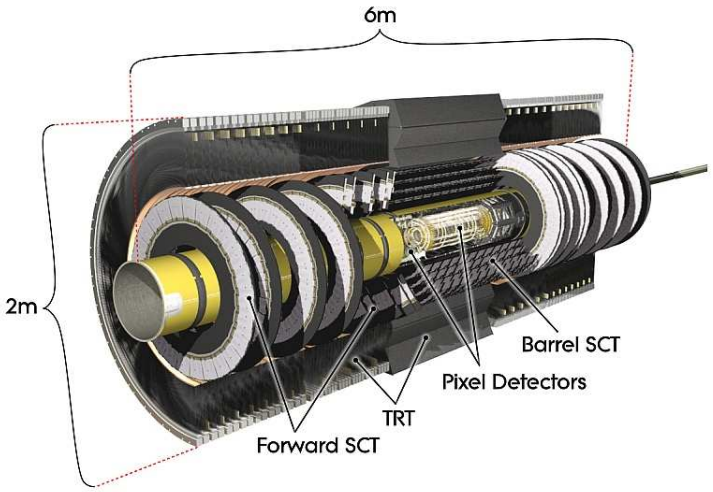

Figure 33: Cut-away view of the inner detector [183].

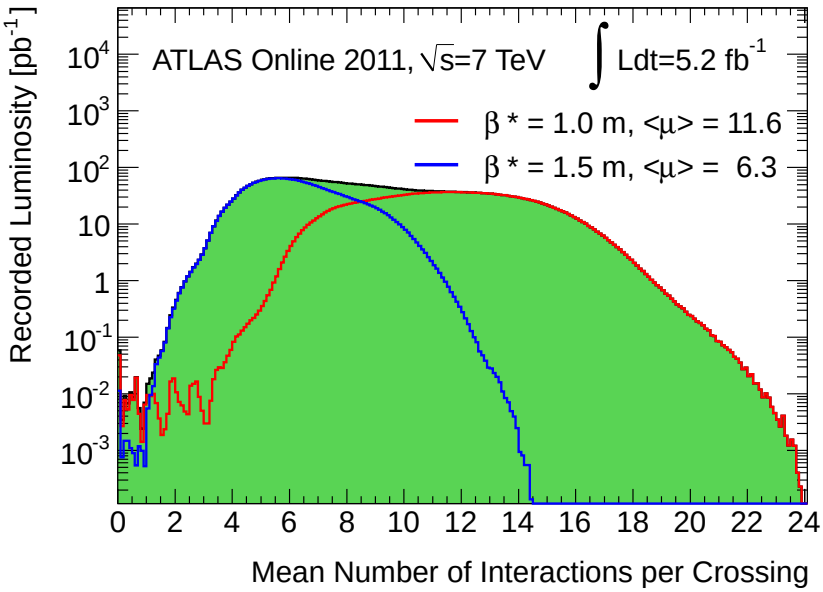

Figure 34: Average number of interactions per crossing in 2011 [176].

The outermost component of the inner detector is formed by the Transition Radiation Tracker (TRT) consisting of densely packed straw tubes filled with Xenon and containing a central wire as an electrode. The straw tubes are enclosed within polypropylene fibers producing transition radiation from highly relativistic particles due to the transition between materials with different dielectric constants. The photon emission depends on the relativistic velocity p/m with a threshold around $\beta\gamma > 1000$ [182]. These transition radiation photons produce energy depositions in the straw gas (high-threshold TRT hits) that can be distinguished from the lower-energy track ionization (TRT hits). By this means, the TRT provides information for the identification of electrons in addition to the track reconstruction as will be discussed in chapter 6.3.

The combination of Pixel Detector, SCT and TRT is used for the reconstruction of tracks in ATLAS by measuring spatial points (Hits) along the trajectory of a charged particle with high precision as discussed in chapter 6.1. The presence of the magnetic field provided by the solenoid magnet allows for the determination of the momenta of charged particles by measuring the curvature of the corresponding tracks. Both Pixel and SCT detector cover pseudorapidities $|\eta| < 2.5$ while the TRT is limited to $|\eta| < 2$.

5.2.3. The Calorimeter System

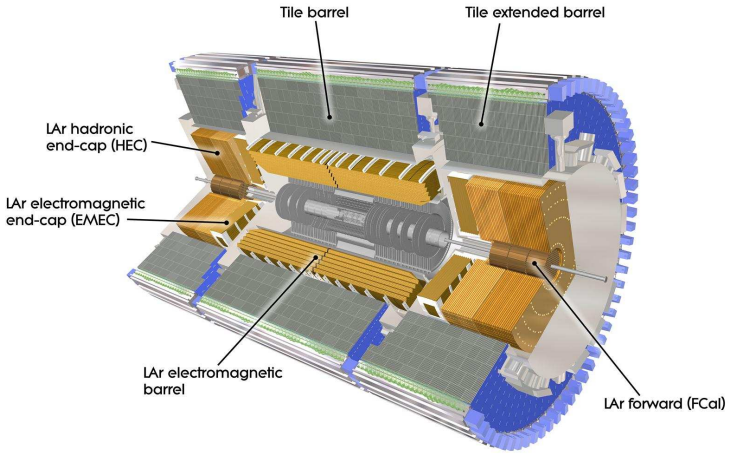

Figure 35: Cut-away view of the ATLAS calorimeters [183].

The ATLAS detector provides two calorimeter systems for measuring the energies of the particles produced in the proton-proton collisions: The electromagnetic and the hadronic calorimeter as shown in Figure 35.

Surrounding the inner detector and the solenoid magnet, the electromagnetic calorimeter follows the typical design of a *sampling* calorimeter. The absorber that stops electrons and photons via electromagnetic interactions leading to typical electromagnetic showers (see chapter 6.3) consists of lead layers arranged in an accordion-like structure. Liquid Argon (LAr) is used for the active material providing a homogeneous response that allows for the determination of the energy of electrons and photons. As shown in Figure 35, the electromagnetic calorimeter is separated into a central barrel ($|\eta| < 1.475$), end-cap wheels ($1.375 < |\eta| < 3.2$) and forward calorimeters ($3.1 < |\eta| < 4.9$). Longitudinally the barrel and end-cap calorimeters are segmented in three different

layers with different granularities $\Delta\eta$ and $\Delta\phi$ to separate two photons or electrons. For the central region $|\eta| < 1.8$ an additional presampler detector has been installed to correct for energy losses upstream of the calorimeter. More details on the performance of the reconstruction of electrons using the electromagnetic calorimeter will be discussed in chapter 6.3.

As neutral and charged hadrons which form the jets produced by the hadronization of quarks and gluons have a longer radiation length than photons and electrons, a hadronic calorimeter is installed around the electromagnetic calorimeter to measure their energies. Like the electromagnetic calorimeter, the hadronic calorimeter is a sampling calorimeter using steel for the absorption and plastic scintillators (*tiles*) as active material for detecting the hadronic showers of strongly interacting particles. For the very forward region ($|\eta| > 3.2$), liquid Argon and copper or tungsten are used for the active and passive components to cope with the higher radiation levels. The granularity of the hadronic calorimeter is coarser ($\Delta\eta \times \Delta\phi = 0.1 \times 0.1$) as it is not necessary to identify single hadrons in jets in order to reconstruct the energy and direction of the initial parton. The reconstruction of jets using the hadronic calorimeter will be described in chapter 6.5. The identification of jets originating from b- and c-quarks is made possible via backwards extrapolation from the calorimeter to the inner detector and the beam pipe as discussed in chapter 6.6.

In general, the resolution of a sampling calorimeter as a function of energy can be described by three terms:

$$\frac{\sigma_E}{E} = \frac{N}{\sqrt{E}} \oplus \frac{S}{E} \oplus C$$

Here, the noise term N describes electronic and detector noise as well as pileup contributions[22] which are independent of the energy and dominate the overall resolution for the low energy regime. The constant term C contains the contributions that scale with the energy such as the signal loss in passive material. As such, the constant term is most relevant for the measurement of particles with high energy. In the intermediate regime, the sampling term S containing the stochastical fluctuations in the energy measurement of the sampling calorimeter is of high importance. The performance of the ATLAS calorimeters will be further discussed in terms of the resulting systematic uncertainties on the leptons, jets and missing transverse energy in chapter 9.

5.2.4. The Muon System

Being mimimal ionizing particles, muons traverse the complete ATLAS calorimeter as they do not interact hadronically and emit no bremsstrahlung[23]. Therefore a large muon spectrometer as the outermost detector (Figure 36) is used to identify muons and to reconstruct their momenta using the magnetic field provided by the toroid magnet combined with information from the inner detector. The toroidal magnetic field deflects the muons orthogonal to the transversal detector plane within $|\eta| < 2.7$ using an inhomogeneous field with on average 0.5 T. For the central part ($|\eta| < 2.0$), layers of monitored drift tubes (MDT) provide the measurement of the muon track components while for $2.0 < |\eta| < 2.7$ cathode strip chambers (CSC) are used as shown in Figure 36. MDT and CSC are accompanied by resistive plate chambers (RPC) and thin-gap chambers (TGC) for fast triggering and to complement the muon reconstruction as described in chapter 6.4.

[22] In addition to the *in-time pileup* from multiple interactions per bunch crossing, also *out-of-time pileup* due to energy depositions from previous or later bunch crossings can impact the calorimeter measurements.
[23] below energies of ≈ 500 GeV

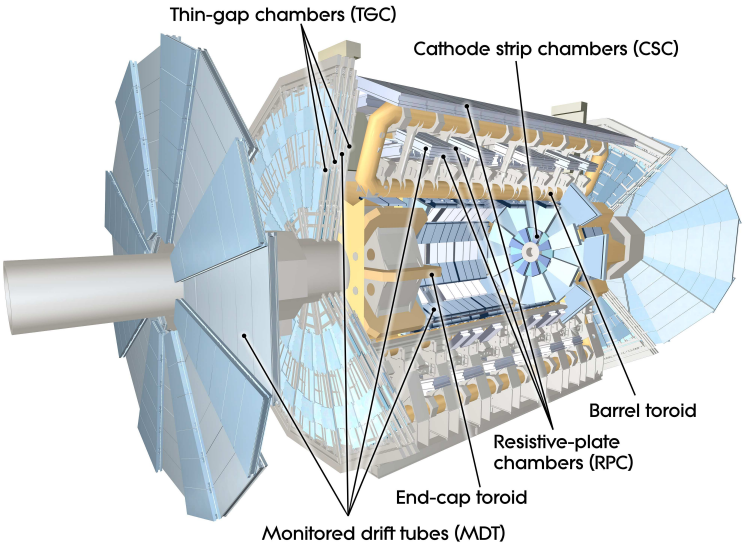

Figure 36: Cut-away view of the ATLAS muon system [185].

5.2.5. The Luminosity Detectors

Several detectors are used for a precise determination of the instantaneous and the integrated luminosity delivered by the LHC. While the absolute luminosity is obtained from the LHC beam conditions measured via *van der Meer* scans [186], the relative luminosity is constantly determined using several dedicated forward detectors, with LUCID[24] [187] and BCM[25] [188] providing the main measurement. LUCID is a Cherenkov detector consisting of 20 optically reflecting gas tubes installed around the beampipe at the longitudinal ends of ATLAS covering $5.6 < |\eta| < 5.9$. It measures the number of inelastic proton-proton interactions per bunch crossing by detecting the Cherenkov radiation produced from the interaction of charged particles in the gas tubes. The BCM detector consists of each two arms of radiation-hard diamond sensors located around the beampipe on both sides of ATLAS at $z = \pm 184$ cm (corresponding to $|\eta| \approx 4.2$), thus allowing for a coincidence measurement of the number of collisions. Furthermore, the BCM detector is also used to monitor the beam gas and beam halo backgrounds providing a fast feedback for the accellerator operation as well as a very important detector protection via emergency beam dumps in case of beam losses.

5.2.6. The Trigger System

With a nominal interaction rate of 40 MHz and more than 160 million readout channels, it is impossible to record and store all collisions provided by the LHC. Therefore a dedicated trigger system is used to identify and select events stemming from interesting rare processes while rejecting most of the ordinary QCD events in real-time [189, 190].

The ATLAS Trigger system is composed of three layers as shown in Figure 37. The first level trigger (LVL1) is purely hardware-based. It reduces the event rate to 100 kHz using fast algorithms scanning regions of the calorimeters and the muon system for possibly interesting information.

[24] LUminosity measurement using a Cherenkov Integrating Detector
[25] Beam Conditions Monitor

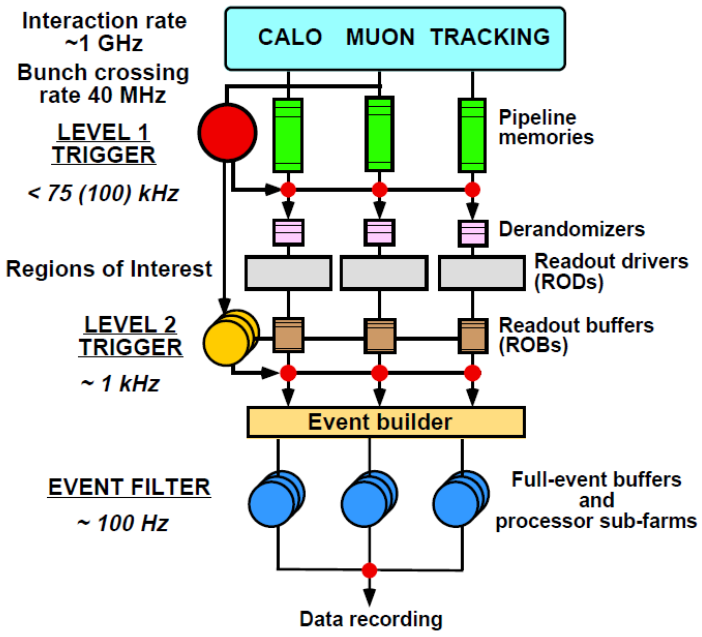

Figure 37: Block diagram of the Trigger/DAQ system [182]. The actual trigger rates used for the 2011 data taking period surpass those given in the diagram.

The second level trigger (LVL2) combines these information using additional selection algorithms reducing the rate to 2 kHz. The last layer is formed by the "Event Filter" (EF) which uses the full event information for the trigger decision and further decreases the event rate to ≈ 400 Hz which is small enough for permanent storage. Both LVL2 and EF rely on software-based algorithms run on a small computer cluster. This multi-layered trigger system allows for the usage of complex trigger chains as each subsequent layer has more time for its decision. The triggering of interesting physics processes is further complicated by the presence of pileup. This is one of the reasons why additional upgrades of the ATLAS trigger system are foreseen for the shutdown in 2013-2014 [191].

5.2.7. Data Acquisition and Computing

Following a positive trigger decision, events will be recorded and fully reconstructed by the data acquisition (DAQ) system at the Tier-0 site, a dedicated computer cluster forming the lowest layer of the ATLAS computing system [192] as part of the worldwide LHC Computing Grid (LCG) [193]. After the reconstruction, the data is further transfered to several large computing centers (Tier-1) which then serve additional smaller centers (Tier-2) and universities (Tier-3) downstream in order to spread-out the data. This decentral layout guarantees the parallel access by many physics analysts independent of the geographical location.

5.2.8. Physics and Detector Simulation

In order to compare the measured results from the LHC collisions to the theoretical predictions, it is necessary to use Monte Carlo simulation. At first the matrix element of a certain physics processes as well as the hadronization of the quarks and gluons leading to jets is calculated using various

generators. Subsequently, the Monte Carlo events produced by these generators are simulated using the GEANT4-based [194] ATLAS detector simulation *Athena* [192, 195]. The presence of additional interactions from pileup is included within the simulation. Using common data formats it is possible to run the same digitization, reconstruction and Trigger algorithms on the output of the simulation and on measured data.

6. Object Definition and Reconstruction

In order to search for supersymmetry in the dileptonic final state, it is necessary to identify the jets and leptons and to reconstruct their transversal energy by using the information from the subdetectors, magnets and calorimeters described in the previous chapter 5. In the following, a brief summary on the definition and reconstruction of the physics objects relevant for this analysis will be layed out before further discussing the event selection requirements in chapter 7.

6.1. Tracks

Charged particles produced in the proton-proton collisions traversing the inner detector leave hits in the Pixel, SCT and TRT detectors. From these hits, particle trajectories (tracks) are reconstructed using several different algorithms, with the *inside-out* algorithm being most important for tracks with a transverse momentum of several GeV [196]. Starting from track seeds using three space-points closest to the interaction point, further hits are associated by extrapolation outwards to the TRT and ambiguities between overlapping tracks are resolved. In order to further increase the track reconstruction efficiency, this track reconstruction scheme is accompanied by an additional back-tracking algorithm starting from seeds in the TRT. The lowest transverse momentum in the track reconstruction for the 2011 dataset at $\sqrt{s} = 7$ TeV has been set to 500 MeV. As an example, Figure 38 shows the expected track reconstruction efficiency as a function of η for electrons and muons with different transverse momenta. Additional information on the reconstruction of tracks in ATLAS are contained in [183, 196–198]

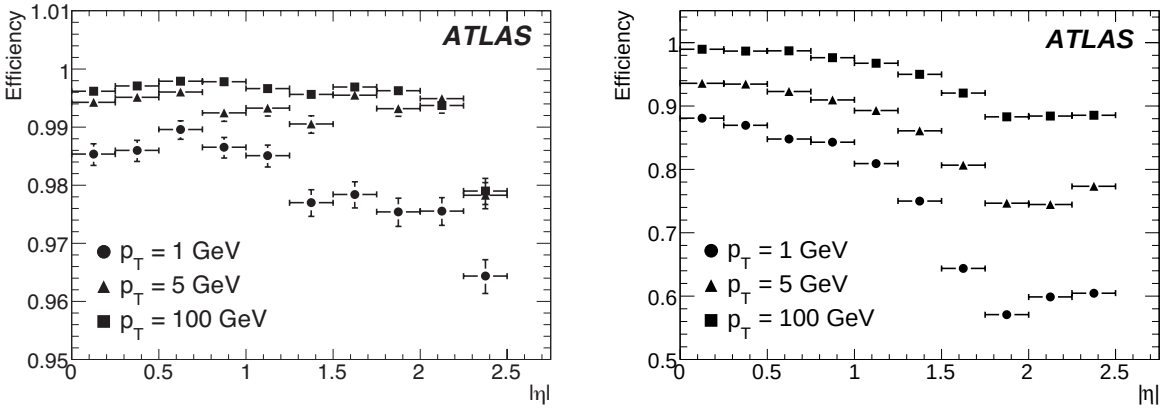

Figure 38: Simulated track reconstruction efficiencies as a function of $|\eta|$ for muons (left) and electrons (right) with p_T of 1, 5 and 100 GeV [183].

6.2. Vertices

Vertices are reconstructed based on the tracking information provided by the inner detector. Both primary and secondary vertices are identified using dedicated algorithms. The main primary vertex is defined as the one with the largest sum of $|p_T^2|$ of associated tracks. The reconstruction of the vertices from additional interactions provides a handle for the treatment of pileup as shown in Figure 39 and for the suppression of jets originating from such additional interactions as described in

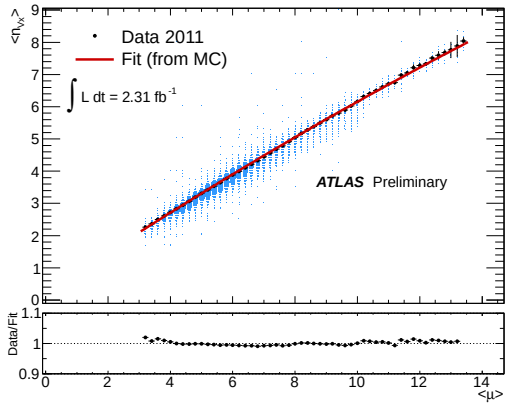

Figure 39: Distribution of the average number of reconstructed vertices as function of the average number of interactions per bunch crossing [201].

chapter 6.5. Information on secondary vertices is highly relevant for the identification of jets originating from the decays of B-Hadrons as further discussed in chapter 6.6. Details on the performance of the reconstruction of primary vertices in ATLAS can be found in [198–200].

6.3. Electrons

The reconstruction and identification is based on the tracks reconstructed in the inner detectror and the energy clusters in the electromagnetic calorimeter.

6.3.1. Electron Reconstruction

In the main reconstruction algorithm[26], seeds for the electron reconstruction are obtained from energy clusters in the electromagnetic calorimeter with a transverse energy above ≈ 3 GeV. These seed clusters are found using a *sliding window* algorithm [202] with a fixed rectangular size of 3×7 (5×5) cells in (η, ϕ) in the barrel (endcap) region. The clusters are loosely matched to tracks from the inner detector to form electron candidates [203]. The energy of the electron candidate is set to the cluster energy, which itself combines the information from the presampler and the three calorimeter layers. The electron momentum information is usually taken from the corresponding track (providing higher resolution) unless the track contains less than four pixel and SCT hits such that the cluster information is used as η and ϕ. Additional details on the electron reconstruction can be found in [183].

The performance of the electron reconstruction has been investigated using simulation [203], test beams [204, 205] and measured with collision data [206]. Further updates using a Gaussian Sum Filter-based model for bremsstrahlung are being investigated [207].

[26] There are additional dedicated algorithms for electrons with very low energy and for electrons in the forward region.

6.3.2. Electron Identification

The identification of electrons is based on the shape information of the electromagnetic shower as well as the quality of the corresponding reconstructed track. Three different sets of identification requirements denoted as *loose*, *medium* and *tight* have been defined using the variables shown in Table 5. The cut requirements on these variables are varied as a function of p_T and η to achieve identification efficiencies that are approximately independent of p_T and η. In the transition region between barrel and endcap calorimeter of ($1.37 < |\eta| < 1.52$), the efficiency and resolution is reduced.

Type	Description	Name
Loose selection		
Acceptance	$\|\eta\| < 2.47$	
Hadronic leakage	Ratio of E_T in the first layer of the hadronic calorimeter to E_T of the EM cluster (used over the range $\|\eta\| < 0.8$ and $\|\eta\| > 1.37$)	R_{had1}
	Ratio of E_T in the hadronic calorimeter to E_T of the EM cluster (used over the range $\|\eta\| > 0.8$ and $\|\eta\| < 1.37$)	R_{had}
Middle layer of EM calorimeter	Ratio of the energy in 3×7 cells over the energy in 7×7 cells centred at the electron cluster position	R_{η}
	Lateral width of the shower	$w_{\eta 2}$
Medium selection (includes loose)		
Strip layer of EM calorimeter	Total shower width	w_{stot}
	Ratio of the energy difference between the largest and second largest energy deposits in the cluster over the sum of these energies	E_{ratio}
Track quality	Number of hits in the Pixel Detector (≥ 1)	n_{pixel}
	Number of total hits in the Pixel and SCT detectors (≥ 7)	n_{Si}
	Transverse impact parameter ($\|d_0\|$ <5 mm)	d_0
Track–cluster matching	$\Delta\eta$ between the cluster position in the strip layer and the extrapolated track ($\|\Delta\eta\| < 0.01$)	$\Delta\eta$
Tight selection (includes medium)		
Track–cluster matching	$\Delta\phi$ between the cluster position in the middle layer and the extrapolated track ($\|\Delta\phi\| < 0.02$)	$\Delta\phi$
	Ratio of the cluster energy to the track momentum	E/p
	Tighter $\Delta\eta$ requirement ($\|\Delta\eta\| < 0.005$)	$\Delta\eta$
Track quality	Tighter transverse impact parameter requirement ($\|d_0\|$ <1 mm)	d_0
TRT	Total number of hits in the TRT	n_{TRT}
	Ratio of the number of high-threshold hits to the total number of hits in the TRT	f_{HT}
Conversions	Number of hits in the b-layer (≥ 1)	n_{BL}
	Veto electron candidates matched to reconstructed photon conversions	

Table 5: Definition of variables used for *loose*, *medium* and *tight* electron identification cuts for the central region of the detector with $|\eta| < 2.47$ [206].

These three sets of criteria correspond to different levels of selection efficiency for real electrons and rejections of fake backgrounds.

For the 2011 data taking period, the identification criteria have been updated requiring a tighter track-cluster matching in η, stricter pixel and TRT hit requirements and tighter shower-shape requirements for $|\eta| > 2.0$ compared to [206]. These updated identification requirements will be denoted as "++" in the following, whereas identification criteria without the "++" suffix correspond to the definitions of the 2010 data taking period.

Figure 40 left shows the measured loose++ identification efficiency as an example. A mild depen-

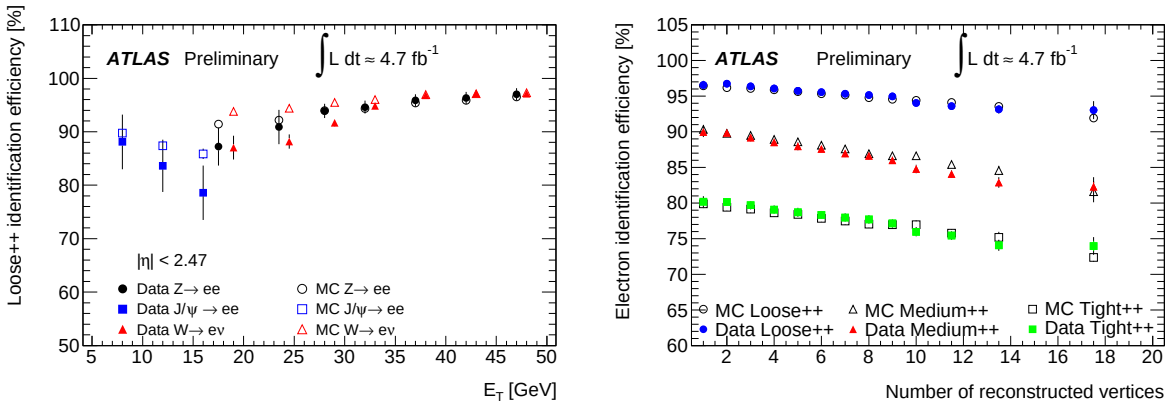

Figure 40: Left: Loose++ electron identification efficiency measurement for electrons with transverse energy between 7 and 50 GeV [208]. Right: Electron identification efficiency dependence on pileup for electron transverse energies between 20-50GeV [209].

dence of the identification efficiencies on the number of reconstructed vertices is observed as shown in Figure 40 right.

6.3.3. Electron Identification Efficiency from J/Ψ Decays using the ${}_sPlot$ Technique

The determination of efficiencies is a crucial ingredient to any physics analysis. In the context of this analysis, the inclusion of leptons with low transverse momenta is beneficial (especially with respect to the soft lepton analysis, see chapter 7). As such it is necessary to extend the measurement of efficiencies to low transverse momenta. In the following, the measurement of electron identification efficiencies for electrons with low transverse momentum from J/Ψ decays using the ${}_sPlot$ technique [210] is described as a short excursus.

In general, efficiencies related to the reconstruction and identification of leptons can be obtained using the *tag-and-probe* method [211, 212], usually based on leptonic Z boson decays. In this data-driven method, a tight selection criteria is applied to one of the decay candidates (the *tag*), while only loose criteria are required for the second candidate lepton (the *probe*). By requiring a reconstructed dilepton mass close to the Z boson mass, a high purity sample of events stemming from Z boson decays is selected. As such, the reconstruction and identification criteria can then be tested on the probe candidate, allowing for a efficiency measurement in data. For electrons with transverse momenta below ≈ 15 GeV, electrons from Z boson decays are below the kinematic reach. To extend this reach to very low p_T, electrons from $J/\Psi \to e^+e^-$ decays can be used instead[27].

In contrast to the standard tag-and-probe method using Z bosons, a much larger background from hadrons faking electrons is present for very low p_T electrons that needs to be subtracted to perform the efficiency measurement as a function of the electron p_T and η. Such a background subtraction is the purpose of the ${}_sPlot$ technique and will be used here to derive the loose identification efficiency with respect to a track matched to an electron candidate. The ${}_sPlot$ technique allows to separate several different sources of a given sample of events as a function of *control* variables by utilizing uncorrelated *discriminating* variables for which the distributions are known. As such it will be used in the following to derive the p_T and η distributions for the probe electrons from true $J/\Psi \to ee$ before and after requiring the loose electron identification criterium.

[27] The J/Ψ meson has a large branching ratio to leptons as hadronic decays are suppressed according to the OZI rule.

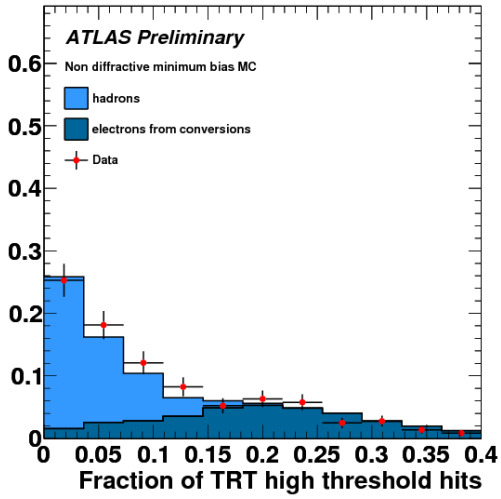

Figure 41: Fraction of high threshold TRT hits for loose electron candidates obtained using data from 2009 [213].

For this purpose, simulated samples for the direct production of $J/\Psi \rightarrow ee$[28] and a background estimate based on an inclusive minimum bias sample[29] with cross sections of ≈ 100 nb and ≈ 2 mb respectively are used. From the sum of these samples, a simulated dataset is randomly generated corresponding to an integrated luminosity of 20 pb^{-1} .

Tag-and-probe candidates are preselected with the following requirements starting from two electron candidates:

- Track selection: 8 pixel+SCT hits, 20 TRT hits
- Cut on TR fraction, i.e. fraction of High Treshold Hits > 0.2
- Cut on tag $p_T > 5$ GeV, probe $p_T > 3$ GeV and opposite sign
- Require a tight reconstructed electron as tag electron
- Match probe tracks to reconstructed electron candidates

This preselection is necessary to obtain a reasonable signal-to-background ratio. Figure 41 shows the fraction of high threshold TRT hits for electrons from conversions and for hadrons motivating a corresponding selection.

As a first step, it is necessary to fit the inclusive reconstructed invariant mass distribution of the two electrons forming the discriminating variable to obtain a probability distribution function (pdf) for the J/Ψ signal and the corresponding inclusive background as shown in Figure 42. For the signal pdf, a Crystal Ball function [214, 215] has been used while the background is assumed to have exponential shape.

Using these pdfs, an event weight ($_sWeight$) can be derived as a function of invariant mass which represents the probability for a given event to be of signal type. The following brief description of a simplified derivation of this event weight is fully taken from [216]:

[28] mc08.105751.Pythia_directJpsie3e3.merge.AOD.e347_s462_s520_r808_r838
[29] mc08.105805.filtered_minbias6.merge.AOD.e347_s462_s520_r808_r838

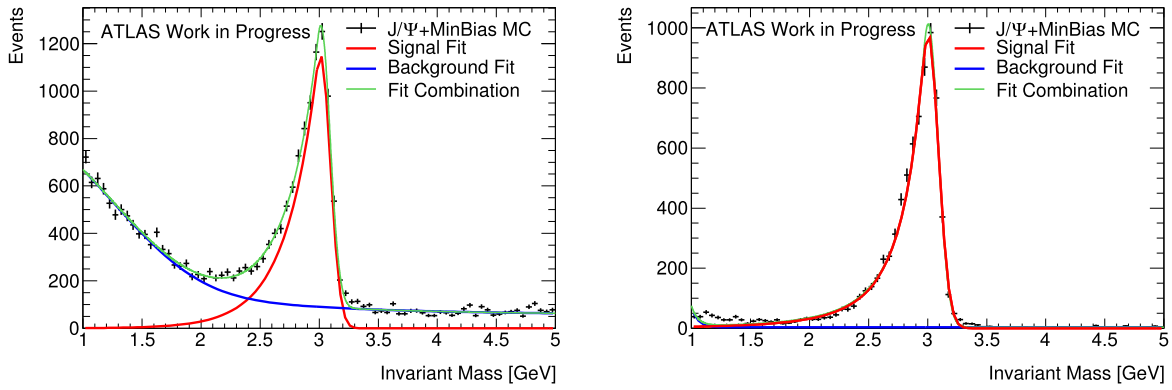

Figure 42: Invariant mass distribution for all electron candidates (left) and for those candidates where the probe track is matched to a loose electron (right) using 20 pb^{-1} of simulated data.

Let $f^s(p_T, m)$ and $f^b(p_T, m)$ be the two-dimensional pdfs for signal and background for an event with probe track transverse momentum p_T and invariant mass m. With the approximation that p_T and mass are independent it follows that:

$$f^s(p_T, m) = f^s(p_T) f^s(m) \tag{24}$$

$$f^b(p_T, m) = f^b(p_T) f^b(m) \tag{25}$$

$f^s(m)$ and $f^b(m)$ are known from the invariant mass fits, therefore it remains to find the $f^s(p_T)$ and $f^b(p_T)$ parts. The probability for an event in the mass bin m to be of type signal is:

$$P^s(m) \equiv \frac{N^s(m)}{N^s(m) + N^b(m)} = \frac{N^s f^s(m)}{N^s f^s(m) + N^b f^b(m)} \tag{26}$$

with N^s and N^b being the total number of signal and background events and $N^s(m)$ and $N^b(m)$ the number of events in the mass bin m. The goal is to estimate the number of signal events in a given p_T bin:

$$\hat{N}^s(p_T) = N^s \hat{f}^s(p_T) \equiv \sum_m N(p_T, m) P^s(m) = \sum_m [N^s(p_T, m) + N^b(p_T, m)] P^s(m) \tag{27}$$

With equation 24-26, it follows that:

$$N^s \hat{f}^s(p_T) = \sum_m [N^s f^s(p_T, m) + N^b f^b(p_T, m)] \frac{N^s f^s(m)}{N^s f^s(m) + N^b f^b(m)} \tag{28}$$

$$= \sum_m [N^s f^s(p_T) f^s(m) + N^b f^b(p_T) f^b(m)] \frac{N^s f^s(m)}{N^s f^s(m) + N^b f^b(m)} \tag{29}$$

$$= f^s(p_T) \sum_m \frac{[N^s f^s(m)]^2}{N^s f^s(m) + N^b f^b(m)} + f^b(p_T) \sum_m \frac{N^s f^s(m) N^b f^b(m)}{N^s f^s(m) + N^b f^b(m)} \tag{30}$$

As such, $\hat{f}^s(p_T)$ is a linear combination of $f^s(p_T)$ and $f^b(p_T)$:

$$\hat{f}^s(p_T) = N^s(p_T) \sum_m \frac{f^s(m) f^s(m)}{N^s f^s(m) + N^b f^b(m)} + N^b(p_T) \sum_m \frac{f^s(m) f^b(m)}{N^s f^s(m) + N^b f^b(m)} \tag{31}$$

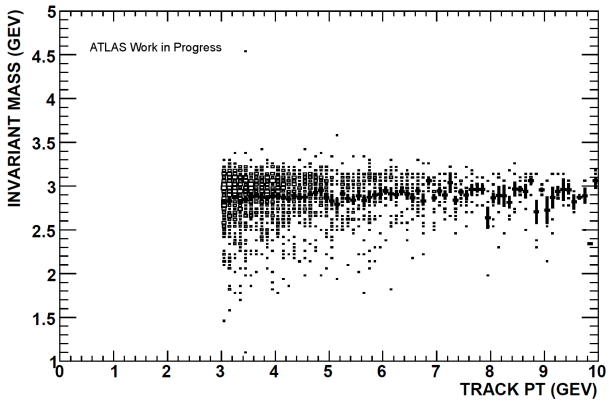

Figure 43: Invariant mass distribution of the candidate dielectron pair from $J/\Psi \rightarrow e^+e^-$ decays as a function of the transverse momentum of the probe track.

In analogy, $\hat{f}^b(p_T)$ can also be expressed as a similar linear combination yielding two linear equations that can be solved for $N^s(p_T)$ and $N^b(p_T)$. For this purpose, the weight in equation 26 has to be replaced. The corresponding ${}_sWeight$ to get these is defined as

$$P^s(m) = \frac{\sum_{j=s,b} V^{sj} f^j(m)}{\sum_{j=s,b} N^j f^j(m)} \qquad (V^{ij})^{-1} \equiv \frac{\sum_m f^i(m) f^j(m)}{N^i f^i(m) + N^j f^j(m)} \tag{32}$$

The general proof that these weights sum up to the number of signal events in a given bin, known as the ${}_sPlot$ technique, as well as its properties can be found in [210].

The ${}_sPlot$ technique is applicable in this context as the candidate invariant mass and the probe p_T are approximately independent as shown in Figure 43.

The ${}_sWeight$ (equation 32) is calculated for each event and summed to arrive at predictions for the p_T and η distributions for the J/Ψ signal as shown in Figure 44. The overall agreement between the shapes derived using the ${}_sPlot$ technique and the input distributions is reasonable.

To determine the final efficiency of reconstructing a cluster fulfilling the *loose* identification criterium, the ratio of the corresponding distributions of Figure 44 is calculated as shown in Figure 45. Note that efficiencies larger than one can occur due to the background subtraction method being used.

The ${}_sPlot$ technique has been implemented within the `InsituPerformance` framework [217, 218] of the ATLAS Simulation Software (see chapter 5.2.8) and has been successfully applied to data since the first observation of J/Ψ mesons at the beginning of the data taking in 2010 [219]. Figure 46 shows the corresponding reconstructed dielectron mass distribution obtained with the full 2010 dataset of 40 pb^{-1}.

6.4. Muons

The reconstruction of muons is based on the tracks reconstructed in the inner detector in combination with the information provided by the muon spectrometer.

In contrast to the detectors used for the electron reconstruction, the layout of the muon system is rather inhomogeneous. Furthermore, the magnetic field exhibits a large dependence on η as well such that the resulting muon trajectories have no simple analytical shape.

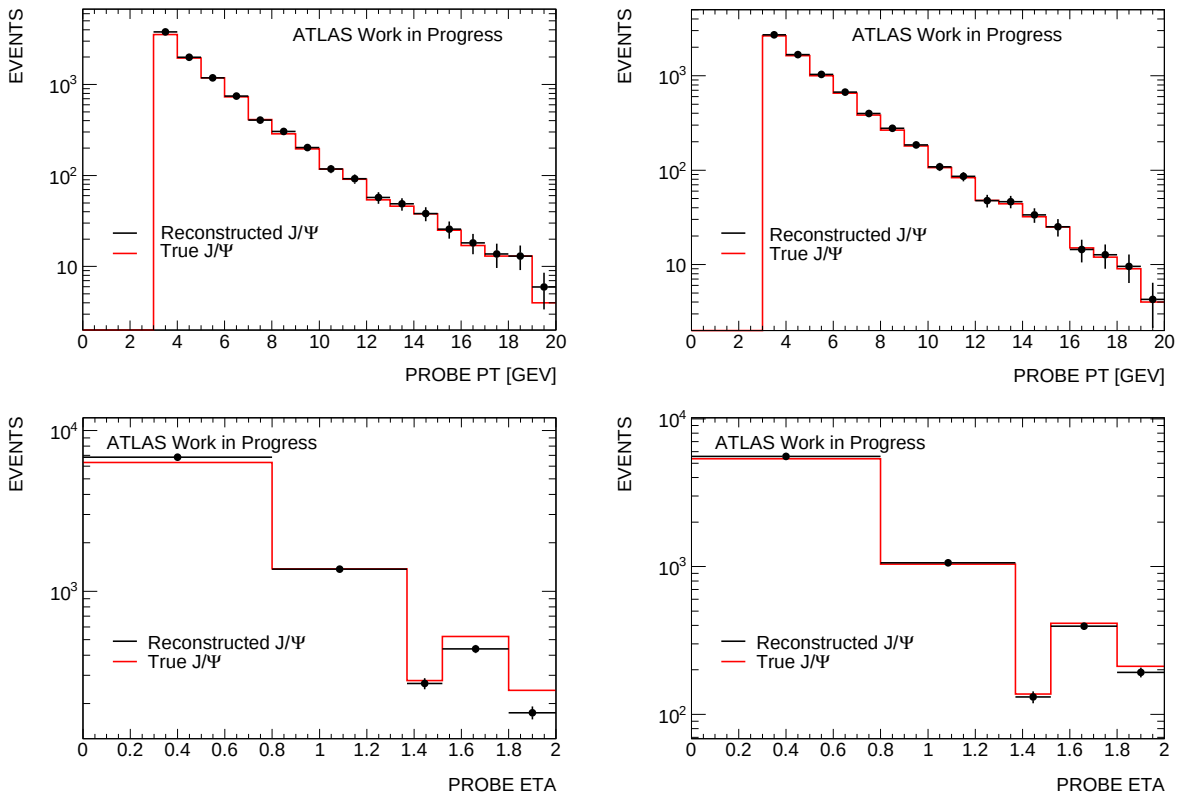

Figure 44: p_T (top) and η (bottom) distributions for all electron candidates (left) and for those fulfilling the loose electron ID (right).

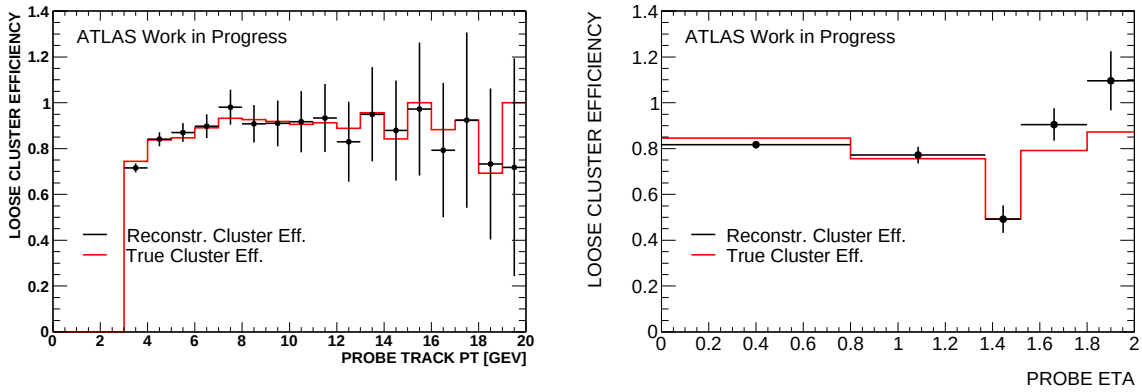

Figure 45: Loose electron identification efficiency with respect to probe tracks as a function of p_T (left) and η (right).

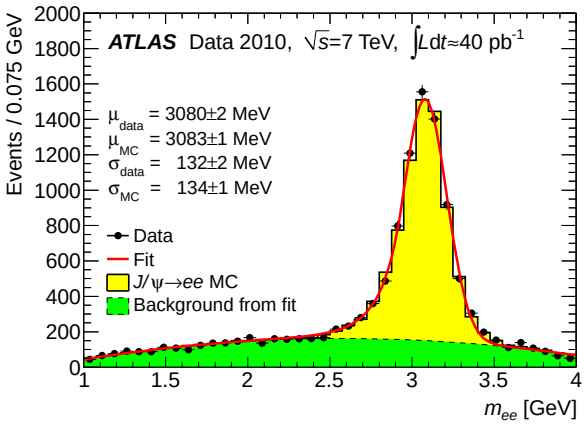

Figure 46: Reconstructed dielectron mass distribution for $J/\Psi \to e^+e^-$ decays [206].

For the track reconstruction in the muon system, chambers of the muon detectors are grouped in *stations*. Local track segments are reconstructed from the hit information in the precision chambers of these stations. From the track segments, the full muon track is reconstructed using sophisticated fitting techniques [220].

Several identification and reconstruction algorithms are available:

- `Standalone`: Muons are reconstructed only using the muon spectrometer and extrapolated to the interaction point.
- `Combined`: Standalone muon tracks are combined with the tracks reconstructed in the inner detector using a STAtistical COmbination (`STACO`).
- `Segment Tagged`: Muon track reconstruction is seeded from inner detector tracks extrapolated to the Muon Spectrometer
- `Calomuons`: Algorithm designed to recover not instrumented region around $\eta \approx 0$ using calorimeter information.

The performance of the muon reconstruction has been investigated based on simulation [183] and using test beam data [221], muons from cosmic rays [222] and collision data [223, 224].

Figure 47 shows the reconstruction efficiencies for muons from Z boson decays reconstructed using the combined+segment tagged algorithm for data from 2011 compared to Monte Carlo simulation. For $\eta \sim 0$, results for the calomuon algorithm are shown as well.

6.5. Jets

Jets are the particle showers emerging from the hadronization of quarks and gluons. Most of the jet energy is deposited in the hadronic calorimeter. Due to the presence of charged particles in the jets, these hadronic showers are usually accompanied by a number of tracks in the inner detector as well.

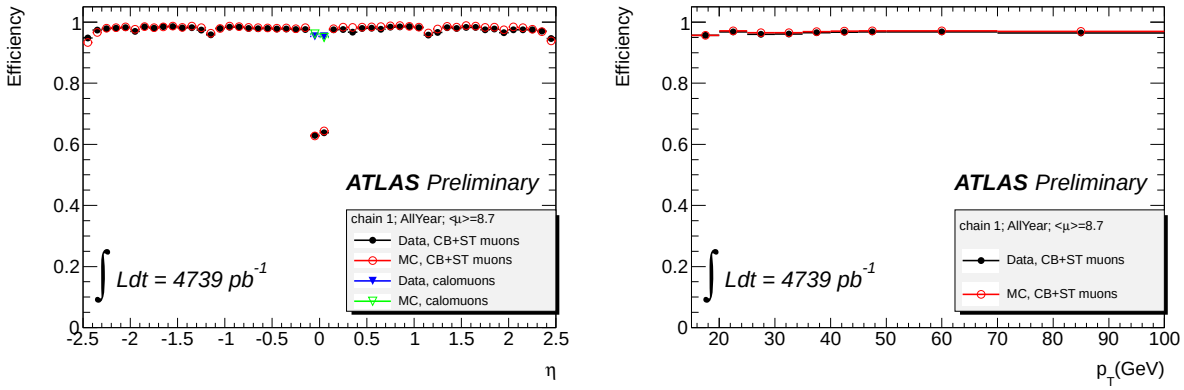

Figure 47: Reconstruction efficiencies for combined+segment tagged muons from Z boson decays as a function of p_T (left) and η (right) [225].

6.5.1. Jet Reconstruction

A number of jet reconstruction algorithms are available in the ATLAS reconstruction software, with the `anti-`k_t algorithm [226, 227] using a radius parameter R = 0.4 being the default choice. Jets are reconstructed combining the energy depositions in the hadronic calorimeter iteratively. This clustering algorithm is known to be infrared and collinear safe.

In contrast to electrons and muons, jets are complex objects. As such, the definition of the jet energy scale that translates to the energy of the initial parton is more delicate. Initially, the cells of the hadronic calorimeter forming the topoclusters are calibrated to the electromagnetic (EM) scale. As hadronic interactions differ from electromagnetic interactions, this energy needs to be adjusted, for which several calibration schemes exist [228]. In the following, the `EM+JES` calibration will be used, while global (GCW) and local (LCW) cluster weighting calibration schemes are possible as well. The important jet energy scale-related systematic uncertainties and their impact on this analysis will be further discussed in chapter 9.1.3.

6.5.2. Jet Vertex Fraction

While the jet reconstruction takes the existence of pileup into account [229], it is desirable to remove the jets from additional interactions for the analysis as their presence degrades the separation power between the supersymmetric signal and the backgrounds with less jet activity. For this purpose, the Jet Vertex Fraction (JVF) variable [230] provides a strong handle. The JVF measures the probability of a jet to originate from a specific primary vertex by dividing the sum of the transverse momenta of tracks matched to this vertex by the sum of the transverse momenta of tracks associated to the jet as shown in Figure 48 left. Figure 48 right shows the distribution of the resulting JVF variable which provides the separation power between jets from the hard scatter and those originating from additional interactions.

Further details on the determination of the JVF and its performance are contained in [231, 232].

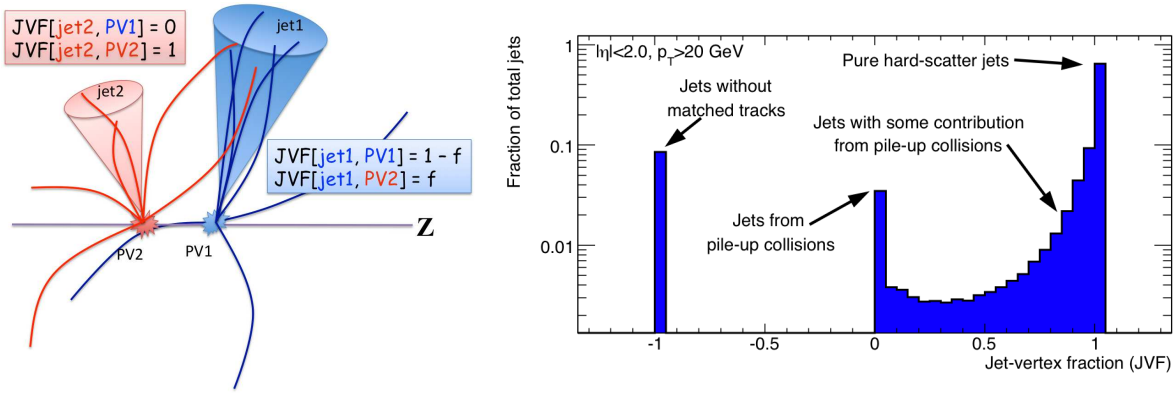

Figure 48: Left: Schematic representation of the jet-to-vertex association provided by the jet-vertex fraction (JVF) discriminant corresponding to the fraction of a jet originating from vertex i [231]. Right: Reconstructed jet-vertex fraction (JVF) with respect to the selected primary vertex for jets with $p_T > 20$ GeV and $|\eta| < 2.0$ using simulated dijet events [231].

6.6. b-Tagging

Jets originating from b-quarks can be identified using *b-tagging* algorithms as the life-time of the corresponding B-Hadrons is of $\mathcal{O}$(ps). As such, B-Hadrons decay after having traversed a distance of $\mathcal{O}$(mm) within the Pixel Detector leading to the creation of secondary vertices and displaced tracks. Furthermore, also the possibility of semi-leptonic decays of b-quarks into leptons with a branching ratio of 10% [233] can be exploited.

In the following, the `JetFitterCombNN` b-tagging algorithm [234] will be used which itself combines the output of the `IP3D` [234] and the `JetFitter` [235] algorithms using a neural network. The operating point is chosen such that the b-tagging efficiency in simulated $t\bar{t}$ events is approximately 60% while the jets originating from light quarks or gluons are rejected by a factor of 200-400, depending on the jet p_T. Figure 49 shows the corresponding performance in comparison to several other algorithms. The JetFitterCombNN algorithm is calibrated using the 2011 dataset [236].

6.7. Missing Transverse Energy

Particles interacting only via the weak interaction (such as neutrinos or the supersymmetry LSPs) leave the ATLAS detector without hits or energy depositions, leading to an imbalance of the total energy in the transverse plane called missing tranverse energy (E_T^{miss}). In general, E_T^{miss} is computed in ATLAS as the transverse component of the vector sum of all reconstructed physics objects adding the residual not assigned calorimeter cells. In this computation, the appropriate energy scales are taken into account.

For this analysis, the `Simplified20_RefFinal` algorithm is used which is a modification of the default `RefFinal` reconstruction algorithm [237], that does not apply a dedicated energy scale for hadronically decaying τ leptons. The performance and calibration of the missing transverse energy reconstruction has been measured using the 2011 dataset correcting for the presence of pileup [238]. Figure 6.7 shows the resolution of the missing transverse energy measured in data and computed in the Monte Carlo simulation as an example.

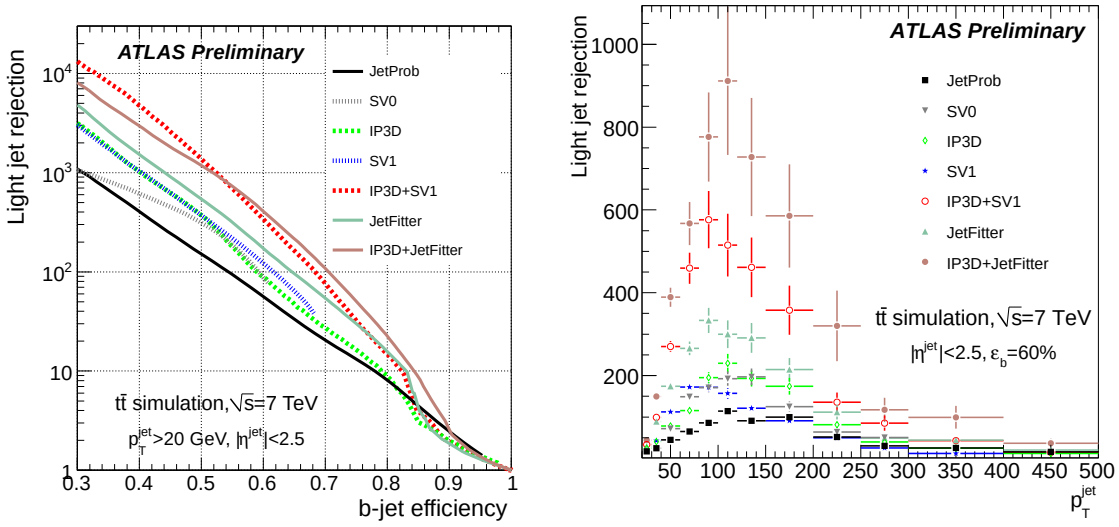

Figure 49: Light-jet rejection as a function of b-tagging efficiency (left) and as a function of jet p_T (right) for several b-tagging algorithms using simulated $t\bar{t}$ events [234].

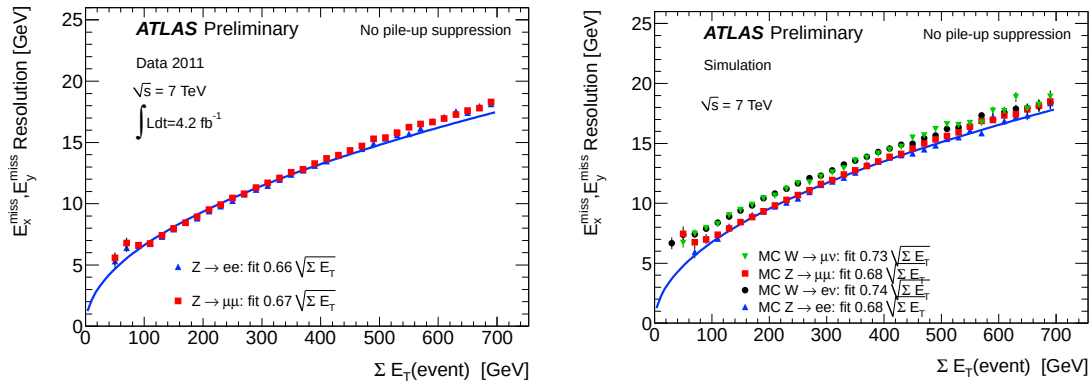

Figure 50: E_x^{miss} and E_y^{miss} resolution as a function of the total transverse energy in the event measured in $Z \to \ell\ell$ events in data (left) as well as in simulated $W \to \ell\nu$ and $Z \to \ell\ell$ Monte Carlo events (right) [238].

7. Analysis

After having discussed the details of the reconstruction and identification of physics objects in the previous chapter, the event and object selection for the analysis will be introduced and a first comparison of data to the Standard Model backgrounds will be shown.

The results obtained in this dileptonic search channel will be further combined with two orthogonal single lepton search channels requiring exactly one lepton with high or low transverse momentum to maximize the sensitivity to different supersymmetry models:

- *Hard dilepton channel*: For the dilepton channel, at least two leptons are required as introduced in chapter 4. The two leptons with the highest transverse momentum are required to be of opposite charge[30], leading to three different final states ($ee, e\mu$ and $\mu\mu$). This search channel will form the main channel analyzed within this thesis, providing high sensitivity to decay chains involving sleptons.
- *Hard single-lepton channel*: The dilepton channel will be accompanied by a search requiring exactly one electron or muon. This hard single-lepton channel targets decay chains involving charginos which decay leptonically via a (real or virtual) W boson.
- *Soft single-lepton channel*: Additionaly, an analysis channel requiring exactly one soft lepton with low transverse momentum and soft jets is introduced to improve the coverage of supersymmetry models with compressed mass spectra in which the mass differences between the sparticles involved in the decay chains are small.

The three analysis channels partially share common background estimations as described in detail in chapter 10 and as such will be discussed together when appropriate. This combined analysis has been published by ATLAS [19]. Figure 51 shows a schematic overview of the analysis channels and their combination as discussed in the following chapters.

7.1. Trigger and Data Collection

The analysis is based on the full 2011 dataset of proton-proton collisions at a center of mass energy of $\sqrt{s} = 7$ TeV. After applying data-quality requirements demanding good LHC and ATLAS running conditions in all parts of the detector[31], the total integrated luminosity is 4.71 ± 0.18 fb^{-1} [240, 241]. The maximum instantaneous luminosity in this dataset reached $3.65 \times 10^{33}\,\mathrm{cm}^{-2}\mathrm{s}^{-1}$, with an average number of interactions per bunch crossing of 10 as discussed in chapter 5.

Events are selected using single lepton triggers as shown in Table 6. The 2011 dataset is divided in several *periods* with different run conditions and trigger menus. For the ee and $\mu\mu$ final states, the corresponding single lepton triggers with thresholds of 20-22GeV (electrons) and 18GeV (muons) will be used. For the $e\mu$ final state, events are selected using both the single electron trigger or the single muon trigger (avoiding overlaps) to maximize the selection efficiency. Additionaly, a muon+jet trigger is used for periods J–M to recover an inefficiency in the corresponding single muon trigger. As the ATLAS simulation fully simulates the triggers, the trigger requirements can be applied to Monte Carlo simulations as well. Small remaining discrepancies are corrected as discussed in more detail in [242].

[30] A similar analysis focussing on same-sign dileptons is contained in [239].

[31] The data quality in all detector components is ascertained by applying the official ATLAS Good Runs List `data11_7TeV.periodAllYear_DetStatus-v36-pro10_CoolRunQuery-00-04-08_Susy.xml`

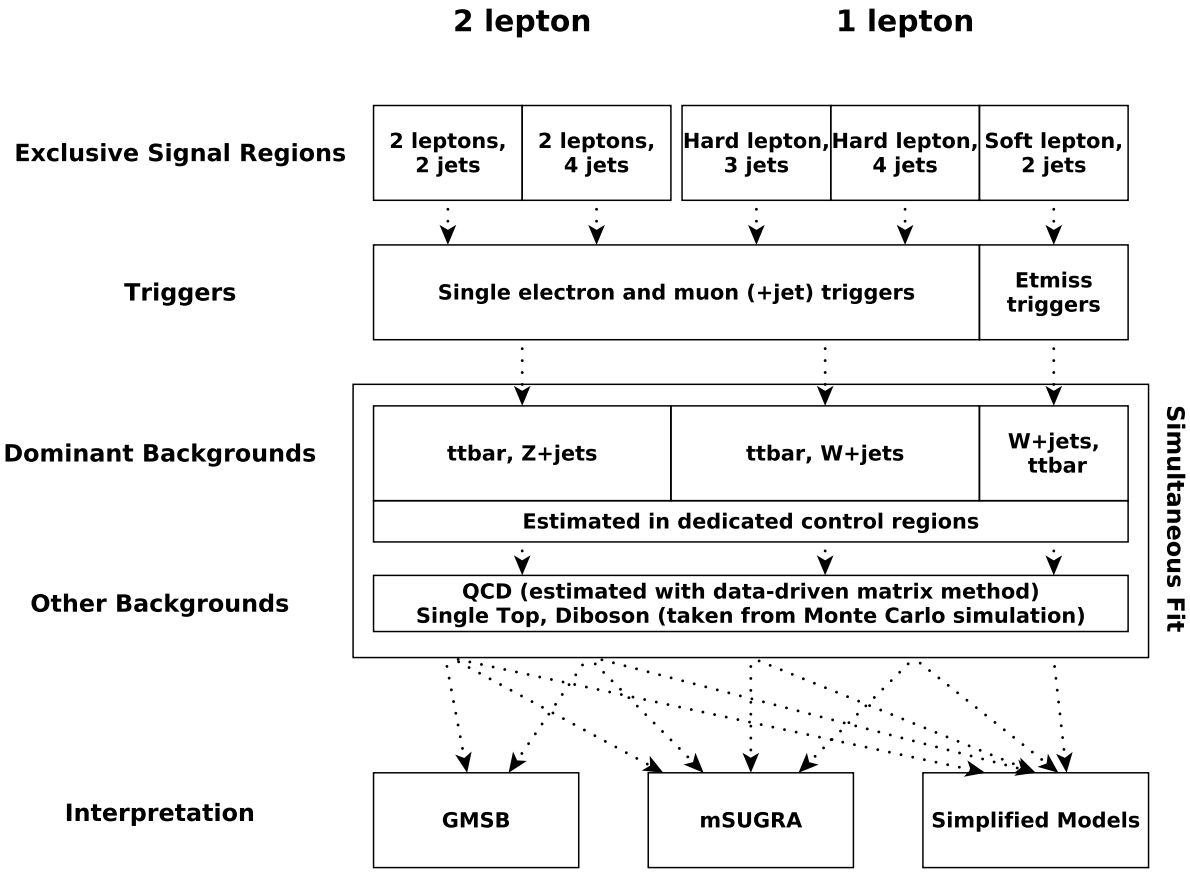

Figure 51: Schematic overview of the combined analysis setup.

Period	Data	MC
	Single Electron Trigger	
B–J	EF_e20_medium	EF_e20_medium + trigger scale factor (1)
K	EF_e22_medium	EF_e20_medium + trigger scale factor (1)
L–M	EF_e22vh_medium1 OR EF_e45_medium1	EF_e22vh_medium1 + trigger scale factor (2)
	Single Muon Trigger	
B–I	EF_mu18	Trigger reweighting (1)
J–M	EF_mu18_medium, EF_mu18_L1J10	Trigger reweighting (2)

Table 6: Triggers used to select events for the different data taking periods as applied on data (left) and Monte Carlo simulation (right). The numbers in parentheses indicate, that different reweightings are necessary for different data taking periods.

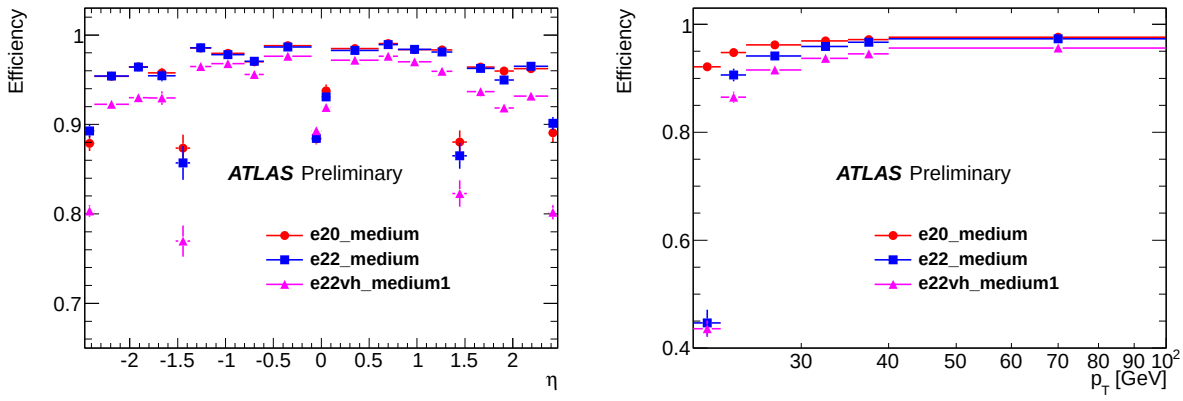

Figure 52: Trigger efficiency with respect to offline reconstructed electrons for the different single electron triggers used in this analysis as a function of offline η and p_T [243]. The efficiencies have been determined using the tag-and-probe method on $Z \to ee$ events.

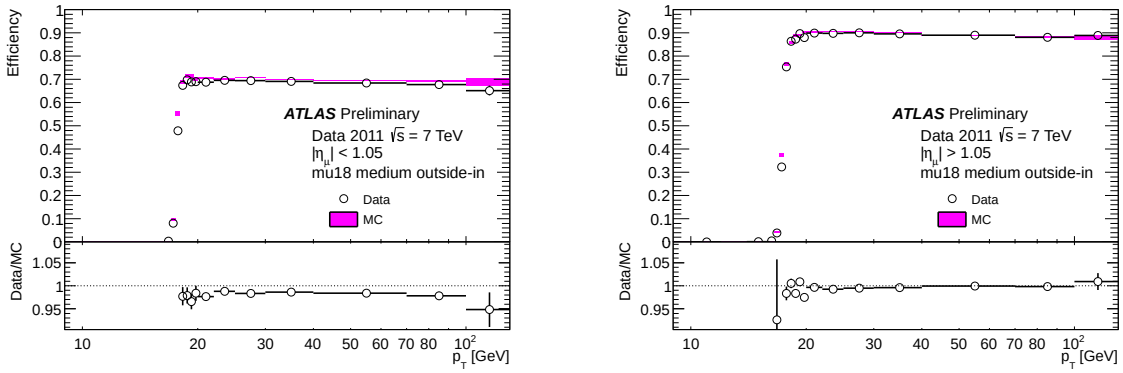

Figure 53: Trigger efficiency with respect to offline reconstructed muons for single muon triggers in the barrel (left) and endcap (right) regions [244]. The efficiencies have been determined using the tag-and-probe method on $Z \to \mu\mu$ events.

The trigger requirements are adjusted to avoid prescaled triggers[32] while ascertaining that the event selection based on reconstruced objects is in the efficiency plateau as shown in figures 52 and 53. The usage of single lepton triggers for this dilepton analysis is possible as the targeted supersymmetry scenarios involve large mass differences leading to leptons with high transverse momenta as was shown in Figure 20. The usage of common triggers simplifies the combination of the results from this dilepton analysis with the hard one lepton channel further discussed in chapter 10.

7.2. Object Selection

While the main properties of the object reconstruction and identification have already been layed out in chapter 6, the exact object definitions for jets, electrons and muons used for this analysis will be detailed in the following. For these objects, first a *preselection* with looser requirements is

[32] Prescaled triggers artificially record only a subset of events passing the trigger criteria to reduce the trigger rate as imposed by the limited trigger bandwidth.

Cut	Value/description	
Jet Type	no	b-jet
	Preselected jet	
Algorithm	AntiKt4Topo	
Acceptance	$p_T > 20$ GeV, $\|\eta\| < 2.5$	
Overlap	$\Delta R(jet, e) > 0.2$	
Quality	reject events with bad jet quality	
Jet Vertex Fraction	JVF > 0.75	
	Signal jet	
Acceptance	$p_T > 25$ GeV, $\|\eta\| < 2.5$	
Other	–	JetFitterCombNN>1.8

Table 7: Summary of the jet and b-jet selection criteria. The signal selection requirements are applied on top of the preselection.

Cut	Value/description
Preselected Electron	
Algorithm	AuthorElectron
Acceptance	$p_T > 10$ GeV, $\|\eta^{\text{clust}}\| < 2.47$ (hard lepton channels) 7 GeV $< p_T < 25$ GeV, $\|\eta^{\text{clust}}\| < 2.47, 1.37 < \|\eta^{\text{clust}}\| < 1.52$ excluded (soft lepton channels)
Quality	Medium++
Overlap	$\Delta R(e, jet) > 0.4$
Signal Electron	
Quality	Tight++
Acceptance	$p_T > 25$ GeV (leading electron)
Track isolation	$\sum p_T$ in ΔR cone of $0.2/p_T < 0.10$

Table 8: Summary of the electron selection criteria. The signal selection requirements are applied on top of the preselection.

defined. The preselected objects are used for the overlap removal between jets, electrons and muons to avoid double-counting of objects. Afterwards, the final selection is tightened using *signal* objects. Track isolation requirements are imposed on both electrons and muons.

This object selection is applied via the `SUSYTools` package [245], which in turn fixes various small discrepancies for the efficiencies not yet contained in the ATLAS simulation using the packages listed in appendix B. Tables 7, 8 and 9 contain the corresponding definitions for jets, electrons and muons respectively, which are commonly used in the ATLAS supersymmetry analyses.

7.3. Event Selection

In addition to the general assessment of data quality described in chapter 7.1, individual events are rejected if noise bursts or data integrity problems in the electromagnetic [246] or hadronic calorimeters [247, 248] are present.

For approximately 20% of the dataset, the region $0 < \eta < 1.4$ and $-0.8 < \phi < -0.6$ in the electromagnetic calorimeter had an electronic failure in the corresponding Front End Boards preventing the recording of signals. As such, events in the dataset are vetoed if an electron is reconstructed in this region [246, 249]. Furthermore, events are vetoed if the jet-related contribution to E_T^{miss}

Cut	Value/description
Preselected muon	
Algorithm	STACO, combined or segment-tagged muon
Acceptance	$p_T > 10$ GeV, $\|\eta\| < 2.4$ (hard lepton channels) 6 GeV $< p_T < 20$ GeV, $\|\eta\| < 2.4$ (soft lepton channels)
Quality	Loose
Inner detector	Number of pixel hits + number of crossed dead pixel sensors > 1 Number of SCT hits+number of crossed dead SCT sensors ≥ 6 Pixel holes + SCT holes < 3 ≥ 1 b-layer hit when it can be expected
Track quality	If $\|\eta\| < 1.9$: $n_{TRT} > 5$ and $n_{\mathrm{TRT}}^{outliers} < 0.9 n_{TRT}$ If $\|\eta\| \geq 1.9$ and $n_{\mathrm{TRT}} > 5$: $n_{\mathrm{TRT}}^{outliers} < 0.9 n_{TRT}$
Overlap	$\Delta R(\mu, jet) > 0.4$
Signal muon	
Acceptance	$p_T > 20$ GeV (leading muon)
Track isolation (excluding muon track)	$\sum p_T$ in ΔR cone of $0.2 < 1.8$ GeV

Table 9: Summary of the muon selection criteria. In this table, n_{TRT} is the total number of TRT hits, including outliers. The signal selection requirements are applied on top of the preselection.

pointing to this defective region is large and provides a significant fraction of the total E_T^{miss}. The contribution is estimated using the information on the energy in the neighbouring calorimeter cells. This effect is included in the detector simulation for the Monte Carlo datasets used in the following. Further studies on this event veto are contained in [250] showing that the overall loss of signal accceptance from this requirement is neglible.

Moreover, the presence of cosmic muons is taken into account by rejecting events containing preselected muons with impact parameters of $|z_{0,PV}| > 1\ mm$ or $|d_{0,PV}| > 0.2\ mm$ with respect to the primary vertex. The remaining contribution from cosmic muons has been estimated using a Control Region with large $|z_{0,PV}|$ and found to be negligible [242].

7.4. Background Prediction

Simulated Monte Carlo samples are used for the description of the different Standard Model backgrounds utilizing several generators as shown in Table 10[33]. As the correct description of final states with additional jet radiation is of high relevance for the dominant $t\bar{t}$ and Z+jets backgrounds, ALPGEN [251] is used to generate the corresponding processes including up to five additional partons in the matrix element calculation, which allows for a more precise prediction of the emission of additional hard jets compared to a description via parton shower algorithms. Single-top samples are simulated using MC@NLO [252], while Herwig [253] is used for the diboson backgrounds. For all the samples, the parton shower and fragmentation processes are simulated using Herwig in combination with Jimmy [254] for the underlying event modeling using the ATLAS AUET2B_LO** tunes [255]. The overlap between the heavy-flavored and light-flavored W/Z+jets samples is removed using the

[33]The full list of samples is contained in appendix A.

heavy flavor overlap removal (HFOR) tool [256].

In addition to the information on the generators and PDF sets used for the simulation of the backgrounds, the corresponding cross sections and parton distribution function sets are contained in Table 10 as well. For most of the processes, higher order calculations of the cross sections are available and will thus be used for the (nominal) background normalization.

All these samples have been simulated and reconstructed using the ATLAS simulation framework taking into account the presence of pileup as described in chapter 5.2.8.

7.5. Signal Prediction

For the different supersymmetry signal models, samples are simulated as follows: The GMSB and MSUGRA mass spectra are calculated with ISAJET 7.80 [267] and ISASUSY [268] using the SUSY Les Houches Accord format [269, 270]. Signal events are generated using Herwig++ 2.5.2 [271] and MRST2007LO* [272] parton distribution functions.

For the Simplified Models, the signal samples are generated using MADGRAPH5 [273] with the CTEQ6L1 [257] PDF set and PYTHIA [274] for the parton showering. The samples are generated including one extra parton in the matrix element calculation and applying the MLM matching scheme [275] setting the scale parameter to one-fourth of the LSP mass.

The signal cross sections are calculated at NLO+NLL accuracy using NLL-fast [146–150] for the pure strong production processes and at NLO accuracy using Prospino 2.1[34] [146, 151–153] for all other production mechanisms. The corresponding uncertainties on the signal cross sections will be discussed in chapter 9.3.

[34] Prosino 2.1 as of 11/20/2011.

Physics process	Generator	PDF Set (Generator)	Cross section (pb)	PDF Set (Cross Section)	Calculation accuracy	
$t\bar{t}$	ALPGEN 2.13 [251]	CTEQ6L1 [257]	166.8	MSTW2008NNLO [258]	NLO+NLL	[259]
$W(\to \ell\nu)$ + jets	ALPGEN 2.13 [251]	CTEQ6L1 [257]	10460	MSTW2008NNLO [258]	NNLO	[260]
$W(\to \ell\nu) + b\bar{b}$ + jets	ALPGEN 2.13 [251]	CTEQ6L1 [257]	130		LO×K	
$W(\to \ell\nu) + c\bar{c}$ + jets	ALPGEN 2.13 [251]	CTEQ6L1 [257]	360		LO×K	
$W(\to \ell\nu) + c$ + jets	ALPGEN 2.13 [251]	CTEQ6L1 [257]	1100		LO×K	
$Z/\gamma^*(\to \ell\ell)$ + jets ($m_{\ell\ell} > 40$ GeV)	ALPGEN 2.13 [251]	CTEQ6L1 [257]	1070	MSTW2008NNLO [258]	NNLO	[260]
$Z/\gamma^*(\to \ell\ell)$ + jets (10 GeV $< m_{\ell\ell} <$ 40 GeV)	ALPGEN 2.13 [251]	CTEQ6L1 [257]	3970	MSTW2008NNLO [258]	NNLO	[260]
$Z/\gamma^*(\to \ell\ell) + b\bar{b}$ + jets ($m_{\ell\ell} > 40$ GeV)	ALPGEN 2.13 [251]	CTEQ6L1 [257]	10.3		LO	
Single-top (t-chan)	MC@NLO 4.01 [252]	CT10 [261]	7.0	MSTW2008NNLO [258]	NNLO+NNLL	[262]
Single-top (s-chan)	MC@NLO 4.01 [252]	CT10 [261]	0.5	MSTW2008NNLO [258]	NNLO+NNLL	[263]
Single-top (Wt-chan)	MC@NLO 4.01 [252]	CT10 [261]	15.7	MSTW2008NNLO [258]	NNLO+NNLL	[264]
WW	HERWIG 6.5.20 [253]	MRSTMCal (LO**) [265]	44.9	MSTW2008NLO [258]	NLO	[266]
WZ/γ^*	HERWIG 6.5.20 [253]	MRSTMCal (LO**) [265]	18.5	MSTW2008NLO [258]	NLO	[266]
$Z/\gamma^*Z/\gamma^*$	HERWIG 6.5.20 [253]	MRSTMCal (LO**) [265]	5.96	MSTW2008NLO [258]	NLO	[266]

Table 10: Simulated background event samples used in this analysis, with the corresponding production cross sections. The notation LO×K indicates that the process is calculated at leading-order and corrected by a factor derived from the ratio of NLO to LO cross sections for a closely related process. The $t\bar{t}$, W+ light-jets and Z+ light-jets samples are normalized using the inclusive cross sections; the values shown for the W+ light-jets and Z+ light-jets samples are for a single lepton flavor. The single-top cross sections are listed for a single lepton flavor in the s- and t-channels. Further details are given in the text.

	dilepton preselection		
	$e^{\pm}e^{\mp}$	$\mu^{\pm}\mu^{\mp}$	$e^{\pm}\mu^{\mp}$
Trigger	Single electron	Single muon (+jet)	Single electron or muon (+jet)
N_{ele}	≥ 2	$= 0$	≥ 1
N_{muo}	$= 0$	≥ 2	≥ 1
$p_{\text{T}}^{\ell_1}$ (GeV)	>25	> 20	> 25 (20)
$p_{\text{T}}^{\ell_2}$ (GeV)	> 10	> 10	> 10
$m_{\ell\ell}$ (GeV)	> 12	> 12	-
N_{jet}	≥ 2	≥ 2	≥ 2
$p_{\text{T}}^{\text{jet}}$ (GeV)	$> 50, 50$	$> 50, 50$	$> 50, 50$

Table 11: Overview of the selection criteria for the preselection.

7.6. Kinematic Distributions

In the following, the simulated Monte Carlo backgrounds will be compared to data after a loose preselection as shown in Table 11. In addition to the event preselection described above, at least two leptons of opposite sign with $p_T > 10$ GeV are required. To assure a flat trigger efficiency, the leading lepton has to have $p_T > 25$ (20) GeV for electrons (muons). In the dielectron and dimuon channels, the invariant mass of the leading two leptons is required to be larger than 12 GeV to suppress low mass resonances such as J/Ψ and Υ. Furthermore, the presence of at least two jets with $p_T > 50$ GeV is required to loosely preselect a phase space-region matching the signal properties[35].

Figure 54 shows the transverse momentum of the leading and second leading lepton for the ee, $e\mu$ and $\mu\mu$ final states, while Figure 55 shows the invariant mass of the two leading leptons and the missing transverse energy. Furthermore, Figure 56 contains the distribution of the vectorial sum of transverse momenta of the two leading leptons as well as the number of jets with transverse momentum above 25 GeV. Finally, Figure 57 provides the transverse momentum of the leading jet and the effective mass. In addition to the stacked Standard Model backgrounds, exemplary distributions for the GMSB signal model with $\Lambda = 45$ TeV and $\tan\beta = 5$ are overlayed. The insets denoted as "Data/SM" show the ratio between data and the total Standard Model expectation and as such allow for a visual check of consistency. The yellow band in the figures reflects the uncertainties due to limited Monte Carlo statistics as well as the systematic uncertainties that will be discussed in detail in chapter 9. The data-driven estimate for the misidentified leptons in multijet events will be described in chapter 8.1.

It can be seen that with this preselection, the ee and $\mu\mu$ channels are dominated by the Z+jets background, while the $e\mu$ events are composed mainly of $t\bar{t}$ production. The overall agreement between the simulation and data is satisfactory, while some discrepancy in the modelling of the transverse momentum of the Z boson can be observed in the Zp_T and lepton p_T distributions. The correction of this mismodelling is the topic of chapter 8.3.

As observable when comparing the total Standard Model expectation to the exemplary signal model, an enrichment of signal events compared to the Standard Model backgrounds can be achieved by applying phase space cuts on different variables such as N_{jet}, E_T^{miss} or m_{eff} which will be discussed in chapter 7.7.

[35] This also fulfills the requirement of at least one jet due to the trigger requirements in the muon+jet trigger.

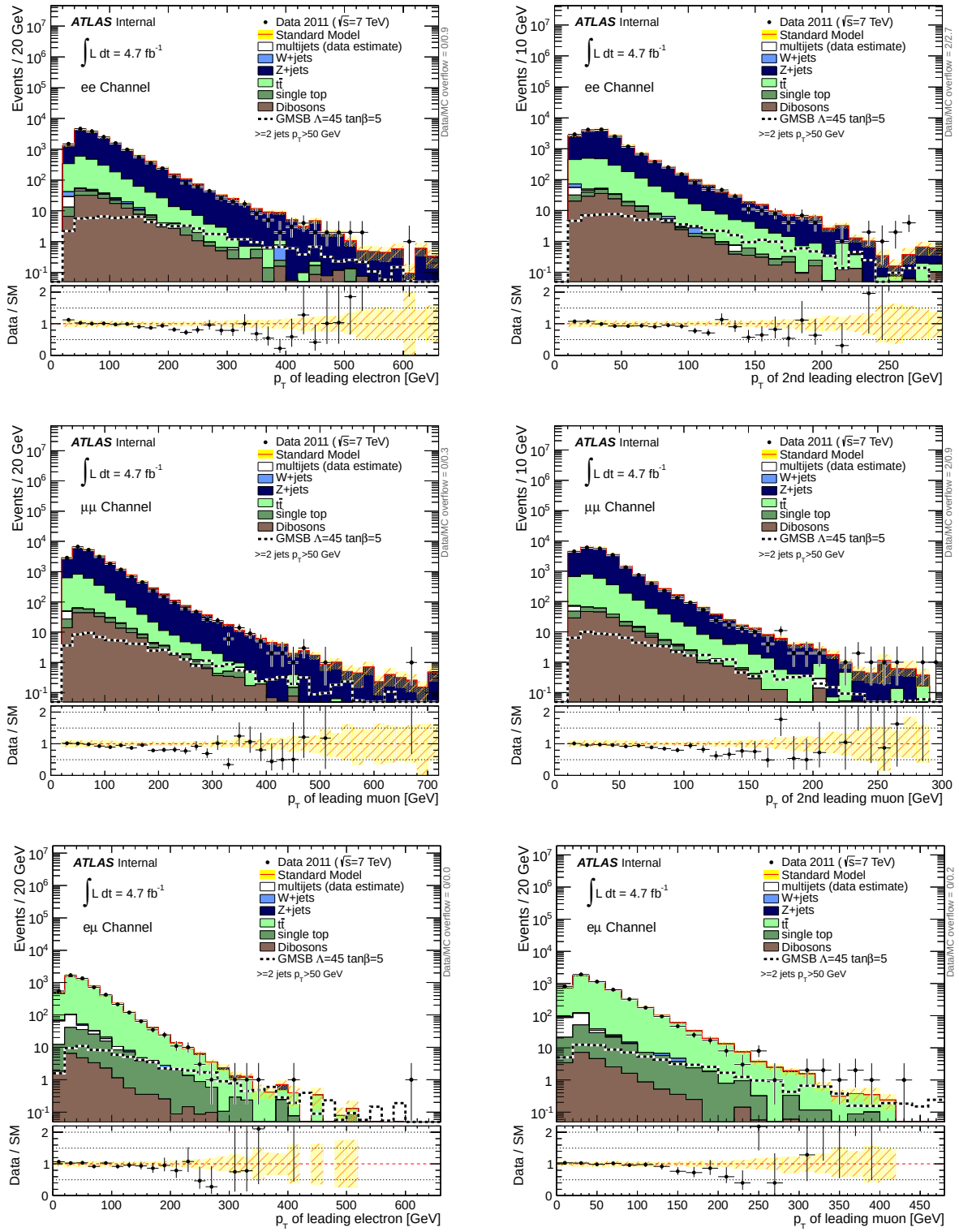

Figure 54: Distribution of the transverse momentum for the leading (left) and second leading lepton (right) in data and Monte Carlo for the ee channel (top) and the $\mu\mu$ channel (middle) as well as the leading electron (left) and leading muon (right) for the $e\mu$ channel (bottom) after the lepton plus two jets kinematic selection. The yellow band definition is given in the text. For each distribution data Monte Carlo ratio plots are also shown.

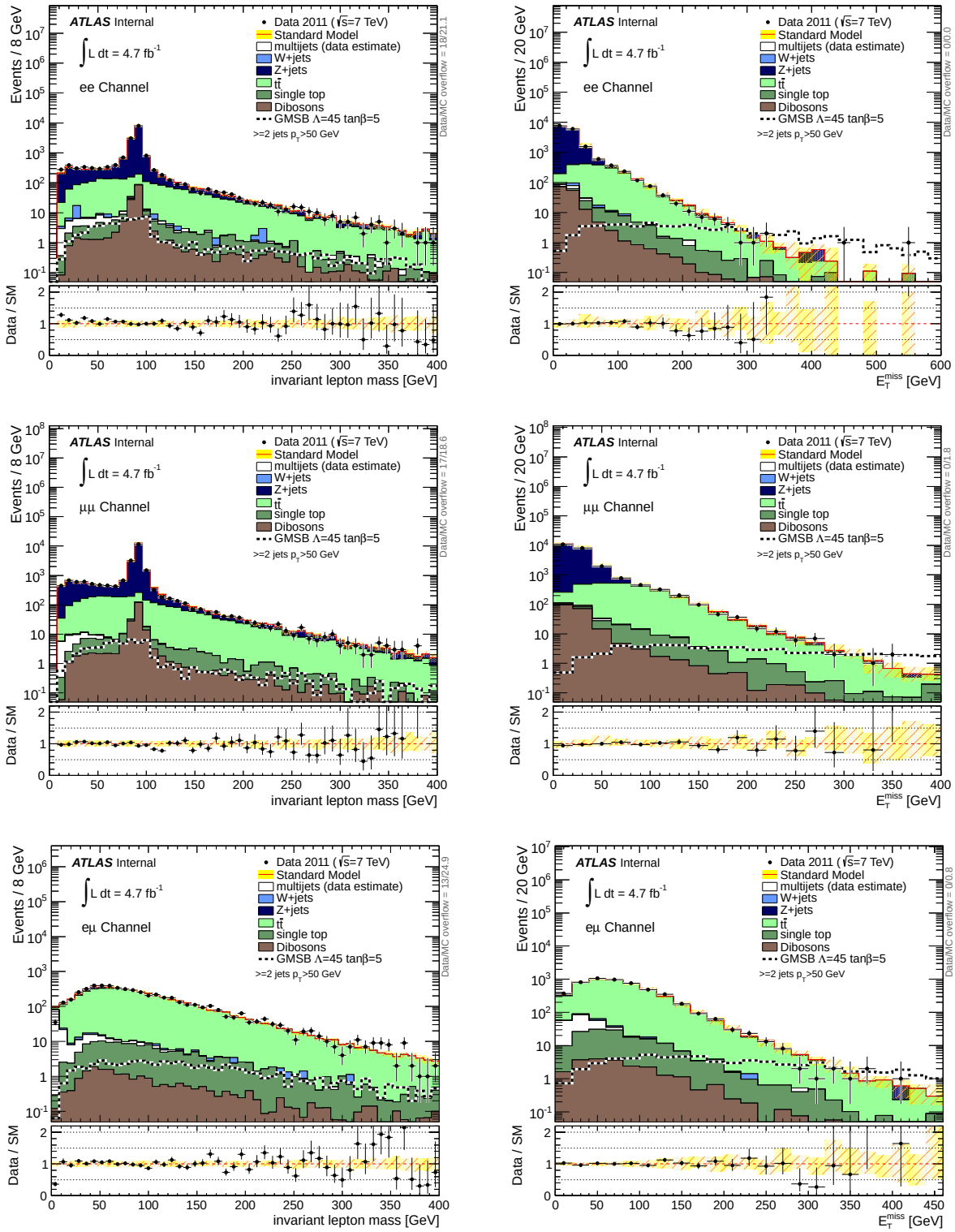

Figure 55: Distribution of the invariant mass (left) and missing transverse energy (right) in data and Monte Carlo for the ee channel (top), the $\mu\mu$ channel (middle) and the $e\mu$ channel (bottom) after the lepton plus two jets kinematic selection. The yellow band definition is given in the text. For each distribution data Monte Carlo ratio plots are also shown.

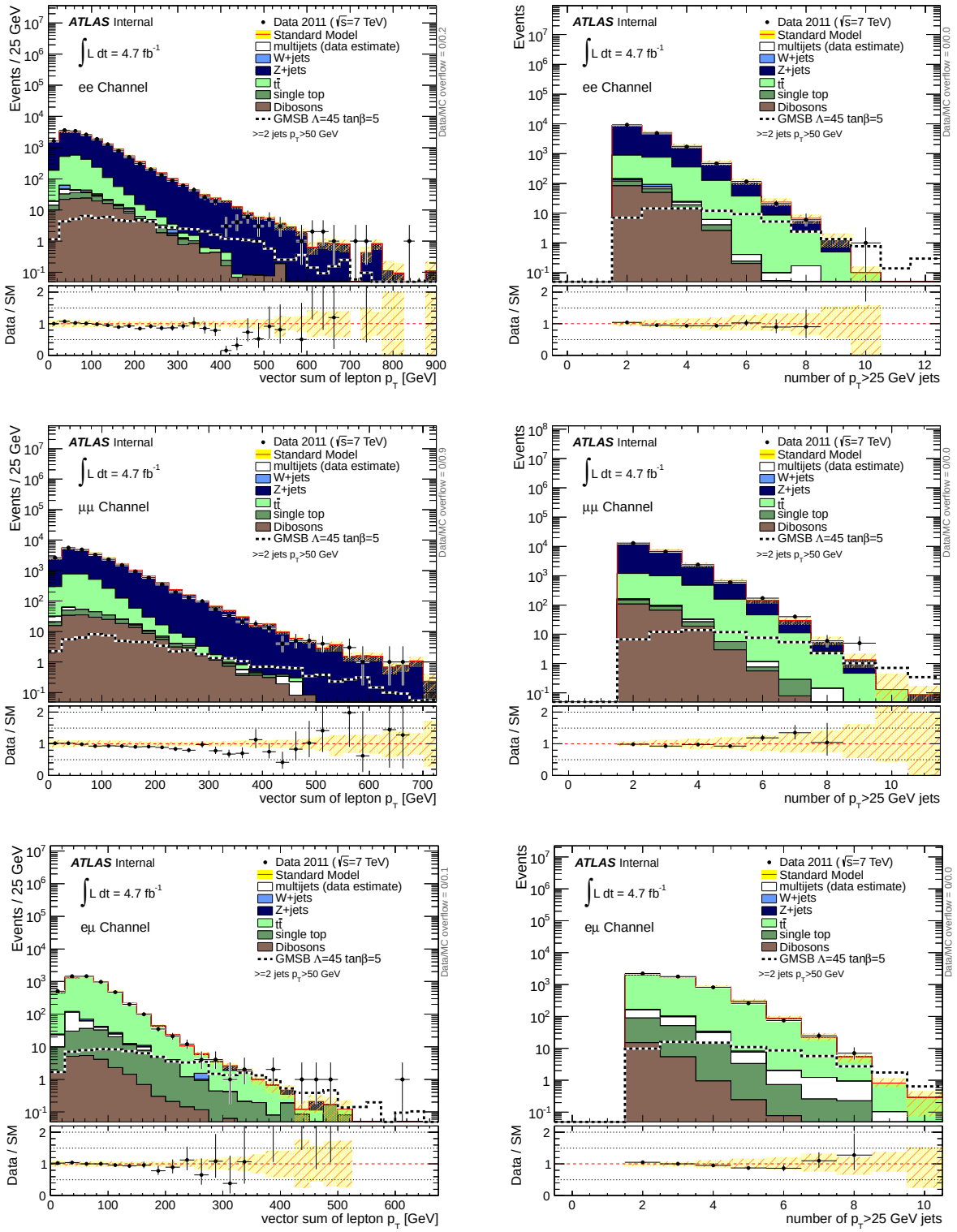

Figure 56: Distribution of the vectorial sum of the transverse momenta of the leading two leptons (left) and of the number of jets with transverse momenta above 25 GeV (right) in data and Monte Carlo for the ee channel (top), the $\mu\mu$ channel (middle) and the $e\mu$ channel (bottom) after the lepton plus two jets kinematic selection. The yellow band definition is given in the text. For each distribution data Monte Carlo ratio plots are also shown.

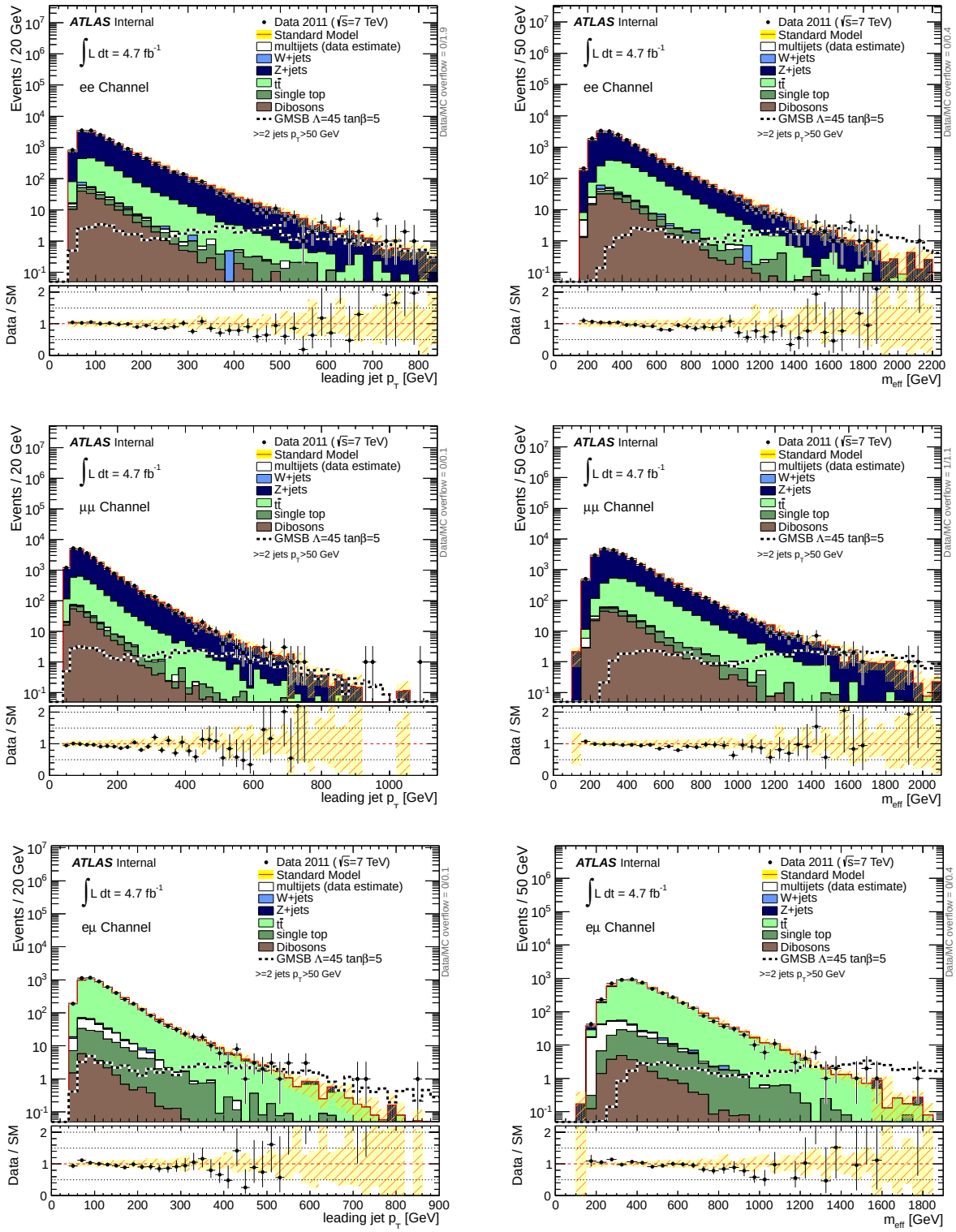

Figure 57: Distribution of the transverse momentum of the leading jet (left) and of effective mass (right) in data and Monte Carlo for the ee channel (top), the $\mu\mu$ channel (middle) and the $e\mu$ channel (bottom) after the lepton plus two jets kinematic selection. The yellow band definition is given in the text. For each distribution data Monte Carlo ratio plots are also shown.

7.7. Signal Region Optimization

The goal of this analysis is the discovery or exclusion of certain supersymmetry models introduced in chapter 4. As such it is necessary to maximize the possibility to distinguish a supposed number of signal events S from the background B such that an excess in the data cannot be attributed to a statistical fluctuation of the background. In high energy physics, this is often done by maximizing the significance

$$Sig = \frac{S+B-B}{\sqrt{B}} = \frac{S}{\sqrt{B}} \tag{33}$$

which measures the difference between the $S+B$ and the B hypothesis in relation to the 1σ uncertainty of the background expectation $\sqrt{B}$, assuming Gaussian distributions for both signal and background expectations. Therefore large significances correspond to high probabilities for a deviation from the background-only model. If the expectation values S and B are small, the expected number of events are better described via Poisson-distributions

$$f(n;\lambda) = \frac{\lambda^n}{n!}e^{-\lambda} \tag{34}$$

Correspondingly, the significance definition is modified to the following implicit definition

$$\sum_{n=S+B}^{\infty} f(n;B) = \frac{1}{\sqrt{2\pi}}\int_{Sig}^{\infty} exp(-x^2/2)dx \tag{35}$$

which translates the probability density function of the background expectation $f(n;B)$ into widths of a Gaussian normal distribution. For large values of B, equation 35 approaches equation 33.

In addition to these statistical properties, it is necessary to take into account systematic uncertainties on the expected number of signal and background events. Such systematic uncertainties can be incorporated into the significance definition by convoluting the Poisson distribution $f(n;\lambda)$ with an additional Gaussian distribution of mean $\lambda = B$ and width σ_{sys}. For the optimization described in the following, a systematic uncertainty σ_{sys} of 30% was assumed based on previous experience[36].

Using this significance definition as a figure of merit, *Signal Regions* can be defined by applying phase space region cuts on different variables. To maximize the sensitivity, several variables are scanned in parallel for all model points of a given supersymmetry scenario: For each model point, the possible cut combinations of all considered variables are scanned with a small stepsize and the remaining number of signal and background events is calculated.

The cut combination maximizing the following criteria (in this order of importance) for a given model is chosen as the Signal Region:

- Maximize the number of excludable points (using `TLimit` [276, 277])
- Maximize the number of discoverable points ($> 5\sigma$)
- Maximize the total sum of signficances

Further details on the method applied here can be found in [278].

Two Signal Regions are optimized for the dilepton analysis targeting different supersymmetry scenarios and assuming an integrated luminosity of 5 fb^{-1}. As discussed in chapter 4, in the GMSB

[36] The exact size of the systematic uncertainties was unknown at the time this optimization was performed.

scenario the dominant production mechanisms are gluino-squark and squark-pair production, which corresponds to the production of two or three jets. Furthermore, the mass difference between squarks and sleptons is large, leading to relatively hard jets. Correspondingly, the following set of variables has been scanned

- number of jets between 2 and 4
- transverse momenta of the leading to fourth leading jet between 30 GeV and 450 GeV in steps of 10 GeV
- missing transverse momentum between 100 GeV and 400 GeV in steps of 10 GeV

This set of variables is chosen as it provides strong separation between the signal models and the Standard Model backgrounds as visible in figures 55, 56 and 57.

In the signal scenarios where gluino pair production dominates (such at the gluino-based Simplified Models or mSUGRA for large m_0), larger jet multiplicities are present leading to a Signal Region definition requiring at least four jets. As the Simplified Model Monte Carlo was mostly unavailable at the time the optimization was performed, a generic selection based on the effective mass

$$m_{\text{eff}} = \sum_{i=0}^{N_{jets}} \mathrm{p}_{T,i} + \sum_{j=0}^{N_{leptons}} \mathrm{p}_{T,j} + E_T^{\text{miss}} \tag{36}$$

was used in addition to imposing soft selection requirements on the individual jets and on E_T^{miss}. Furthermore, the ratio of $E_T^{\text{miss}}/m_{\text{eff}}$ is used to discriminate the signal from the Standard Model backgrounds as the fraction of missing transverse energy of the total mass of the event (as measured by m_{eff}) in supersymmetric events is relatively large due to the presence of the two LSPs.

The results of the optimization are shown in Table 12 and illustrated in Figure 58. Here, m_{eff} denotes the effective mass including only the explicitly selected number of jets, while $m_{\text{eff}}^{\text{inc}}$ sums the transverse momenta of all signal jets in the event. Similarly, Signal Regions have been optimized for the hard one lepton and soft lepton Signal Regions [163] which are contained in Table 12 as well[37].

In order to search for the presence of a possible signal in these Signal Regions, it is necessary to have a precise prediction for the expected Standard Model background. The corresponding methods used for this purpose will be layed out in the following chapter 8.

[37] For the single-lepton Signal Regions, the transverse mass

$$m_T = \sqrt{2p_T^{\text{lep}} E_T^{\text{miss}} [1 - \cos(\Delta\phi(lep, E_T^{\text{miss}}))]} \tag{37}$$

is used. As the projection of the invariant mass of the lepton and E_T^{miss} in the transverse plane, m_T exhibits an endpoint at m_W in W+jets and semi-leptonic $t\bar{t}$ events and therefore can be used to suppress these backgrounds.

	multi-lepton		single-lepton		
	2-jet	**4-jet**	**3-jet**	**4-jet**	**soft-lepton**
Trigger	Single electron or muon (+jet)		Single electron or muon (+jet)		Missing E_{T}
N_{lep}	≥ 2	≥ 2	1	1	1
$p_{\mathrm{T}}^{\ell_1}$ (GeV)	> 25 (20)	> 25 (20)	> 25 (20)	> 25 (20)	7 to 25 (6 to 20)
$p_{\mathrm{T}}^{\ell_2}$ (GeV)	> 10	> 10	< 10	< 10	< 7 (6)
N_{jet}	≥ 2	≥ 4	≥ 3	≥ 4	≥ 2
$p_{\mathrm{T}}^{\mathrm{jet}}$ (GeV)	> 200,200	> 50,50,50,50	> 100, 25, 25	> 80, 80, 80, 80	> 130,25
$p_{\mathrm{T}}^{\mathrm{4th\ jet}}$ (GeV)	< 50	—	< 80	—	—
E_T^{miss} (GeV)	> 300	> 100	> 250	> 250	> 250
m_{T} (GeV)	—	—	> 100	> 100	> 100
$E_T^{\mathrm{miss}}/m_{\mathrm{eff}}$	—	0.2	> 0.3	> 0.2	> 0.3
$m_{\mathrm{eff}}^{\mathrm{inc}}$ (GeV)	—	> 650	> 1200	> 800	—

Table 12: Overview of the selection criteria for the Signal Regions used in this analysis. The p_T selections for leptons are given for electrons (muons).

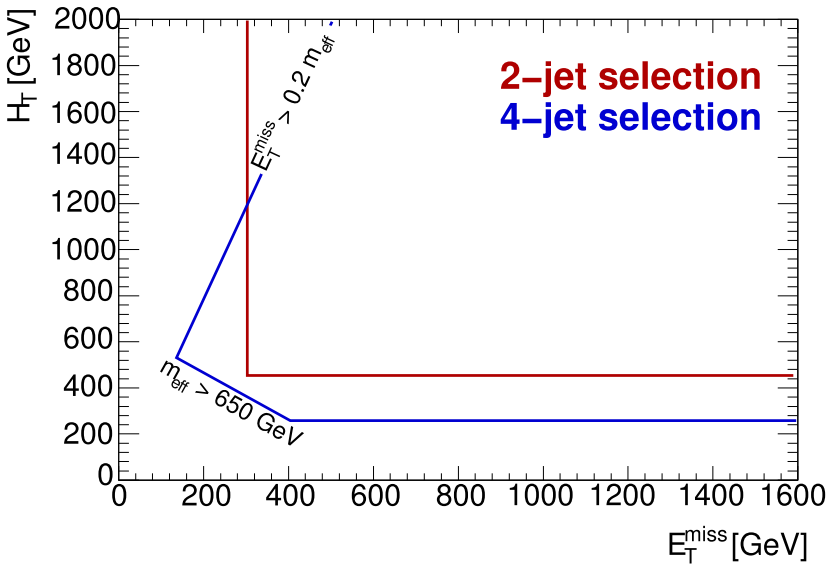

Figure 58: Signal Region definition for the 2-jet and the 4-jet Signal Region as a function of E_T^{miss} and $\mathrm{H_T} = \sum_i p_{T,i}^{jet} + \sum_j p_{T,j}^{lepton}$.

8. Background Estimation

In the following, details on the background estimation techniques will be given. For this purpose, *Control Regions* will be defined that are used to constrain the main Standard Model backgrounds contributing to the Signal Regions defined in the previous chapter 7. The information obtained from the Control Regions will then be combined in a simultaneous fit as discussed in chapter 10.

8.1. Fake Background Estimation

As discussed in chapter 4.6 several backgrounds are present in the analysis where one or both leptons are *fake* leptons due to misidentification. A sufficient description of the QCD background involving two fake leptons using the Monte Carlo simulation is impossible as large amounts of simulated Monte Carlo events would be necessary due to the combination of high cross section and low fake rate. Furthermore the description of fake leptons in the simulation can be problematic. Therefore, the contribution due to events involving two fake leptons is obtained using the matrix method [279].

Equation 38 defines the 4×4 matrix connecting the number of real (R) and fake (L) leptons to those passing the tight (T) and those passing the loose but failing the tight lepton requirements (L').

$$\begin{pmatrix} N_{TT} \\ N_{TL'} \\ N_{L'T} \\ N_{L'L'} \end{pmatrix} = \begin{pmatrix} \epsilon_1\epsilon_2 & \epsilon_1 f_2 & f_1\epsilon_2 & f_1 f_2 \\ \epsilon_1(1-\epsilon_2) & \epsilon_1(1-f_2) & f_1(1-\epsilon_2) & f_1(1-f_2) \\ (1-\epsilon_1)\epsilon_2 & (1-\epsilon_1)f_2 & (1-f_1)\epsilon_2 & (1-f_1)f_2 \\ (1-\epsilon_1)(1-\epsilon_2) & (1-\epsilon_1)(1-f_2) & (1-f_1)(1-\epsilon_2) & (1-f_1)(1-f_2) \end{pmatrix} \cdot \begin{pmatrix} N_{RR} \\ N_{RF} \\ N_{FR} \\ N_{FF} \end{pmatrix} \quad (38)$$

Here, ϵ_i (f_i) are the probabilities of a real (fake) loose lepton to pass the tight identification criteria. By inverting equation 38, the number of events involving one (N_{FR}, N_{RF}) or two (N_{FF}) can be obtained from data yielding the total number of fake dilepton events:

$$N_{Fake \to TT} = \epsilon_1 f_2 \times N_{RF} + f_1 \epsilon_2 \times N_{FR} + f_1 f_2 \times N_{FF} \quad (39)$$

Fake rates are obtained for electron- and muon-fakes as a function of η and p_T using dedicated QCD-enriched single lepton Control Regions as discussed in [242]. For the loose identification criterium, the preselected electrons and muons are used, while the tight criterium corresponds to the signal electrons and muons as defined in Tables 8 and 9. The measured true electron efficiency varies from 70.7% to 94.6%, while the true muon efficiency is measured to be $\approx 97\%$. For central electrons, the fake efficiency varies from 32% to 22%, and the fake muon efficiency changes from 35% to 23% as a function of p_T. Further dependencies of the rate measurements on the jet multiplicity are incorporated as systematic uncertainties. The measured rates are used for the estimation of the QCD background with two fake leptons in all Signal and Control Regions and applied via the `FakeLeptBkg` [280] package. The contribution involving one fake lepton in processes such as W+jets or semi-leptonic $t\bar{t}$ is directly taken from the Monte Carlo simulation after cross-checking with the matrix method results as shown in Fig. 59.

8.2. Control Regions

In order to validate the Monte Carlo simulation of the Standard Model backgrounds, Control Regions with a high purity are defined for the dominant Z and $t\bar{t}$ backgrounds. Similar Control Regions are

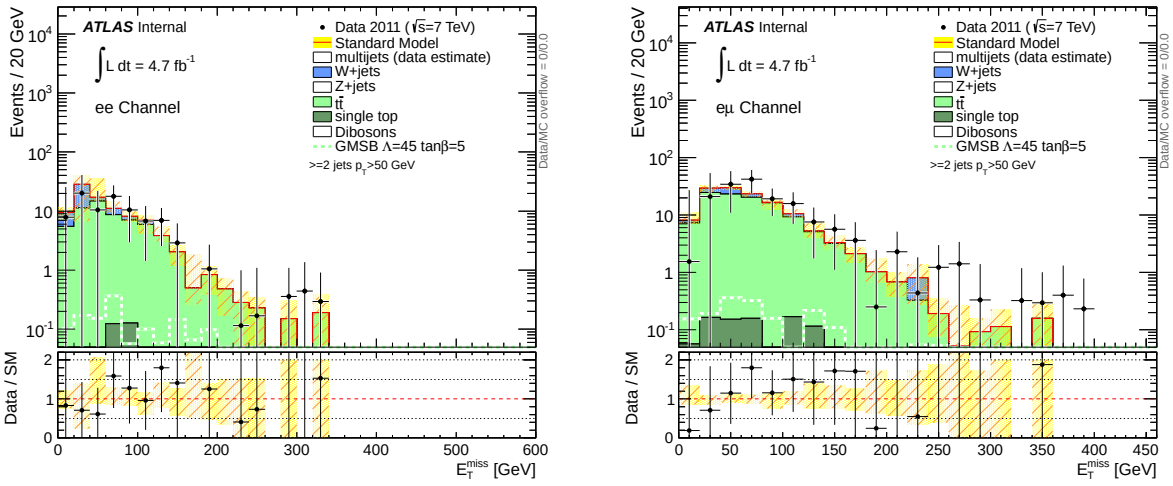

Figure 59: Distribution of the single fake lepton component determined from data via the matrix method compared to the Monte Carlo estimate as a function of missing transverse energy for the ee channel (left) and the $e\mu$ channel (right) after the lepton plus two jets kinematic selection (cf. Table 11).

defined for the hard and soft one lepton analyses as well, where W+jets and $t\bar{t}$ provide the largest backgrounds. For all remaining backgrounds, the Monte Carlo based background estimate will be used, as their contribution is rather small.

For the Z Control Region, only ee and $\mu\mu$ final states are used (as the dileptonic $Z \to \tau\tau$ background is very small compared to $t\bar{t}$ and does not result in a clear peak), while for $t\bar{t}$ all three dileptonic final states are investigated. Similar jet requirements as in the Signal Region definition are imposed to select events with comparable kinematical properties as those entering the Signal Regions, reducing uncertainties from extrapolating between Control and Signal Regions. With respect to the 2-jet Signal Region, the jet p_T requirements are softer in order to keep sufficiently many events while still being reasonably close to the Signal Region requirements. In order to minimize the contribution from possible signal events and to keep the regions disjoint, cuts on E_T^{miss} are imposed. To further separate the Control Regions, the invariant mass of the leading lepton pair is required to be within (outside of) $[81, 101]$ GeV for the Z ($t\bar{t}$) Control Region. Furthermore, at least one of the three leading jets is required to be b-tagged for the $t\bar{t}$ region to enhance the purity. Table 13 shows the selection criteria used to define the Control Regions. The corresponding selection is further illustrated in Figure 60.

Figure 61 shows the distributions of the jet multiplicity and the effective mass in the $t\bar{t}$ region, while Figure 62 provides the same distributions for the Z Control Region. Both the purity of the investigated process and the general agreement between data and simulation are reasonable and the signal contamination for the depicted GMSB model point is small.

	multi-lepton		hard-lepton		soft-lepton	
	Z **CR**	$t\bar{t}$ **CR**	W **CR**	$t\bar{t}$ **CR**	W **CR**	$t\bar{t}$ **CR**
N_{jet}	≥ 2	≥ 2	≥ 3	≥ 3	≥ 2	≥ 2
$p_{\text{T}}^{\text{jet}}$ (GeV)	$>$ 80,50 or $>$ 50,50,50,50	$>$ 80,50 or $>$ 50,50,50,50	$>$ 80, 25, 25	$>$ 80, 25, 25	$>$ 130,25	$>$ 130,25
N_{jet} (b-tagged)	—	≥ 1	$=0$	≥ 1	$=0$	≥ 1
E_T^{miss} (GeV)	$<$ 50	[30,80]	[40,150]	[40,150]	[180,250]	[180,250]
m_{T} (GeV)	—	—	[40,80]	[40,80]	[40,80]	[40,80]
$m_{\text{eff}}^{\text{inc}}$ (GeV)	—	—	$>$ 500	$>$ 500	—	—
$m_{\ell\ell}$ (GeV)	[81,101]	$<$ 81 or $>$ 101	—	—	—	—

Table 13: Overview of the selection criteria for the W+jets, Z+jets and $t\bar{t}$ Control Regions (CR). Only the criteria that are different from the signal selection criteria listed in Table 12 are shown.

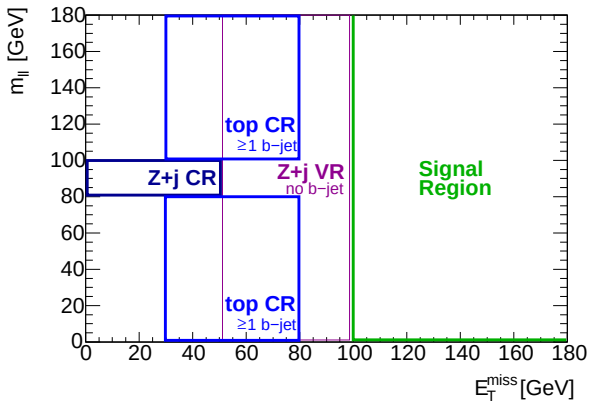

Figure 60: Control Region definition for the Z and the $t\bar{t}$ Control Region as a function of E_T^{miss} and $m_{\ell\ell}$ compared to the Signal Region definition. The Validation Region shown in addition will be discussed in chapter 11.2.

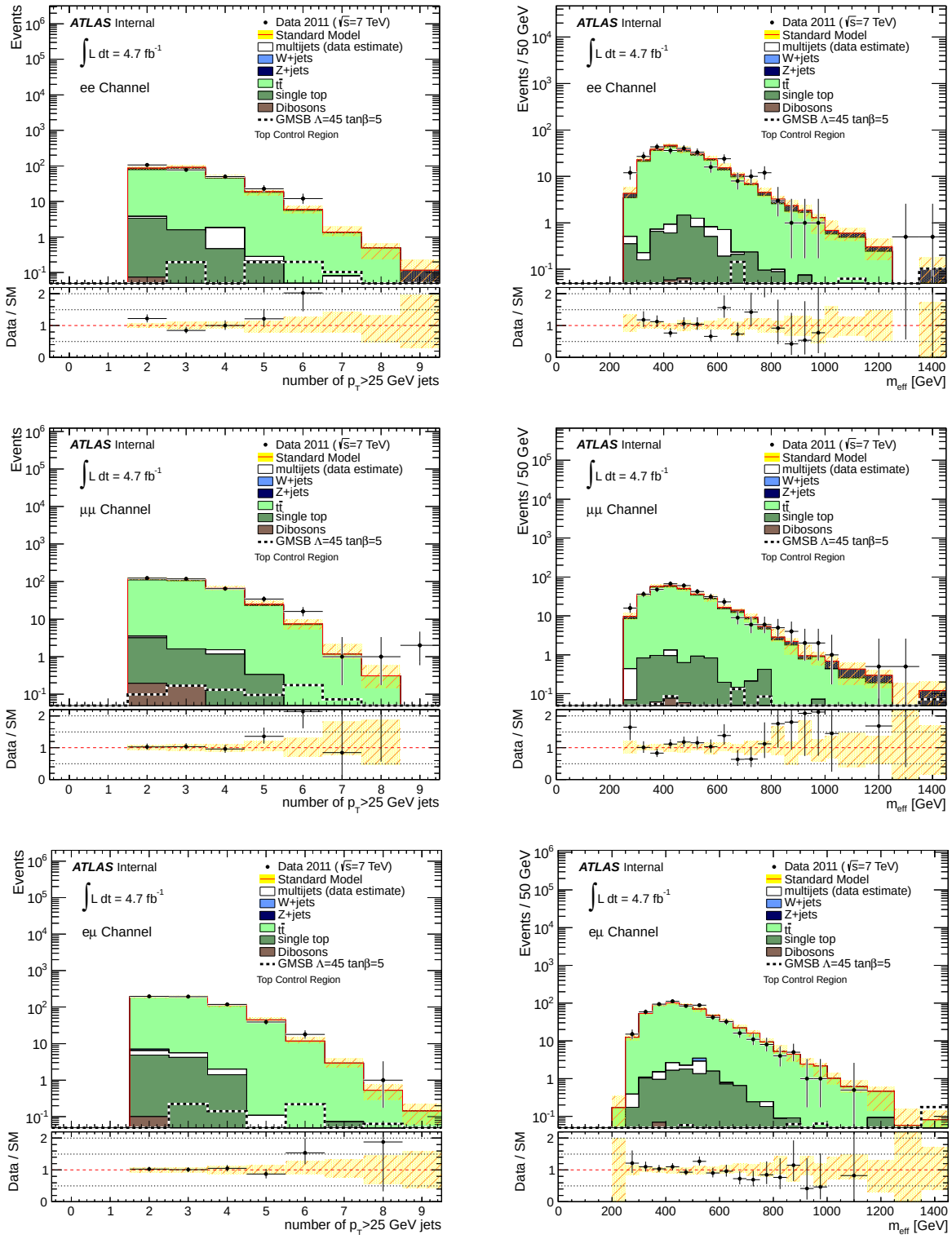

Figure 61: Distribution of the number of jets (left) and of effective mass (right) in data and Monte Carlo for the ee channel (top), the $\mu\mu$ channel (middle) and the $e\mu$ channel (bottom) in the $t\bar{t}$ Control Region.

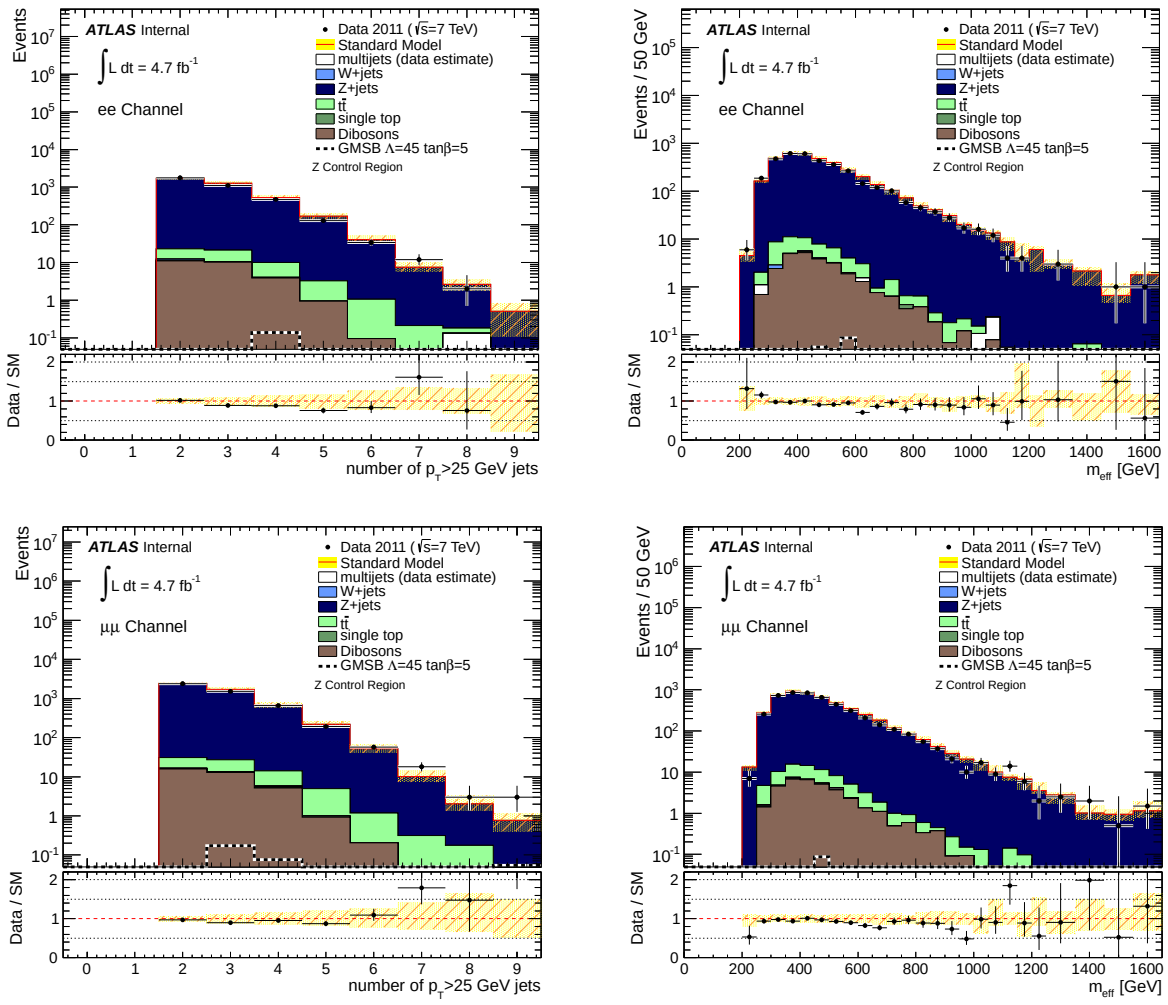

Figure 62: Distribution of the number of jets (left) and of effective mass (right) in data and Monte Carlo for the ee channel (top) and the $\mu\mu$ channel (bottom) in the Z Control Region.

Truth p_T^Z bin	Fitted scale factor
[0 GeV, 50 GeV]	1.0 (fixed)
[50 GeV, 100 GeV]	0.893±0.043
[100 GeV, 150 GeV]	0.866±0.056
[150 GeV, 200 GeV]	0.737±0.061
> 200 GeV	0.772±0.079

Table 14: Fitted scale factors for the p_T^Z-reweighting for the different bins in truth p_T of the Z boson [163].

8.3. Z pt Fit

As already observable in Figure 56 in chapter 7.6, the transverse momentum of the Z-boson p_T^Z is not correctly described by the simulation based on the ALPGEN generator. A similar discrepancy is observed in W+jets events in the hard one lepton analysis using the same generator [281]. To correct this mismodelling, a data-driven reweighting approach is used [163].

Events are selected in a Z+jets enriched region by requiring two opposite-sign, same-flavor leptons with invariant mass between 80 GeV and 100 GeV as well as at least three jets with $p_T > 25$ GeV. Furthermore, $m_{eff}^{inc} > 400$ GeV is required to mimick the W Control Region used in the hard one lepton channel.

The ALPGEN Z+jets Monte Carlo sample is divided in four 50 GeV bins of generated Z p_T between 0 GeV and 200 GeV and one inclusive bin above 200 GeV. The measured p_T^Z distribution in data is compared to the reconstructed p_T^Z predicted by the simulation and relative normalization factors with respect to the lowest p_T^Z bin are fitted for each true p_T^Z bin keeping the overall normalization constant. A common set of factors is determined for both the ee and the $\mu\mu$ channel.

The resulting normalization factors are listed in Table 14. Figure 63 shows the reconstructed p_T^Z before and after applying these fitted normalization factors. Good agreement is observed after applying the correction.

The same set of normalization factors will also be applied to the W+jets Monte Carlo fixing the analogous discrepancy in the p_T^W modelling observed in the one lepton channels. This approach is reasonable as the physics behind W- and Z+jets production is very similar and a possible impact due to the different gauge boson masses is expected to be small[38].

8.4. K-factor Fit

The $t\bar{t}$ and Z Control Regions will be used to validate and correct the background modelling and in addition to constrain systematic uncertainties. As the Signal Regions contain high jet multiplicities, the modelling of additional jet radiation is vital. For this reason, ALPGEN is chosen as the generator for $t\bar{t}$, Z+jets as well as W+jets production as discussed in chapter 7.4. Although implementing matrix elements only at tree level, events containing a fixed number of additional final-state partons can be generated and matched to a parton-shower algorithm using the MLM matching scheme [275]

[38] It is reasonable to use the p_T^Z instead of the p_T^W distribution for the correction of this mismodelling as the dilepton final state is purer and not affected by jet energy uncertainties which would occur via the incorporation of E_T^{miss} in the W reconstruction.

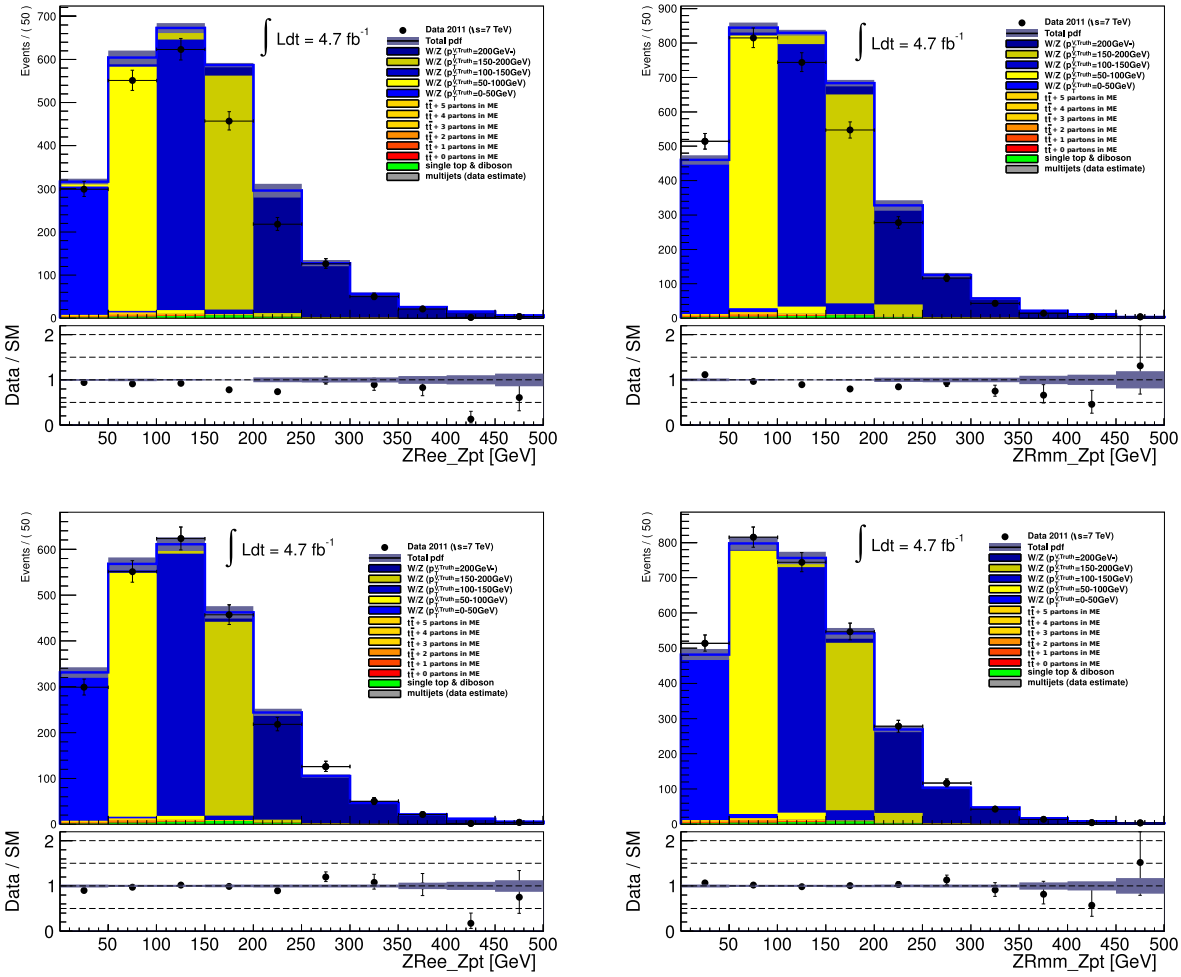

Figure 63: Distribution of the p_T of the Z boson in the dielectron (left) and dimuon final state (right) before (top) and after (bottom) applying the fit binned in truth p_T of the Z boson in a Z dominated region (see text) [163].

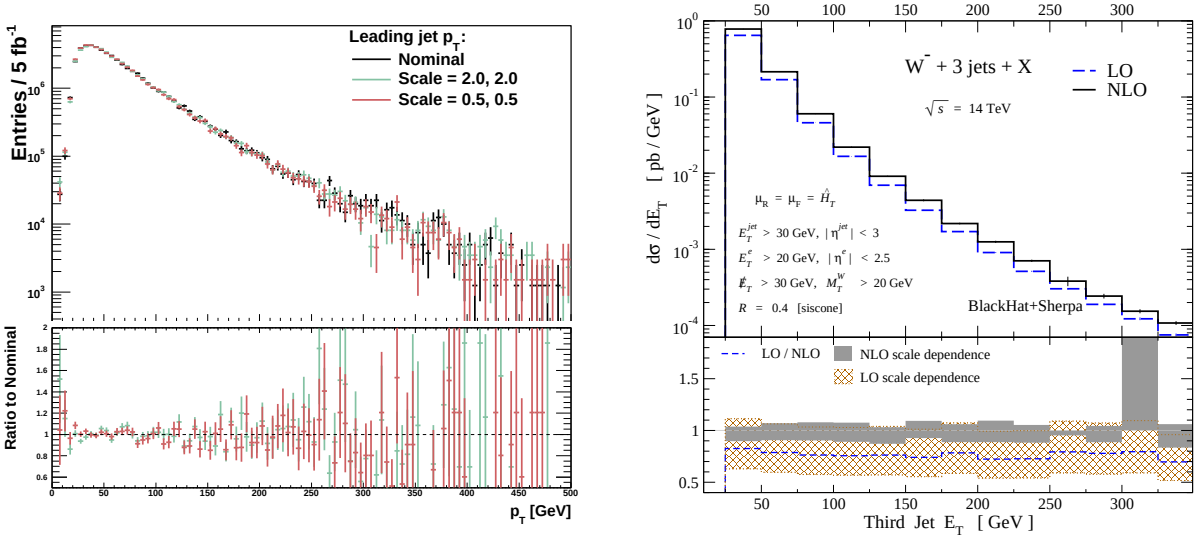

Figure 64: Left: Comparison of the transverse momentum of the leading jet for the W+jets sample including one additional parton varying the factorization and renormalization scales jointly by a factor of two normalized to the same cross section [285]. Right: The E_T distribution of the third leading jet in W^-+jets events predicted by Blackhat [288].

providing an improved description of the additional jet radiation compared to generators such as MC@NLO or POWHEG [282, 283].

While the inclusive cross sections can be predicted with high accurancy [260, 284], significant systematic uncertainties on the individual light parton bins related to the renormalization and factorization scales k_T^{fac} and Q_{fac} (see chapter 4.1) as well as the matching scale p_T^{min} arise. These systematic uncertainties and their impact on supersymmetry analyses have been investigated extensively [285, 286]. It has been observed [287] that a variation of both the renormalization and the factorization scales only affects the cross sections of the individual N_{parton} samples while leaving the shape of the transverse momenta of the jets within each N_{parton} subsample unchanged. This observation has the important consequence that the scale-related theory uncertainties can be constrained by a data-driven determination of the individual normalization k_i of the N_{parton} subsamples [285], provided that the shape prediction at leading order is not too different from predictions at higher orders.

Figure 64 left shows the impact of the varations of the factorization and renormalization scales on the transverse momentum of the leading jet for the W+jets sample including one additional parton as an example, while Figure 64 right contains a comparison between LO and NLO predictions of the transverse momenta of the third hardest jet in W^-+jets events using Blackhat [288]. It can be observed that a variation of the factorization scale does not lead to a shape variation. Furthermore, the predicted jet p_T shape at NLO is very similar to the LO prediction for this reasonable scale choice. The figures are included here as an example, many more details on the method and its validity can be found in [285].

The extraction of these individual normalization factors k_i from data is possible as the jet multiplicity distribution provides sensitivity to the individual parton bins as shown in Figure 65, i.e. the reconstructed number of jets corresponds to the true number of partons apart from pileup as well as jet splitting or jet merging effects.

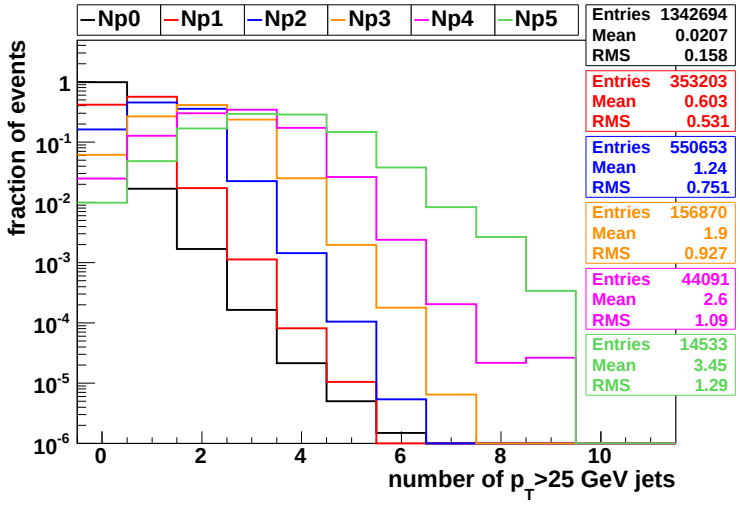

Figure 65: Jet multiplicity distribution for the ALPGEN $Z \to ee$ samples with 0 to 5 partons after a dielectron preselection normalized to unity.

After having discussed the impact of other systematic uncertainties in the following chapter 9, these normalization factors will be fit in the Control Regions and applied to the W, Z and $t\bar{t}$ samples in the Signal Regions as well to obtain an improved background prediction as further discussed in chapter 10.

9. Systematic Uncertainties

Before discussing the combined fit to Control and Signal Regions that forms the core part of this analysis, it is necessary to discuss the impact of experimental and theoretical systematic uncertainties on the prediction for the signal and background processes. These uncertainties arise from various sources, but can be partially constraint further using data as discussed in the next chapter.

9.1. Experimental Uncertainties

9.1.1. Luminosity

The luminosity is measured with several dedicated subdetectors with the corresponding luminosity scale being obtained via van der Meer scans as discussed in chapter 5.2.5. Uncertainties on the luminosity estimate of 4.71 ± 0.18 fb^{-1} have been investigated in detail in [240, 241]. The luminosity uncertainty is dominanted by the bunch charge product, the product of the number of protons in the two colliding bunches. The total luminosity uncertainty has been measured to be 3.8% for the full 2011 dataset.

9.1.2. Trigger

Electron and Muon trigger efficiencies are measured with a tag-and-probe method using Z decays with a total uncertainty of $\lesssim 1\%$ [243, 244]. Residual discrepancies in the trigger description between data and simulation are corrected [289].

9.1.3. Jet Energy Scale and Resolution

Jets are composite objects resulting from the fragmentation and hadronization of quarks and gluons. As such, the jet energy scale that translates the measured energy depositions in the calorimeters to the parton energy is subject to substantial systematic uncertainties from various sources, such as the non-instrumented detector material, neutral particles or the single-particle response of the calorimeter. The jet energy scale has been estimated from Monte Carlo simulation and measured using testbeam studies as well as in situ using among others Z+jet [290, 291] and photon+jet [292] events. In addition to the jet energy scale, the jet energy resolution (i.e. the fluctuation of the measured jet energy around a central value) has been measured using data-driven techniques [293, 294]. The corresponding systematic uncertainties have been derived [295] including additional uncertainties for multi-jet final states as well [296]. Figure 66 left shows the resulting jet energy scale uncertainty for jets reconstructed with the `anti-`k_t algorithm with a radius parameter R = 0.6. For central jets with $p_T < 60$ GeV, the resulting uncertainty is between 2% and 4%, while for jet transverse momenta between 60 GeV $< p_T <$ 800 GeV uncertainties range from 2% to 2.5% and between 2.5% and 4% for momenta above 800 GeV. For jet transverse momenta > 100 GeV, the uncertainty is dominated by the single-particle response of the calorimeter, while for smaller momenta several sources contribute. In the endcap region, larger uncertainties of up to 7% occur due to larger intercalibration uncertainties. Figure 66 right shows the result from a test of the jet energy scale measurement using Z+jet events as an additional example.

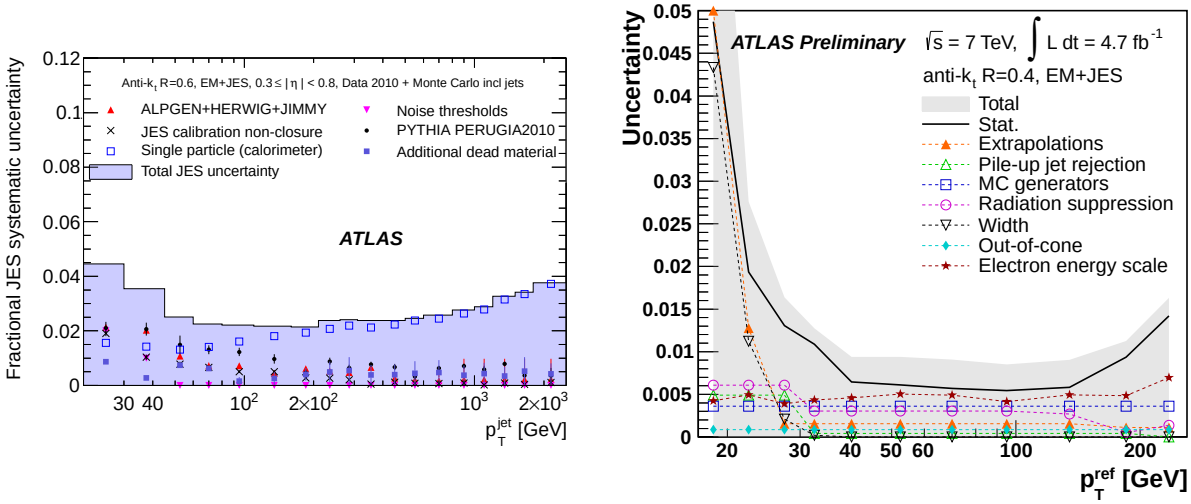

Figure 66: Left: Fractional jet energy scale uncertainty and its contributions as a function of jet transverse momentum for central jets with $0.3 < |\eta| < 0.8$. Right: Probing of the jet energy scale uncertainty (grey band) for jets reconstructed with the `anti-`k_t algorithm with a radius parameter R = 0.4 using Z+jets events as a function of $p_T^{ref} = p_T^Z \times |cos(\Delta\phi(jet, Z))|$ [291].

9.1.4. Lepton Scale, Resolution and Efficiency

As for the jets, the simulation of energy scale and resolution for both electrons and muons is cross-checked using data [206, 225] and corresponding systematic uncertainties have been derived [297]. Additionally, also the reconstruction and identification efficiencies are subject to systematic uncertainties that will be taken into account [298, 299]. The impact of the lepton-related systematic uncertainties is expected to be relatively small. Figure 67 shows the measured energy scale corrections as well as the dimuon mass resolution as an example.

9.1.5. Missing Energy Uncertainties

As described in chapter 6.7, the missing transverse energy combines the information on jets and leptons as well as residual cells not assigned to any physics object. While the scale and resolution uncertainties on the former objects have been discussed above and are propagated to the missing transverse energy, additional uncertainties on the `CellOut` term containing the unassigned energy cells are present as well and have been assessed [238, 300]. Further pileup-related uncertainties with respect to [300] have been studied and are included as well via [301].

9.1.6. b-tagging Uncertainties

Data-driven corrections and systematic uncertainties on the b-tagging efficiency and rejection in the simulation have been measured using events with jets containing muons as well as in $t\bar{t}$ events with several techniques [236, 302, 303]. Up to 20 different sources of uncertainties are combined and determined as a function of jet transverse momentum and jet flavor [304].

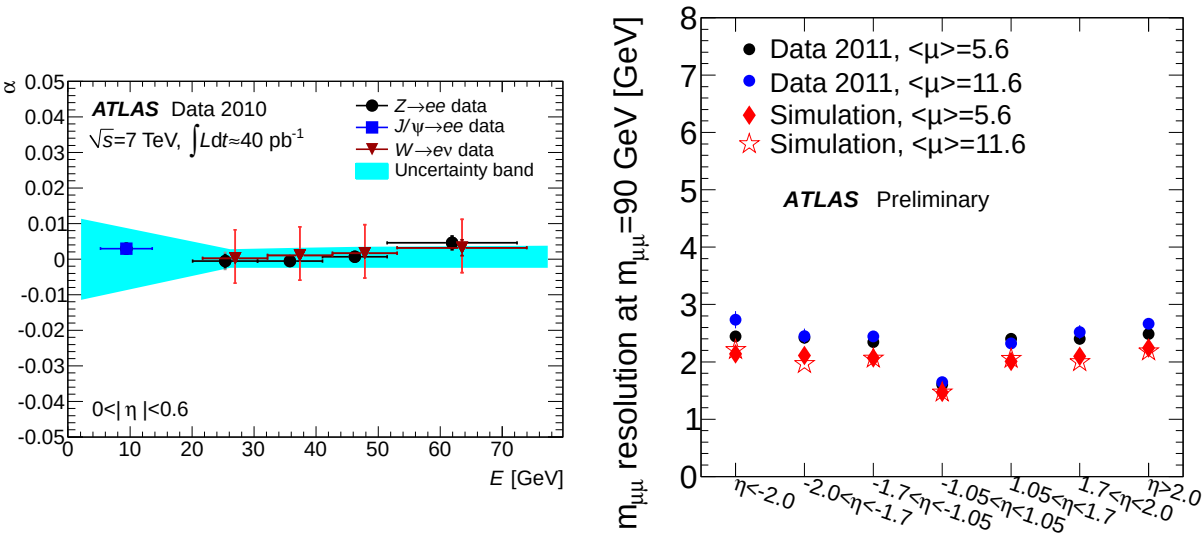

Figure 67: Left: Electron energy scale corrections and corresponding systematic uncertainties for central electrons as a function of electron energy obtained using tag and probe techniques [206]. Right: Dimuon mass resolution obtained in $Z \to \mu\mu$ events combining the measurements from the inner detector and the muon system in bins of η [225].

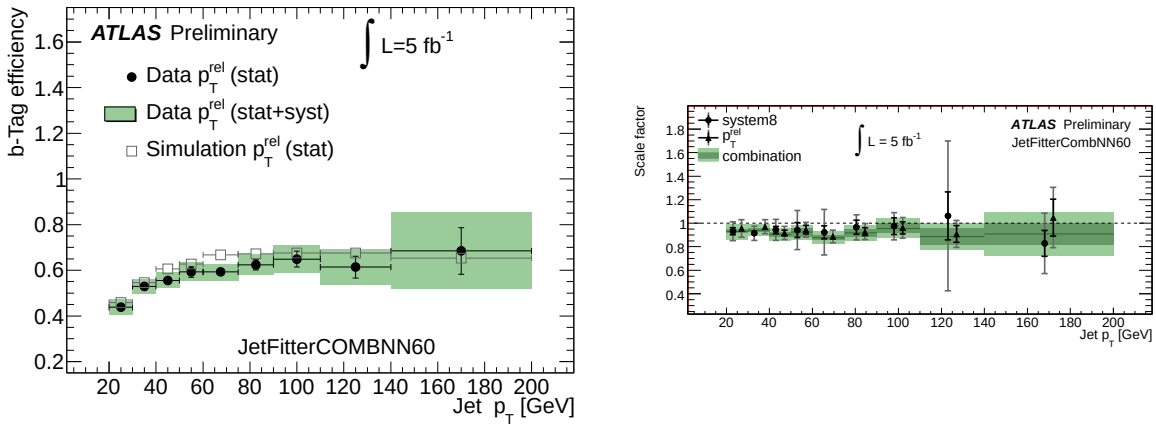

Figure 68: The b-tagging efficiency measured in data and simulation (left) as well as the derived data-to-simulation scale factors for the JetFitterCombNN tagging algorithm at 60% efficiency [303].

9.2. Theory Uncertainties

In addition to the experimental uncertainties described so far, several theory-related uncertainties impact the prediction of the standard model backgrounds as well as the supersymmetry signal.

9.2.1. Scale Uncertainties

Scale uncertainties arise in the prediction for $t\bar{t}$, Z and W events with high jet multiplicities using the ALPGEN generator in the MLM matching procedure as discussed in chapter 8.4. The factorization and renormalization scale uncertainties will be absorbed in the uncertainties on the k-factors as described in chapter 8.4 and as such do not need to be considered explicitly. In addition, also uncertainties related to the MLM matching parameter p_T^{min} separating the matrix element calculation from the parton shower algorithm have to be considered. The impact of a variation of the p_T^{min} parameter has been studied in detail using Monte Carlo simulations with varied parameter settings [281, 285]. The resulting uncertainties range from 0.1% to 14% in the Control Regions and up to 14% in the Signal Regions as shown in Table 15.

Region	Process	p_T^{min} Variation	Njet Bin 2	3	4	5	6	7
Top CR	$t\bar{t}$	up	1.003	1.04	–	–	–	1.11
		down	–	–	0.9	0.86	0.88	–
Z CR	Z+$jets$	up	1.03	–	–	–	1.05	1.13
		down	–	0.97	0.93	0.96	–	–
2-jet SR	$t\bar{t}$	up	1.11					
		down	0.89					
	Z+$jets$	up	1.14					
		down	0.86					
4-jet SR	$t\bar{t}$	up	1.01					
		down	0.99					
	Z+$jets$	up	1.08					
		down	0.92					

Table 15: Systematic uncertainties from p_T^{min} variations due to the MLM matching scheme in the ALPGEN Monte Carlo simulation of $t\bar{t}$ and Z+$jets$ for the Control and Signal Regions [281]. The listed numbers correspond to the resulting change of normalization in bins of the N_{jet} distributions (CR) or the total normalization (SR). For the Signal Regions, only a total normalization has been derived due to the limited number of Monte Carlo events.

9.2.2. Parton Shower and Hadronization

Systematic uncertainties related to parton shower and hadronization are partially already contained in the jet energy scale uncertainties. In addition, dedicated studies have been performed regarding their impact on extrapolations into the rather extreme phase space regions that are of relevance for supersymmetry searches [163]. Using $t\bar{t}$ (W/Z) events generated with POWHEG (ALPGEN) combined with the parton shower and hadronization model of either Herwig/Jimmy or Pythia, extrapolation uncertainties of 12% (10%) on the transfer factors from Control to Signal Region

(see next chapter 10) have been assigned based on the different m_{eff} requirements in the different regions [305].

9.3. Signal-related Systematic Uncertainties

9.3.1. Cross Section Uncertainties

The signal cross section prediction is subject to systematic uncertainties due to the PDF, the renormalization and factorization scales as well as the strong coupling constant α_s. The size of the uncertainties is determined for each model following a common approach between the ATLAS, CMS and LPCC supersymmetry working groups described in detail in [154] and as implemented via [306].

For the determination of scale uncertainties, both factorization and renormalization scales are varyied up and down by a factor of two with respect to the nominal choice $Q = (m_1 + m_2)/2$ with $m_{1,2}$ being the masses of the produced supersymmetric particles for a given production process. PDF uncertainties are calculated via the set of 22 (20) different variations of the CTEQ6.6 (MSTW2008) PDF sets spanning the range of uncertainties for the corresponding PDF fit. α_s uncertainties are included via the CTEQ6.6AS variations. The impact on the cross section is derived by quadratically summing the resulting deviations from the nominal cross section. The maximum of the resulting deviations from the two different PDF sets

$$\begin{aligned} U &= max(CTEQ_{nom} + CTEQ_{up}, MSTW_{nom} + MSTW_{up}) \\ L &= min(CTEQ_{nom} - CTEQ_{down}, MSTW_{nom} - MSTW_{down}) \end{aligned}$$

is used to arrive at the final cross section and the symmetrized total uncertainty

$$\begin{aligned} \sigma &= (U + L)/2 \\ \Delta\sigma &= (U - L)/2. \end{aligned}$$

This calculation is performed for each production process of a given model of supersymmetry breaking. In both the GMSB and the mSUGRA model, several production processes occur as described in chapter 4. Therefore, the total systematic uncertainty is obtained as the quadratic sum over the different production processes, weighted with the relative contribution to the corresponding Signal Region[39].

Figure 69 shows the relative uncertainties on the cross section for the main production processes in the GMSB model. The relative uncertainties grow with Λ due to the growing sparticle masses, thus probing PDFs at higher x where the uncertainties increase. Furthermore, production mechanisms via gluons in the initial state have larger uncertainties than those via quarks as the uncertainty on the gluon PDF is larger. The resulting total relative uncertainty is shown in Figure 70. For small values of Λ, the resulting signal cross section uncertainties are approximately 10%, while for larger values of Λ, the uncertainty is increased to approximately 25% due to the heavy squark and gluino masses. More information on the signal cross section uncertainties in the GMSB model are contained in [307].

[39] Only the 2-jet Signal Region is used for this calculation here for technical reasons in the context of the limit setting procedure described in chapter 12. The 2-jet Signal Region was chosen as the resulting uncertainties were larger with respect to the 4-jet Signal Region.

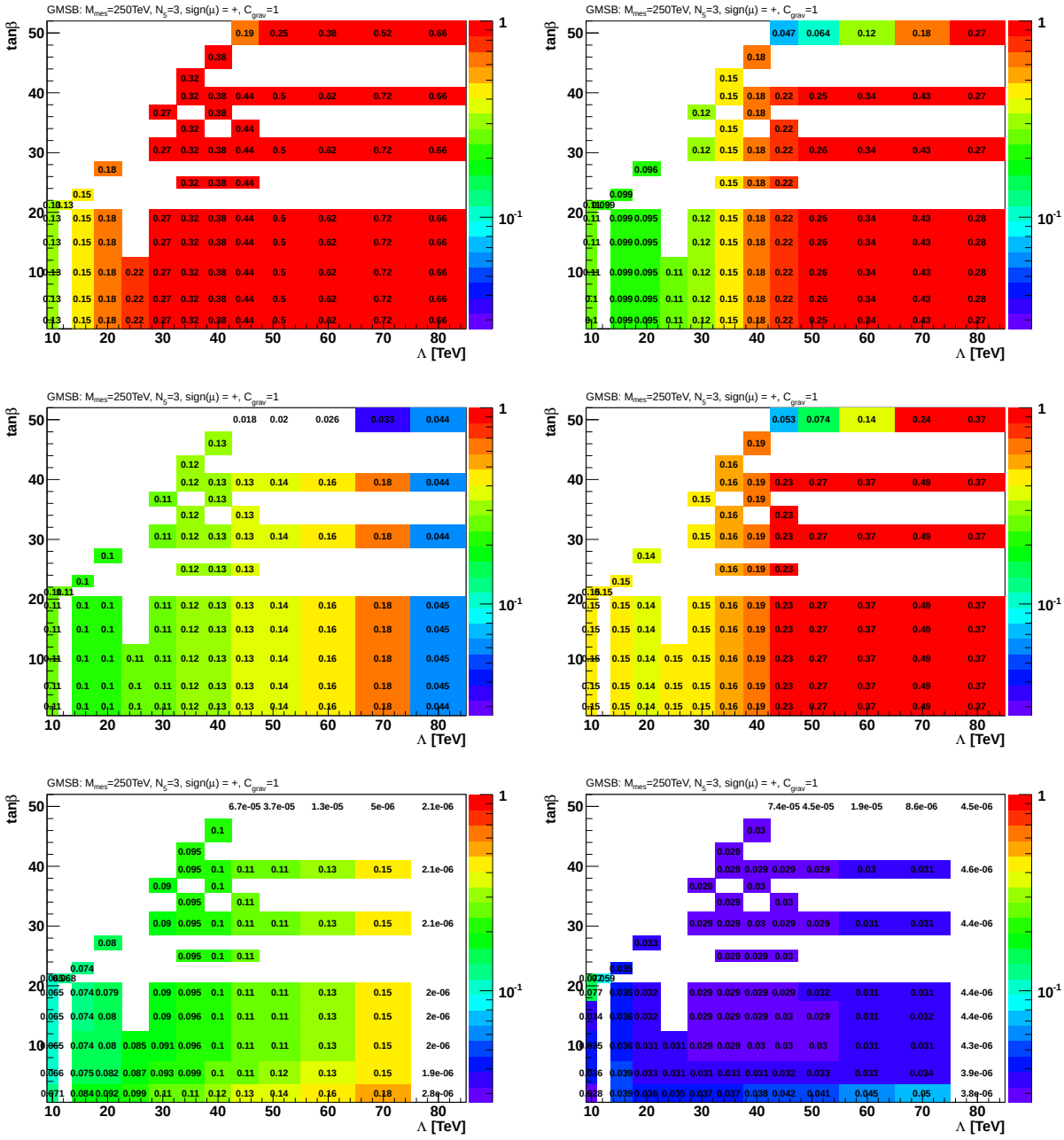

Figure 69: Relative cross section uncertainty in the GMSB model for gluino-gluino (top left), gluino-squark (top right), squark-squark (middle left), squark-antisquark (middle right), squark–gaugino (bottom left) and gaugino-pair production (bottom right) as a function of Λ and $\tan\beta$.

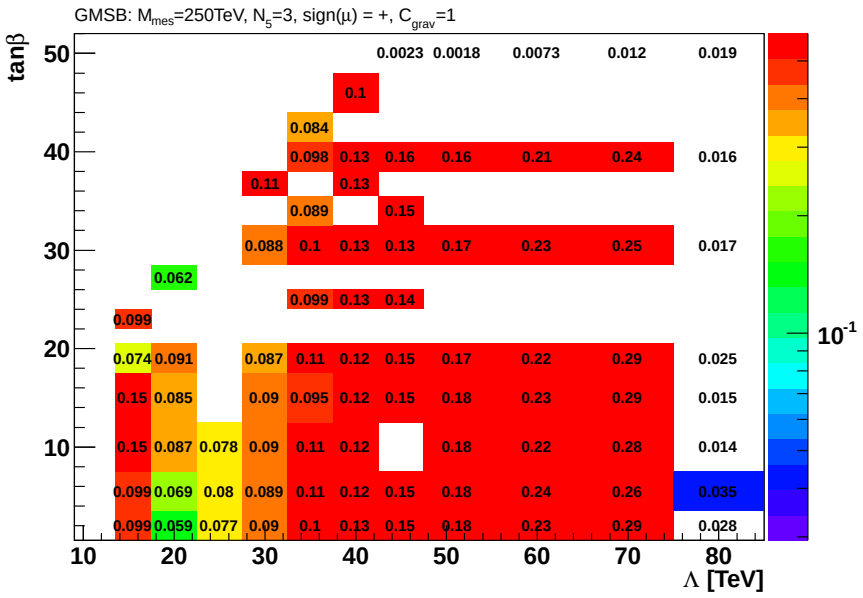

Figure 70: Total production cross section uncertainty in the GMSB model as a function of Λ and $\tan\beta$. The entries in the plane correspond to the simulated grid discussed in chapter 7.5.

9.3.2. Initial State Radiation

Uncertainties on the radiation of additional jets in the dominant backgrounds are already covered by the ALPGEN scale variations. For the Simplified Model-based supersymmetry signals, uncertainties related to Initial State Radiation (ISR) are of special importance for the soft lepton analysis as it relies on the ISR boost for models with small mass splittings between squark/gluino and LSP. The impact of ISR variations is investigated by generating samples with different Pythia PDF tunes and with varied matching scale parameters for the MADGRAPH samples of the Simplified Models [163]. The resulting uncertainty is parametrized as a function of the squark/gluino and the LSP mass.

10. Simultaneous Fit

After having introduced the Signal and Control Regions as well as the relevant systematic uncertainties, a simultaneous fit providing a combined statistical treatment will be discussed in the following chapter. The approach uses a profile likelihood method taking into account the systematic uncertainties as nuisance parameters. The method itself and the description in the following closely follows [308].

10.1. Overview & Statistical Procedure

The maximum likelihood method is a well-known technique for parameter estimation. The likelihood function is the combined probability density that a measured set of data could have been produced from a set of model parameters. In the context of this analysis, the likelihood function can be written as a product of Poisson distribution functions P for Signal and Control Regions accompanied by additional systematic uncertainty distributions P_{Syst}:

$$\begin{aligned} L(\boldsymbol{n}, \boldsymbol{\theta}^0 | \mu, \boldsymbol{b}, \boldsymbol{\theta}) &= P_{SR} \times P_{CR} \times P_{Syst} && (40) \\ &= \prod_{i \in SR} P(n_i | \lambda_i(\mu, \boldsymbol{b}, \boldsymbol{\theta})) \times \prod_{j \in CR} P(n_j | \lambda_j(\mu, \boldsymbol{b}, \boldsymbol{\theta})) \times P_{Syst}(\boldsymbol{\theta}^0, \boldsymbol{\theta}) && (41) \end{aligned}$$

Here, n_i and n_j are the number of observed events in Signal and Control Regions i and j, while λ_i and λ_j are the Poisson expectation values. The expectation values depend on the background normalization factors $\boldsymbol{b}$, the nuisance parameters $\boldsymbol{\theta}$ modelling the systematic uncertainties as well as the signal strength μ, with $\mu = 1$ corresponding to the nominal signal under consideration and $\mu = 0$ describing a background-only likelihood. In addition to the product over Signal and Control Regions, the probability density functions will be binned in jet multiplicity (CR) and effective mass (SR) as shown in Table 16. As all Signal and Control Regions are disjoint in phase space, a direct combination is possible.

Systematic uncertainties are incorporated as nuisance parameters via the probability density function $P_{Syst}(\boldsymbol{\theta}^0, \boldsymbol{\theta})$, with $\boldsymbol{\theta}^0$ being the set of nominal values and $\boldsymbol{\theta}$ a possible variation in the progress of maximizing the likelihood[40]. Without loss of generality, the parametrization can be chosen such that θ_i^0=0 for the nominal value and $\theta_i = \pm 1$ corresponding to the one sigma deviations. Here, all systematic uncertainties will be modelled by Gaussian normal distributions.

The expectation values for Signal and Control Regions λ are chosen such that the measurements between different regions are connected via *transfer functions* c obtained from the Monte Carlo simulation

$$\lambda_i(\mu, \boldsymbol{b}, \boldsymbol{\theta}) = \mu \cdot c_{s,i}(\boldsymbol{\theta}) \cdot s + \sum_{j \in bkgs} c_{j,i}(\boldsymbol{\theta}) \cdot b_j. \quad (42)$$

These transfer functions connect the dedicated Control Region for a process j to the other Signal and Control Regions:

$$c_{\text{process j,region i}} = \frac{n_{j,i}^{MC}}{n_{j,j}^{MC}} \times \left(1 + \sum_k \Delta_{j,i;k} \theta_k\right). \quad (43)$$

[40] The property of the method to adjust the size of systematic uncertainties is called *profiling*.

Here, $\Delta_{j,i;k}$ corresponds to the impact of a given systematic θ_k on this Monte Carlo based extrapolation.

Therefore, a globally fitted normalization on the signal and background components is shared and extrapolated between Signal and Control Regions. The nuisance parameters can be (partially) shared between different samples and/or regions via the transfer functions.

Technically, this setup leads to the following set of fit parameters:

- Free Parameters: Unconstraint normalization factors for signal and background normalization denoted as mu_XXX, with mu_XXX=1 corresponding to the nominal value for process XXX.
- Nuisance Parameters: In addition to the free parameters, systematic uncertainties are incorporated via two types of nuisance parameters allowing for changing both the central value (leading to changes in normalization and shape) as well as the size of the systematic (changing the uncertainty estimate). alpha_XXX denotes Gaussian PDFs with alpha_XXX=0 being the nominal value for the systematic XXX. The according uncertainty Δalpha_XXX corresponds to the width of the Gaussian, with Δalpha_XXX=1 corresponding to the nominal 1σ uncertainty before the fit. Similarly, gamma_XXX denote Poissonian PDFs describing the statistical uncertainties due to a limited number of MC events.

The profile likelihood method will be implemented using the `HistFitter` package [309] which is based on the RooStats [310] extension `HistFactory` [311].

10.2. Fit Configuration

Three different fit configurations will be used in the following:

- Background-only fit: This fit configuration starts from the background-only hypothesis. Only the information provided by the Control Regions is used to constrain the fit parameters. This default fit configuration will be used for testing the method and obtaining the main results of the analysis.
- Exclusion fit: A specific supersymmetry signal is included as a component of the fit. Both Signal and Control Regions are used, fully including the predicted signal contribution in all regions and using the shape of the m_{eff} distribution in the Signal Region to further enhance the sensitivity with the binning defined in Table 16. This configuration will be used to test and exclude specific models.
- Discovery fit: Both Signal and Control Regions are used in the fit to constrain the background model. In the Signal Region, no shape information is used, and a possible signal contamination in the Control Region is neglected. An additional fit parameter corresponding to the number of Signal Events in the Signal Region is introduced. This fit configuration will be used to derive model-independent limits on the visible cross section.

In the Control Regions, the jet multiplicity distribution of jets with $p_T > 25$ GeV will be used, starting at two jets for the soft and dilepton analyses and at three jets for the hard one lepton analysis channel. The main fit parameters are the free normalization factors for the different parton multiplicity bins of the W, Z and $t\bar{t}$ backgrounds that can be fit with data to constrain scale uncertainties as discussed in chapter 8.4. The normalization factors are shared between the analysis channels and furthermore between the W- and Z-samples as they are based on similar physics and

channel	Signal Region	number of bins	bin ranges
dilepton	2 jet	5	m_{eff}=[700-1500+]GeV
dilepton	4 jet	5	m_{eff}=[600-1400+]GeV
hard one lepton	3 jet	5	m_{eff}=[600-1400+]GeV
hard one lepton	4 jet	5	m_{eff}=[800-1600+]GeV
soft one lepton	2 jet	6	$E_T^{\text{miss}}/m_{\text{eff}}$=[0.1-0.7+]

Table 16: Binning of the distribution of the discriminating variable in the Signal Regions of the different analysis channels. Equidistant bins are chosen, the last bin includes the overflow.

the same generator[41]. Similarly, the normalization factors on the $t\bar{t}$ parton multicplicity bins are shared between the semileptonic and the dileptonic decay mode as the jet radiation is independent of the $t\bar{t}$ decay mode. Due to the jet requirements in the W- and Z-Control Regions, the sensitivity to the normalization factors of the $W/Z + 0$ parton and the $W/Z + 1$ parton samples is low and as such the corresponding parameters will be fixed to one. The corresponding factorization and renormalization scale uncertainties will be included as an overall normalization uncertainty on the corresponding sample. Furthermore, the $t\bar{t}$ samples with 3–5 additional partons are jointly treated with a single free normalization factor to increase the fit stability.

In addition to the free normalization factors, systematic uncertainties are incorporated via nuisance parameters. The following types of systematic uncertainties will be used:

- OverallSys: This type corresponds to a systematic uncertainty that only changes the normalization of a certain variable and process while leaving the shape unchanged. Technically this corresponds to a Gaussian constrain of mean $(1 \pm \alpha)$ and width $\sigma \cdot E$ with E being the input uncertainty
- HistoSys: This type corresponds to a systematic uncertainty changing both the normalization and the shape of a given variable and process coherently. Three histograms representing the nominal distribution as well as the $\pm 1\sigma$ variations are used as input distributions and linearly interpolated in the process of profiling the related uncertainty $\alpha \pm \sigma \cdot E_i$ with E_i being the uncertainty in bin i.
- normHistoSys: This configuration is identical to the HistoSys type, but the overall normalization is kept constant.
- MCStatError: Uncertainties due to limited Monte Carlo statistics are modelled by Poisson distributions in each bin. For performance reasons, the uncertainty is neglected in a given bin if it is smaller than 5%.

While the origin of the systematic uncertainties has been described in chapter 9, Table 17 contains the corresponding type characterization used for the fit.

The jet energy scale uncertainty is separated into three nuisance parameters for jets with low ($p_T < 40$ GeV), medium ($40 < p_T < 100$ GeV) and high ($p_T > 100$ GeV) transverse momentum and split between signal and background samples as several components contribute differently to the combined jet energy scale uncertainty for soft and hard jets (see chapter 9) and a treatment with a single parameter could lead to potential over-profiling. For similar reasons, the lepton-

[41] Possible differences involve effects due to the different masses. The W- and Z samples with one (two) additional heavy quarks and N partons in the matrix element are combined with the corresponding N+1 (N+2) light flavor sample.

Uncertainty	Parameter	Type	Correlations
Luminosity	Lumi	OverallSys	all regions & samples
Jet Energy Scale	alpha_JLow alpha_JMedium alpha_JHigh	HistoSys	all regions & samples
	alpha_JSignal		all regions, signal only
b-tagging efficiency	alpha_BT	OverallSys	all regions with b-tagging/veto, all samples
Trigger efficiency	alpha_TE	OverallSys	one parameter per region, all samples
Lepton identification efficiency	alpha_LE	OverallSys	one parameter per region, all samples
Lepton energy scale	alpha_LES	OverallSys	one parameter per region, all samples
Muon energy resolution (ID)	alpha_LRI	OverallSys	one parameter per region with muons, all samples
Muon energy resolution (MS)	alpha_LRM	OverallSys	one parameter per region with muons, all samples
E_T^{miss} cell-out uncertainty	alpha_MC	HistoSys	all regions & samples
E_T^{miss} pileup uncertainty	alpha_MP	HistoSys	all regions & samples
Zp_T fit uncertainty	alpha_Zpt	OverallSys	all regions & samples, four Zpt bins
Renormalization and factorization scale	alpha_err_WZ	OverallSys	all regions, $W/Z + 0, 1$ parton samples
MLM matching scale	alpha_PtMin	NormHistoSys	all regions, one joint parameter for $t\bar{t}$ and W/Z samples
Hadronization	alpha_had	OverallSys	all signal regions, one joint parameter for $t\bar{t}$ and W/Z samples
Heavy Flavour	alpha_HF	HistoSys	all regions, W/Z samples
QCD normalization	alpha_QCDNorm	HistoSys	one parameter per region, QCD only
Other Backgrounds	alpha_err_BG	OverallSys	all regions, single top and diboson samples
Monte Carlo statistics	gamma_stat	MCStatError	one parameter per region and histogram bin

Table 17: Nuisance parameters describing the systematic uncertainties in the Combined Fit.

related uncertainties are treated as uncorrelated between the Control and Signal Regions. The QCD nuisance parameters correspond to the uncertainties predicted by the matrix method and are also treated as uncorrelated between the regions. While the dominant renormalization and factorization scale uncertainties on $t\bar{t}$ and W/Z are implictly determined by the fit approach, the remaining MLM matching and hadronization uncertainties as well as the uncertainty describing the additional W/Z+heavy flavor cross sections are included separately.

10.3. Fit Setup Validation

Before applying the profile likelihood fit to the observed data, it is important to validate the fit configuration with a closure test using toy data generated from the input distributions. Thereby it is possible to check the self-consistency of the method by investigating the fit stability as well as the resulting fit parameters.

For this purpose, toy data sets have been generated and fitted with the background-only fit configuration layed out above. Consequently the resulting fit parameters should follow a Gaussian distribution around their nominal value of one. Furthermore, the error estimate should correspond to the width of the distribution.

Figure 71 contains the resulting distribution for the normalization factors of the $t\bar{t}$ and W/Z parton multiplicity bins. The distributions have been transformed such that the nominal value corresponds to zero and the nominal width of the distribution to one. Overall, the fit is stable with a failure rate of less than 1‰ and the spread of the parameters follow Gaussian distributions, while some bias on the parameters is observed: It can be seen that the width of the Gaussian distributions is larger than one, corresponding to an underestimation of the related uncertainty, presumably due to the complexity of the combined fit setup[42].

After having discussed the fit configuration, the results from the application to data and further validation with respect to the extrapolation to the Signal Regions will be discussed in the following chapter 11.

[42] For simple fit configurations without so many systematic uncertainties, this problem is not present.

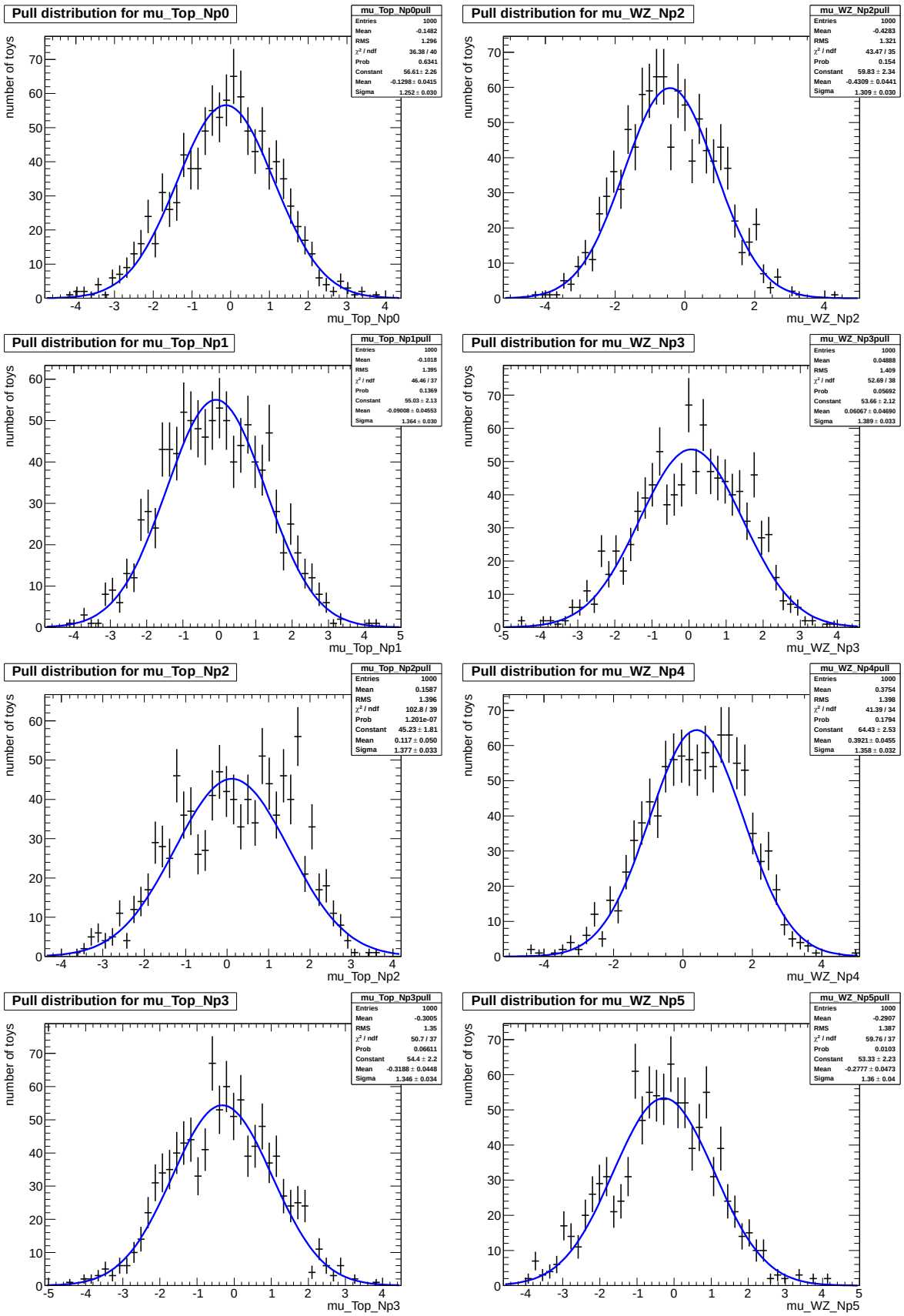

Figure 71: Pull distributions for the $t\bar{t}$ and W/Z normalization factors obtained from toy datasets.

11. Results

In the following, the results from the application of the profile likelihood method described in the previous chapter will be presented. The results will be discussed with emphasis on the dilepton Control and Signal Regions, results with respect to the single lepton regions are contained in appendix F.

11.1. Background-only Fit

In the background-only fit configuration, the fit is performed in the Control Regions only without assuming the presence of a possible signal. All single- and dilepton Control Regions are used to constrain the fit parameters. The resulting fit parameters are listed in Table 18.

The free normalization parameters for the different parton multiplicity bins of the W/Z and $t\bar{t}$ samples have been constraint with uncertainties of 6-13% and are in general in good agreement with their nominal values of one. Several of the systematic uncertainties such as the jet energy scale for soft, medium and high p_T jets have been constraint significantly as these change the corresponding jet multiplicity distributions and to which the fit is thus sensitive[43]. In constrast, the lepton-related uncertainties (energy scale and resolution as well as trigger and reconstruction efficiencies) are mostly kept unchanged, as they have nearly no impact on the Control Regions. Figure 72 shows scans of the likelihood projected on the free normalization parameters. It can be seen that the curves are well-behaved parabolas.

Table 19 shows the resulting event numbers for the dilepton Control Regions after the fit in comparison to the pure Monte Carlo estimate separated by final state. Good agreement between the fitted and the measured number of events is observed in all regions, with the largest discrepancy being 1.1σ in the dimuon $t\bar{t}$ Control Region.

In addition to the individual fit parameter results, it is also important to study the correlation between the parameters. Figure 73 shows the correlation matrix for the most relevant parameters, the full matrix is contained in appendix D. It can be seen that the fit is able to disentangle the parameters, leading to an improved description of the profiled systematic uncertainties. For simpler fit configurations, a chessboard-like correlation matrix with large anti-correlations between neighboring and large correlations between next-to-neighboring parton multiplicity bins has been observed [285], caused by large mutual contributions of these samples in the jet multiplicity distribution. This pattern is only partially realized in this fit configuration, as the different dilepton and single-lepton Control Regions together with the sizeable set of systematic uncertainties are combined.

To compare the impact on the jet multiplicity, the corresponding distributions before and after applying the fit are shown in Figure 74 for the $t\bar{t}$ and in Figure 75 for the Z Control Regions. A clear improvement of the agreement between data and Monte Carlo simulation can be observed, especially in the two-jet bin of the dielectron channels. Additionally, the size of the total uncertainty on the background estimate is reduced as expected. In the highest jet multiplicity bins, the simulation somewhat underestimates the data[44]. The expected impact on the analysis is nevertheless low, as only at least two or four jets are required for the Signal Regions.

[43] The sensitivity to JHigh is large due to the requirements on the leading jet as well as on the effective mass in the one-lepton channels.

[44] As single and dilepton Control Regions are fitted at the same time, such discrepancies can remain after applying the fit, depending on their impact on the fit parameters.

Floating Parameter	Fit Result
mu_Top_Np0	1.27 ± 0.10
mu_Top_Np1	0.99 ± 0.06
mu_Top_Np2	1.07 ± 0.09
mu_Top_Np3	0.92 ± 0.08
mu_WZ_Np2	1.14 ± 0.08
mu_WZ_Np3	1.07 ± 0.06
mu_WZ_Np4	1.02 ± 0.06
mu_WZ_Np5	1.24 ± 0.13
alpha_BT	0.82 ± 0.28
alpha_HF	0.12 ± 0.46
alpha_JHigh	-0.90 ± 0.27
alpha_JLow	-0.29 ± 0.29
alpha_JMedium	-0.56 ± 0.36
alpha_LESee	0.14 ± 0.20
alpha_LESem	0.01 ± 0.96
alpha_LESmm	-0.01 ± 0.98
alpha_LEee	1.25 ± 0.62
alpha_LEem	-0.06 ± 0.84
alpha_LEmm	0.02 ± 0.86
alpha_LRIem	-0.01 ± 0.95
alpha_LRImm	-0.01 ± 0.86
alpha_LRMem	-0.03 ± 0.95
alpha_LRMmm	0.04 ± 0.92
alpha_MC	-0.86 ± 0.47
alpha_MP	0.28 ± 0.48
alpha_PtMinTop	0.01 ± 0.18
alpha_PtMinWZ	1.14 ± 0.68
alpha_QCDNorm_TRee	0.53 ± 0.75
alpha_QCDNorm_TRem	0.05 ± 1.11
alpha_QCDNorm_TRmm	0.11 ± 1.25
alpha_QCDNorm_ZRee	0.01 ± 0.96
alpha_QCDNorm_ZRmm	0.03 ± 1.02
alpha_TEee	0.36 ± 0.92
alpha_TEel	-0.27 ± 0.94
alpha_TEem	-0.15 ± 0.65
alpha_TEmm	0.46 ± 0.54
alpha_TEmu	0.43 ± 0.48
alpha_Zpt50GeV	0.12 ± 0.70
alpha_Zpt100GeV	0.21 ± 0.61
alpha_Zpt150GeV	0.08 ± 0.74
alpha_Zpt200GeV	-0.27 ± 0.72
alpha_err_BG	-0.05 ± 0.97
alpha_err_WZ_Np0	0.01 ± 0.96
alpha_err_WZ_Np1	0.29 ± 0.18

Table 18: Fit parameter results obtained with the background-only fit configuration. Only the parameters connected to the dilepton Control Regions are shown, the full list of parameters is contained in appendix D.

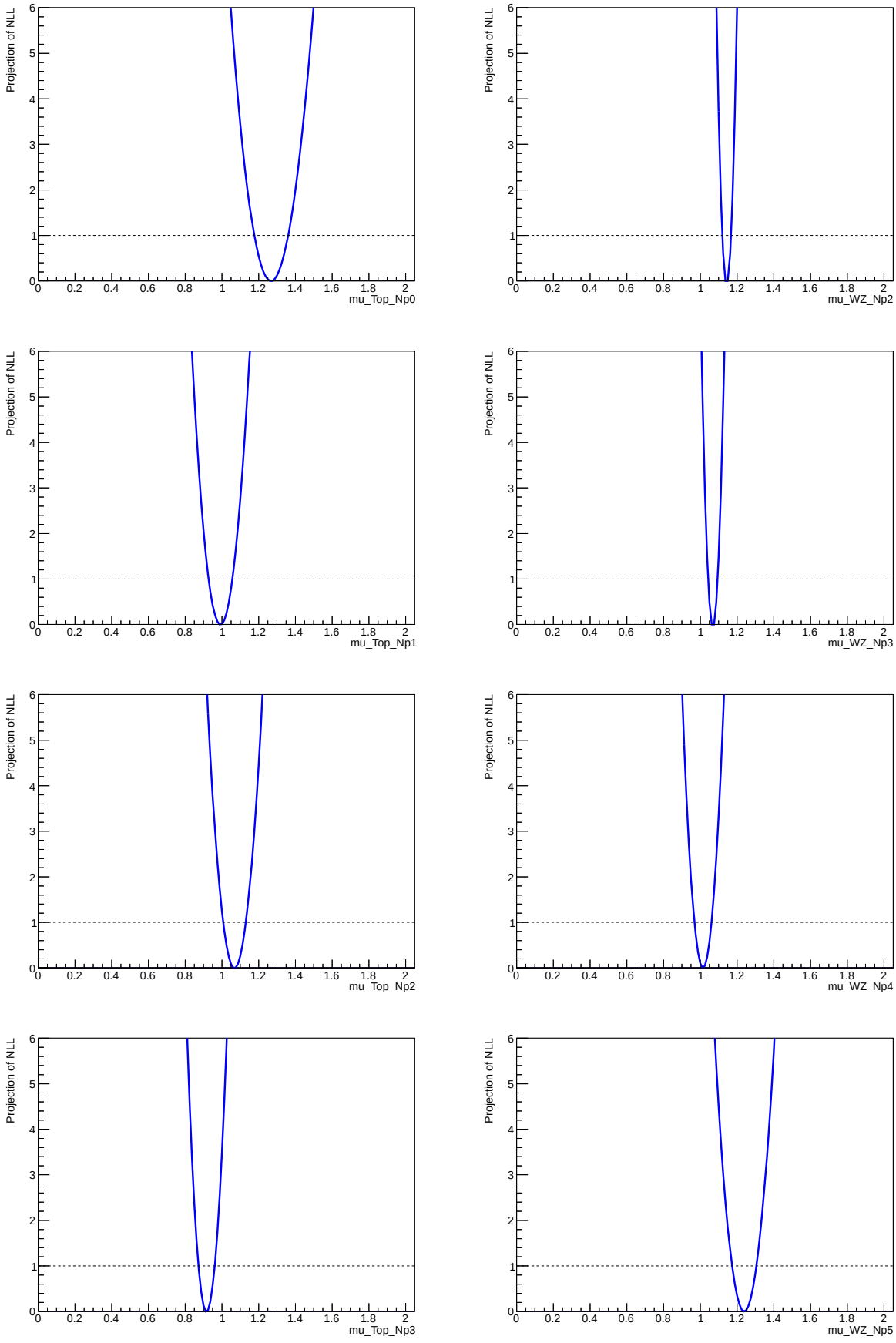

Figure 72: Projections of the likelihood on the free normalization parameters.

Control Region	Z		$t\bar{t}$		
Number of events	ee	$\mu\mu$	ee	$\mu\mu$	$e\mu$
Observed	8090	10915	574	740	1165
Fitted bkg	8065.1 ± 91.8	10937.5 ± 102.5	559.3 ± 16.1	706.9 ± 15.6	1168.0 ± 29.4
Fitted top	67.8 ± 1.9	82.2 ± 2.2	495.8 ± 13.2	648.3 ± 15.9	1129.5 ± 31.2
Fitted W/Z+jets	7924.2 ± 104.2	10763.6 ± 102.8	36.5 ± 0.9	40.5 ± 1.0	3.2 ± 0.3
Fitted other bkg	69.8 ± 14.0	91.2 ± 18.3	11.8 ± 2.3	16.6 ± 3.3	26.4 ± 5.3
Fitted multijet	3.2 ± 37.4	0.5 ± 4.0	15.1 ± 14.9	1.6 ± 2.7	8.9 ± 13.7
MC exp. SM	7393.4	10273.0	510.1	678.6	1141.5
MC exp. top	65.1	80.9	461.3	619.4	1101.5
MC exp. W/Z+jets	7253.2	10093.8	34.1	40.9	3.4
MC exp. other bkg	73.0	98.0	11.5	17.0	28.5
Data-driven multijet	2.2	0.3	3.2	1.2	8.1

Table 19: The observed numbers of events in the Z and $t\bar{t}$ Control Regions and the background expectations from the fit. The inputs to the fit are also shown; these consist of the data-driven multijet background estimate and the nominal expectations from simulation (MC), normalized to theoretical cross sections. The errors shown are the statistical plus systematic uncertainties.

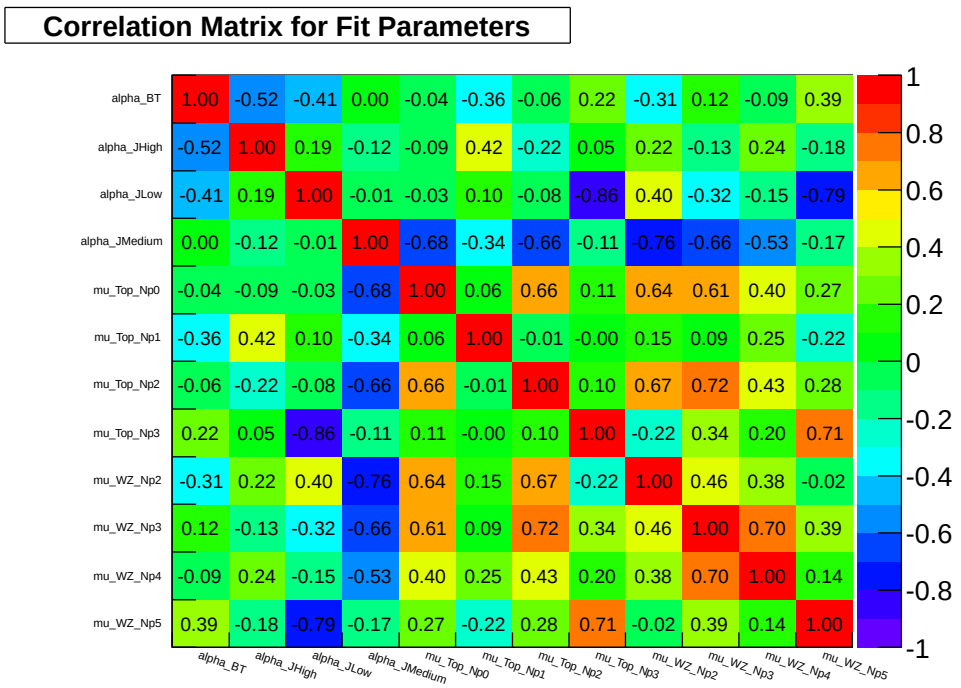

Figure 73: Correlation matrix for a subset of the fitparameters in the background-only fit.

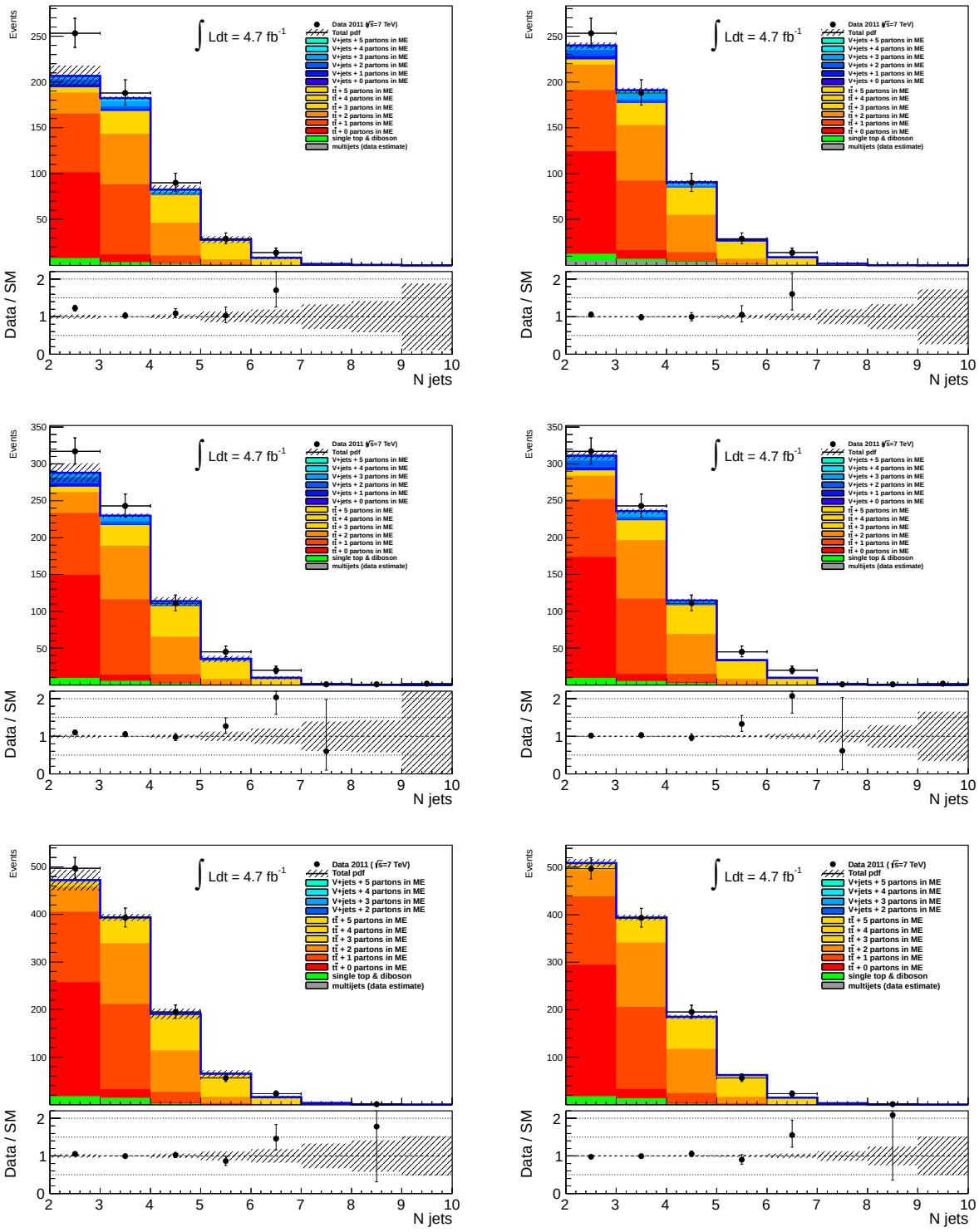

Figure 74: Distribution of the number of jets in the top Control Region (TRL2) in the dielectron (top), dimuon (middle) and electron-muon final state (bottom) before (left) and after (right) applying the background-only fit.

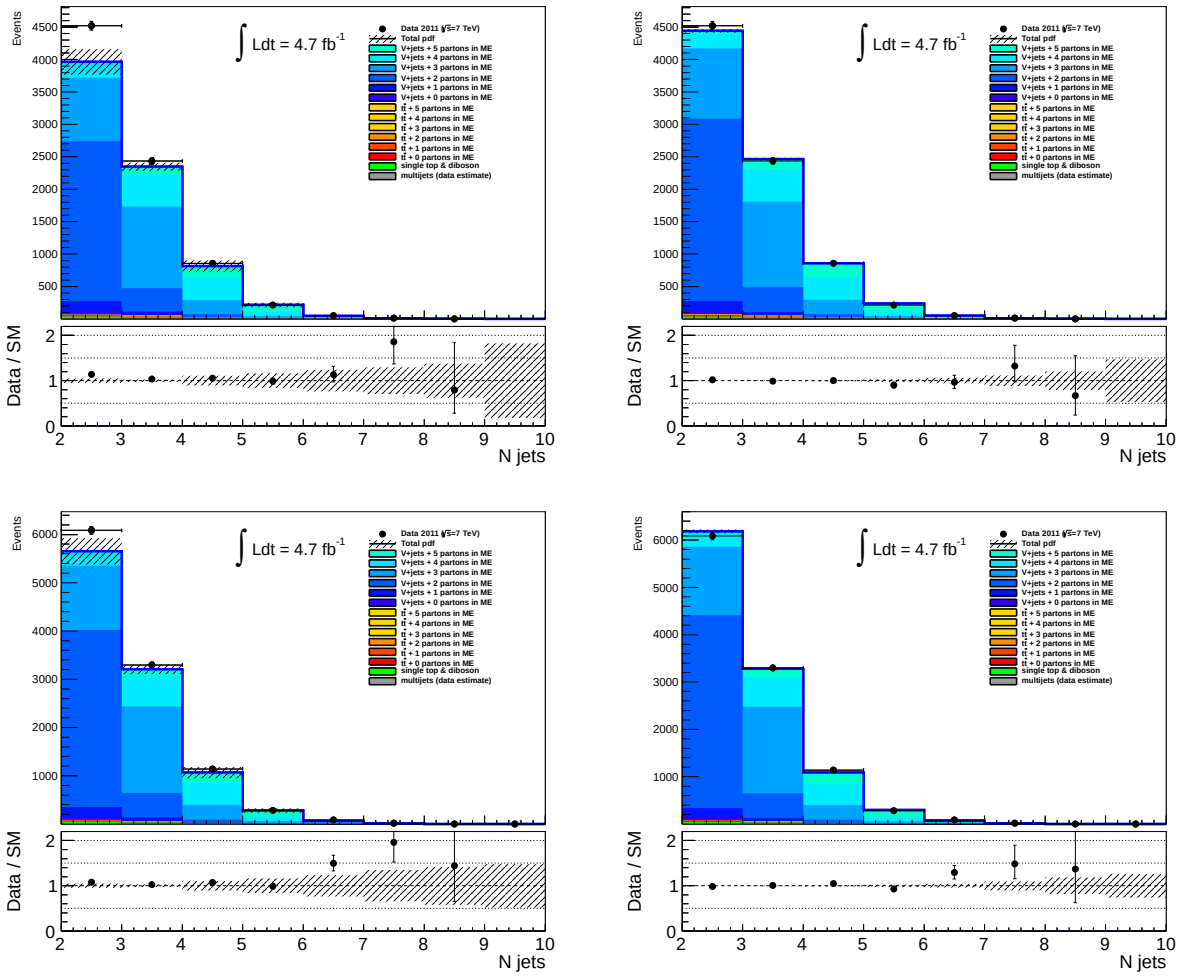

Figure 75: Distribution of the number of jets in the Z Control Region (ZRL2) in the dielectron (top) and dimuon final state (bottom) before (left) and after (right) applying the background-only fit.

11.2. Fit Results Validation

Before discussing the results in the Signal Regions, it is necessary to validate the extrapolation from the Control to the Signal Region phase spaces. For this purpose, additional Validation Regions are defined as shown in tables 20 and 21[45]. These phase space regions are not used to constrain the fit parameters. Instead, the extrapolation of the fit results from Control to Signal Regions is validated by applying the fit parameters obtained from the Control Regions in these Validation Regions. For the dilepton analysis, 2-jet and 4-jet Validation Regions are defined for both $t\bar{t}$ and Z production. The jet requirements correspond to the dilepton Signal Regions and the E_T^{miss} requirements are chosen such that the Validation Regions cover part of the phase space between the Signal and Control Regions. Thus the validity of the extrapolation from Control to Signal Regions can be tested[46].

	dilepton 2-jet		**dilepton 4-jet**	
	Z **VR**	$t\bar{t}$ **VR**	Z **VR**	$t\bar{t}$ **VR**
N_{jet}	≥ 2	≥ 2	≥ 4	≥ 4
$p_{\text{T}}^{\text{jet}}$ (GeV)	$>$ 120, 120	$>$ 120, 120	$>$ 80,50,50,50	$>$ 80,50,50,50
N_{jet} (b-tagged)	—	≥ 1	—	≥ 1
E_T^{miss} (GeV)	[50,100]	[100,300]	[50,100]	[80,100]
$m_{\ell\ell}$ (GeV)	[81,101]	$<$ 81 or $>$ 101	[81,101]	$<$ 81 or $>$ 101

Table 20: Overview of the selection criteria for the background Validation Regions. Only the criteria that are different from the signal selection criteria listed in Table 12 are shown. For the 2-jet Validation Regions, the fourth leading jet (if present) is required to have $p_T < 50$ GeV.

	hard-lepton			**soft-lepton**
	W **VR**	$t\bar{t}$ **VR**	**High-**m_{T} **VR**	
N_{jet}	≥ 3	≥ 3	≥ 3	≥ 2
$p_{\text{T}}^{\text{jet}}$ (GeV)	$>$ 80, 25, 25	$>$ 80, 25, 25	$>$ 80, 25, 25	$>$ 130,25
N_{jet} (b-tagged)	0	≥ 1	—	
E_T^{miss} (GeV)	[150,250]	[150,250]	[40,250]	[180,250]
m_{T} (GeV)	[40,80]	[40,80]	$>$ 100	[80,100]
$m_{\text{eff}}^{\text{inc}}$ (GeV)	$>$ 500	$>$ 500	$>$ 500	–

Table 21: Overview of the selection criteria for the background Validation Regions (VR) for the single-lepton channels. Only the criteria that are different from the signal selection criteria listed in Table 12 are shown.

Tables 22 and 23 contain the corresponding results before and after applying the fit. Similarly, the distributions of the jet multiplicity and of the effective mass are shown in figures 76-79. A good agreement is observed within the large statistical uncertainties[47].

[45] The Validation Regions for the one lepton channels are given here as well to allow for a full overview over the impact of the fit on the combined analysis as shown in Figure 80.

[46] assuming small signal contamination in these Validation Regions.

[47] In some of the regions, the agreement is slightly worse than before applying the fit results. This is caused by the impact of the statistically dominant hard one lepton top Control Regions on the fit which pull the predicted $t\bar{t}$ background towards lower values.

2-jet Validation Region	Z		$t\bar{t}$		
Number of events	ee	$\mu\mu$	ee	$\mu\mu$	$e\mu$
Observed	150	181	64	83	117
Fitted bkg	134.4 ± 7.3	173.3 ± 8.7	53.4 ± 3.7	74.7 ± 4.8	110.9 ± 7.8
Fitted top	7.7 ± 1.3	10.5 ± 1.3	39.8 ± 2.9	54.5 ± 4.1	100.4 ± 7.2
Fitted W/Z+jets	125.6 ± 6.2	161.6 ± 8.3	11.5 ± 0.8	17.8 ± 1.0	5.3 ± 0.4
Fitted other bkg	1.1 ± 0.3	1.2 ± 0.3	2.1 ± 0.4	2.5 ± 0.5	5.3 ± 1.1
Fitted multijet	< 0.05	< 0.05	< 0.05	< 0.05	< 0.05
MC exp. SM	137.3	176.5	61.3	85.5	134.5
MC exp. top	12.3	16.1	47.1	65.5	122.8
MC exp. W/Z+jets	123.8	158.9	12.0	17.2	5.6
MC exp. other bkg	1.3	1.5	2.2	2.8	6.1
Data-driven multijet	< 0.05	< 0.05	< 0.05	< 0.05	< 0.05

Table 22: The observed numbers of events in the dijet Validation Regions and the background expectations from the fit. The inputs to the fit are also shown; these consist of the data-driven multijet background estimate and the nominal expectations from simulation (MC), normalized to theoretical cross sections. The errors shown are the statistical plus systematic uncertainties.

4-jet Validation Region	Z		$t\bar{t}$		
Number of events	ee	$\mu\mu$	ee	$\mu\mu$	$e\mu$
Observed	40	34	8	12	22
Fitted bkg	33.1 ± 1.9	36.8 ± 2.2	9.4 ± 1.2	11.0 ± 1.0	20.0 ± 1.5
Fitted top	8.6 ± 0.7	12.5 ± 0.9	8.6 ± 0.9	10.2 ± 1.0	19.7 ± 1.5
Fitted W/Z+jets	24.0 ± 1.4	24.1 ± 1.6	0.3 ± 0.1	0.4 ± 0.1	< 0.05
Fitted other bkg	0.2 ± 0.1	0.2 ± 0.1	0.3 ± 0.1	0.3 ± 0.1	0.3 ± 0.1
Fitted multijet	0.2 ± 0.6	< 0.05	0.2 ± 0.6	< 0.05	< 0.05
MC exp. SM	34.5	39.7	10.3	12.7	23.0
MC exp. top	11.4	15.9	9.6	12.0	22.7
MC exp. W/Z+jets	22.6	23.5	0.3	0.3	< 0.05
MC exp. other bkg	0.4	0.3	0.2	0.4	0.3
Data-driven multijet	0.2	< 0.05	0.2	< 0.05	< 0.05

Table 23: The observed numbers of events in the 4-jet Validation Regions and the background expectations from the fit. The inputs to the fit are also shown; these consist of the data-driven multijet background estimate and the nominal expectations from simulation (MC), normalized to theoretical cross sections. The errors shown are the statistical plus systematic uncertainties.

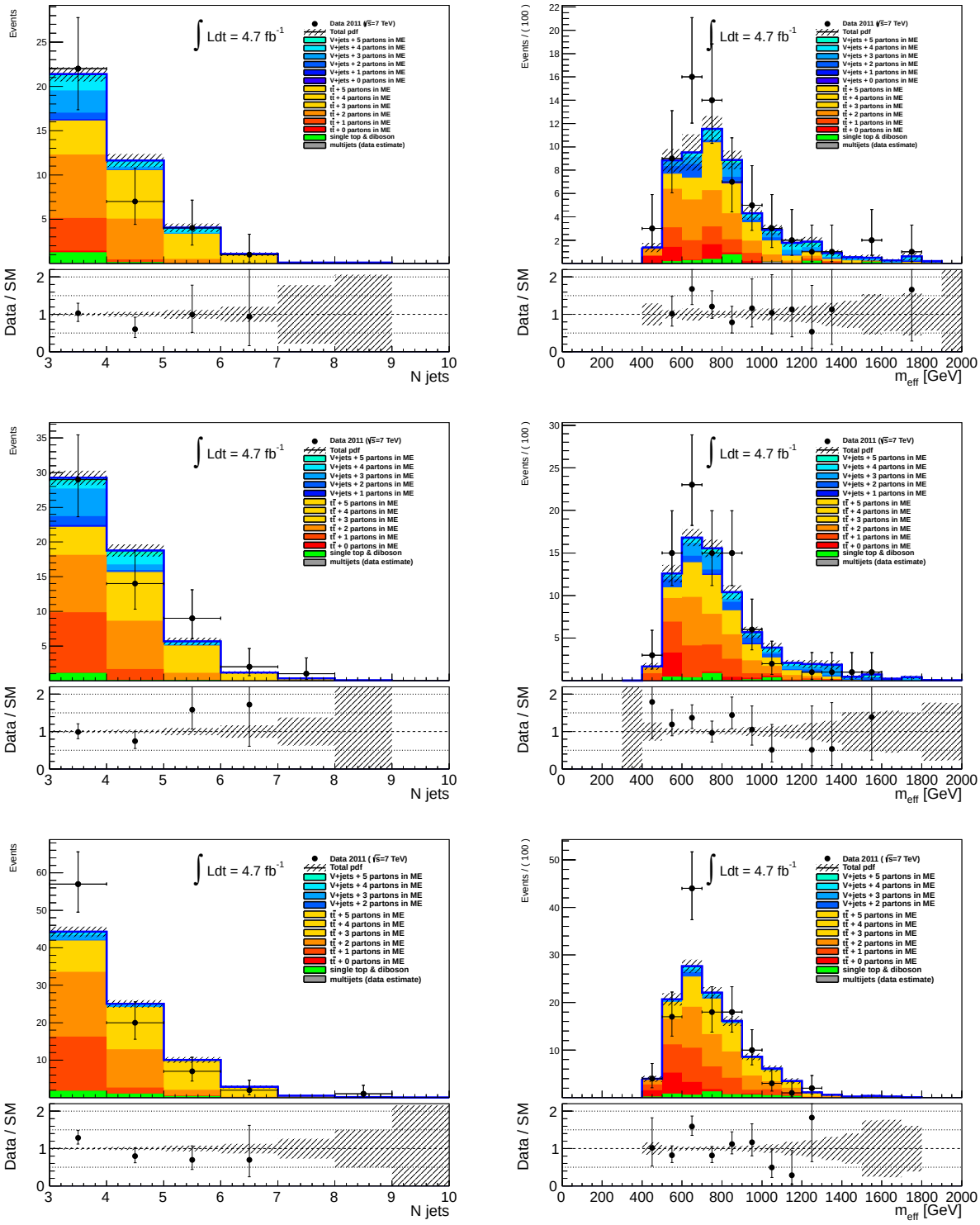

Figure 76: Distribution of the number of jets (left) and of the effective mass (right) in the dileptonic top Validation Region with two jets in the dielectron (top), dimuon (middle) and electron-muon final state (bottom) after applying the background-only fit.

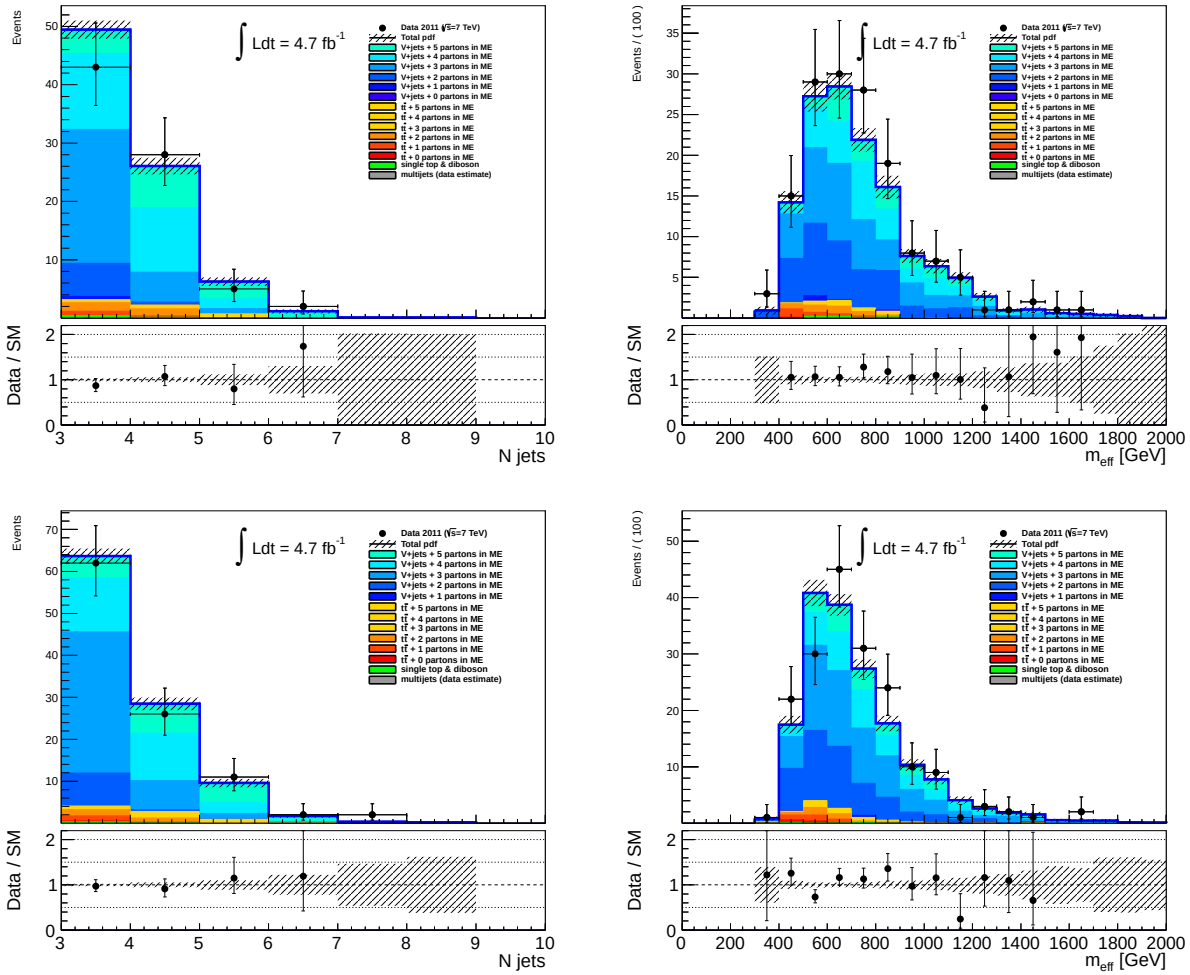

Figure 77: Distribution of the number of jets (left) and of the effective mass (right) in the Z Validation Region with two jets in the dielectron (top) and dimuon final state (bottom) after applying the background-only fit.

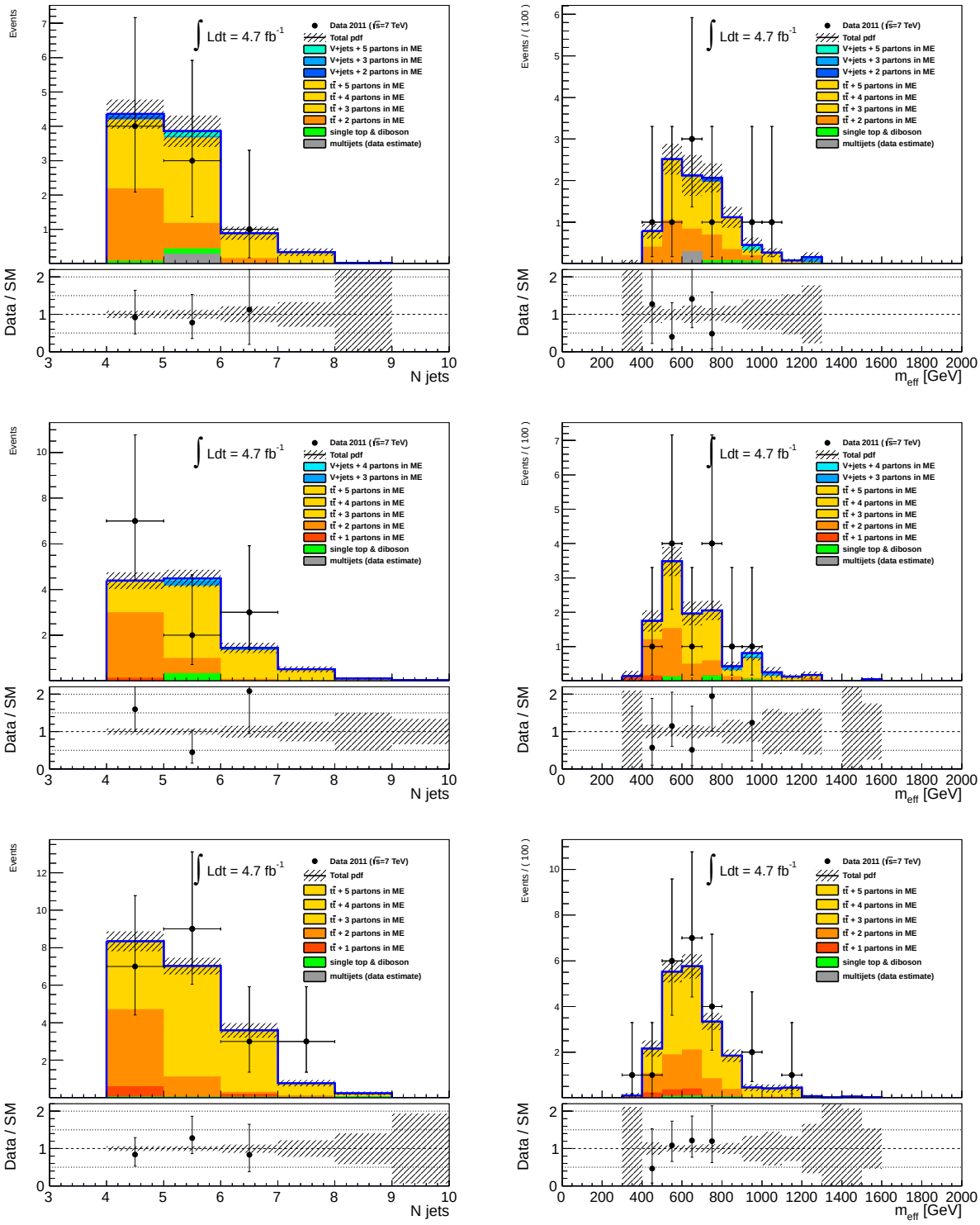

Figure 78: Distribution of the number of jets (left) and of the effective mass (right) in the dileptonic top Validation Region with four jets in the dielectron (top), dimuon (middle) and electron-muon final state (bottom) after applying the background-only fit.

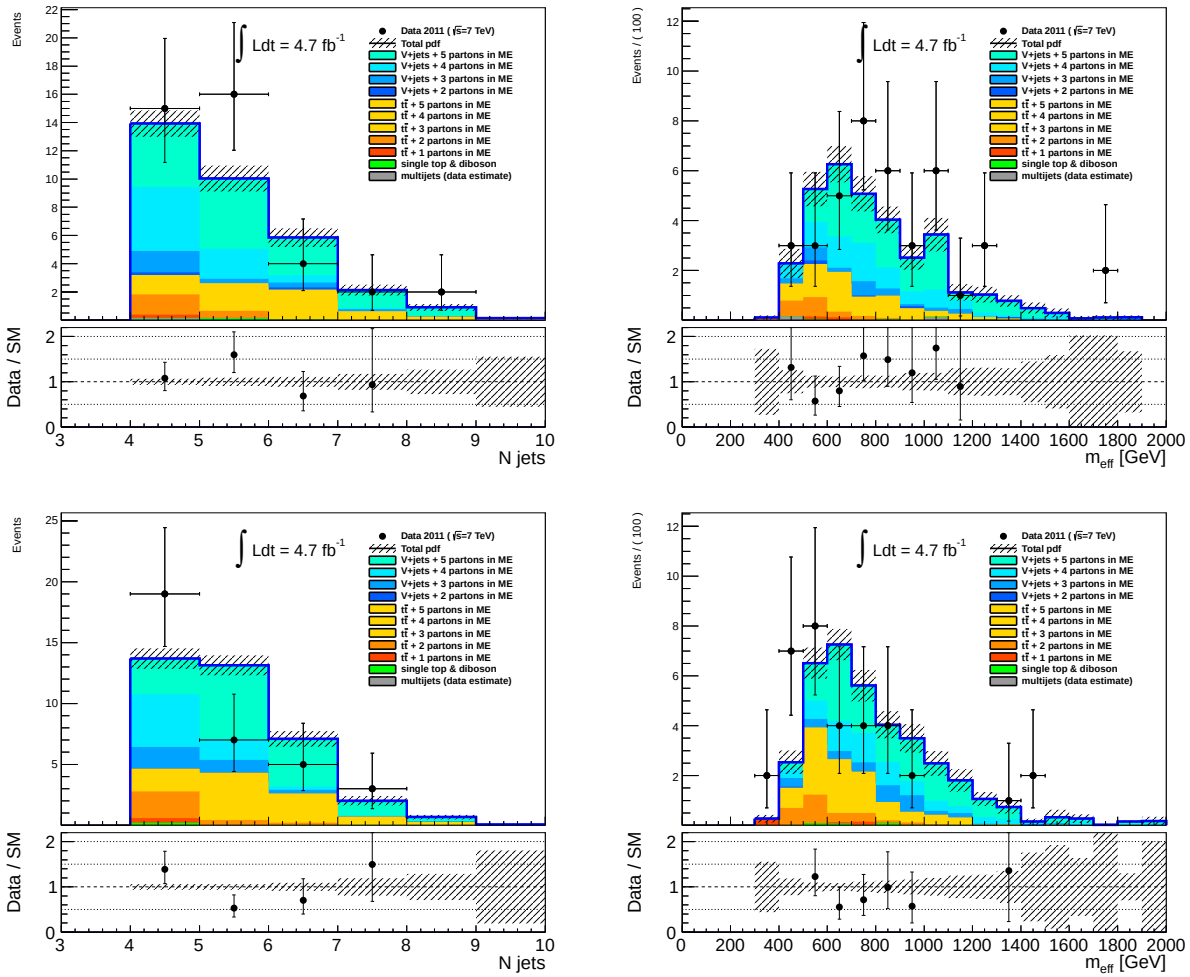

Figure 79: Distribution of the number of jets (left) and of the effective mass (right) in the Z Validation Region with four jets in the dielectron (top) and dimuon final state (bottom) after applying the background-only fit.

To further check the validity of the fit results, pull distributions for the Control and Validation Regions are shown in Figure 80. It can be seen that for the dielectron and dimuon $t\bar{t}$ Control Regions, the observed number of events is larger than the predicted number of events. This discrepancy is still present after the fit as the $t\bar{t}$ normalization factors are shared between the single- and dilepton analyses, and as such the opposite discrepancy in the hard one electron $t\bar{t}$ Control Region compensates the dileptonic regions. The overall pull distribution for the Control Regions shows that the observed discrepancies are consistent with statistical fluctuations. Furthermore, no significant trends are observed in the Validation Regions[48].

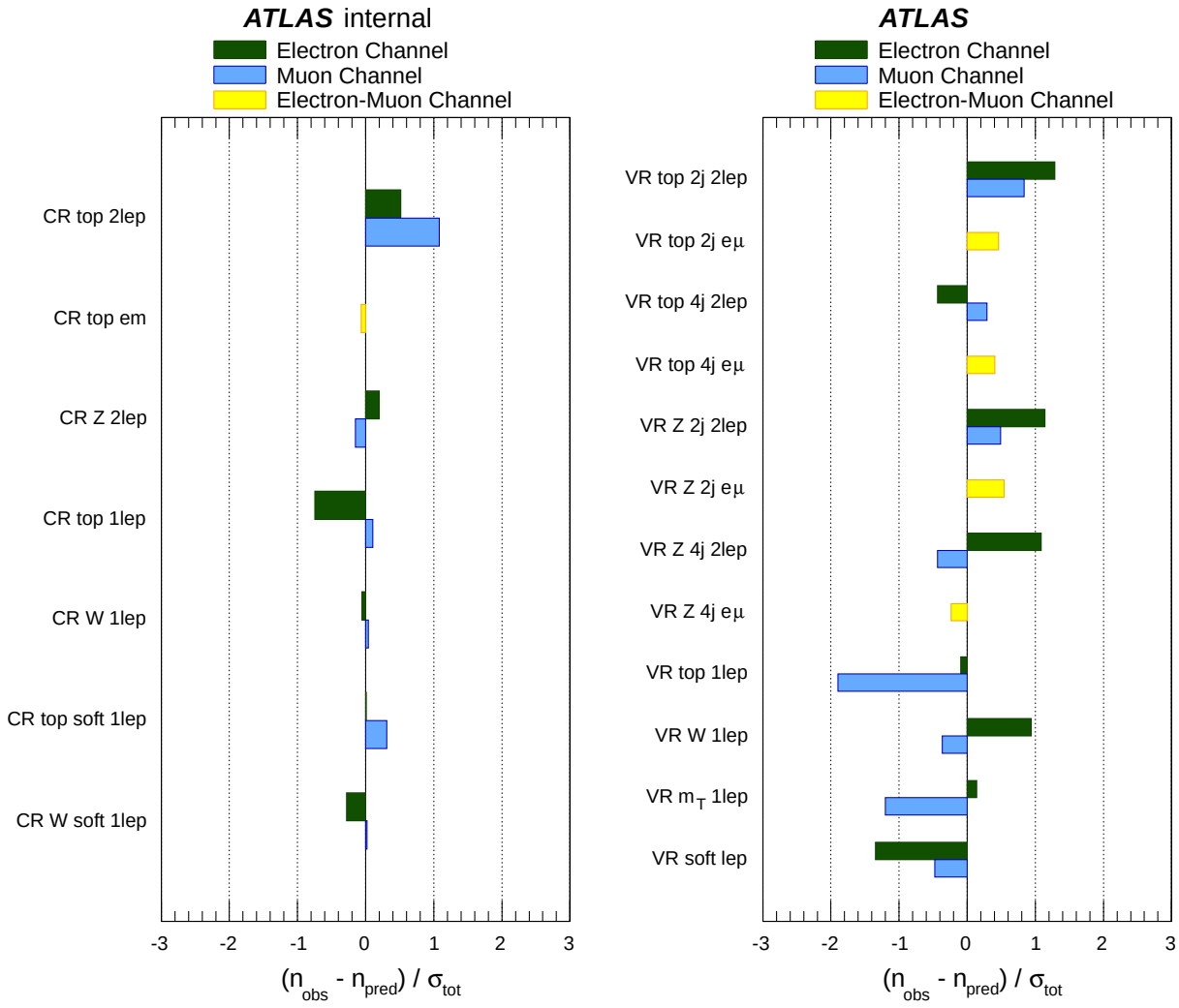

Figure 80: Summary of the fit results in the Control Regions (left) and Validation Regions (right). The difference between the observed and predicted number of events, divided by the total (statistical and systematic) uncertainty on the prediction, is shown for each Control and Validation Region.

[48] Some tension between the dilepton and the one lepton channels can be observed, caused by the differing results with respect to the $t\bar{t}$ normalization.

11.3. Signal Region Results

After having scrutinized the results of the combined fit with respect to the Control and Validation Regions, the results of the analyses in the Signal Regions can be investigated. For this purpose, the results from the background-only fit are applied to the events in the Signal Regions. Table 24 contains the predicted and observed event yields in the dilepton Signal Regions for the different final states as the main result of this analysis.

Signal Region		2-jets			4-jets	
Number of events	ee	$\mu\mu$	$e\mu$	ee	$\mu\mu$	$e\mu$
Observed	0	0	1	8	12	18
Fitted bkg	0.31 ± 0.17	0.42 ± 0.16	0.65 ± 0.21	9.1 ± 1.5	11.7 ± 1.7	21 ± 3
Fitted top	0.11 ± 0.06	0.24 ± 0.09	0.58 ± 0.19	9.1 ± 1.4	11.1 ± 1.7	20 ± 3
Fitted W/Z+jets	0.11 ± 0.06	0.11 ± 0.04	0.01 ± 0.02	0.04 ± 0.04	0.23 ± 0.07	0.41 ± 0.05
Fitted other bkg	0.09 ± 0.05	0.07 ± 0.03	0.06 ± 0.02	0.01 ± 0.03	0.36 ± 0.12	0.61 ± 0.12
Fitted multijet	< 0.01	< 0.01	< 0.01	0.04 ± 0.22	< 0.01	< 0.01
MC exp. SM	0.34	0.48	0.89	11.4	14.7	27.1
MC exp. top	0.16	0.31	0.73	11.1	13.9	26.0
MC exp. W/Z+jets	0.10	0.10	0.10	0.08	0.28	0.38
MC exp. other bkg	0.09	0.07	0.06	0.17	0.49	0.67
Data-driven multijet	< 0.01	< 0.01	< 0.01	0.04	< 0.01	< 0.01

Table 24: The observed numbers of events in the dilepton Signal Regions, and the background expectations from the fit. The inputs to the fit are also shown; these consist of the data-driven multijet background estimate and the nominal expectations from simulation (MC), normalized to theoretical cross sections. The errors shown are the statistical plus systematic uncertainties.

It can be seen that the observed data agree well with the predicted Standard Model backgrounds, such that there is no apparent sign for the presence of a possible supersymmetry signal. To further illustrate the Signal Regions, Figure 81 shows the effective mass distributions in all the Signal Regions. The systematic uncertainties on the background prediction in the Signal Regions will be discussed in the following chapter.

As for the Control and Validation Regions, it is interesting to study the resulting pull distributions for the Signal Regions shown in Figure 82. None of the Signal Regions show evidence for a possible supersymmetry signal. Correspondingly, these null results will be translated into exclusion limits on several supersymmetry models in chapter 12.

[49] The QCD prediction in the third bin of the 4-jet ee Signal Region of ≈ 0.06 events is partially compensated by a negative expectation of ≈ 0.02 QCD events in the second bin, leading to the total prediction of 0.04 events shown in Table 24.

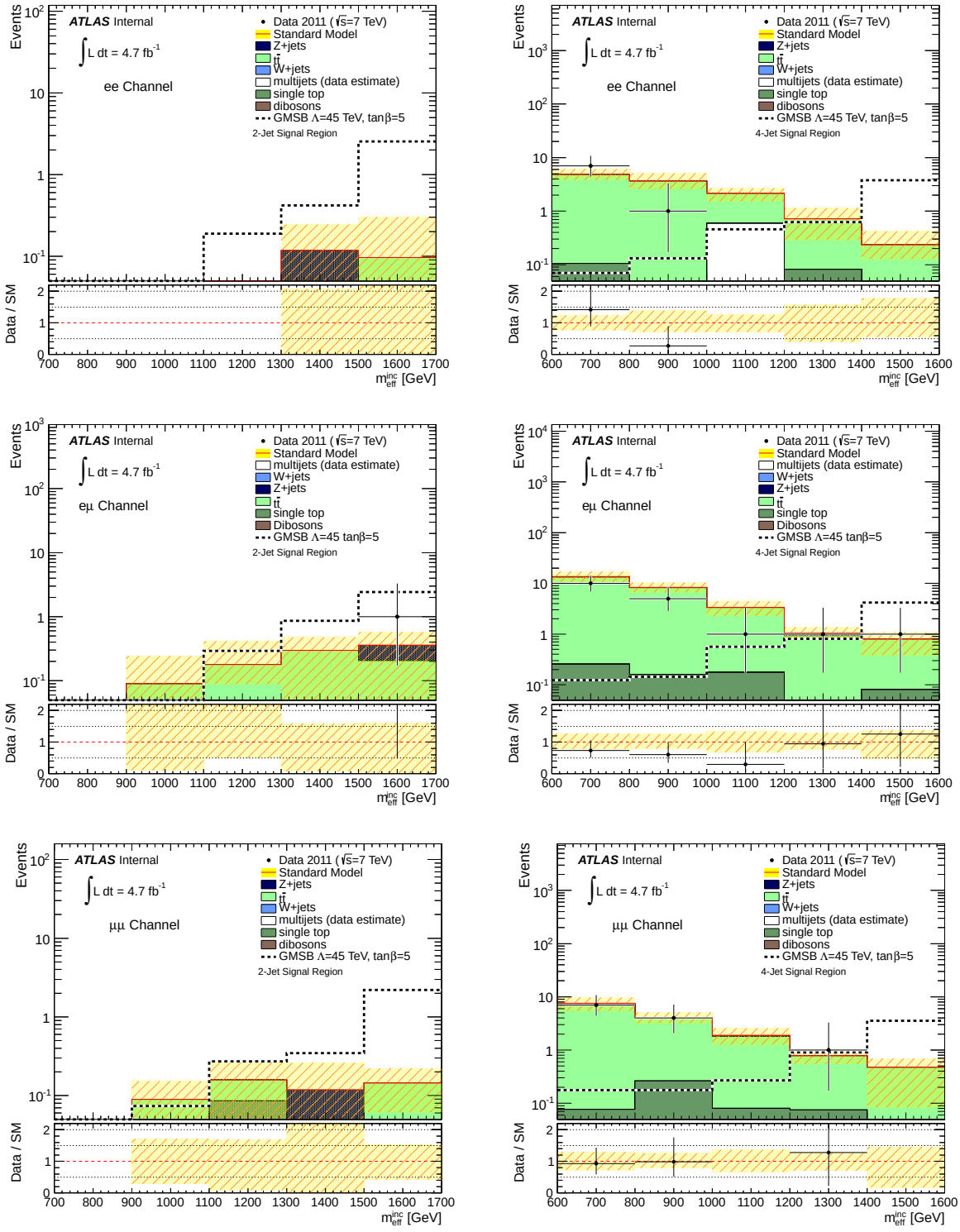

Figure 81: Distribution of $m_{\text{eff}}^{\text{inc}}$ after all selection requirements for the 2-jet (left) and the 4-jet Signal Region (right) in the ee (top), $e\mu$ (middle) and $\mu\mu$ (bottom) final state. The last bin includes all overflows. The Standard Model expectation shown here is the input to the final fit, and is derived from simulation only, normalized to the theoretical cross sections[49]. The uncertainty band around the Standard Model expectation combines the statistical and systematic uncertainties. An example of the distribution for a simulated signal is also shown (not stacked).

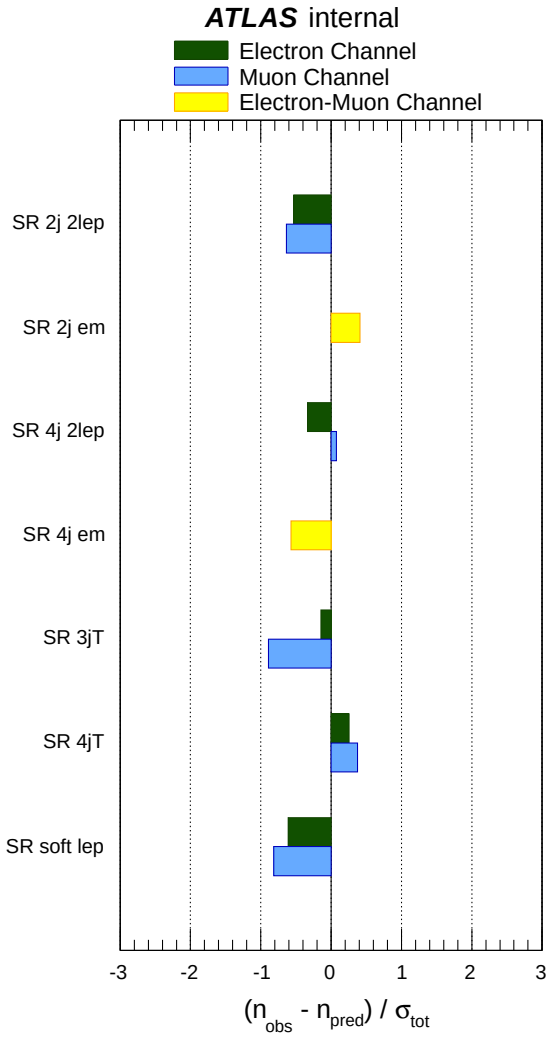

Figure 82: Summary of the fit results in both the single and the dilepton Signal Regions. The difference between the observed and predicted number of events, divided by the total (statistical and systematic) uncertainty on the prediction is shown for each region.

11.4. Impact of Systematic Uncertainties

Tables 25 and 26 contain the breakdown of the systematic uncertainties on the final result calculated by propagating the uncertainty due to a specific parameter into the corresponding phase space region. The given numbers are the absolute uncertainty on the total background prediction. Only parameters resulting in an uncertainty of at least 0.01 events in one of the Signal Regions are shown. It should also be noted that the shown uncertainties are partially correlated as discussed in chapter 11.1, such that they do not simply add up quadratically to the total background uncertainty.

In the 2-jet Signal Region, the uncertainties are fully dominated by the limited number of Monte Carlo events as a consequence of the very tight selection. In the 4-jet Signal Region, also the $t\bar{t}$ normalization, the uncertainty on the hadronization as well as jet energy scale uncertainties are of relevance.

The total systematic uncertainty in the 2-jet Signal Regions amounts to 30-50%, while in the 4-jet Signal Regions the uncertainties are approximately 15%.

Signal channel	S2ee	S2mm	S2em
Total statistical ($\sqrt{N_{\text{pred}}}$)	0.56	0.65	±0.81
Total background systematic	±0.17	±0.16	±0.22
alpha_JHigh	±0.02	±0.01	±0.06
alpha_JMedium	< 0.01	±0.01	< 0.01
alpha_LEem	< 0.01	< 0.01	±0.01
alpha_QCDNorm_S2em_meffInc	< 0.01	< 0.01	±0.01
alpha_TEem	< 0.01	< 0.01	±0.02
alpha_TEmm	< 0.01	±0.01	< 0.01
alpha_Zpt200GeV	±0.01	< 0.01	< 0.01
alpha_err_BG	±0.02	±0.01	±0.01
alpha_hadTop	±0.01	±0.03	±0.07
alpha_hadWZ	±0.01	±0.01	< 0.01
gamma_stat_S2ee_meffInc	±0.17	< 0.01	< 0.01
gamma_stat_S2em_meffInc	< 0.01	< 0.01	±0.19
gamma_stat_S2mm_meffInc	< 0.01	±0.15	< 0.01
mu_Top_Np1	< 0.01	< 0.01	±0.01
mu_Top_Np2	±0.01	±0.01	±0.02
mu_Top_Np3	< 0.01	±0.01	±0.02
mu_WZ_Np3	±0.01	< 0.01	< 0.01
mu_WZ_Np4	< 0.01	±0.01	< 0.01

Table 25: Breakdown of the absolute systematic uncertainties on background estimates in the various Signal Regions. Note that the individual uncertainties can be correlated, and do not necessarily add up quadratically to the total background uncertainty.

Signal channel	S4ee	S4mm	S4em
Total statistical ($\sqrt{N_{\text{pred}}}$)	±3.02	±3.42	±4.58
Total background systematic	±1.49	±1.75	±2.91
MET cell-out	±0.04	±0.04	< 0.01
MET pile-up	±0.10	±0.06	±0.02
alpha_JHigh	±0.39	±0.41	±0.73
alpha_JLow	±0.21	±0.16	±0.34
alpha_JMedium	±0.62	±0.76	±1.37
alpha_LESee	±0.01	< 0.01	< 0.01
alpha_LESem	< 0.01	< 0.01	±0.16
alpha_LEee	±0.25	< 0.01	< 0.01
alpha_LEem	< 0.01	< 0.01	±0.35
alpha_LEmm	< 0.01	±0.02	< 0.01
alpha_LRIem	< 0.01	< 0.01	±0.05
alpha_LRMem	< 0.01	< 0.01	±0.06
alpha_QCDNorm_S4ee_meffInc	±0.22	< 0.01	< 0.01
alpha_TEee	±0.09	< 0.01	< 0.01
alpha_TEem	< 0.01	< 0.01	±0.59
alpha_TEmm	< 0.01	±0.21	< 0.01
alpha_Zpt200GeV	< 0.01	±0.01	±0.02
alpha_err_BG	< 0.01	±0.07	±0.12
alpha_hadTop	±1.00	±1.22	±2.21
alpha_hadWZ	< 0.01	±0.02	±0.04
gamma_stat_S4ee_meffInc	±0.58	< 0.01	< 0.01
gamma_stat_S4em_meffInc	< 0.01	< 0.01	±0.93
gamma_stat_S4mm_meffInc	< 0.01	±0.66	< 0.01
mu_Top_Np1	< 0.01	< 0.01	±0.02
mu_Top_Np2	±0.12	±0.18	±0.36
mu_Top_Np3	±0.72	±0.84	±1.44
mu_WZ_Np3	< 0.01	< 0.01	±0.01
mu_WZ_Np4	< 0.01	±0.01	±0.01
mu_WZ_Np5	< 0.01	±0.01	±0.02

Table 26: Breakdown of the absolute systematic uncertainties on background estimates in the various Signal Regions. Note that the individual uncertainties can be correlated, and do not necessarily add up quadratically to the total background uncertainty.

12. Interpretation

After having investigated the Signal Region results in the previous chapter, the agreement between the observed number of events and the predicted Standard Model backgrounds will be translated into exclusion limits on several supersymmetry models in the following using hypothesis tests based on the profile log likelihood ratio (LLR) in a frequentist treatment. For this purpose, the exclusion as well as the discovery fit configurations discussed in chapter 10.2 will be used.

12.1. Introduction

In the following, a brief introduction into the calculation of upper limits using the profile LLR and the CL_s [277, 312] method will be given. The discussion is based on the description in [308], additional information on the method is contained in [313] as well as [314].

The profile LLR is defined as

$$\Lambda(\mu) \equiv \Lambda(\mu, \boldsymbol{n}, \boldsymbol{\theta}^0) = -2\left(\ln L(\boldsymbol{n}, \boldsymbol{\theta}^0|\mu, \hat{\hat{\boldsymbol{b}}}_\mu, \hat{\hat{\boldsymbol{\theta}}}_\mu) - \ln L(\boldsymbol{n}, \boldsymbol{\theta}^0|\hat{\mu}, \hat{\boldsymbol{b}}, \hat{\boldsymbol{\theta}})\right) \tag{44}$$

using the likelihood function defined in equation 40. Here, $\hat{\mu}, \hat{\boldsymbol{b}}, \hat{\boldsymbol{\theta}}$ are the set of parameter values maximizing the (unconditional) likelihood function while $\hat{\hat{\boldsymbol{b}}}_\mu, \hat{\hat{\boldsymbol{\theta}}}_\mu$ are the conditional maximum-likelihood estimators of $\boldsymbol{b}$ and $\boldsymbol{\theta}$ maximizing L for a fixed value of the signal strength μ. As such, higher values of Λ correspond to larger incompabilities between the data and the prediction for a given μ. Further complications arise when taking into account the fact that only $\mu \geq 0$ corresponds to physical values and that upward fluctuations of the data resulting in $\hat{\mu} > \mu$ should not be treated as evidence against the signal with strength μ as discussed in detail in [313, 314].

This test statistics $\Lambda(\mu)$ is evaluated on data to arrive at the observed value $\Lambda(\mu), obs$ for a given signal strength μ, together with the nuisance parameters $\hat{\hat{\boldsymbol{b}}}_\mu$ and $\hat{\hat{\boldsymbol{\theta}}}_\mu$ for both the *signal+background* as well as the *background-only* ($\mu = 0$) hypothesis.

The level of disagreement can be translated into the corresponding p-values

$$p_\mu = \int_{\Lambda(\mu),obs}^{\infty} f(\Lambda|\mu) d\Lambda \tag{45}$$

$$1 - p_b = \int_{\Lambda(0),obs}^{\infty} f(\Lambda|0) d\Lambda \tag{46}$$

with $f(\Lambda|\mu)$ being the probability density function of $\Lambda(\mu)$ for a given signal strength μ. The corresponding probability density function f can either been obtained via Monte Carlo methods or using approximate distributions following the theorems of Wilks [315, 316] and Wald [317]. Figure 83 left shows a sketch of the probability density functions for the test statistics.

Thus, exclusion limits are set using the CL_s value

$$CL_s(\mu) = \frac{p_\mu}{1 - p_b} = \frac{CL_{s+b}}{1 - CL_b} \tag{47}$$

as a ratio of the two probabilities for the signal+background and the background-only hypotheses. A certain signal strength μ is said to be excluded at 95% Confidence Level if $CL_s(\mu) < 0.05$.

This approach has the advantage of preventing strong exclusion limits in case of large downward fluctuations, though leading to overcoverage of the frequentist probability [318]. Figure 83 right shows an example for the dependence of CL_{s+b}, CL_b and CL_s on the signal strength μ. It can be seen that $\mu \lesssim 2.7$ is excluded for this model.

The method described above will be applied to the results of the discovery fit (for determining model-independent upper limits) and the exclusion fit (for testing specific models) configurations described in chapter 10.2. In addition to the calculation of *observed* limits using the measured data, *expected* limits will be derived from the median limit of the background-only hypothesis using pseudo-data. Furthermore, the $\pm 1\sigma_{exp}$ variations around the median expected limit are determined including all experimental uncertainties. The theoretical uncertainties on the signal in turn are separated and used to determine the $\pm 1\sigma^{SUSY}_{theory}$ limits around the nominal model cross section following the common agreement between ATLAS & CMS [319]. As such, the impact of theory uncertainties (changing the predicted signal cross section) is clearly separated from the experimental uncertainties.

Technically the limit setting is implemented using the `RooStats` [310]-based `HistFitter` package [309]. For better visualisation, the CL_s limits obtained for the different signal model points will be interpolated using Delaunay triangulation [320] to obtain smooth exclusion contours.

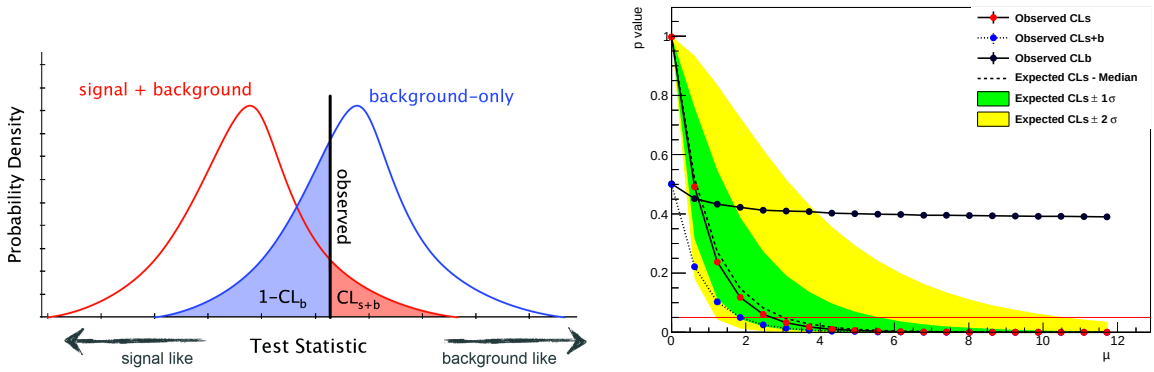

Figure 83: Left: Sketch of test statistics distributions for the signal+background and background-only hypotheses [321]. Right: Exemplary CL_{s+b}, CL_b and CL_s distributions as a function of the signal strength μ.

12.2. Model-independent Upper Limits

Before investigating specific models of supersymmetry breaking, it is illustrative to derive model-independent limits on the visible cross section in each of the different Signal Regions, i.e. on the product of the production cross section, branching ratio, acceptance and efficiency of a hypothetical signal. These limits are determined using the discovery-fit configuration as discussed in chapter 10.2 without specific assumptions on the signal model by including an additional floating signal parameter in the fit in each of the Signal Regions. Table 27 contains the expected and observed 95% CL upper limits on the number of signal events derived via the CL_s method as well as the corresponding limit on the visible cross section in the Signal Regions[50]. Furthermore, the confidence level for the background-only hypothesis CL_b is given.

[50] The model-independent upper limits for the one-lepton analyses are contained in appendix F.

Signal channel	$\langle\epsilon\sigma\rangle^{95}_{\text{obs}}$[fb]	S^{95}_{obs}	S^{95}_{exp}	CL_b
ee, 2-jet	0.71	3.3	3.5 ± 0.1	0.48
$\mu\mu$, 2-jet	0.76	3.6	3.5 ± 0.1	0.46
$e\mu$, 2-jet	0.83	3.9	$3.6^{+0.6}_{-0.2}$	0.85
ee, 4-jet	1.53	7.2	$7.7^{+3.2}_{-2.1}$	0.39
$\mu\mu$, 4-jet	1.93	9.1	$8.8^{+3.3}_{-3.0}$	0.55
$e\mu$, 4-jet	2.14	10.1	$11.5^{+4.8}_{-3.5}$	0.28

Table 27: Left to right: 95% CL upper limits on the visible cross section ($\langle\epsilon\sigma\rangle^{95}_{\text{obs}}$) in the various Signal Regions, and on the number of signal events (S^{95}_{obs}). The third column (S^{95}_{exp}) shows the 95% CL upper limit on the number of signal events, given the expected number (and $\pm 1\sigma$ uncertainty on the expectation) of background events. The last column indicates the CL_b value, i.e. the observed confidence level for the background-only hypothesis.

As already visible in the comparison between data and fit results, the overall agreement is good leading to large CL_b values between 0.28 and 0.85. Due to the small background expectation, stronger bounds on the visible cross sections between 0.71 fb and 0.83 fb are obtained from the 2-jet Signal Regions, while the limits in the 4-jet Signal Regions range from 1.53 fb to 2.14 fb.

12.3. Limits in the GMSB Model

After having discussed the model-independent upper limits derived using the discovery fit configuration, model-specific limits are obtained using the exclusion-fit configuration taking into account a specific signal in all Signal and Control Regions and using the shape of the m_{eff} distribution in the Signal Region[51]. Exclusion limits are set in the GMSB model using all six dilepton[52] Signal Regions as shown in Figure 84. Models with $\Lambda \leq 55$ TeV are excluded at 95% CL, approximately independent of $\tan\beta$, testing gluino masses of up to 1300 GeV and squark masses of up to 1250 GeV. The strongest bounds are obtained in the slepton-NLSP region, while the limits in the stau-NLSP region are slightly weaker due to the smaller branching ratio into leptonic final states as discussed in chapter 4.3. Overall, the limits strongly exceeds those of previous publications by ATLAS and the LEP experiments and currently provide the strongest exclusion limit in this GMSB scenario for low values of $\tan\beta$.

For further illustration, Figure 85 contains a comparison of the exclusion limit obtained in this analysis to a similar ATLAS analysis using tau-final states [155]. Both analyses complement each other in the different regions of the $\Lambda - \tan\beta$ plane.

[51] The impact of this fit configuration on the main fit parameters compared to the background-only fit is shown in appendix E.

[52] In the GMSB model, the Branching Ratio to one lepton final states is small and as such the contribution of these channels is neglected. The acceptance times efficiency of the individual dilepton Signal Regions is contained in appendix C.

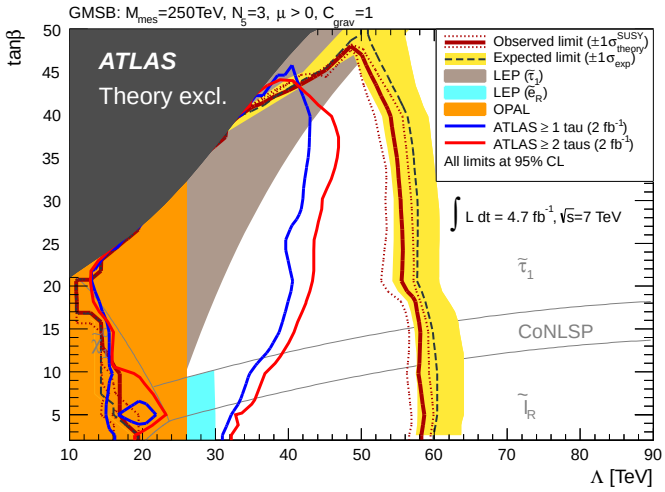

Figure 84: Expected and observed 95% CL exclusion limits in the minimal GMSB model, combining six Signal Regions from the dilepton channels. The band around the median expected limit shows the $\pm 1\sigma$ variations, including all uncertainties except theoretical uncertainties on the signal. The dotted lines around the observed limit indicate the sensitivity to $\pm 1\sigma$ variations on these theoretical uncertainties. The different next-to-lightest particle (NLSP) regions are indicated. The coNLSP region denotes the region where $\tilde{\tau}_1$ and $\tilde{\ell}_R$ are nearly mass degenerate. Previous OPAL and ATLAS limits in this model are taken from [129] and [156, 157], respectively. Limits derived from the LEP slepton mass limits [128] are also shown.

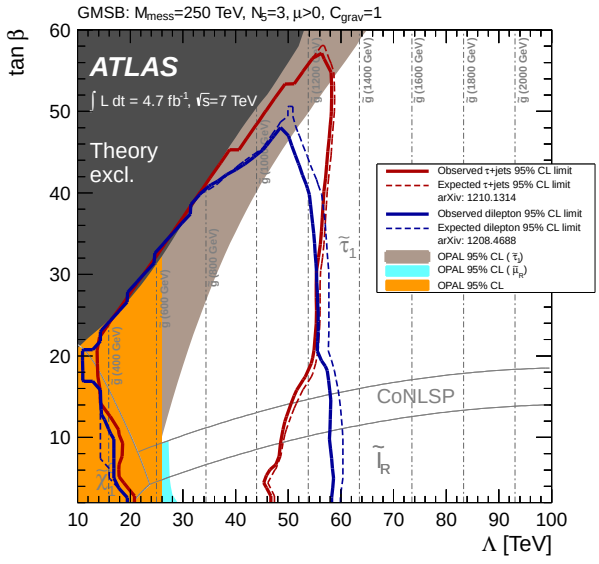

Figure 85: Expected and observed 95% CL exclusion limits in the minimal GMSB model from this analysis in comparison to limits obtained in the ATLAS supersymmetry searches requiring taus [155].

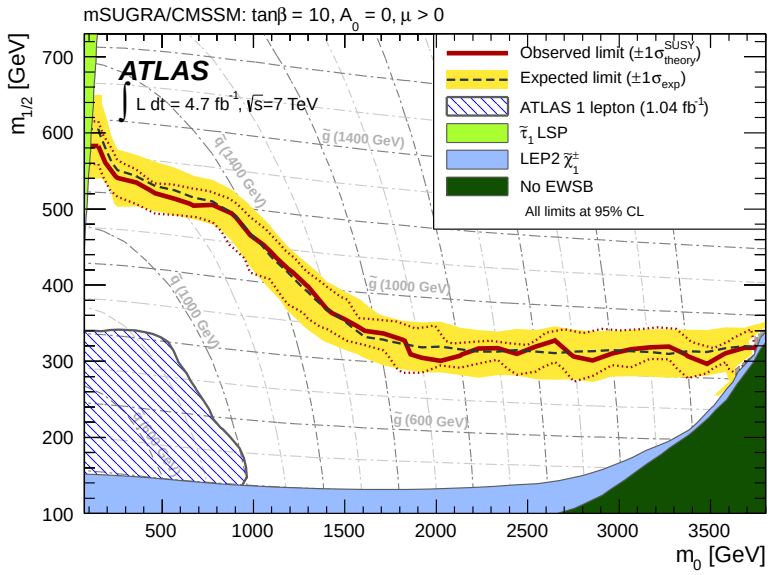

Figure 86: Expected and observed 95% CL exclusion limits in the mSUGRA model with $\tan\beta = 10, A_0 = 0$ and the sign of μ taken to be positive. The results are obtained by combining ten Signal Regions from the hard single-lepton and dilepton channels. The band around the median expected limit shows the $\pm 1\sigma$ variations, including all uncertainties except theoretical uncertainties on the signal. The dotted lines around the observed limit indicate the sensitivity to $\pm 1\sigma$ variations on these theoretical uncertainties. The dashed grid shows contours of constant squark (curved lines) and gluino (nearly horizontal lines) masses. The previous limit from ATLAS [327] and the results from the LEP experiments [328] are also shown. The parameter space labelled as "No EWSB" is theoretically excluded as no electroweak symmetrybreaking is possible in this region.

12.4. Limits in the mSUGRA Model

For the interpretation within the mSUGRA scenario, the ten Signal Regions from the dilepton and the hard one-lepton analysis are combined[53]. Figure 86 shows the exclusion limit in the $m_0 - m_{1/2}$ plane, providing a large improvement compared to previous analyses based on the hard one lepton channel. Assuming the validity of this mSUGRA scenario and equal masses, squarks and gluinos with masses below approximately 1.2 TeV are excluded at 95% CL. Compared to similar ATLAS analyses on the same dataset and model in final states without leptons and 2-6 jets [322] or 6-9 jets [323], a similar sensitivity is obtained for intermediate to large values of m_0 despite the smaller branching ratio of squarks and gluinos into leptonic final states, while [322] is slightly more sensitive for small values m_0 and large values of $m_{1/2}$. Furthermore, similar analyses have also been carried out by CMS using either single [324] or dilepton [325, 326] final states leading to comparable sensitivities.

To illustrate the performance of the different Signal Regions within this scenario, Figure 87 contains the expected limits obtained from the individual Signal Regions when combining only the different flavor final states[54]. It can be seen that both the 4-jet dilepton as well as the 4-jet hard one lepton

[53] The soft-lepton Signal Regions are not taken into account as they provide only very low sensitivity in this scenario due to the relatively large transverse momenta of the leptons in the relevant parameter space.
[54] The acceptance times efficiency of the individual dilepton Signal Regions is contained in appendix C.

Signal Regions contribute to the limit for large values of m_0, while for large values of $m_{1/2}$ the exclusion reach is driven by the one lepton Signal Regions. For large values of m_0, gluino pair production dominates, leading to four jet final states due to the three-body gluino decays as the squark masses are larger than the gluino masses. In contrast, for large values of $m_{1/2}$, squark pair production as well as mixed squark-gluino production contribute significantly, which in turn leads to less, but harder jets in the final states. To illustrate the impact of using the shape information from the m_{eff} distribution, Figure 88 contains a comparison to a cut-and-count analysis using a single inclusive bin for each Signal Region. It can be seen that the inclusion of the shape information significantly improves the sensitivity.

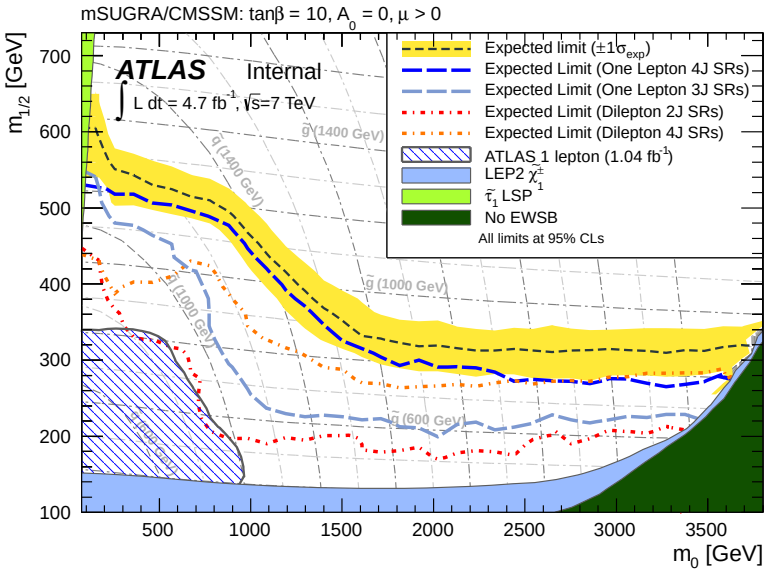

Figure 87: Contributions from the different dilepton and single hard lepton Signal Regions to the combined limit shown in Figure 86.

12.5. Limits in the Simplified Models

In addition to the specific interpretations in the GMSB and the mSUGRA scenario, exclusion limits are derived in the one- and the two-step Simplified Models. For all the Simplified Models, all one- and dilepton Signal Regions (including the soft-lepton channel) are combined to maximize the exclusion reach. In contrast to the previous scenarios where the model completely specifies all sparticle masses, cross sections and branching ratios, the excluded model cross section $\sigma_{\text{nominal}} \cdot \mu_{95}$ for the different Simplified Models is calculated explicitly by scanning the excluded signal strength μ as shown in Figure 83 right. For the calculation of the exclusion curves, the nominal MSSM production cross section is used, while the branching ratio to the specific decay chain is fixed to one.

Figure 89 contains the exclusion limits for the one-step Simplified Models. The limits are dominated by the one lepton Signal Regions as the dilepton channel only contributes if both W bosons decay leptonically[55]. For model points with small mass differences between the squark/gluino and the LSP

[55] The acceptance times efficiency of the individual dilepton Signal Regions for all the Simplified Models is contained in appendix C.

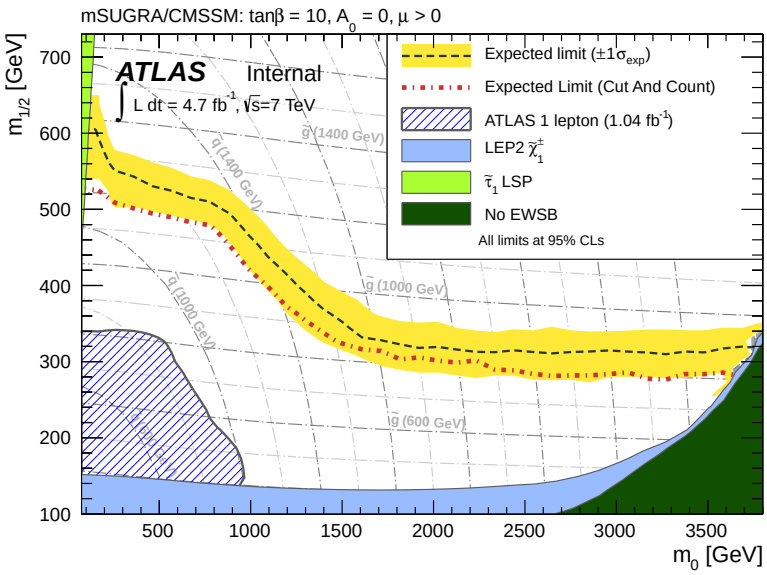

Figure 88: Comparison of the combined expected mSUGRA limit using the shape information from the m_{eff} distribution compared to a cut-and-count analysis using a single inclusive bin for each Signal Region.

(or respectively for models with small mass splitting x), the soft lepton Signal Regions significantly extend the exclusion reach. In both the scenario with fixed mass splitting $x = 1/2$ as well as in the scenario with 60 GeV LSP mass, gluinos masses of up to 900 GeV are excluded. In the squark pair production models, the limit is weaker due to the smaller production cross section as well as the smaller selection efficiency due to the lower jet multiplicity. Here, squark masses of up to 600 GeV are excluded.

In the same way, Figure 90 shows the exclusion limits in the two-step Simplified Models for gluino pair production. In the Simplified Model involving sleptons, the 4-jet dilepton Signal Region provides the largest contribution to the reach as always two leptons and four jets are produced, while in the Simplified Model involving W/Z bosons, contributions from all Signal Regions are present.

Finally, Figure 91 contains the exclusion limits obtained in the two-step Simplified Models for squark pair production. Again the exclusion reach is dominated by the dilepton Signal Regions in the models involving sleptons, while some contribution from the one-lepton channels is present as well for model with χ_2^0 due to the decays via sneutrinos. As for the two-step gluino pair production, the model with decay chains via W/Z bosons is affected by the lower leptonic branching ratio compared to the slepton grids, which is partially compensated by the higher acceptance of the one-lepton signal regions.

Limits in the two-step Simplified Models exclude gluino masses around 900-1000 GeV, while squark masses of 500-700 GeV are excluded for low LSP masses. The exclusion limits for the Simplified Models obtained in the context of this work significantly extend previous constraints or exclude types of models for the first time. A similar combination of several analysis channels and a corresponding interpretation within many Simplified Models has also been carried out by now by the CMS collaboration, resulting in comparable exclusion limits [329].

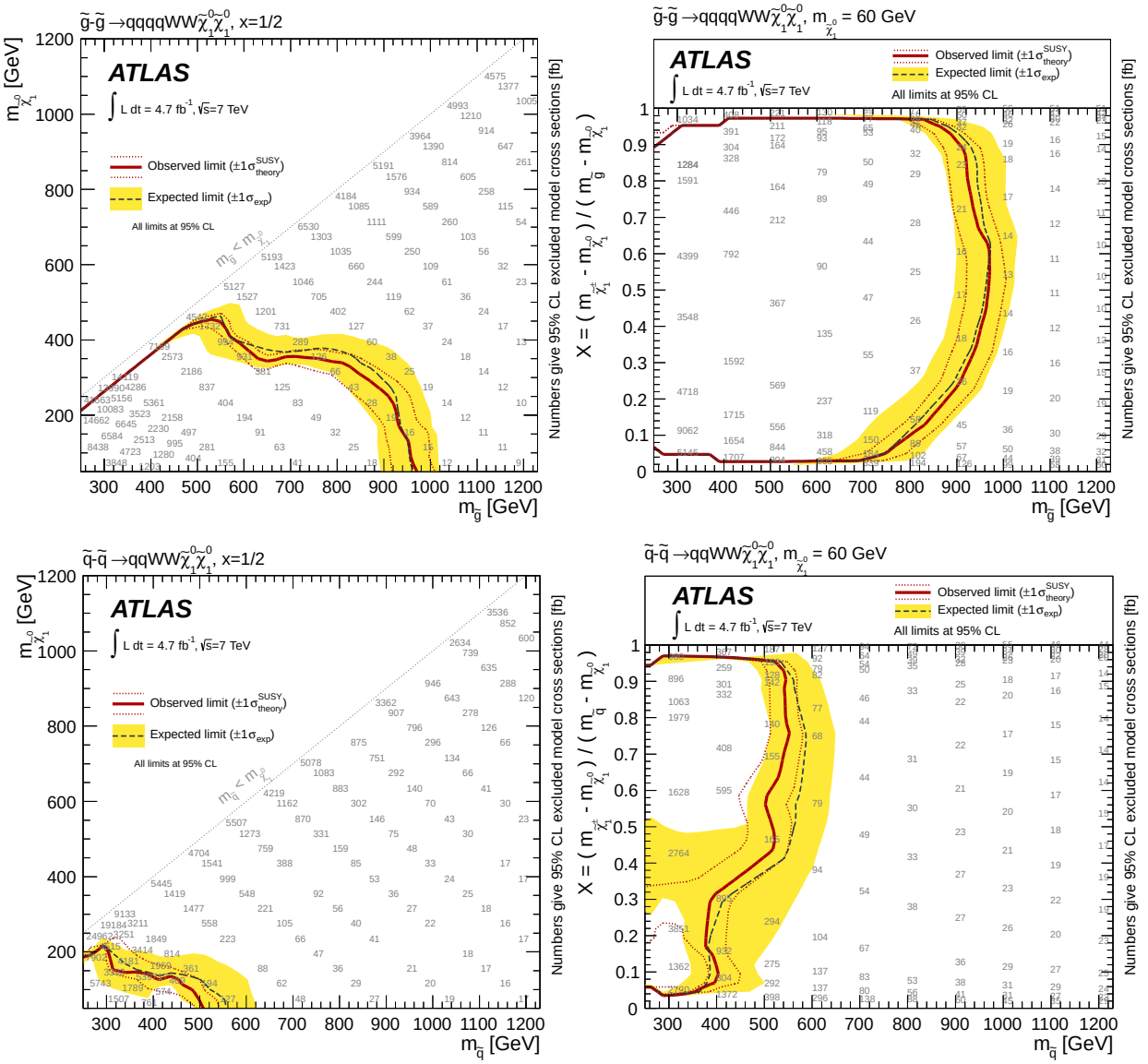

Figure 89: Excluded regions at 95% confidence level in the parameter space of one-step Simplified Models. Top row: gluino pair production with $\tilde{g} \to q\overline{q}'\tilde{\chi}_1^{\pm} \to q\overline{q}'W^{\pm}\tilde{\chi}_1^0$. Bottom row: squark pair production with $\tilde{q}_L \to q'\tilde{\chi}_1^{\pm} \to q'W^{\pm}\tilde{\chi}_1^0$. In the left column, the chargino mass is set to be halfway between gluino (top) or squark (bottom) and LSP masses. In the right column, the LSP mass is fixed at 60 GeV and the masses of the chargino and gluino (top) or squark (bottom) are varied. The band around the median expected limit shows the $\pm 1\sigma$ variations, including all uncertainties except theoretical uncertainties on the signal. The dotted lines around the observed limit indicate the sensitivity to $\pm 1\sigma$ variations on these theoretical uncertainties. The plots are from the combination of all single and dilepton channels. The numbers indicate the excluded cross section in fb. A smaller excluded cross section implies a more stringent limit.

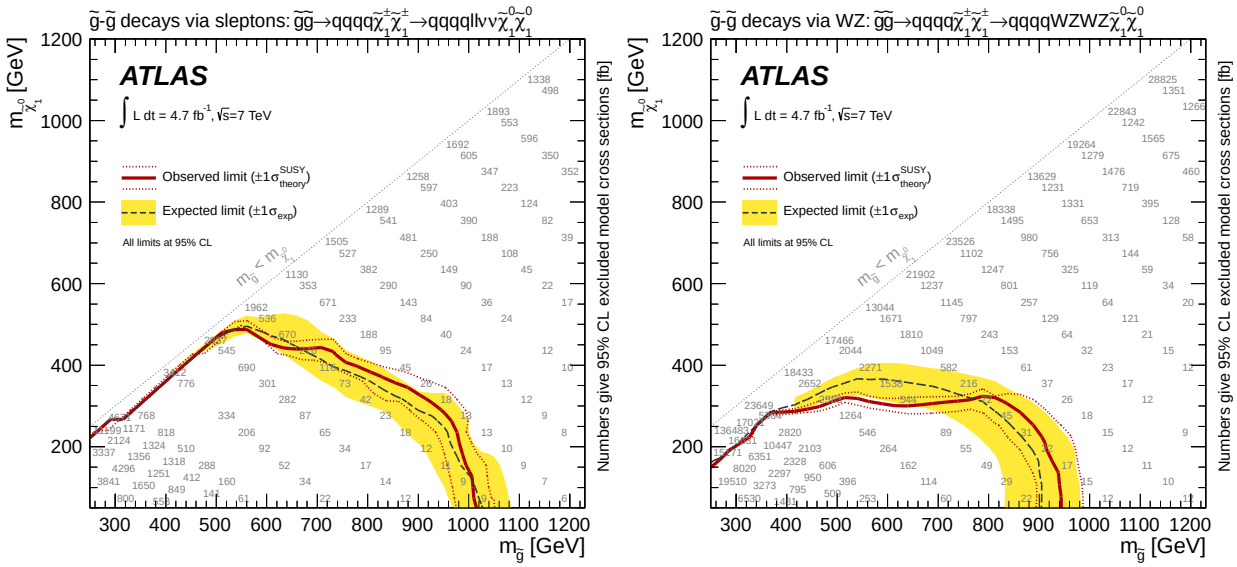

Figure 90: Excluded regions at 95% confidence level in the parameter space of two-step Simplified Models with gluino pair production. Left: both gluinos decay via $\tilde{g} \to q\overline{q}'\tilde{\chi}_1^{\pm} \to q\overline{q}'\ell^{\pm}\tilde{\nu}_L \to q\overline{q}'\ell^{\pm}\nu\tilde{\chi}_1^0$ or $\tilde{g} \to q\overline{q}'\tilde{\chi}_1^{\pm} \to q\overline{q}'\nu\tilde{\ell}_L^{\pm} \to q\overline{q}'\nu\ell^{\pm}\tilde{\chi}_1^0$. Right: both gluinos decay via $\tilde{g} \to q\overline{q}'\tilde{\chi}_1^{\pm} \to q\overline{q}'W^{(*)\pm}\tilde{\chi}_2^0 \to W^{(*)\pm}Z^{(*)}\tilde{\chi}_1^0$. The band around the median expected limit shows the $\pm 1\sigma$ variations, including all uncertainties except theoretical uncertainties on the signal. The dotted lines around the observed limit indicate the sensitivity to $\pm 1\sigma$ variations on these theoretical uncertainties. The plots are dominated by the dilepton channels. The numbers indicate the excluded cross section in fb. A smaller excluded cross section implies a more stringent limit.

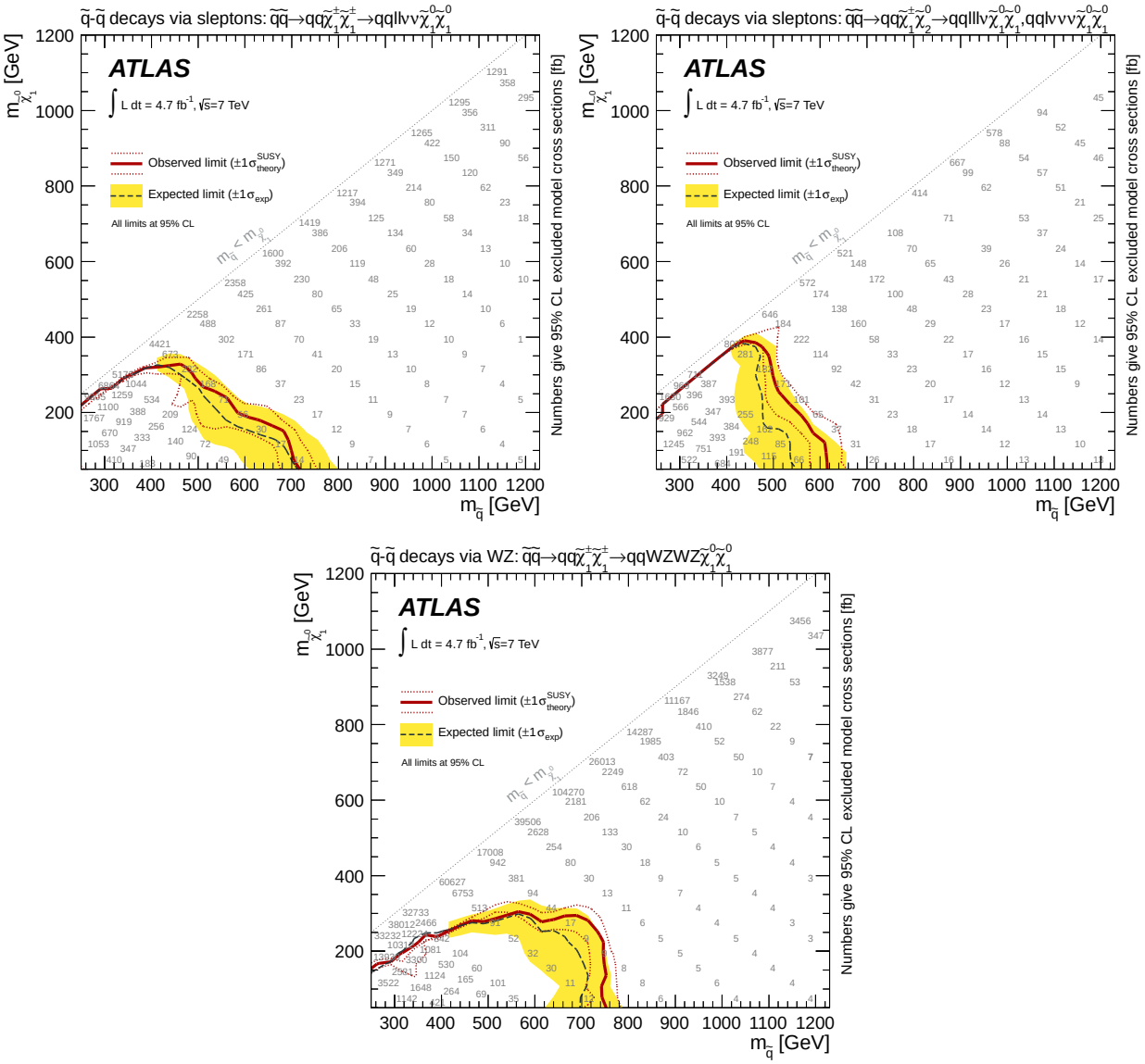

Figure 91: Excluded regions at 95% confidence level in the parameter space of two-step Simplified Models with squark pair production. Top left: both squarks decay via $\tilde{q}_L \to q'\tilde{\chi}_1^\pm \to q'\ell^\pm\tilde{\nu}_L \to q'\ell^\pm\nu\tilde{\chi}_1^0$ or $\tilde{q}_L \to q'\tilde{\chi}_1^\pm \to q'\tilde{\ell}^\pm\nu \to q'\ell^\pm\nu\tilde{\chi}_1^0$. Top right: one squark decays via $\tilde{q}_L \to q'\tilde{\chi}_1^\pm \to q'\ell^\pm\tilde{\nu}_L \to q'\ell^\pm\nu\tilde{\chi}_1^0$ or $\tilde{q}_L \to q'\tilde{\chi}_1^\pm \to q'\tilde{\ell}^\pm\nu \to q'\ell^\pm\nu\tilde{\chi}_1^0$ and the other squark decays via $\tilde{q}_L \to q\tilde{\chi}_2^0 \to q\ell^\pm\tilde{\ell}_L^\mp \to q\ell^\pm\ell^\mp\tilde{\chi}_1^0$ or $\tilde{q}_L \to q\tilde{\chi}_2^0 \to q\nu\tilde{\nu}_L \to q\nu\nu\tilde{\chi}_1^0$. Bottom row: both squarks decay via $\tilde{q}_L \to q'\tilde{\chi}_1^\pm \to W^{(*)\pm}\tilde{\chi}_2^0 \to W^{(*)\pm}Z^{(*)}\tilde{\chi}_1^0$. The band around the median expected limit shows the $\pm1\sigma$ variations, including all uncertainties except theoretical uncertainties on the signal. The dotted lines around the observed limit indicate the sensitivity to $\pm1\sigma$ variations on these theoretical uncertainties. The plots are dominated by the dilepton channels. The numbers indicate the excluded cross section in fb. A smaller excluded cross section implies a more stringent limit.

13. Summary & Outlook

In the present work, a search for supersymmetry with the ATLAS detector in final states containing jets, E_T^{miss} and at least two isolated leptons has been presented. The requirement of at least two leptons efficiently suppresses otherwise dominant Standard Model backgrounds such as QCD multijet and W+jet events and as such simplifies the control of the background. The full dataset from the 2011 data-taking period with an integrated luminosity of 4.7 fb^{-1} of $\sqrt{7}$ TeV proton-proton collisions provided by the LHC has been analyzed and results have been found to be consistent with the Standard Model predictions.

The main emphasis of this work has been set on the configuration, validation and application of a simultaneous fit to several Control and Signal Regions, combining results of this dilepton analysis with two additional one lepton analyses. The combined fit improves the modelling of the Standard Model background processes and reduces the systematic uncertainties significantly, thus resulting in a more precise background prediction for the Signal Regions and as such a higher sensitivity to supersymmetry models and an extended exclusion reach. Dominant systematics arise due to the limited Monte Carlo statistics in the extreme phase space regions of the Signal Regions. In the Signal Region requiring at least four jets with high transverse momenta, the uncertainties on the $t\bar{t}$+jets normalization as well as jet energy scale and hadronization uncertainties are also of relevance.

In all the Signal Regions, the observed data is consistent with the Standard Model prediction and as such exclusion limits have been derived in several scenarios. The exclusion limits set by this analysis strongly exceed limits from the LEP and Tevatron experiments. Visible cross sections between 0.71 fb and 2.14 fb are excluded at 95% CL in the Signal Regions. In the GMSB scenario investigated in this analysis, models with $\Lambda < 55$ TeV are excluded at 95% CL, corresponding to gluino masses of about 1.2 TeV. Similarly, squark and gluino masses below 1.2 TeV are excluded 95% CL in the mSUGRA scenario for models with equal squark and gluino masses. Furthermore, exclusion limits have been set in several different one- and two-step Simplified Models for the first time in leptonic supersymmetry searches. For not too large LSP masses, gluinos with masses below $900 - 1000$ GeV and squarks with masses below $500 - 600$ GeV are excluded at 95% CL for several possible decay modes.

Further supersymmetry searches are being carried out by ATLAS using the dataset from the 2012 data taking period with an integrated luminosity of up to 20 fb^{-1} at a slightly higher center of mass energy of 8 TeV. While updates for the hard one lepton analysis are ongoing [330], no immediate update for this dilepton analysis is currently forseen and the complexity of this combined analysis in terms of the constraining of theoretical uncertainties on the Standard Model background prediction is unrivaled at this point in time. Apart from the inclusion of more data at higher center of mass energies, further improvements of the analysis could be realized by combining the results of an exclusive dilepton analysis with a dedicated multilepton analysis which would strongly improve the sensitivity to scenarios with light sleptons such as the GMSB model.

With the discovery of a Higgs boson with a mass of approximately 125 GeV and properties consistent with the Standard Model predictions, the last remaining ingredient of the Standard Model has been found. Nevertheless, even this presumptive completion of the Standard Model does not provide a full answer to all the open questions of particle physics, necessitating physics beyond the Standard Model. The absence of any signal observation in many different search channels combined with the observed Higgs boson mass, the null results from dark matter experiments such as

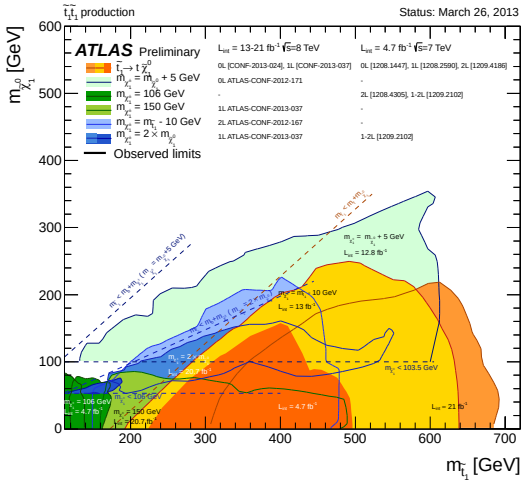

Figure 92: Summary of the dedicated ATLAS searches for top squark pair production based on up to 20.7 fb^{-1} of pp collision data taken at $\sqrt{s}$ = 8 TeV and 4.7 fb^{-1} of pp collision data taken at $\sqrt{s}$ = 7 TeV [334].

XENON100 [331] as well as the constraints on the $B_s \to \mu^+\mu^-$ branching ratio [332] have ruled out several supersymmetry models that had been favoured before the start of the LHC [333]. Thus, the focus of the ongoing supersymmetry searches at the LHC is shifting towards supersymmetry models in which only the top squark, the gauginos and the gluino are light, while all other sparticles have masses beyond the kinematic reach of the LHC. Such "natural" supersymmetry models still provide a solution to the hierarchy problem and for dark matter, but lead to scenarios that are harder to detect and thus could have escaped the current supersymmetry searches at the LHC. Figure 92 shows the corresponding limits in the $\tilde{t}_1 - \tilde{\chi}_1^0$ plane from several ATLAS analyses.

Apart from such more specific searches, further improved sensitivities can also be expected with higher center of mass energies and integrated luminosites after the upgrade of the LHC. As shown in Figure 93, the LHC and its experiments will be able to further test supersymmetry models on unprecedented scales in the coming years.

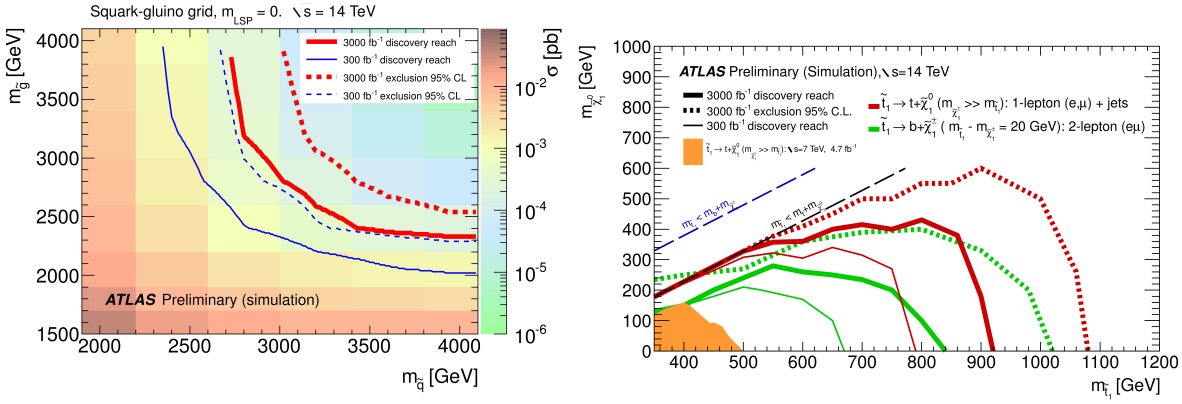

Figure 93: Expected 95% CL exclusion limits and 5σ discovery reaches for integrated luminosities of 300 fb^{-1} and 3000 fb^{-1} at $\sqrt{s}$ = 14 TeV in a simplified squark-gluino model with massless neutralino (left) and in the $\tilde{t}_1 - \tilde{\chi}_1^0$ mass plane (right) assuming $\tilde{t}_1 \to t + \tilde{\chi}_1^0$ or $\tilde{t}_1 \to b + \tilde{\chi}_1^{\pm}$ decays [335].

A. Monte Carlo Samples

For the analysis, the following official datasets provided by the ATLAS supersymmetry working group using the `SUSYD3PDMaker` package [336] have been used:

group10.phys-susy.data11_7TeV.periodB.physics_Egamma.PhysCont.NTUP_SUSYSKIM.pro10_v01_p832
group10.phys-susy.data11_7TeV.periodD.physics_Egamma.PhysCont.NTUP_SUSYSKIM.pro10_v01_p832
group10.phys-susy.data11_7TeV.periodE.physics_Egamma.PhysCont.NTUP_SUSYSKIM.pro10_v01_p832
group10.phys-susy.data11_7TeV.periodF.physics_Egamma.PhysCont.NTUP_SUSYSKIM.pro10_v01_p832
group10.phys-susy.data11_7TeV.periodG.physics_Egamma.PhysCont.NTUP_SUSYSKIM.pro10_v01_p832
group10.phys-susy.data11_7TeV.periodH.physics_Egamma.PhysCont.NTUP_SUSYSKIM.pro10_v01_p832
group10.phys-susy.data11_7TeV.periodI.physics_Egamma.PhysCont.NTUP_SUSYSKIM.pro10_v01_p832
group10.phys-susy.data11_7TeV.periodJ.physics_Egamma.PhysCont.NTUP_SUSYSKIM.pro10_v01_p832
group10.phys-susy.data11_7TeV.periodK.physics_Egamma.PhysCont.NTUP_SUSYSKIM.pro10_v01_p832
group10.phys-susy.data11_7TeV.periodL.physics_Egamma.PhysCont.NTUP_SUSYSKIM.pro10_v01_p832
group10.phys-susy.data11_7TeV.periodM.physics_Egamma.PhysCont.NTUP_SUSYSKIM.pro10_v01_p832

group10.phys-susy.data11_7TeV.periodB.physics_Muons.PhysCont.NTUP_SUSYSKIM.pro10_v01_p832
group10.phys-susy.data11_7TeV.periodD.physics_Muons.PhysCont.NTUP_SUSYSKIM.pro10_v01_p832
group10.phys-susy.data11_7TeV.periodE.physics_Muons.PhysCont.NTUP_SUSYSKIM.pro10_v01_p832
group10.phys-susy.data11_7TeV.periodF.physics_Muons.PhysCont.NTUP_SUSYSKIM.pro10_v01_p832
group10.phys-susy.data11_7TeV.periodG.physics_Muons.PhysCont.NTUP_SUSYSKIM.pro10_v01_p832
group10.phys-susy.data11_7TeV.periodH.physics_Muons.PhysCont.NTUP_SUSYSKIM.pro10_v01_p832
group10.phys-susy.data11_7TeV.periodI.physics_Muons.PhysCont.NTUP_SUSYSKIM.pro10_v01_p832
group10.phys-susy.data11_7TeV.periodJ.physics_Muons.PhysCont.NTUP_SUSYSKIM.pro10_v01_p832
group10.phys-susy.data11_7TeV.periodK.physics_Muons.PhysCont.NTUP_SUSYSKIM.pro10_v01_p832
group10.phys-susy.data11_7TeV.periodL.physics_Muons.PhysCont.NTUP_SUSYSKIM.pro10_v01_p832
group10.phys-susy.data11_7TeV.periodM.physics_Muons.PhysCont.NTUP_SUSYSKIM.pro10_v01_p832

mc11_7TeV.116250.AlpgenJimmyZeeNp0_Mll10to40_pt20.merge.NTUP_SUSY.e959_s1310_s1300_r3043_r2993_p832
mc11_7TeV.116251.AlpgenJimmyZeeNp1_Mll10to40_pt20.merge.NTUP_SUSY.e959_s1310_s1300_r3043_r2993_p832
mc11_7TeV.116252.AlpgenJimmyZeeNp2_Mll10to40_pt20.merge.NTUP_SUSY.e944_s1310_s1300_r3043_r2993_p832
mc11_7TeV.116253.AlpgenJimmyZeeNp3_Mll10to40_pt20.merge.NTUP_SUSY.e944_s1310_s1300_r3043_r2993_p832
mc11_7TeV.116254.AlpgenJimmyZeeNp4_Mll10to40_pt20.merge.NTUP_SUSY.e944_s1310_s1300_r3043_r2993_p832
mc11_7TeV.116255.AlpgenJimmyZeeNp5_Mll10to40_pt20.merge.NTUP_SUSY.e944_s1310_s1300_r3043_r2993_p832
mc11_7TeV.116260.AlpgenJimmyZmumuNp0_Mll10to40_pt20.merge.NTUP_SUSY.e959_s1310_s1300_r3043_r2993_p832
mc11_7TeV.116261.AlpgenJimmyZmumuNp1_Mll10to40_pt20.merge.NTUP_SUSY.e959_s1310_s1300_r3043_r2993_p832
mc11_7TeV.116262.AlpgenJimmyZmumuNp2_Mll10to40_pt20.merge.NTUP_SUSY.e944_s1310_s1300_r3043_r2993_p832
mc11_7TeV.116263.AlpgenJimmyZmumuNp3_Mll10to40_pt20.merge.NTUP_SUSY.e944_s1310_s1300_r3043_r2993_p832
mc11_7TeV.116264.AlpgenJimmyZmumuNp4_Mll10to40_pt20.merge.NTUP_SUSY.e944_s1310_s1300_r3043_r2993_p832
mc11_7TeV.116265.AlpgenJimmyZmumuNp5_Mll10to40_pt20.merge.NTUP_SUSY.e944_s1310_s1300_r3043_r2993_p832
mc11_7TeV.116940.AlpgenJimmyZtautaullNp0_Mll10to40Pt15Pt5.merge.NTUP_SUSY.e835_s1310_s1300_r3043_r2993_p832
mc11_7TeV.116941.AlpgenJimmyZtautaullNp1_Mll10to40Pt15Pt5.merge.NTUP_SUSY.e835_s1310_s1300_r3043_r2993_p832
mc11_7TeV.116942.AlpgenJimmyZtautaullNp2_Mll10to40Pt15Pt5.merge.NTUP_SUSY.e835_s1310_s1300_r3043_r2993_p832
mc11_7TeV.116943.AlpgenJimmyZtautaullNp3_Mll10to40Pt15Pt5.merge.NTUP_SUSY.e835_s1310_s1300_r3043_r2993_p832
mc11_7TeV.116944.AlpgenJimmyZtautaullNp4_Mll10to40Pt15Pt5.merge.NTUP_SUSY.e835_s1310_s1300_r3043_r2993_p832
mc11_7TeV.116945.AlpgenJimmyZtautaullNp5_Mll10to40Pt15Pt5.merge.NTUP_SUSY.e835_s1310_s1300_r3043_r2993_p832
mc11_7TeV.105890.AlpgenJimmyttbarlnlnNp0_baseline.merge.NTUP_SUSY.e887_s1372_s1370_r3043_r2993_p832
mc11_7TeV.105891.AlpgenJimmyttbarlnlnNp1_baseline.merge.NTUP_SUSY.e887_s1372_s1370_r3043_r2993_p832
mc11_7TeV.105892.AlpgenJimmyttbarlnlnNp2_baseline.merge.NTUP_SUSY.e887_s1372_s1370_r3043_r2993_p832
mc11_7TeV.117897.AlpgenJimmyttbarlnlnNp3_baseline.merge.NTUP_SUSY.e835_s1372_s1370_r3043_r2993_p832
mc11_7TeV.117898.AlpgenJimmyttbarlnlnNp4_baseline.merge.NTUP_SUSY.e835_s1372_s1370_r3043_r2993_p832
mc11_7TeV.117899.AlpgenJimmyttbarlnlnNp5_baseline.merge.NTUP_SUSY.e835_s1372_s1370_r3043_r2993_p832
mc11_7TeV.105894.AlpgenJimmyttbarlnqqNp0_baseline.merge.NTUP_SUSY.e891_s1372_s1370_r3043_r2993_p832
mc11_7TeV.105895.AlpgenJimmyttbarlnqqNp1_baseline.merge.NTUP_SUSY.e891_s1372_s1370_r3043_r2993_p832
mc11_7TeV.105896.AlpgenJimmyttbarlnqqNp2_baseline.merge.NTUP_SUSY.e887_s1372_s1370_r3043_r2993_p832
mc11_7TeV.117887.AlpgenJimmyttbarlnqqNp3_baseline.merge.NTUP_SUSY.e835_s1372_s1370_r3043_r2993_p832
mc11_7TeV.117888.AlpgenJimmyttbarlnqqNp4_baseline.merge.NTUP_SUSY.e835_s1372_s1370_r3043_r2993_p832
mc11_7TeV.117889.AlpgenJimmyttbarlnqqNp5_baseline.merge.NTUP_SUSY.e835_s1372_s1370_r3043_r2993_p832
mc11_7TeV.105985.WW_Herwig.merge.NTUP_SUSY.e825_s1310_s1300_r3043_r2993_p832
mc11_7TeV.105987.WZ_Herwig.merge.NTUP_SUSY.e825_s1310_s1300_r3043_r2993_p832
mc11_7TeV.105986.ZZ_Herwig.merge.NTUP_SUSY.e825_s1310_s1300_r3043_r2993_p832
mc11_7TeV.107680.AlpgenJimmyWenuNp0_pt20.merge.NTUP_SUSY.e825_s1299_s1300_r3043_r2993_p832
mc11_7TeV.107681.AlpgenJimmyWenuNp1_pt20.merge.NTUP_SUSY.e825_s1299_s1300_r3043_r2993_p832
mc11_7TeV.107682.AlpgenJimmyWenuNp2_pt20.merge.NTUP_SUSY.e825_s1299_s1300_r3043_r2993_p832
mc11_7TeV.107683.AlpgenJimmyWenuNp3_pt20.merge.NTUP_SUSY.e825_s1299_s1300_r3043_r2993_p832
mc11_7TeV.107684.AlpgenJimmyWenuNp4_pt20.merge.NTUP_SUSY.e825_s1299_s1300_r3043_r2993_p832

mc11_7TeV.107685.AlpgenJimmyWenuNp5_pt20.merge.NTUP_SUSY.e825_s1299_s1300_r3043_r2993_p832
mc11_7TeV.107690.AlpgenJimmyWmunuNp0_pt20.merge.NTUP_SUSY.e825_s1299_s1300_r3043_r2993_p832
mc11_7TeV.107691.AlpgenJimmyWmunuNp1_pt20.merge.NTUP_SUSY.e825_s1299_s1300_r3043_r2993_p832
mc11_7TeV.107692.AlpgenJimmyWmunuNp2_pt20.merge.NTUP_SUSY.e825_s1299_s1300_r3043_r2993_p832
mc11_7TeV.107693.AlpgenJimmyWmunuNp3_pt20.merge.NTUP_SUSY.e825_s1299_s1300_r3043_r2993_p832
mc11_7TeV.107694.AlpgenJimmyWmunuNp4_pt20.merge.NTUP_SUSY.e825_s1299_s1300_r3043_r2993_p832
mc11_7TeV.107695.AlpgenJimmyWmunuNp5_pt20.merge.NTUP_SUSY.e825_s1299_s1300_r3043_r2993_p832
mc11_7TeV.107700.AlpgenJimmyWtaunuNp0_pt20.merge.NTUP_SUSY.e835_s1299_s1300_r3043_r2993_p832
mc11_7TeV.107701.AlpgenJimmyWtaunuNp1_pt20.merge.NTUP_SUSY.e835_s1299_s1300_r3043_r2993_p832
mc11_7TeV.107702.AlpgenJimmyWtaunuNp2_pt20.merge.NTUP_SUSY.e835_s1299_s1300_r3043_r2993_p832
mc11_7TeV.107703.AlpgenJimmyWtaunuNp3_pt20.merge.NTUP_SUSY.e835_s1299_s1300_r3043_r2993_p832
mc11_7TeV.107704.AlpgenJimmyWtaunuNp4_pt20.merge.NTUP_SUSY.e835_s1299_s1300_r3043_r2993_p832
mc11_7TeV.107705.AlpgenJimmyWtaunuNp5_pt20.merge.NTUP_SUSY.e835_s1299_s1300_r3043_r2993_p832
mc11_7TeV.107650.AlpgenJimmyZeeNp0_pt20.merge.NTUP_SUSY.e835_s1299_s1300_r3043_r2993_p832
mc11_7TeV.107651.AlpgenJimmyZeeNp1_pt20.merge.NTUP_SUSY.e835_s1299_s1300_r3043_r2993_p832
mc11_7TeV.107652.AlpgenJimmyZeeNp2_pt20.merge.NTUP_SUSY.e835_s1299_s1300_r3043_r2993_p832
mc11_7TeV.107653.AlpgenJimmyZeeNp3_pt20.merge.NTUP_SUSY.e835_s1299_s1300_r3043_r2993_p832
mc11_7TeV.107654.AlpgenJimmyZeeNp4_pt20.merge.NTUP_SUSY.e835_s1299_s1300_r3043_r2993_p832
mc11_7TeV.107655.AlpgenJimmyZeeNp5_pt20.merge.NTUP_SUSY.e835_s1299_s1300_r3043_r2993_p832
mc11_7TeV.109300.AlpgenJimmyZeebbNp0_nofilter.merge.NTUP_SUSY.e835_s1310_s1300_r3043_r2993_p832
mc11_7TeV.109301.AlpgenJimmyZeebbNp1_nofilter.merge.NTUP_SUSY.e835_s1310_s1300_r3043_r2993_p832
mc11_7TeV.109302.AlpgenJimmyZeebbNp2_nofilter.merge.NTUP_SUSY.e835_s1310_s1300_r3043_r2993_p832
mc11_7TeV.109303.AlpgenJimmyZeebbNp3_nofilter.merge.NTUP_SUSY.e835_s1310_s1300_r3043_r2993_p832
mc11_7TeV.107660.AlpgenJimmyZmumuNp0_pt20.merge.NTUP_SUSY.e835_s1299_s1300_r3043_r2993_p832
mc11_7TeV.107661.AlpgenJimmyZmumuNp1_pt20.merge.NTUP_SUSY.e835_s1299_s1300_r3043_r2993_p832
mc11_7TeV.107662.AlpgenJimmyZmumuNp2_pt20.merge.NTUP_SUSY.e835_s1299_s1300_r3043_r2993_p832
mc11_7TeV.107663.AlpgenJimmyZmumuNp3_pt20.merge.NTUP_SUSY.e835_s1299_s1300_r3043_r2993_p832
mc11_7TeV.107664.AlpgenJimmyZmumuNp4_pt20.merge.NTUP_SUSY.e835_s1299_s1300_r3043_r2993_p832
mc11_7TeV.107665.AlpgenJimmyZmumuNp5_pt20.merge.NTUP_SUSY.e835_s1299_s1300_r3043_r2993_p832
mc11_7TeV.109305.AlpgenJimmyZmumubbNp0_nofilter.merge.NTUP_SUSY.e835_s1310_s1300_r3043_r2993_p832
mc11_7TeV.109306.AlpgenJimmyZmumubbNp1_nofilter.merge.NTUP_SUSY.e835_s1310_s1300_r3043_r2993_p832
mc11_7TeV.109307.AlpgenJimmyZmumubbNp2_nofilter.merge.NTUP_SUSY.e835_s1310_s1300_r3043_r2993_p832
mc11_7TeV.109308.AlpgenJimmyZmumubbNp3_nofilter.merge.NTUP_SUSY.e835_s1310_s1300_r3043_r2993_p832
mc11_7TeV.107670.AlpgenJimmyZtautauNp0_pt20.merge.NTUP_SUSY.e835_s1299_s1300_r3043_r2993_p832
mc11_7TeV.107671.AlpgenJimmyZtautauNp1_pt20.merge.NTUP_SUSY.e835_s1299_s1300_r3043_r2993_p832
mc11_7TeV.107672.AlpgenJimmyZtautauNp2_pt20.merge.NTUP_SUSY.e835_s1299_s1300_r3043_r2993_p832
mc11_7TeV.107673.AlpgenJimmyZtautauNp3_pt20.merge.NTUP_SUSY.e835_s1299_s1300_r3043_r2993_p832
mc11_7TeV.107674.AlpgenJimmyZtautauNp4_pt20.merge.NTUP_SUSY.e835_s1299_s1300_r3043_r2993_p832
mc11_7TeV.107675.AlpgenJimmyZtautauNp5_pt20.merge.NTUP_SUSY.e835_s1299_s1300_r3043_r2993_p832
mc11_7TeV.108346.st_Wt_McAtNlo_Jimmy.merge.NTUP_SUSY.e835_s1310_s1300_r3043_r2993_p832
mc11_7TeV.108343.st_schan_enu_McAtNlo_Jimmy.merge.NTUP_SUSY.e825_s1310_s1300_r3043_r2993_p832
mc11_7TeV.108344.st_schan_munu_McAtNlo_Jimmy.merge.NTUP_SUSY.e825_s1310_s1300_r3043_r2993_p832
mc11_7TeV.108345.st_schan_taunu_McAtNlo_Jimmy.merge.NTUP_SUSY.e835_s1310_s1300_r3043_r2993_p832
mc11_7TeV.108340.st_tchan_enu_McAtNlo_Jimmy.merge.NTUP_SUSY.e825_s1310_s1300_r3043_r2993_p832
mc11_7TeV.108341.st_tchan_munu_McAtNlo_Jimmy.merge.NTUP_SUSY.e825_s1310_s1300_r3043_r2993_p832
mc11_7TeV.108342.st_tchan_taunu_McAtNlo_Jimmy.merge.NTUP_SUSY.e835_s1310_s1300_r3043_r2993_p832

mc11_7TeV.*.GMSB_3_2d_*_250_3_*_1_1_herwigpp_susy.merge.NTUP_SUSY.e971_s1310_s1300_r3043_r2993_p832
mc11_7TeV.*.GMSB_3_2d_*_250_3_*_1_1_herwigpp_susy.merge.NTUP_SUSY.e1078_s1411_s1383_r3062_r3063_p832
mc11_7TeV.*.GMSB_3_2d_*_250_3_*_1_1_herwigpp_susy.merge.NTUP_SUSY.e1098_s1372_s1370_r3108_r3109_p832

mc11_7TeV.*.SU_*_*_0_10_P_herwigpp_susy.merge.NTUP_SUSY.e920_s1310_s1300_r3043_r2993_p832
mc11_7TeV.*.SU_*_*_0_10_P_herwigpp_susy.merge.NTUP_SUSY.e971_a131_s1353_a139_r2900_p832
mc11_7TeV.*.SU_*_*_0_10_P_herwigpp_susy.merge.NTUP_SUSY.e1053_a131_s1353_a145_r2993_p832

mc11_7TeV.*.SM_GG_onestepCC_*.merge.NTUP_SUSY.e1007_a131_s1353_a145_r2993_p832
mc11_7TeV.*.SM_SS_onestepCC_*.merge.NTUP_SUSY.e1007_a131_s1353_a145_r2993_p832
mc11_7TeV.*.SM_GG_twostep_*.merge.NTUP_SUSY.e1007_a131_s1353_a145_r2993_p832
mc11_7TeV.*.SM_SS_twostep_*.merge.NTUP_SUSY.e1007_a131_s1353_a145_r2993_p832
mc11_7TeV.*.SM_GG_twostepCC_*.merge.NTUP_SUSY.e1007_a131_s1353_a145_r2993_p832
mc11_7TeV.*.madgraph_SM_GG_twostepCC_slepton_*.merge.NTUP_SUSY.e1145_a131_s1353_a145_r2993_p832
mc11_7TeV.*.madgraph_SM_SS_twostepCC_slepton_*.merge.NTUP_SUSY.e1145_a131_s1353_a145_r2993_p832
mc11_7TeV.*.madgraph_SM_SS_twostepCN_slepton_*.merge.NTUP_SUSY.e1145_a131_s1353_a145_r2993_p832

B. Packages

The following packages provided by the ATLAS combined performance and supersymmetry working groups are used for the event and object selection, partially applying small corrections to the simulation ex post:

```
atlasoff/PhysicsAnalysis/SUSYPhys/SUSYTools/tags/SUSYTools-00-00-61
atlasoff/PhysicsAnalysis/D3PDTools/RootCore/tags/RootCore-00-00-31
atlasoff/PhysicsAnalysis/AnalysisCommon/ObjectSelectorCore/tags/ObjectSelectorCore-00-00-09
atlasoff/PhysicsAnalysis/JetMissingEtID/JetSelectorTools/tags/JetSelectorTools-00-00-11
atlasoff/PhysicsAnalysis/MuonID/MuonIDAnalysis/MuonEfficiencyCorrections/tags/MuonEfficiencyCorrections-01-00-10
atlasoff/PhysicsAnalysis/MuonID/MuonIDAnalysis/MuonMomentumCorrections/tags/MuonMomentumCorrections-00-05-03
atlasoff/Reconstruction/egamma/egammaEvent/tags/egammaEvent-03-06-20
atlasoff/Reconstruction/egamma/egammaAnalysis/egammaAnalysisUtils/tags/egammaAnalysisUtils-00-02-76
atlasoff/PhysicsAnalysis/JetTagging/JetTagPerformanceCalibration/CalibrationDataInterface\
/tags/CalibrationDataInterface-00-01-02
atlasoff/DataQuality/GoodRunsLists/tags/GoodRunsLists-00-00-96
atlasoff/PhysicsAnalysis/AnalysisCommon/PileupReweighting/tags/PileupReweighting-00-02-02
atlasoff/Reconstruction/Jet/JetUncertainties/tags/JetUncertainties-00-03-05-01
atlasgrp/CombPerf/JetETMiss/JetCalibrationTools/ApplyJetCalibration/tags/ApplyJetCalibration-00-00-09
atlasoff/Reconstruction/Jet/JetResolution/tags/JetResolution-01-00-00
atlasoff/Reconstruction/MissingETUtility/tags/MissingETUtility-00-02-13
atlasoff/PhysicsAnalysis/AnalysisCommon/ReweightUtils/tags/ReweightUtils-00-02-06
atlasoff/Trigger/TrigAnalysis/TrigRootAnalysis/tags/TrigRootAnalysis-00-00-07
```

C. Signal Acceptance and Efficiency

Figures 95, 94 and 96 show the signal acceptance times efficiency of the 2-jet and 4-jet Signal Regions for the GMSB, mSUGRA as well as the Simplified Models. The acceptance times efficiency increases with higher sparticle masses and larger mass differences. In the GMSB scenario, a clear separation between the slepton and stau NLSP regions is visible. In the mSUGRA model, the separation between the two-body and the three-body region can be observed, leading to a larger acceptance times efficiency for the 2-jet (4-jet) Signal Region for large $m_{1/2}$ (m_0)[56]. In the Simplified Models, the acceptance times efficiency of the 2-jet Signal Region is usually larger for the squark pair production scenarios, while the 4-jet Signal Region performs better for gluino pair production scenarios.

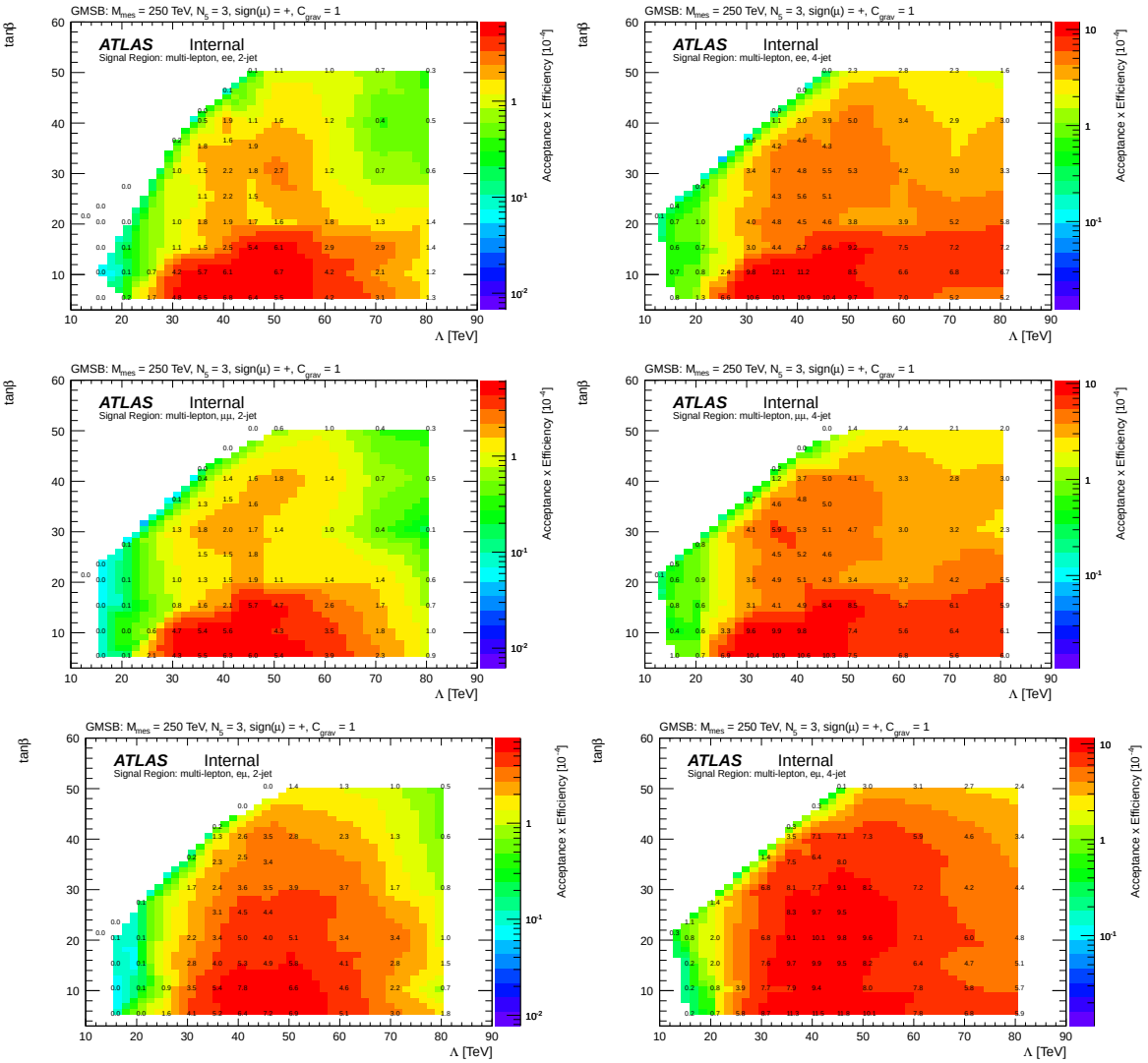

Figure 94: Acceptance times efficiency for the GMSB grid for the dielectron (top), dimuon (middle) and electron muon (bottom) selection in the 2-jet (left) and 4-jet (right) channel.

[56]The large efficiency in the high $m_{1/2}$ region for the four-jet Signal Regions is a consequence of the high E_T^{miss} cut which enhances the two-body region relative to the three-body region.

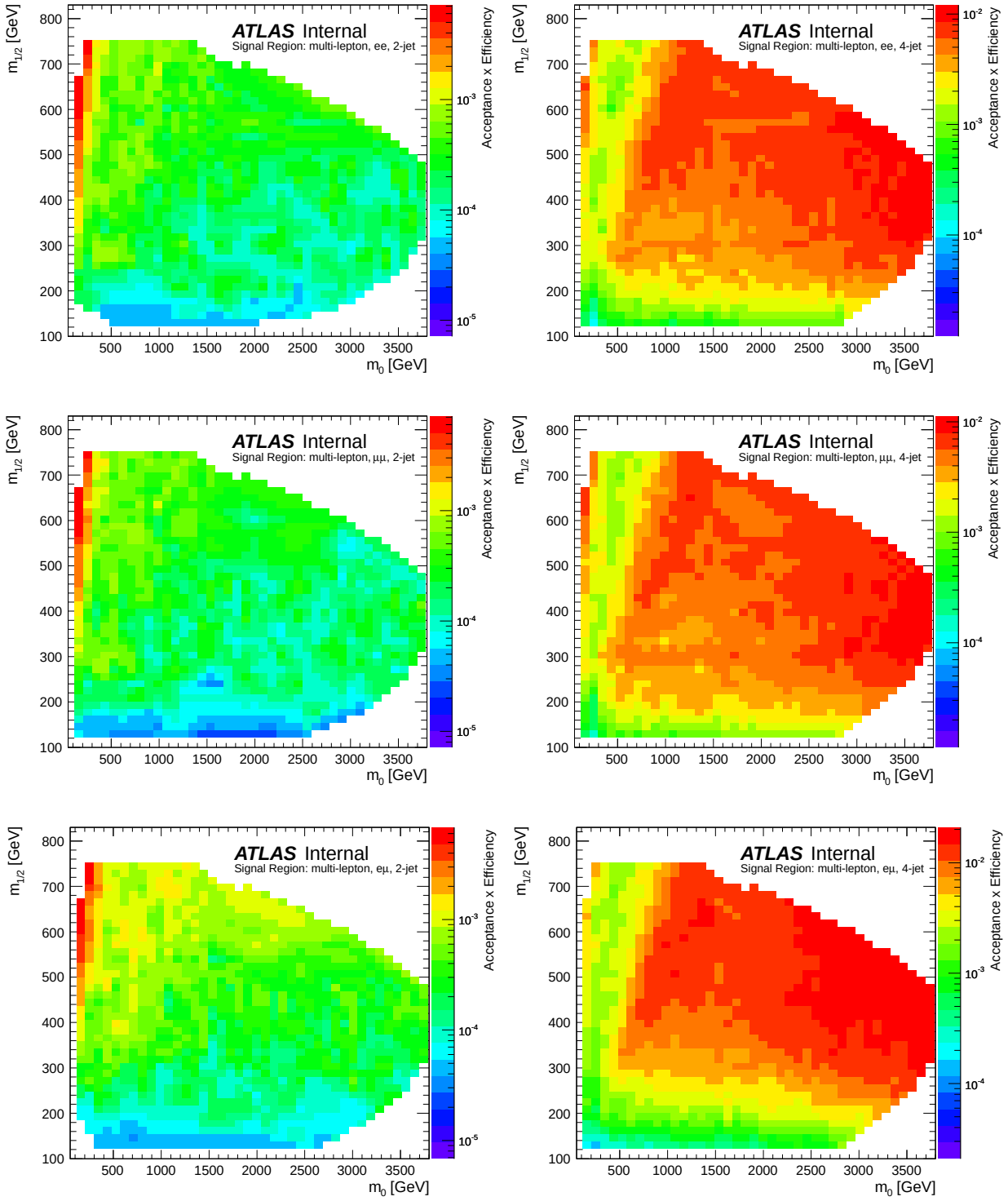

Figure 95: Acceptance times efficiency for the mSUGRA grid for the dielectron (top), dimuon (middle) and electron muon (bottom) selection in the 2-jet (left) and 4-jet (right) channel.

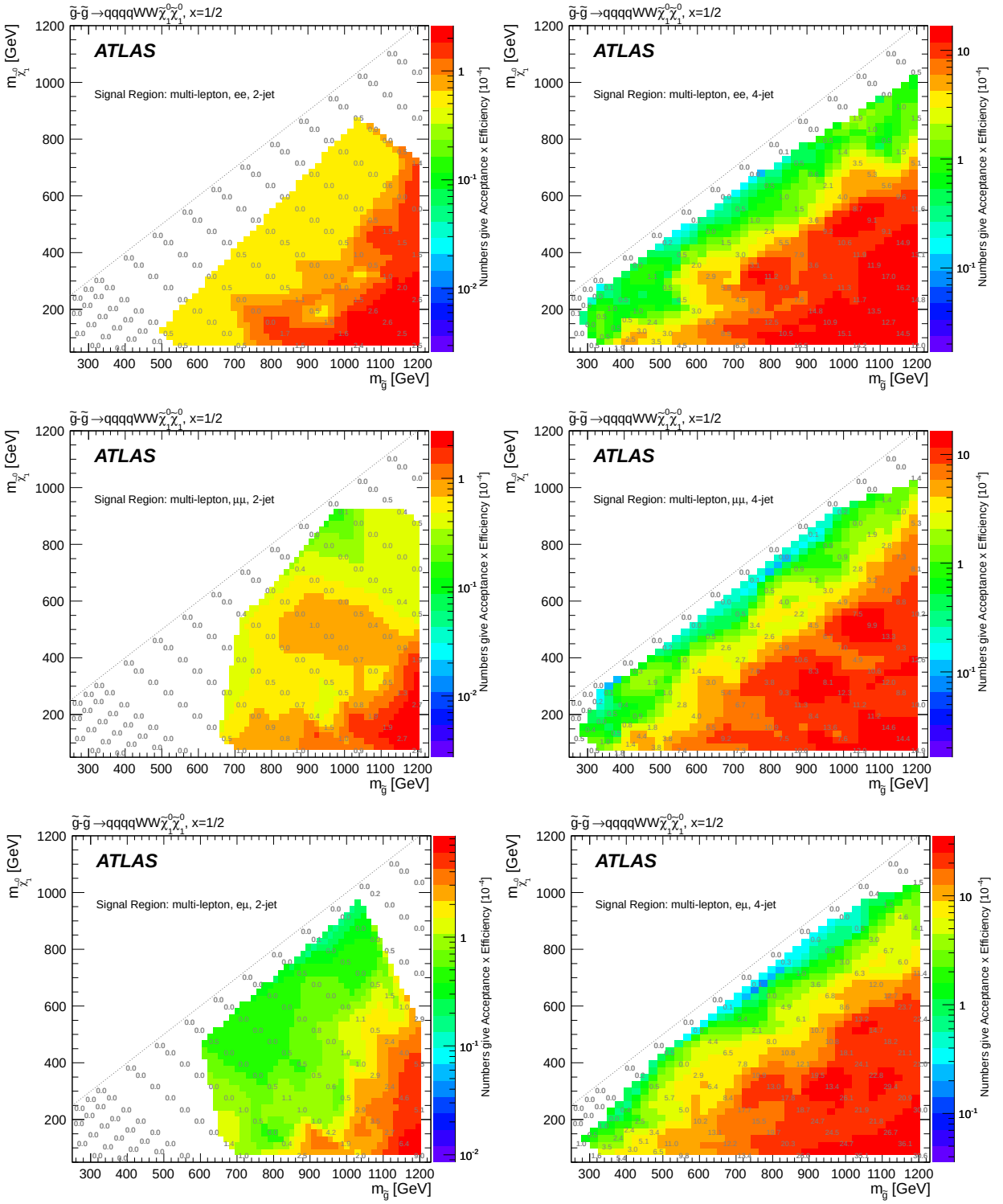

Figure 96: Acceptance times efficiency for the one step Simplified Model grid with gluino pair production and x = 1/2 for the dielectron (top), dimuon (middle) and electron muon (bottom) selection in the 2-jet (left) and 4-jet (right) channel.

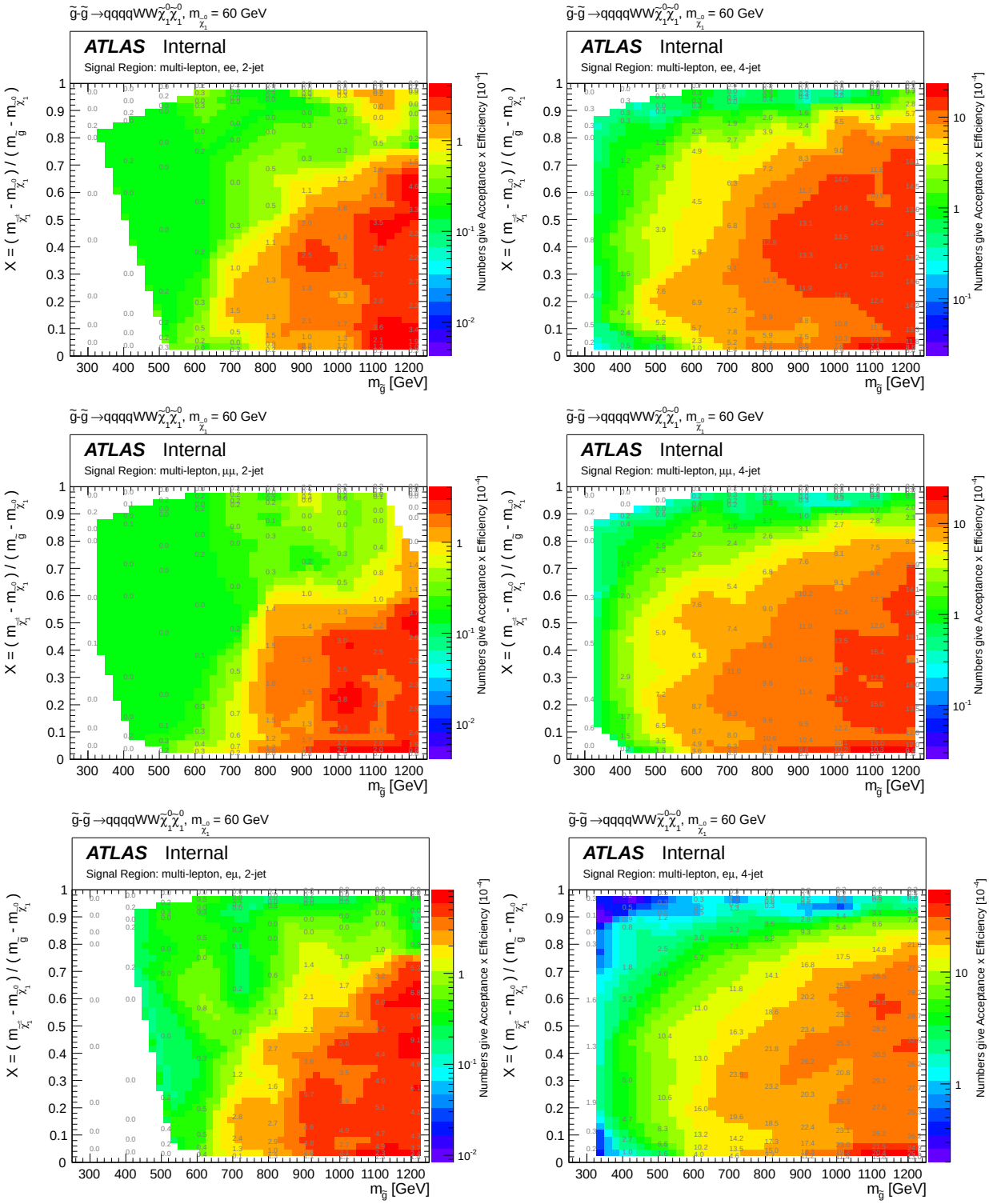

Figure 97: Acceptance times efficiency for the one step Simplified Model grid with gluino pair production and varied x for the dielectron (top), dimuon (middle) and electron muon (bottom) selection in the 2-jet (left) and 4-jet (right) channel.

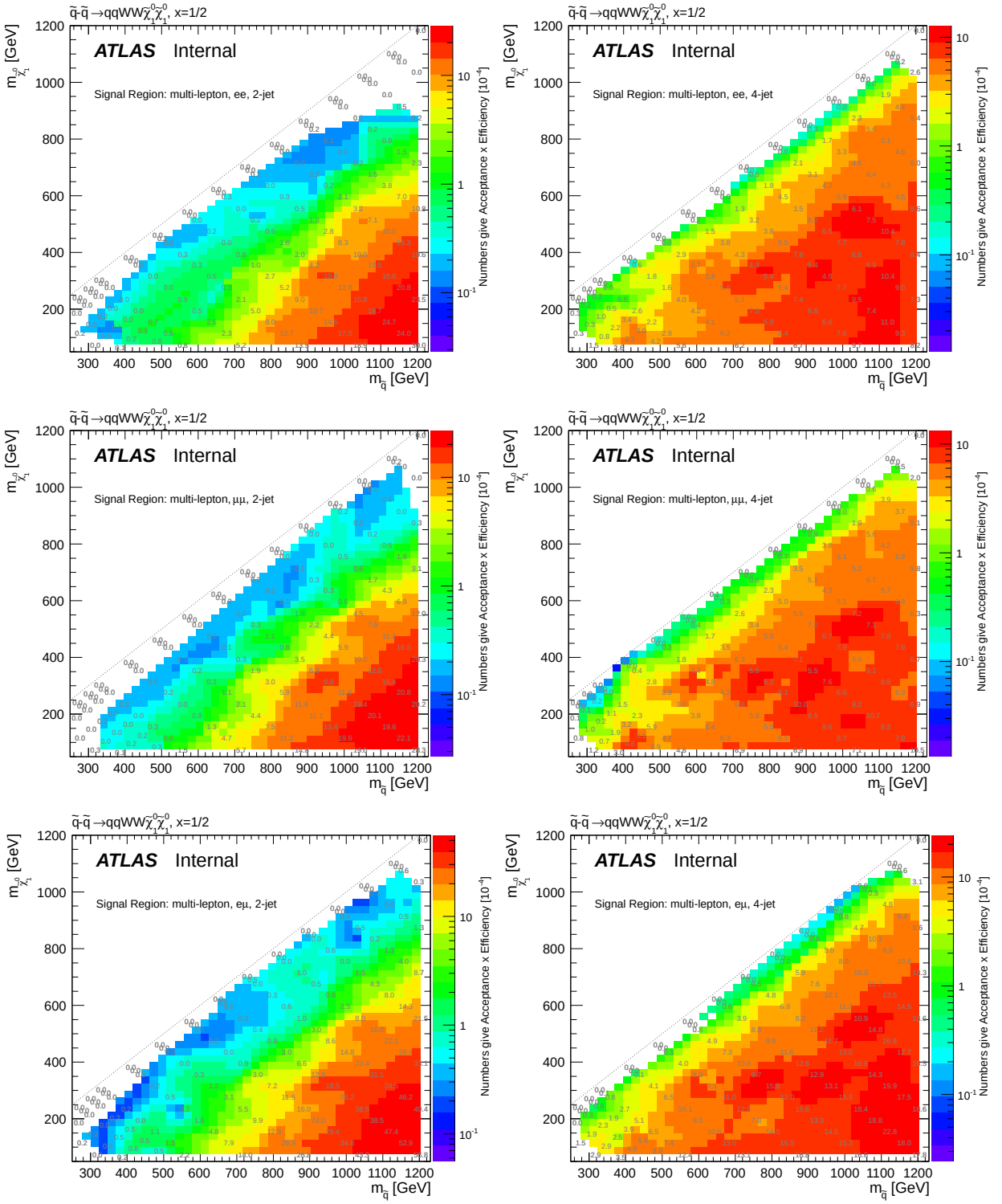

Figure 98: Acceptance times efficiency for the one step Simplified Model grid with squark pair production and x = 1/2 for the dielectron (top), dimuon (middle) and electron muon (bottom) selection in the 2-jet (left) and 4-jet (right) channel.

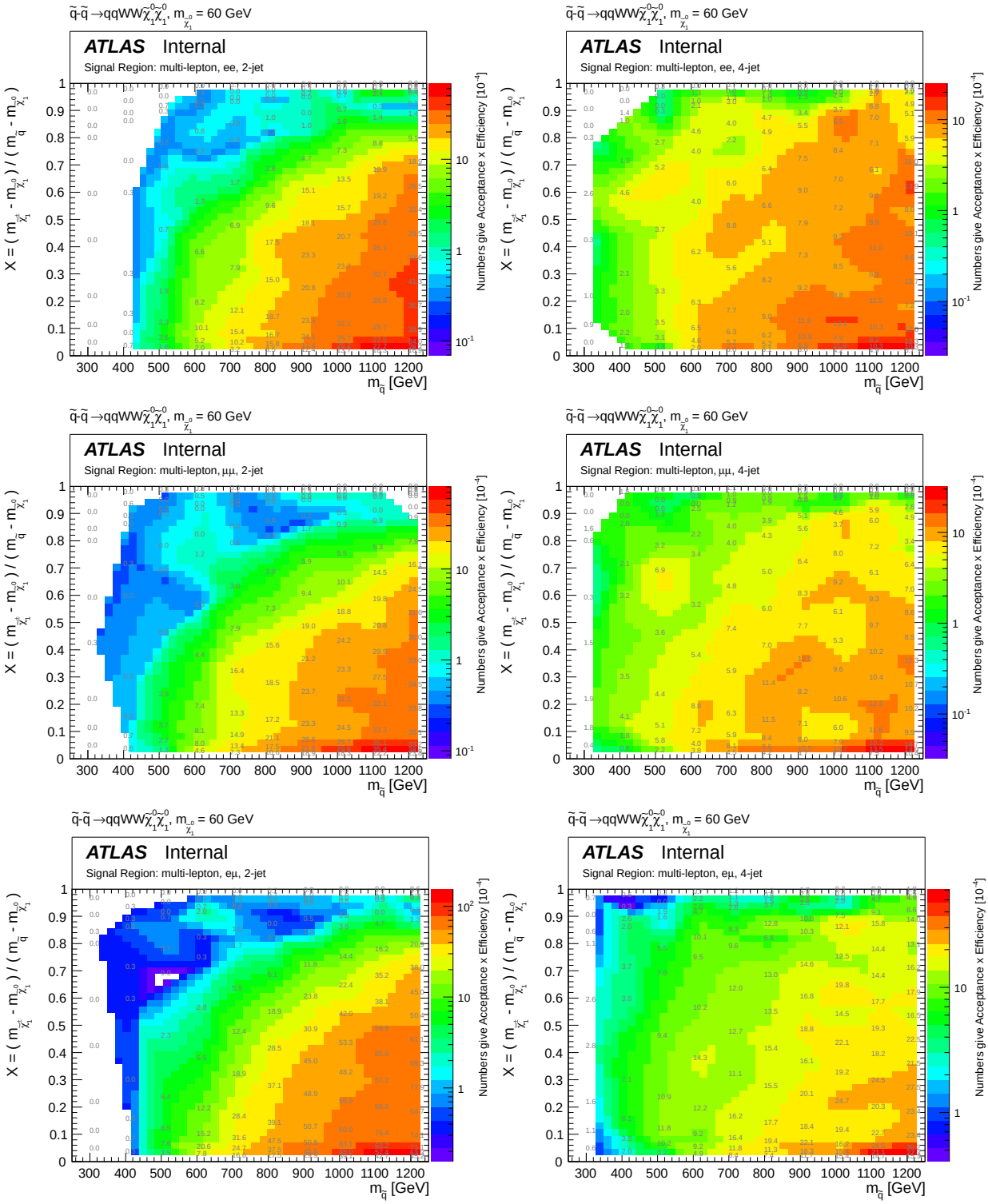

Figure 99: Acceptance times efficiency for the one step Simplified Model grid with squark pair production and varied x for the dielectron (top), dimuon (middle) and electron muon (bottom) selection in the 2-jet (left) and 4-jet (right) channel.

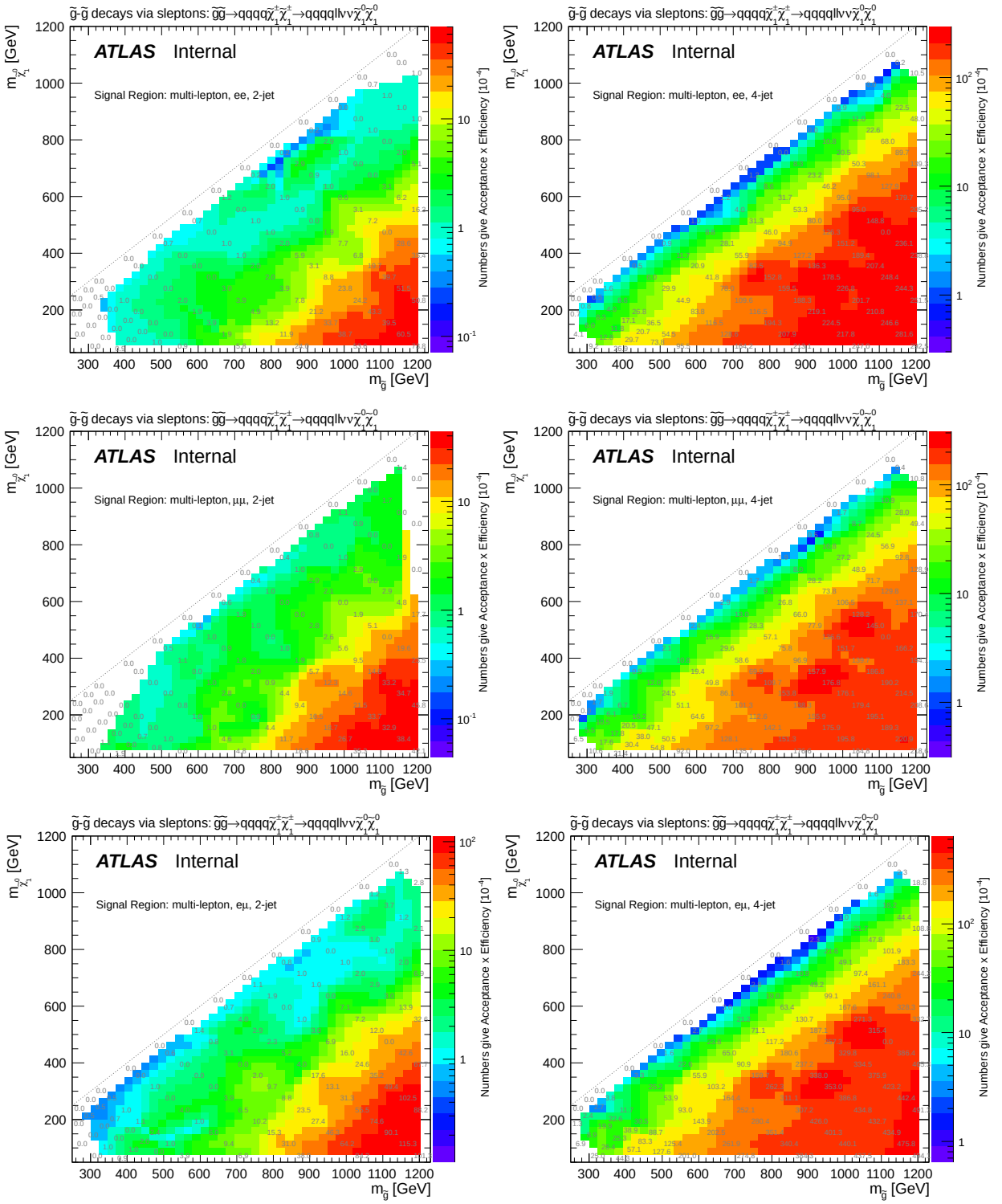

Figure 100: Acceptance times efficiency for the two step Simplified Model grid with gluino pair production and decays via sleptons for the dielectron (top), dimuon (middle) and electron muon (bottom) selection in the 2-jet (left) and 4-jet (right) channel.

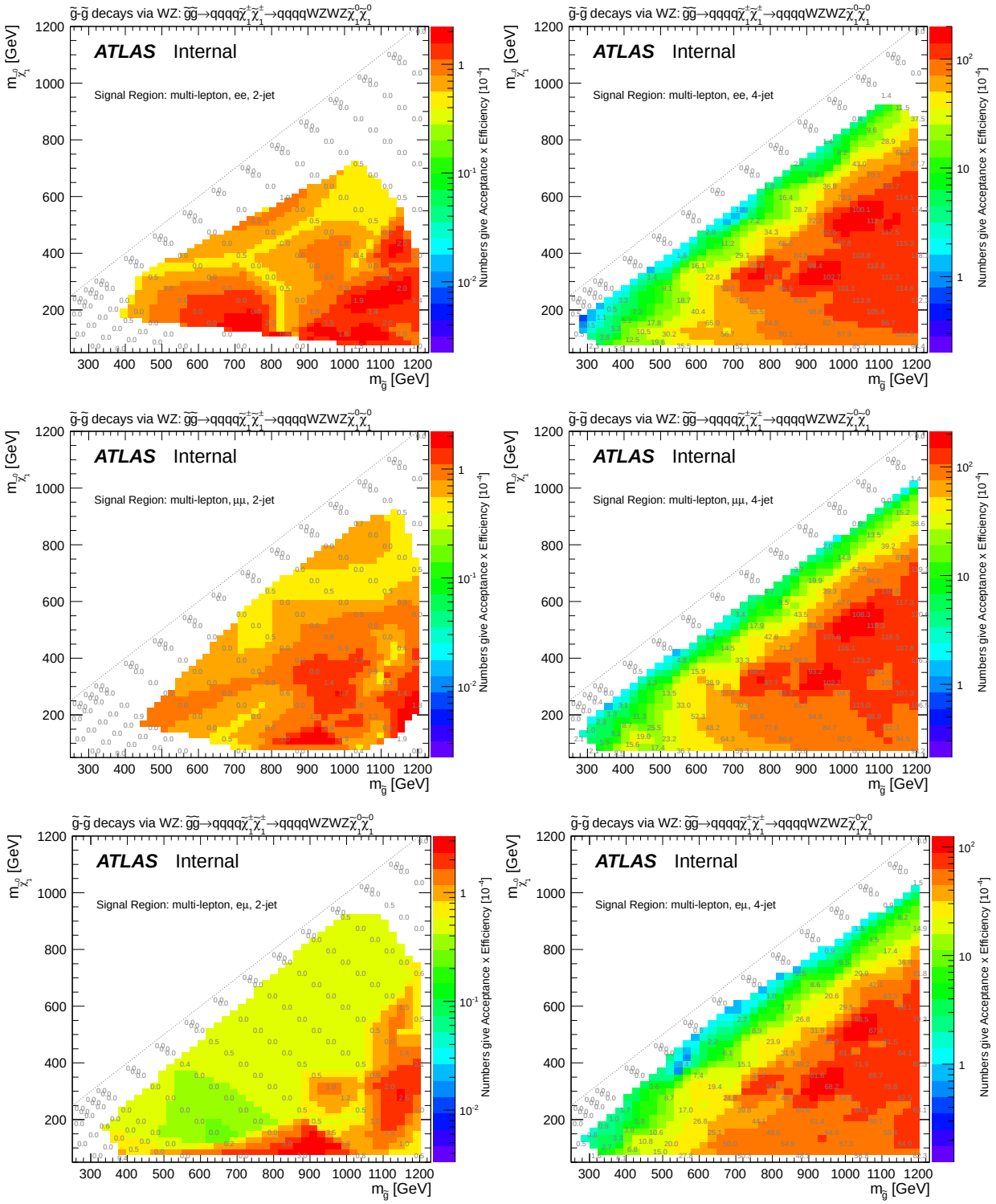

Figure 101: Acceptance times efficiency for the two step Simplified Model grid with gluino pair production and decays via W/Z for the dielectron (top), dimuon (middle) and electron muon (bottom) selection in the 2-jet (left) and 4-jet (right) channel.

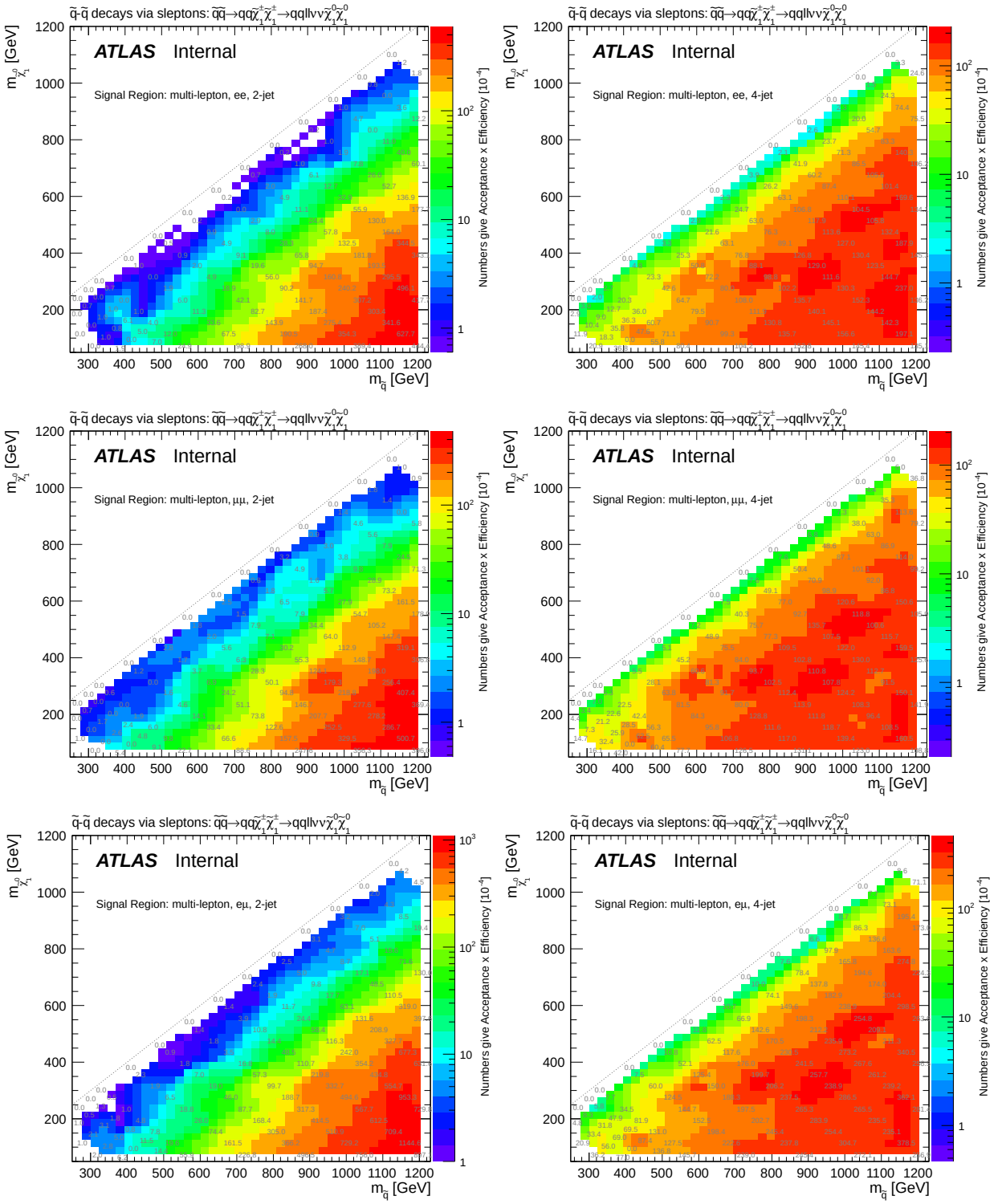

Figure 102: Acceptance times efficiency for the two step Simplified Model grid with squark pair production and decays via sleptons and two charginos for the dielectron (top), dimuon (middle) and electron muon (bottom) selection in the 2-jet (left) and 4-jet (right) channel.

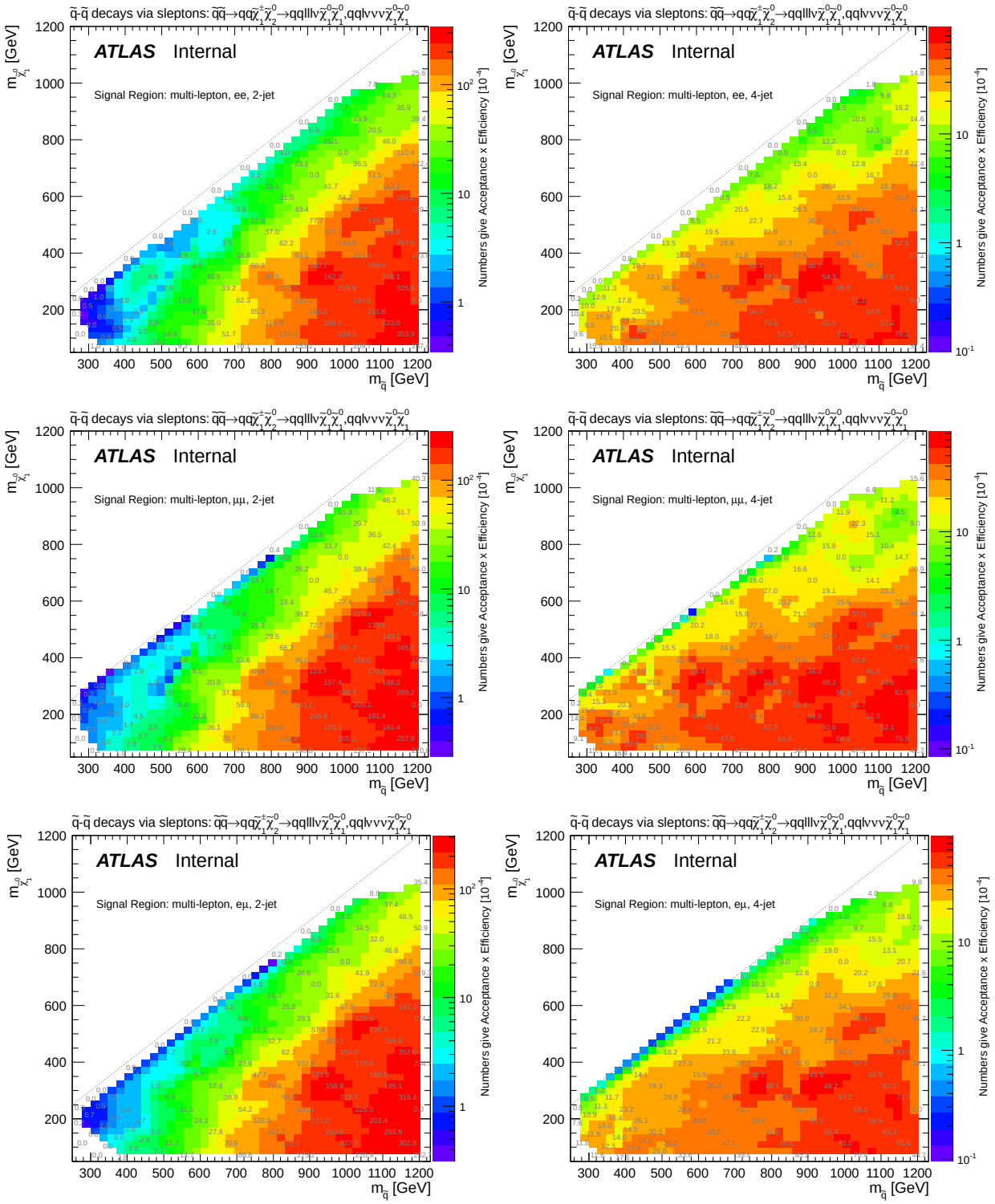

Figure 103: Acceptance times efficiency for the two step Simplified Model grid with squark pair production and decays via sleptons and chargino/neutralino for the dielectron (top), dimuon (middle) and electron muon (bottom) selection in the 2-jet (left) and 4-jet (right) channel.

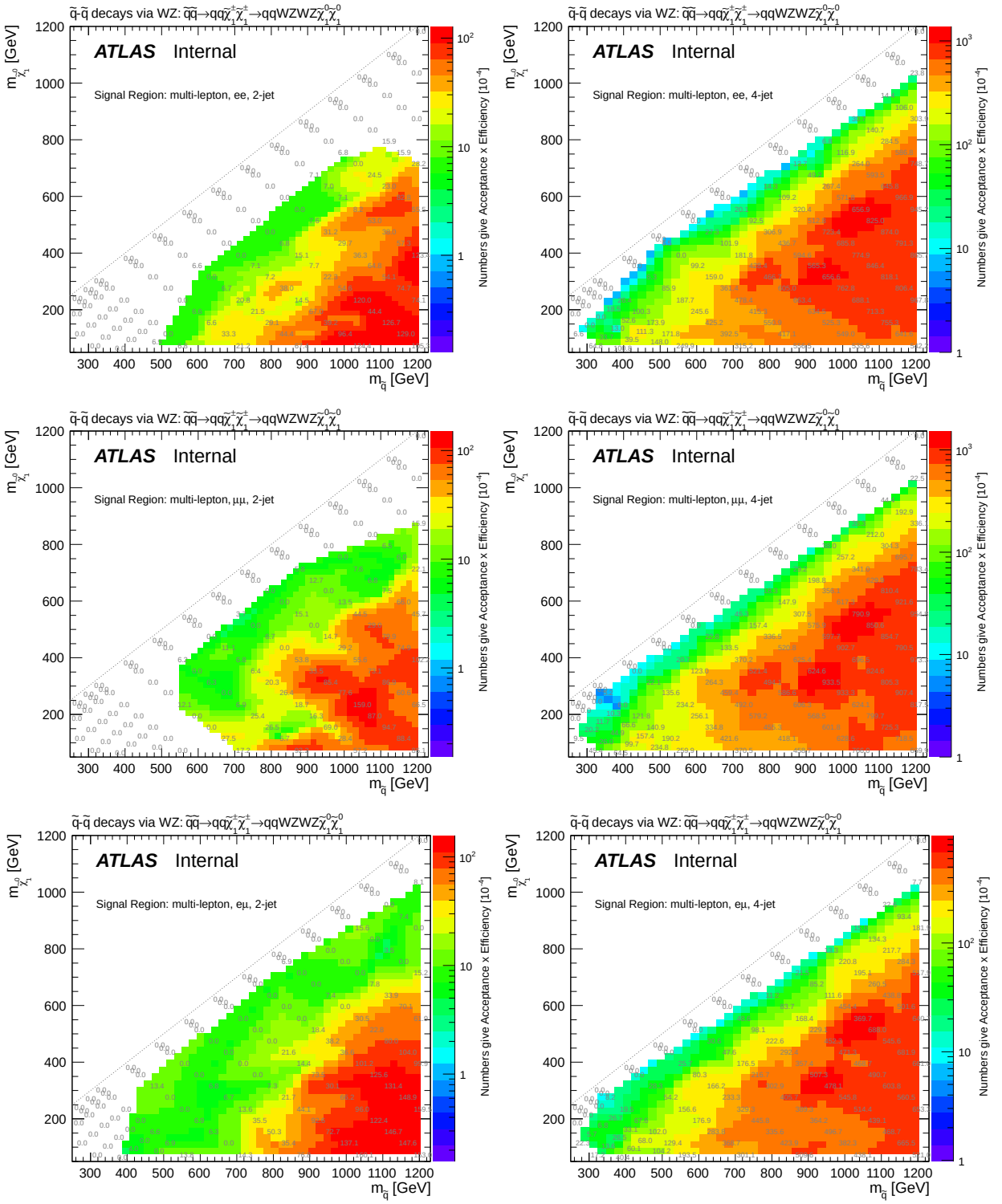

Figure 104: Acceptance times efficiency for the two step Simplified Model grid with squark pair production and decays via W/Z for the dielectron (top), dimuon (middle) and electron muon (bottom) selection in the 2-jet (left) and 4-jet (right) channel.

D. Fit Parameter Results

The following table contains a full set of fit results for the background-only fit:

Floating Parameter	FinalValue +/- Error
alpha_BT	8.2123e-01 +/- 2.77e-01
alpha_HF	1.1700e-01 +/- 4.59e-01
alpha_JHigh	-9.0297e-01 +/- 2.71e-01
alpha_JLow	-2.9170e-01 +/- 2.89e-01
alpha_JMedium	-5.6379e-01 +/- 3.60e-01
alpha_LESee	1.3750e-01 +/- 2.04e-01
alpha_LESel	1.6230e-01 +/- 4.88e-01
alpha_LESem	1.0827e-02 +/- 9.63e-01
alpha_LESmm	-1.0714e-02 +/- 9.79e-01
alpha_LESmu	9.2659e-03 +/- 1.14e+00
alpha_LESse	1.7247e-02 +/- 5.78e-01
alpha_LESsm	-1.2051e-02 +/- 9.93e-01
alpha_LEee	1.2590e+00 +/- 6.20e-01
alpha_LEel	-6.6297e-01 +/- 8.82e-01
alpha_LEem	-5.9210e-02 +/- 8.38e-01
alpha_LEmm	1.8984e-02 +/- 8.56e-01
alpha_LEmu	8.9295e-03 +/- 9.91e-01
alpha_LEse	-3.7047e-01 +/- 5.88e-01
alpha_LEsm	4.6735e-03 +/- 9.93e-01
alpha_LRIem	-1.1518e-02 +/- 9.47e-01
alpha_LRImm	-1.1050e-02 +/- 8.57e-01
alpha_LRImu	-4.2262e-02 +/- 1.01e+00
alpha_LRIsm	-2.7316e-02 +/- 9.15e-01
alpha_LRMem	-2.6651e-02 +/- 9.49e-01
alpha_LRMmm	3.9411e-02 +/- 9.21e-01
alpha_LRMmu	6.4819e-02 +/- 1.01e+00
alpha_LRMsm	-3.0665e-02 +/- 9.66e-01
alpha_MC	-8.6103e-01 +/- 4.68e-01
alpha_MP	2.8320e-01 +/- 4.81e-01
alpha_PtMinTop	5.6652e-03 +/- 1.76e-01
alpha_PtMinWZ	1.1400e+00 +/- 6.77e-01
alpha_QCDNorm_SVTEl_nJet	4.0307e-01 +/- 4.15e-01
alpha_QCDNorm_SVTMu_nJet	3.7979e-01 +/- 6.05e-01
alpha_QCDNorm_SVWEl_nJet	-1.3298e+00 +/- 8.10e-02
alpha_QCDNorm_SVWMu_nJet	-3.9108e-01 +/- 6.09e-01
alpha_QCDNorm_TREl_nJet	-7.6837e-01 +/- 6.47e-01
alpha_QCDNorm_TRMu_nJet	2.6128e-01 +/- 6.53e-01
alpha_QCDNorm_TRee_nJet	5.2791e-01 +/- 7.48e-01
alpha_QCDNorm_TRem_nJet	5.1741e-02 +/- 1.11e+00
alpha_QCDNorm_TRmm_nJet	1.1228e-01 +/- 1.25e+00
alpha_QCDNorm_WREl_nJet	1.3172e-01 +/- 2.41e-01
alpha_QCDNorm_WRMu_nJet	-2.8610e-01 +/- 8.92e-01

```
alpha_QCDNorm_ZRee_nJet    1.4336e-02 +/-  9.55e-01
alpha_QCDNorm_ZRmm_nJet    3.2123e-02 +/-  1.02e+00
          alpha_TEee    3.6007e-01 +/-  9.16e-01
          alpha_TEel   -2.7167e-01 +/-  9.41e-01
          alpha_TEem   -1.5103e-01 +/-  6.49e-01
          alpha_TEmm    4.5870e-01 +/-  5.36e-01
          alpha_TEmu    4.3290e-01 +/-  4.76e-01
     alpha_Zpt100GeV    2.1610e-01 +/-  6.07e-01
     alpha_Zpt150GeV    8.0396e-02 +/-  7.36e-01
     alpha_Zpt200GeV   -2.6990e-01 +/-  7.20e-01
      alpha_Zpt50GeV    1.2496e-01 +/-  6.99e-01
        alpha_err_BG   -4.7096e-02 +/-  9.72e-01
    alpha_err_WZ_Np0    1.1261e-02 +/-  9.56e-01
    alpha_err_WZ_Np1    2.8783e-01 +/-  1.81e-01
gamma_stat_SVTEl_nJet_bin_0    1.1592e+00 +/-  1.48e-01
gamma_stat_SVTEl_nJet_bin_1    9.3785e-01 +/-  9.28e-02
gamma_stat_SVTEl_nJet_bin_2    1.0599e+00 +/-  9.69e-02
gamma_stat_SVTEl_nJet_bin_3    1.0202e+00 +/-  1.33e-01
gamma_stat_SVTEl_nJet_bin_4    9.2554e-01 +/-  1.39e-01
gamma_stat_SVTEl_nJet_bin_5    1.0715e+00 +/-  3.21e-01
gamma_stat_SVTMu_nJet_bin_0    1.0117e+00 +/-  9.76e-02
gamma_stat_SVTMu_nJet_bin_1    9.5312e-01 +/-  8.09e-02
gamma_stat_SVTMu_nJet_bin_2    1.0146e+00 +/-  7.87e-02
gamma_stat_SVTMu_nJet_bin_3    1.0510e+00 +/-  7.29e-02
gamma_stat_SVTMu_nJet_bin_4    1.0045e+00 +/-  1.52e-01
gamma_stat_SVTMu_nJet_bin_5    1.0546e+00 +/-  2.74e-01
gamma_stat_SVWEl_nJet_bin_1    9.6839e-01 +/-  4.70e-02
gamma_stat_SVWEl_nJet_bin_2    9.3503e-01 +/-  7.01e-02
gamma_stat_SVWEl_nJet_bin_3    9.8481e-01 +/-  1.04e-01
gamma_stat_SVWEl_nJet_bin_4    1.0877e+00 +/-  1.64e-01
gamma_stat_SVWEl_nJet_bin_5    9.9079e-01 +/-  2.12e-01
gamma_stat_SVWMu_nJet_bin_2    9.7136e-01 +/-  6.05e-02
gamma_stat_SVWMu_nJet_bin_3    9.4722e-01 +/-  9.02e-02
gamma_stat_SVWMu_nJet_bin_4    1.0650e+00 +/-  1.52e-01
gamma_stat_SVWMu_nJet_bin_5    1.0805e+00 +/-  2.25e-01
gamma_stat_TREl_nJet_bin_5    1.0076e+00 +/-  5.31e-02
gamma_stat_TREl_nJet_bin_6    1.0293e+00 +/-  9.92e-02
gamma_stat_TRMu_nJet_bin_6    9.9807e-01 +/-  7.13e-02
gamma_stat_TRee_nJet_bin_4    1.0334e+00 +/-  7.43e-02
gamma_stat_TRee_nJet_bin_5    9.5275e-01 +/-  1.64e-01
gamma_stat_TRee_nJet_bin_6    9.7862e-01 +/-  2.58e-01
gamma_stat_TRee_nJet_bin_7    9.4746e-01 +/-  6.74e-01
gamma_stat_TRem_nJet_bin_4    1.0219e+00 +/-  4.81e-02
gamma_stat_TRem_nJet_bin_5    9.6577e-01 +/-  1.10e-01
gamma_stat_TRem_nJet_bin_6    1.0326e+00 +/-  2.46e-01
gamma_stat_TRem_nJet_bin_7    9.6471e-01 +/-  4.86e-01
gamma_stat_TRmm_nJet_bin_4    1.0506e+00 +/-  6.34e-02
gamma_stat_TRmm_nJet_bin_5    9.8600e-01 +/-  1.49e-01
```

```
gamma_stat_TRmm_nJet_bin_6    1.0560e+00 +/-  3.05e-01
gamma_stat_TRmm_nJet_bin_7    1.6062e+00 +/-  6.20e-01
gamma_stat_WREl_nJet_bin_4    9.3416e-01 +/-  5.87e-02
gamma_stat_WREl_nJet_bin_5    9.9502e-01 +/-  4.92e-02
gamma_stat_WREl_nJet_bin_6    1.0515e+00 +/-  8.42e-02
gamma_stat_WRMu_nJet_bin_5    1.0042e+00 +/-  4.84e-02
gamma_stat_WRMu_nJet_bin_6    9.9940e-01 +/-  8.26e-02
gamma_stat_ZRee_nJet_bin_5    1.0373e+00 +/-  9.60e-02
gamma_stat_ZRee_nJet_bin_6    9.6586e-01 +/-  1.77e-01
gamma_stat_ZRee_nJet_bin_7    8.8978e-01 +/-  3.96e-01
gamma_stat_ZRmm_nJet_bin_5    1.0445e+00 +/-  7.52e-02
gamma_stat_ZRmm_nJet_bin_6    1.0280e+00 +/-  1.76e-01
gamma_stat_ZRmm_nJet_bin_7    1.2097e+00 +/-  3.04e-01
          mu_Top_Np0    1.2677e+00 +/-  9.95e-02
          mu_Top_Np1    9.8943e-01 +/-  5.91e-02
          mu_Top_Np2    1.0716e+00 +/-  8.62e-02
          mu_Top_Np3    9.2026e-01 +/-  7.59e-02
           mu_WZ_Np2    1.1416e+00 +/-  7.90e-02
           mu_WZ_Np3    1.0677e+00 +/-  5.99e-02
           mu_WZ_Np4    1.0195e+00 +/-  6.25e-02
           mu_WZ_Np5    1.2441e+00 +/-  1.28e-01
```

The following table contains a full set of fit results for an exemplary mSUGRA exclusion fit for the model with $(m_0, m_{1/2}) = (3060\ \text{GeV}, 300\ \text{GeV})$ using the 10 hard single lepton and dilepton SRs. It can be seen that some of the parameters acquire different values compared to the background-only fit configuration, while no significant changes occur for the main free normalization parameters. A further investigation of the fit parameter dependence on the signal model under consideration is contained in appendix E.

```
 Floating Parameter    FinalValue +/-  Error
--------------------  --------------------------
                Lumi    1.0000e+00 +/-  3.68e-02
           alpha_BT    6.1716e-01 +/-  2.01e-01
           alpha_HF   -1.8372e-01 +/-  4.06e-01
         alpha_JHigh   -5.8397e-01 +/-  1.68e-01
          alpha_JLow    1.7754e-02 +/-  1.06e-01
       alpha_JMedium   -4.1112e-01 +/-  2.75e-01
          alpha_JSig   -1.4920e-03 +/-  1.01e+00
         alpha_LESee    1.4343e-01 +/-  1.89e-01
         alpha_LESel    4.2309e-02 +/-  1.32e-01
         alpha_LESem    2.3759e-03 +/-  9.44e-01
         alpha_LESmm   -1.2616e-02 +/-  9.77e-01
         alpha_LESmu    9.6822e-03 +/-  9.78e-01
         alpha_LESse    1.4730e-02 +/-  9.53e-01
         alpha_LESsm   -1.2249e-02 +/-  9.92e-01
          alpha_LEee    1.3428e+00 +/-  5.69e-01
          alpha_LEel   -8.2052e-01 +/-  8.70e-01
          alpha_LEem    1.5764e-02 +/-  9.52e-01
          alpha_LEmm    2.2169e-02 +/-  7.98e-01
```

```
           alpha_LEmu    9.6580e-03 +/-  9.34e-01
           alpha_LEse   -3.7166e-01 +/-  5.85e-01
           alpha_LEsm    5.0370e-03 +/-  9.93e-01
          alpha_LRIem   -1.1064e-02 +/-  9.41e-01
          alpha_LRImm   -1.2561e-02 +/-  8.13e-01
          alpha_LRImu   -4.6099e-02 +/-  8.97e-01
          alpha_LRIsm   -2.8187e-02 +/-  9.78e-01
          alpha_LRMem   -3.1488e-02 +/-  9.49e-01
          alpha_LRMmm    3.9314e-02 +/-  9.03e-01
          alpha_LRMmu    7.9642e-02 +/-  1.05e+00
          alpha_LRMsm   -3.9153e-02 +/-  9.59e-01
             alpha_MC   -9.5757e-01 +/-  4.38e-01
             alpha_MP    4.4960e-02 +/-  1.78e-01
       alpha_PtMinTop    1.6802e-02 +/-  2.10e-01
     alpha_PtMinTopSR    6.9747e-02 +/-  8.56e-01
        alpha_PtMinWZ    1.0601e+00 +/-  6.76e-01
      alpha_PtMinWZSR   -2.2760e-01 +/-  6.63e-01
alpha_QCDNorm_S2em_meffInc    1.0325e-02 +/-  9.88e-01
alpha_QCDNorm_S3El_meffInc   -3.0757e-01 +/-  9.15e-01
alpha_QCDNorm_S3Mu_meffInc    2.3426e-01 +/-  9.87e-01
alpha_QCDNorm_S4El_meffInc    6.9537e-02 +/-  9.05e-01
alpha_QCDNorm_S4ee_meffInc   -8.9678e-02 +/-  8.53e-01
alpha_QCDNorm_S4em_meffInc   -1.2372e-02 +/-  9.38e-01
alpha_QCDNorm_S4mm_meffInc    3.7986e-03 +/-  1.01e+00
alpha_QCDNorm_SVTEl_nJet    4.0287e-01 +/-  4.12e-01
alpha_QCDNorm_SVTMu_nJet    2.6420e-01 +/-  5.64e-01
alpha_QCDNorm_SVWEl_nJet   -1.3652e+00 +/-  1.68e-02
alpha_QCDNorm_SVWMu_nJet   -4.6585e-01 +/-  6.07e-01
alpha_QCDNorm_TREl_nJet   -7.5689e-01 +/-  6.43e-01
alpha_QCDNorm_TRMu_nJet    9.9552e-02 +/-  5.87e-01
alpha_QCDNorm_TRee_nJet    6.9443e-01 +/-  7.20e-01
alpha_QCDNorm_TRem_nJet    2.6732e-01 +/-  9.87e-01
alpha_QCDNorm_TRmm_nJet    1.5028e-01 +/-  1.27e+00
alpha_QCDNorm_WREl_nJet    1.3121e-01 +/-  1.70e-01
alpha_QCDNorm_WRMu_nJet   -1.8093e-01 +/-  6.90e-01
alpha_QCDNorm_ZRee_nJet    2.2489e-02 +/-  9.16e-01
alpha_QCDNorm_ZRmm_nJet    2.8327e-02 +/-  9.93e-01
       alpha_SigXSec    1.4828e-03 +/-  9.00e-01
          alpha_TEee    3.7415e-01 +/-  8.03e-01
          alpha_TEel   -3.3679e-01 +/-  9.02e-01
          alpha_TEem    4.5806e-02 +/-  6.14e-01
          alpha_TEmm    5.9874e-01 +/-  4.85e-01
          alpha_TEmu    4.6970e-01 +/-  4.38e-01
     alpha_Zpt100GeV    1.9573e-01 +/-  5.94e-01
     alpha_Zpt150GeV    1.8136e-01 +/-  6.65e-01
     alpha_Zpt200GeV   -2.1015e-01 +/-  5.89e-01
      alpha_Zpt50GeV    9.7869e-02 +/-  6.59e-01
        alpha_err_BG   -6.1572e-02 +/-  8.16e-01
```

```
    alpha_err_WZ_Np0    9.9890e-03 +/-  1.19e+00
    alpha_err_WZ_Np1    4.7006e-01 +/-  2.69e-01
        alpha_hadTop   -6.1200e-02 +/-  1.22e-01
         alpha_hadWZ    2.2785e-03 +/-  1.35e-01
gamma_stat_S2ee_meffInc_bin_2    9.6831e-01 +/-  9.47e-01
gamma_stat_S2ee_meffInc_bin_3    8.8757e-01 +/-  9.06e-01
gamma_stat_S2ee_meffInc_bin_4    9.0378e-01 +/-  6.52e-01
gamma_stat_S2em_meffInc_bin_1    9.5753e-01 +/-  6.79e-01
gamma_stat_S2em_meffInc_bin_2    9.2854e-01 +/-  4.91e-01
gamma_stat_S2em_meffInc_bin_3    9.2806e-01 +/-  5.45e-01
gamma_stat_S2em_meffInc_bin_4    1.1330e+00 +/-  4.02e-01
gamma_stat_S2mm_meffInc_bin_1    9.5485e-01 +/-  6.76e-01
gamma_stat_S2mm_meffInc_bin_2    9.7035e-01 +/-  5.41e-01
gamma_stat_S2mm_meffInc_bin_3    8.9966e-01 +/-  7.87e-01
gamma_stat_S2mm_meffInc_bin_4    9.6351e-01 +/-  5.04e-01
gamma_stat_S3El_meffInc_bin_0    8.6374e-01 +/-  2.67e-01
gamma_stat_S3El_meffInc_bin_1    9.6756e-01 +/-  1.03e-01
gamma_stat_S3El_meffInc_bin_2    9.7715e-01 +/-  1.10e-01
gamma_stat_S3El_meffInc_bin_3    9.5866e-01 +/-  1.82e-01
gamma_stat_S3El_meffInc_bin_4    7.5094e-01 +/-  3.30e-01
gamma_stat_S3El_meffInc_bin_5    1.1025e+00 +/-  2.59e-01
gamma_stat_S3Mu_meffInc_bin_0    9.7263e-01 +/-  3.00e-01
gamma_stat_S3Mu_meffInc_bin_1    1.0184e+00 +/-  9.39e-02
gamma_stat_S3Mu_meffInc_bin_2    1.0434e+00 +/-  9.65e-02
gamma_stat_S3Mu_meffInc_bin_3    1.0508e+00 +/-  1.64e-01
gamma_stat_S3Mu_meffInc_bin_4    9.6592e-01 +/-  2.69e-01
gamma_stat_S3Mu_meffInc_bin_5    7.6082e-01 +/-  3.83e-01
gamma_stat_S4El_meffInc_bin_0    1.0780e+00 +/-  3.98e-01
gamma_stat_S4El_meffInc_bin_1    1.0017e+00 +/-  1.61e-01
gamma_stat_S4El_meffInc_bin_2    9.5191e-01 +/-  2.77e-01
gamma_stat_S4El_meffInc_bin_3    1.0035e+00 +/-  1.81e-01
gamma_stat_S4Mu_meffInc_bin_0    9.8031e-01 +/-  2.79e-01
gamma_stat_S4Mu_meffInc_bin_1    1.0450e+00 +/-  1.70e-01
gamma_stat_S4Mu_meffInc_bin_2    9.9514e-01 +/-  1.48e-01
gamma_stat_S4Mu_meffInc_bin_3    9.9213e-01 +/-  1.14e-01
gamma_stat_S4ee_meffInc_bin_0    1.0288e+00 +/-  9.45e-02
gamma_stat_S4ee_meffInc_bin_1    9.7751e-01 +/-  1.05e-01
gamma_stat_S4ee_meffInc_bin_2    9.7659e-01 +/-  1.40e-01
gamma_stat_S4ee_meffInc_bin_3    9.8620e-01 +/-  1.82e-01
gamma_stat_S4ee_meffInc_bin_4    9.9022e-01 +/-  2.23e-01
gamma_stat_S4em_meffInc_bin_0    9.9908e-01 +/-  6.17e-02
gamma_stat_S4em_meffInc_bin_1    9.9320e-01 +/-  7.24e-02
gamma_stat_S4em_meffInc_bin_2    9.8899e-01 +/-  1.03e-01
gamma_stat_S4em_meffInc_bin_3    1.0005e+00 +/-  1.53e-01
gamma_stat_S4em_meffInc_bin_4    1.0141e+00 +/-  1.60e-01
gamma_stat_S4mm_meffInc_bin_0    1.0062e+00 +/-  7.37e-02
gamma_stat_S4mm_meffInc_bin_1    1.0104e+00 +/-  1.03e-01
gamma_stat_S4mm_meffInc_bin_2    9.7853e-01 +/-  1.29e-01
```

```
gamma_stat_S4mm_meffInc_bin_3    1.0115e+00 +/-  1.66e-01
gamma_stat_S4mm_meffInc_bin_4    9.8487e-01 +/-  2.32e-01
gamma_stat_SVTEl_nJet_bin_0    1.2096e+00 +/-  1.45e-01
gamma_stat_SVTEl_nJet_bin_1    9.3453e-01 +/-  9.13e-02
gamma_stat_SVTEl_nJet_bin_2    1.0608e+00 +/-  9.45e-02
gamma_stat_SVTEl_nJet_bin_3    1.0080e+00 +/-  1.32e-01
gamma_stat_SVTEl_nJet_bin_4    9.2429e-01 +/-  1.39e-01
gamma_stat_SVTEl_nJet_bin_5    1.0614e+00 +/-  3.18e-01
gamma_stat_SVTMu_nJet_bin_0    1.0177e+00 +/-  9.56e-02
gamma_stat_SVTMu_nJet_bin_1    9.4906e-01 +/-  7.84e-02
gamma_stat_SVTMu_nJet_bin_2    1.0136e+00 +/-  7.76e-02
gamma_stat_SVTMu_nJet_bin_3    1.0453e+00 +/-  7.32e-02
gamma_stat_SVTMu_nJet_bin_4    1.0062e+00 +/-  1.50e-01
gamma_stat_SVTMu_nJet_bin_5    1.0435e+00 +/-  2.69e-01
gamma_stat_SVWEl_nJet_bin_1    9.6470e-01 +/-  4.71e-02
gamma_stat_SVWEl_nJet_bin_2    9.2632e-01 +/-  7.12e-02
gamma_stat_SVWEl_nJet_bin_3    9.7688e-01 +/-  1.04e-01
gamma_stat_SVWEl_nJet_bin_4    1.0836e+00 +/-  1.66e-01
gamma_stat_SVWEl_nJet_bin_5    9.8652e-01 +/-  2.12e-01
gamma_stat_SVWMu_nJet_bin_2    9.6849e-01 +/-  5.93e-02
gamma_stat_SVWMu_nJet_bin_3    9.3858e-01 +/-  8.98e-02
gamma_stat_SVWMu_nJet_bin_4    1.0515e+00 +/-  1.51e-01
gamma_stat_SVWMu_nJet_bin_5    1.0872e+00 +/-  2.25e-01
gamma_stat_TREl_nJet_bin_5    1.0060e+00 +/-  5.31e-02
gamma_stat_TREl_nJet_bin_6    1.0286e+00 +/-  9.72e-02
gamma_stat_TRMu_nJet_bin_6    9.9850e-01 +/-  7.06e-02
gamma_stat_TRee_nJet_bin_4    1.0334e+00 +/-  7.38e-02
gamma_stat_TRee_nJet_bin_5    9.5317e-01 +/-  1.63e-01
gamma_stat_TRee_nJet_bin_6    9.7189e-01 +/-  2.57e-01
gamma_stat_TRee_nJet_bin_7    9.6393e-01 +/-  5.82e-01
gamma_stat_TRem_nJet_bin_4    1.0223e+00 +/-  4.80e-02
gamma_stat_TRem_nJet_bin_5    9.6581e-01 +/-  1.09e-01
gamma_stat_TRem_nJet_bin_6    1.0256e+00 +/-  2.20e-01
gamma_stat_TRem_nJet_bin_7    9.7829e-01 +/-  3.90e-01
gamma_stat_TRmm_nJet_bin_4    1.0513e+00 +/-  6.34e-02
gamma_stat_TRmm_nJet_bin_5    9.8643e-01 +/-  1.46e-01
gamma_stat_TRmm_nJet_bin_6    1.0426e+00 +/-  2.60e-01
gamma_stat_TRmm_nJet_bin_7    1.6056e+00 +/-  6.22e-01
gamma_stat_WREl_nJet_bin_4    9.3146e-01 +/-  5.80e-02
gamma_stat_WREl_nJet_bin_5    9.9431e-01 +/-  4.91e-02
gamma_stat_WREl_nJet_bin_6    1.0496e+00 +/-  8.33e-02
gamma_stat_WRMu_nJet_bin_5    1.0057e+00 +/-  4.82e-02
gamma_stat_WRMu_nJet_bin_6    9.9955e-01 +/-  8.14e-02
gamma_stat_ZRee_nJet_bin_5    1.0393e+00 +/-  9.57e-02
gamma_stat_ZRee_nJet_bin_6    9.6808e-01 +/-  1.77e-01
gamma_stat_ZRee_nJet_bin_7    9.0632e-01 +/-  3.72e-01
gamma_stat_ZRmm_nJet_bin_5    1.0443e+00 +/-  7.51e-02
gamma_stat_ZRmm_nJet_bin_6    1.0232e+00 +/-  1.73e-01
```

```
gamma_stat_ZRmm_nJet_bin_7    1.2075e+00 +/-  3.04e-01
              mu_SIG    3.7596e-08 +/-  1.58e-01
          mu_Top_Np0    1.2305e+00 +/-  9.07e-02
          mu_Top_Np1    9.7231e-01 +/-  5.63e-02
          mu_Top_Np2    1.0398e+00 +/-  6.81e-02
          mu_Top_Np3    8.4885e-01 +/-  4.02e-02
           mu_WZ_Np2    1.1532e+00 +/-  6.08e-02
           mu_WZ_Np3    1.0308e+00 +/-  4.14e-02
           mu_WZ_Np4    9.8793e-01 +/-  6.61e-02
           mu_WZ_Np5    1.1458e+00 +/-  7.46e-02
```

D.1. Correlation Matrix

Figure 105 contains the full correlation matrix between all the fit parameters as discussed in chapter 11.1.

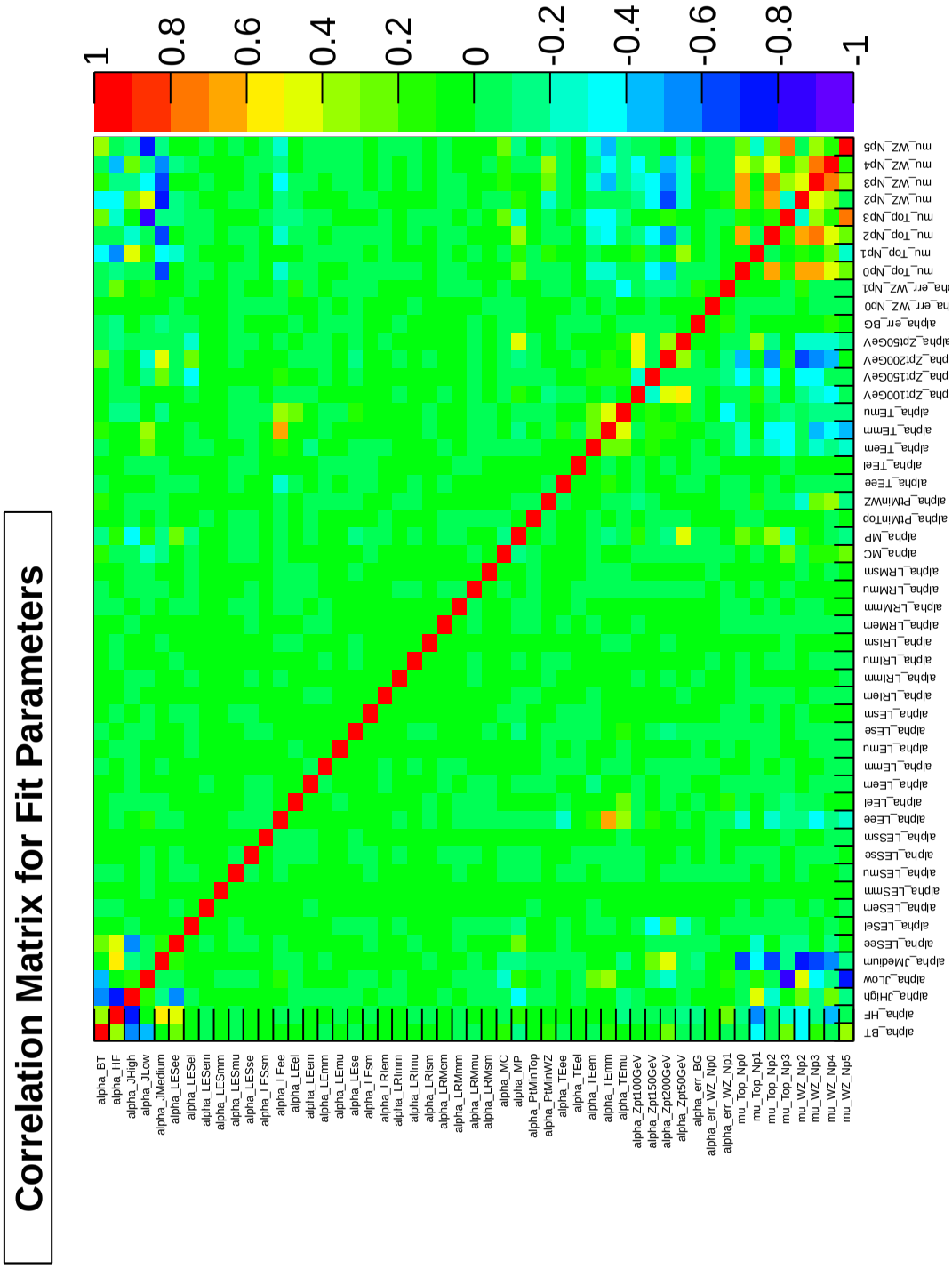

Figure 105: Correlation matrix of the fitparameters in the background-only fit. Not shown are the uncertainties from the fake estimate as well as those describing the limited Monte Carlo statistics.

D.2. Impact of Systematic Uncertainties

Signal channel	S2ee	S2mm	S2em
Total statistical ($\sqrt{N_{\text{pred}}}$)	0.56	0.65	±0.81
Total background systematic	±0.17	±0.16	±0.22
B tagging	< 0.01	< 0.01	< 0.01
MET cell-out	< 0.01	< 0.01	< 0.01
MET pile-up	< 0.01	< 0.01	< 0.01
alpha_HF	< 0.01	< 0.01	< 0.01
alpha_JHigh	±0.02	±0.01	±0.06
alpha_JLow	< 0.01	< 0.01	< 0.01
alpha_JMedium	< 0.01	±0.01	< 0.01
alpha_LESee	< 0.01	< 0.01	< 0.01
alpha_LESem	< 0.01	< 0.01	< 0.01
alpha_LESmm	< 0.01	< 0.01	< 0.01
alpha_LEee	< 0.01	< 0.01	< 0.01
alpha_LEem	< 0.01	< 0.01	±0.01
alpha_LEmm	< 0.01	< 0.01	< 0.01
alpha_LRIem	< 0.01	< 0.01	< 0.01
alpha_LRImm	< 0.01	< 0.01	< 0.01
alpha_LRMem	< 0.01	< 0.01	< 0.01
alpha_LRMmm	< 0.01	< 0.01	< 0.01
alpha_PtMinTop	< 0.01	< 0.01	< 0.01
alpha_PtMinWZ	< 0.01	< 0.01	< 0.01
alpha_QCDNorm_S2emT_meffInc	< 0.01	< 0.01	±0.01
alpha_TEee	< 0.01	< 0.01	< 0.01
alpha_TEem	< 0.01	< 0.01	±0.02
alpha_TEmm	< 0.01	±0.01	< 0.01
alpha_Zpt100GeV	< 0.01	< 0.01	< 0.01
alpha_Zpt150GeV	< 0.01	< 0.01	< 0.01
alpha_Zpt200GeV	±0.01	< 0.01	< 0.01
alpha_Zpt50GeV	< 0.01	< 0.01	< 0.01
alpha_err_BG	±0.02	±0.01	±0.01
alpha_err_WZ_Np0	< 0.01	< 0.01	< 0.01
alpha_err_WZ_Np1	< 0.01	< 0.01	< 0.01
alpha_had	< 0.01	< 0.01	< 0.01
alpha_hadTop	±0.01	±0.03	±0.07
alpha_hadWZ	±0.01	±0.01	< 0.01
gamma_stat_S2eeT_meffInc_bin_0	±0.17	< 0.01	< 0.01
gamma_stat_S2emT_meffInc_bin_0	< 0.01	< 0.01	±0.19
gamma_stat_S2mmT_meffInc_bin_0	< 0.01	±0.15	< 0.01
mu_Top_Np0	< 0.01	< 0.01	< 0.01
mu_Top_Np1	< 0.01	< 0.01	±0.01
mu_Top_Np2	±0.01	±0.01	±0.02
mu_Top_Np3	< 0.01	±0.01	±0.02
mu_WZ_Np2	< 0.01	< 0.01	< 0.01
mu_WZ_Np3	±0.01	< 0.01	< 0.01
mu_WZ_Np4	< 0.01	±0.01	< 0.01
mu_WZ_Np5	< 0.01	< 0.01	< 0.01

Table 28: Breakdown of the dominant systematic uncertainties on background estimates in the various Signal Regions. Note that the individual uncertainties can be correlated, and do not necessarily add up quadratically to the total background uncertainty.

Signal channel	S4ee	S4mm	S4em
Total statistical ($\sqrt{N_{\text{pred}}}$)	±3.02	±3.42	±4.58
Total background systematic	±1.49	±1.75	±2.91
B tagging	< 0.01	< 0.01	< 0.01
MET cell-out	±0.04	±0.04	< 0.01
MET pile-up	±0.10	±0.06	±0.02
alpha_HF	< 0.01	< 0.01	< 0.01
alpha_JHigh	±0.39	±0.41	±0.73
alpha_JLow	±0.21	±0.16	±0.34
alpha_JMedium	±0.62	±0.76	±1.37
alpha_LESee	±0.01	< 0.01	< 0.01
alpha_LESem	< 0.01	< 0.01	±0.16
alpha_LESmm	< 0.01	< 0.01	< 0.01
alpha_LEee	±0.25	< 0.01	< 0.01
alpha_LEem	< 0.01	< 0.01	±0.35
alpha_LEmm	< 0.01	±0.02	< 0.01
alpha_LRIem	< 0.01	< 0.01	±0.05
alpha_LRImm	< 0.01	< 0.01	< 0.01
alpha_LRMem	< 0.01	< 0.01	±0.06
alpha_LRMmm	< 0.01	< 0.01	< 0.01
alpha_PtMinTop	< 0.01	< 0.01	< 0.01
alpha_PtMinWZ	< 0.01	< 0.01	< 0.01
alpha_QCDNorm_S4eeT_meffInc	±0.22	< 0.01	< 0.01
alpha_TEee	±0.09	< 0.01	< 0.01
alpha_TEem	< 0.01	< 0.01	±0.59
alpha_TEmm	< 0.01	±0.21	< 0.01
alpha_Zpt100GeV	< 0.01	< 0.01	< 0.01
alpha_Zpt150GeV	< 0.01	< 0.01	< 0.01
alpha_Zpt200GeV	< 0.01	±0.01	±0.02
alpha_Zpt50GeV	< 0.01	< 0.01	< 0.01
alpha_err_BG	< 0.01	±0.07	±0.12
alpha_err_WZ_Np0	< 0.01	< 0.01	< 0.01
alpha_err_WZ_Np1	< 0.01	< 0.01	< 0.01
alpha_had	< 0.01	< 0.01	< 0.01
alpha_hadTop	±1.00	±1.22	±2.21
alpha_hadWZ	< 0.01	±0.02	±0.04
gamma_stat_S4eeT_meffInc_bin_0	±0.58	< 0.01	< 0.01
gamma_stat_S4emT_meffInc_bin_0	< 0.01	< 0.01	±0.93
gamma_stat_S4mmT_meffInc_bin_0	< 0.01	±0.66	< 0.01
mu_Top_Np0	< 0.01	< 0.01	< 0.01
mu_Top_Np1	< 0.01	< 0.01	±0.02
mu_Top_Np2	±0.12	±0.18	±0.36
mu_Top_Np3	±0.72	±0.84	±1.44
mu_WZ_Np2	< 0.01	< 0.01	< 0.01
mu_WZ_Np3	< 0.01	< 0.01	±0.01
mu_WZ_Np4	< 0.01	±0.01	±0.01
mu_WZ_Np5	< 0.01	±0.01	±0.02

Table 29: Breakdown of the dominant systematic uncertainties on background estimates in the various Signal Regions. Note that the individual uncertainties can be correlated, and do not necessarily add up quadratically to the total background uncertainty.

E. Fit Validation for Exclusion Fits

Figures 106 and 107 show the resulting fit parameters for the $t\bar{t}$ and W/Z normalization parameters for the different GMSB signal model points as a cross check of the exclusion fit setup on data. It can be seen that the resulting parameters have no strong dependence on the signal model. For very small values of Λ, the signal contamination in the Control Regions gets larger due to the larger signal cross sections, which has a small impact on the background normalization.

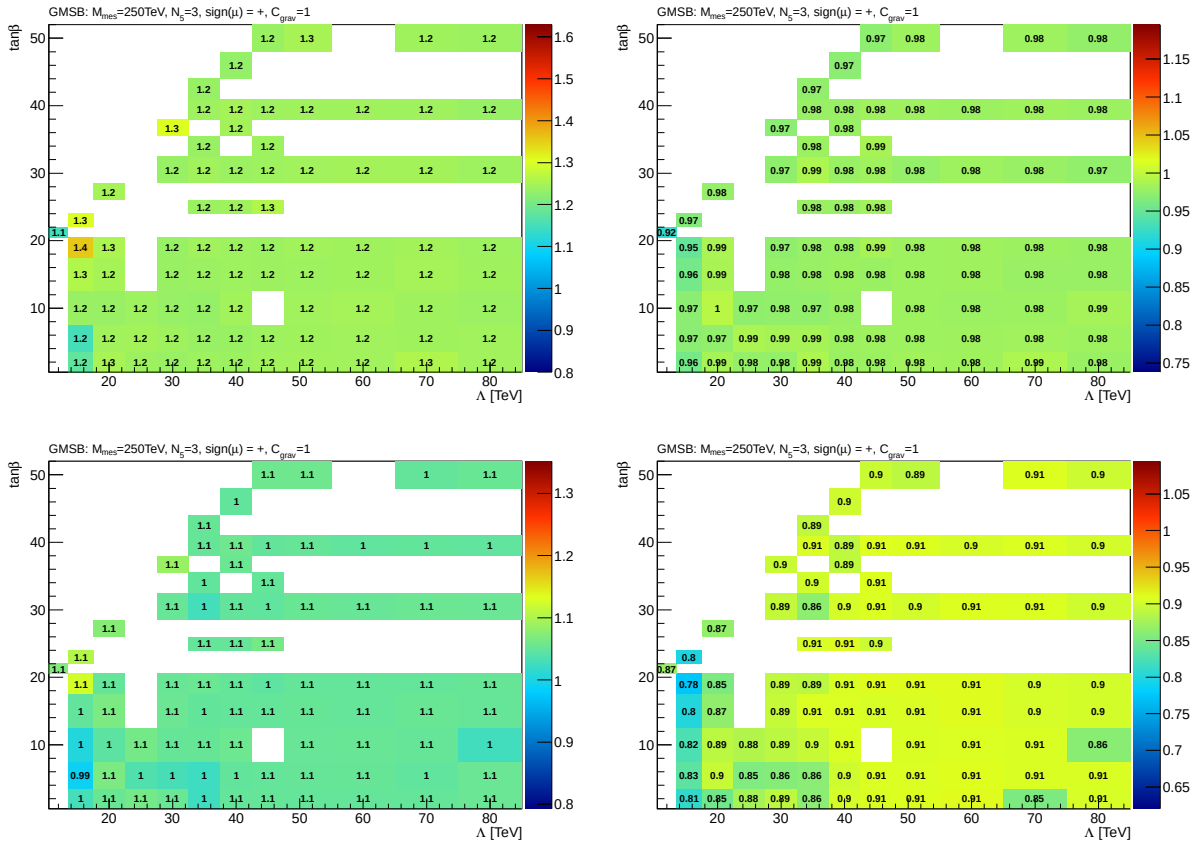

Figure 106: Fit results for the Top Normalization factors mu_Top_Np0 (top left), mu_Top_Np1 (top right), mu_Top_Np2 (bottom left), mu_Top_Np3 (bottom right) for the GMSB exclusion fits.

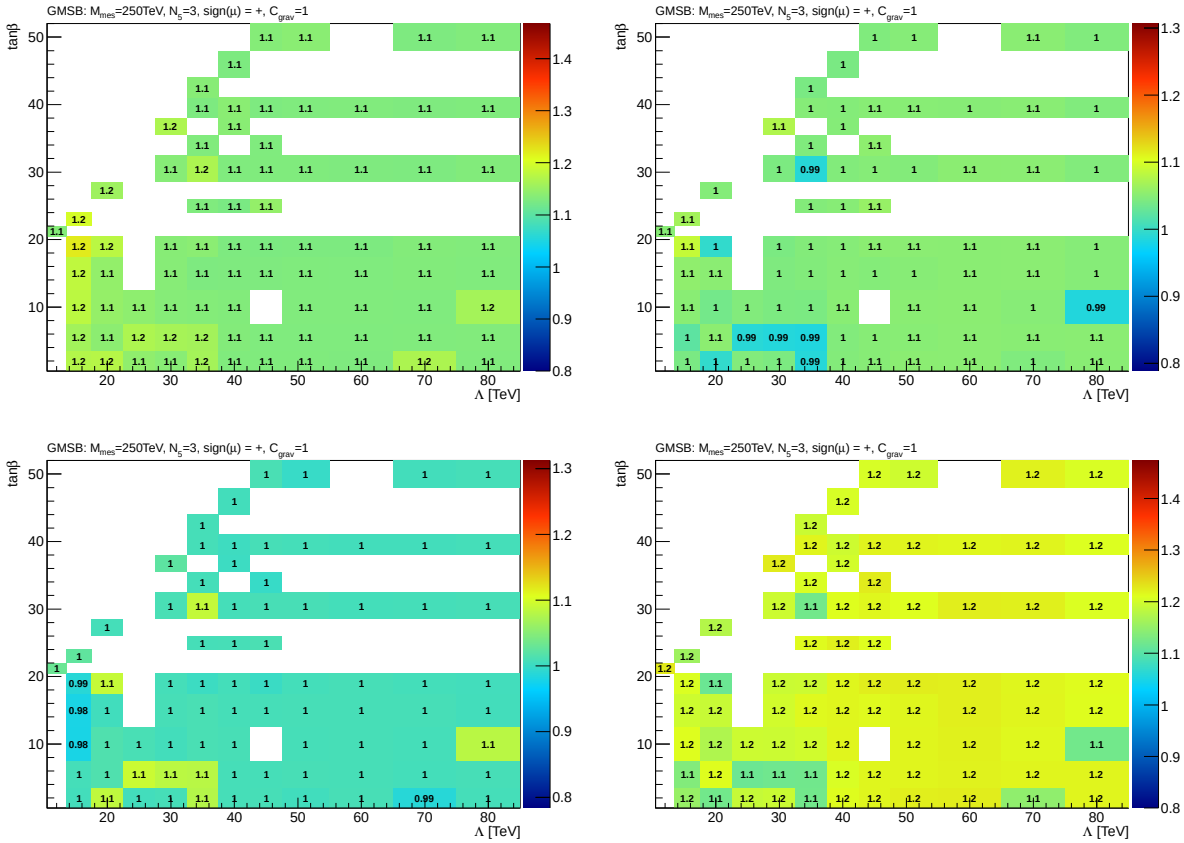

Figure 107: Fit results for the W/Z Normalization factors mu_WZ_Np2 (top left), mu_WZ_Np3 (top right), mu_WZ_Np4 (bottom left), mu_WZ_Np5 (bottom right) for the GMSB exclusion fits.

F. One Lepton Results

For completeness, the full set of results in Control, Validation and Signal Regions for the hard and the soft single lepton analyses are given in the following. Further details and discussions of these results are contained in [19, 163, 281].

F.1. Control Regions

Table 30 contains the fit results in the hard one lepton Control Regions as defined in chapter 8.2, while Figures 108 and 109 show the jet multiplicity distributions in these regions before and after applying the fit results. Similarly, Table 31 and Figures 110 and 111 show the results for the soft one lepton Control Regions.

F.1.1. Hard One Lepton

channel	TREl	TRMu	WREl	WRMu
Observed events	2225	2137	4510	4064
Fitted bkg events	2270.9 ± 40.1	2130.8 ± 39.0	4515.3 ± 62.9	4060.4 ± 60.3
Fitted top events	1842.2 ± 53.0	1724.0 ± 50.5	882.5 ± 63.7	806.8 ± 57.2
Fitted WZ events	292.6 ± 40.7	255.0 ± 36.3	3103.0 ± 89.3	3116.3 ± 72.1
Fitted other BGs events	119.6 ± 23.6	101.2 ± 21.0	90.9 ± 19.0	73.7 ± 15.8
Fitted QCD & fake lepton events	16.6 ± 33.4	50.6 ± 26.6	438.9 ± 107.6	63.6 ± 68.2
MC exp. SM events	2533.4	2232.4	4932.1	4317.3
MC exp. top events	2012.4	1816.7	1154.0	1006.6
MC exp. WZ events	315.5	261.4	3281.5	3119.8
MC exp. other BGs events	132.2	116.4	115.7	104.1
Data-driven QCD & fake lepton events	73.3	37.9	380.8	86.8

Table 30: Background fit results for the hard one lepton W- and $t\bar{t}$ Control Regions for an integrated luminosity of 4.7 fb^{-1}. Nominal MC expectations (normalized to MC cross sections) are given for comparison. The errors shown are the statistical plus systematic uncertainties.

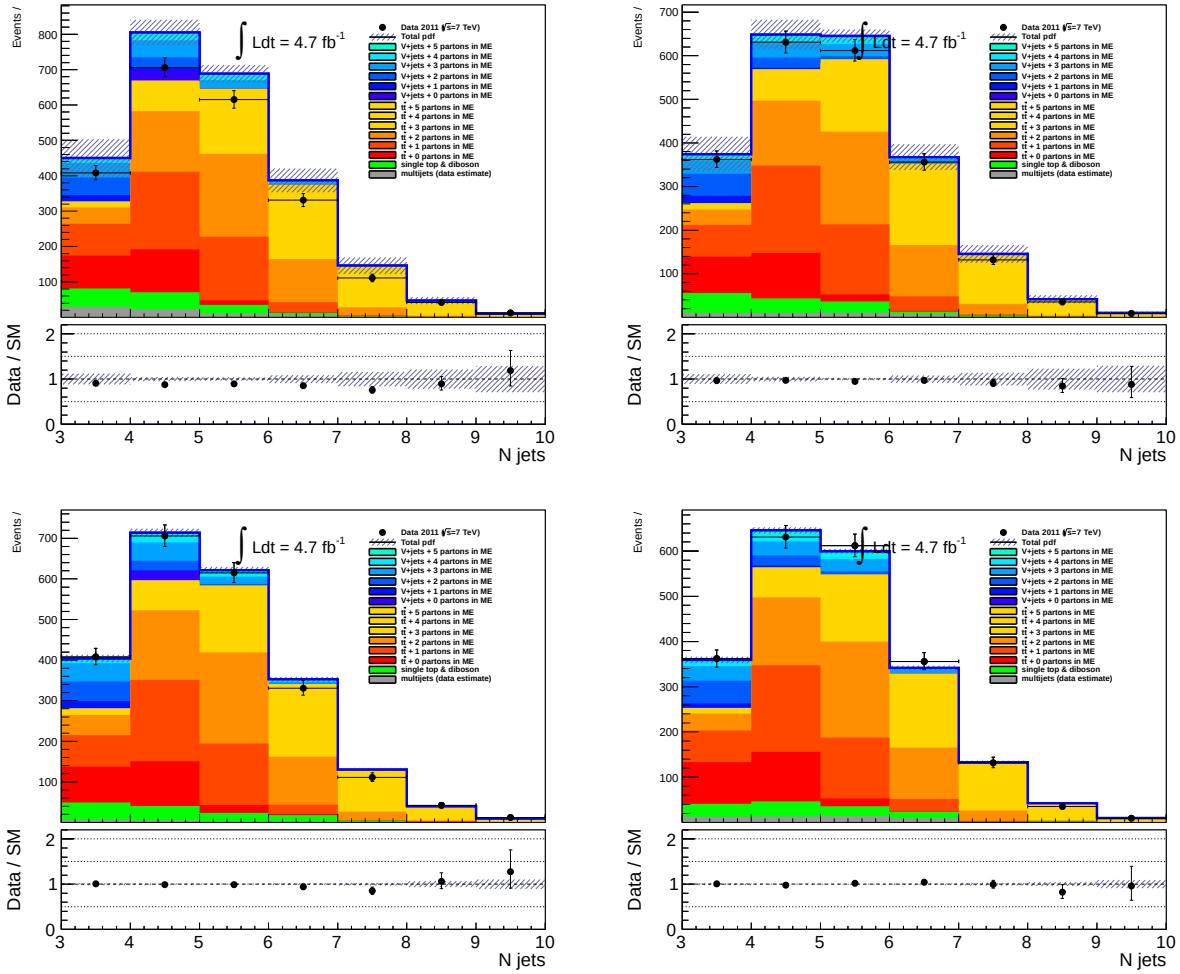

Figure 108: Distribution of the number of jets in the $t\bar{t}$ Control Region (TRL1) in the electron (left) and muon final state (right) before (top) and after (bottom) applying the background-only fit.

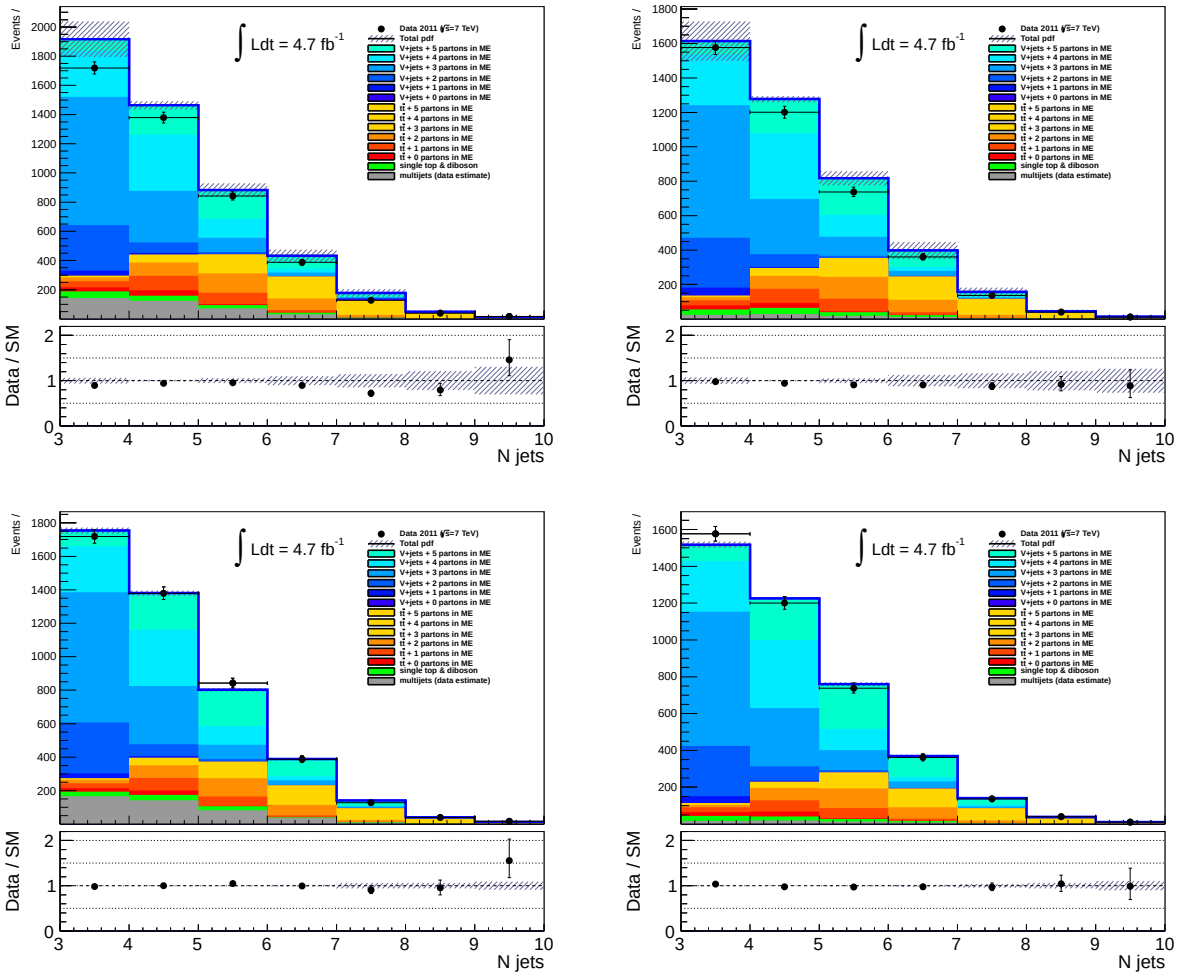

Figure 109: Distribution of the number of jets in the W Control Region (WRL1) in the electron (left) and muon final state (right) before (top) and after (bottom) applying the background-only fit.

F.1.2. Soft One Lepton

channel	SVTEl	SVWEl	SVTMu	SVWMu
Observed events	131	633	200	1092
Fitted bkg events	131.0 ± 10.2	640.1 ± 20.9	194.4 ± 11.7	1093.5 ± 28.0
Fitted top events	69.4 ± 5.8	31.8 ± 3.2	107.4 ± 6.4	57.7 ± 5.0
Fitted WZ events	34.4 ± 4.4	593.9 ± 19.9	43.1 ± 6.2	998.7 ± 28.8
Fitted other BGs events	10.6 ± 2.2	11.2 ± 2.3	16.2 ± 3.3	12.0 ± 3.2
Fitted QCD & fake lepton events	16.5 ± 11.4	3.1 ± 0.5	27.7 ± 11.4	25.1 ± 21.1
MC exp. SM events	125.7	679.3	212.8	1091.5
MC exp. top events	78.8	44.3	122.6	72.5
MC exp. WZ events	30.3	597.0	50.0	961.5
MC exp. other BGs events	11.2	14.2	19.5	21.0
Data-driven QCD & fake lepton events	5.4	23.9	20.7	36.4

Table 31: Background fit results for the soft one lepton Control Regions regions, for an integrated luminosity of 4.7 fb^{-1}. Nominal MC expectations (normalized to MC cross sections) are given for comparison. The errors shown are the statistical plus systematic uncertainties.

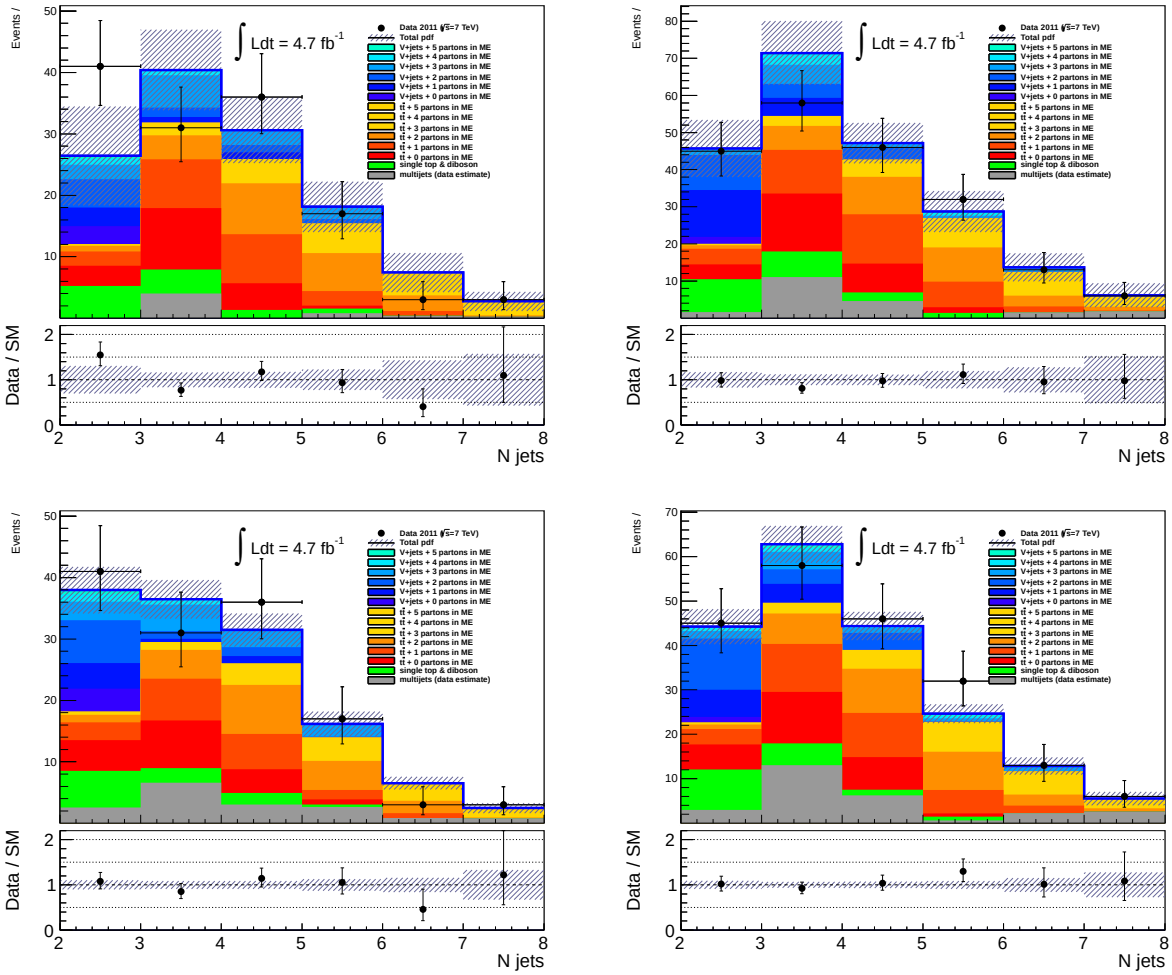

Figure 110: Distribution of the number of jets in the soft lepton $t\bar{t}$ Control Region (SLTR) in the electron (left) and muon final state (right) before (top) and after (bottom) applying the background-only fit.

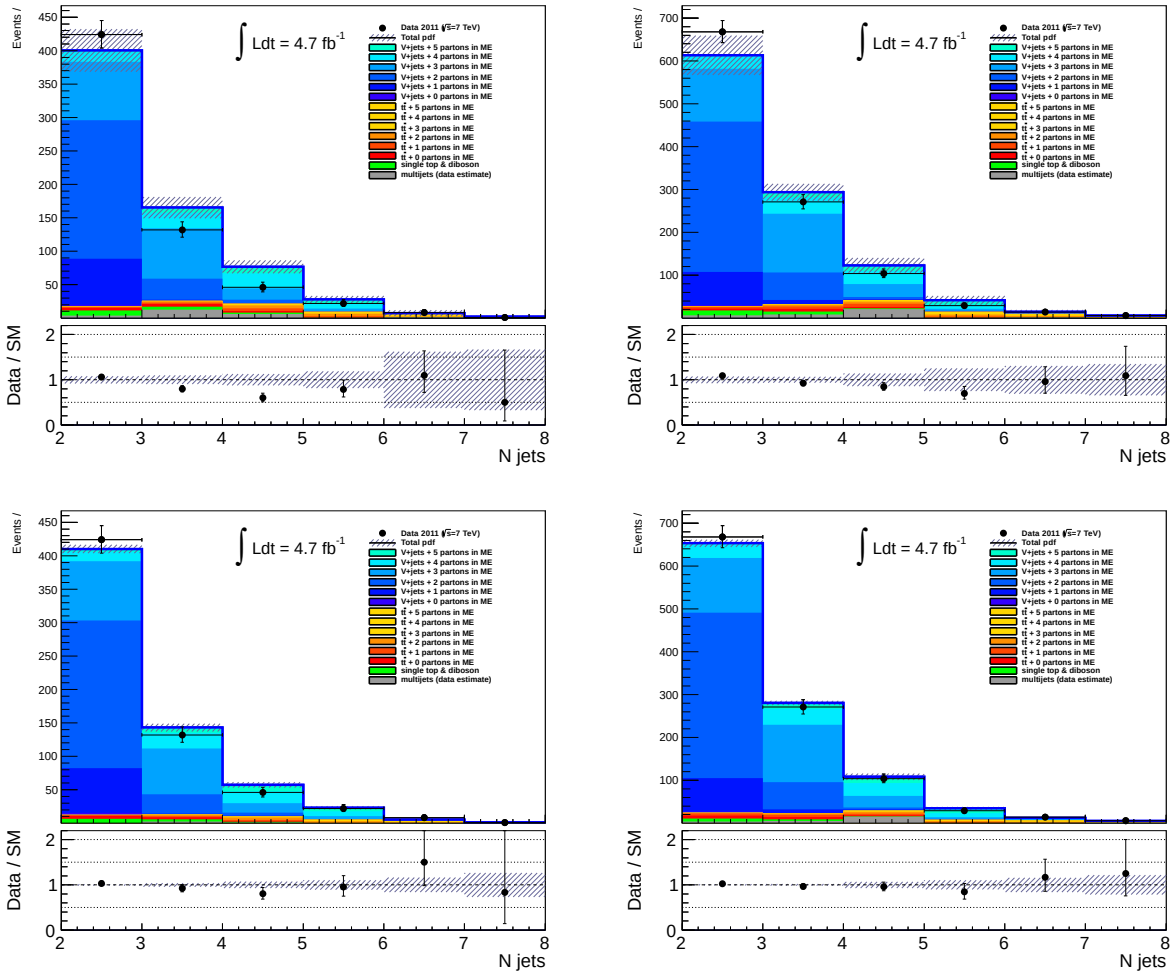

Figure 111: Distribution of the number of jets in the soft lepton W Control Region (SLWR) in the electron (left) and muon final state (right) before (top) and after (bottom) applying the background-only fit.

F.2. Signal Regions

Table 32 contains the fit results in the hard and soft one lepton Signal Regions as defined in chapter 7.7, while Figure 112 shows corresponding distributions of data and Standard Model backgrounds in the Signal Regions.

Single-lepton		Electron			Muon	
Number of events	3-jet	4-jet	soft lepton	3-jet	4-jet	soft lepton
Observed	2	4	11	1	2	14
Fitted bkg	2.3 ± 0.9	3.5 ± 0.9	14.0 ± 3.3	2.6 ± 0.8	1.5 ± 0.3	19 ± 5
Fitted top	0.4 ± 0.2	2.3 ± 0.6	3.8 ± 0.6	0.5 ± 0.2	1.3 ± 0.3	3.8 ± 0.8
Fitted W/Z+jets	1.5 ± 0.6	0.9 ± 0.2	5.8 ± 1.0	2.0 ± 0.6	0.2 ± 0.1	11.4 ± 2.3
Fitted other bkg	0.0 ± 0.0	$0.0^{+0.3}_{-0.0}$	0.6 ± 0.1	0.1 ± 0.1	0.0 ± 0.0	0.2 ± 0.1
Fitted multijet	0.3 ± 0.4	0.3 ± 0.4	3.8 ± 2.5	0.0 ± 0.0	0.0 ± 0.0	3.6 ± 2.5
MC exp. SM	2.7	5.3	14.2	2.8	2.4	18.0
MC exp. top	0.9	3.1	4.3	0.6	2.0	3.8
MC exp. W/Z+jets	1.5	1.3	5.5	2.0	0.3	10.5
MC exp. other bkg	0.0	0.5	0.5	0.2	0.1	0.1
Data-driven multijet	0.3	0.3	3.8	0.0	0.0	3.6

Table 32: The observed numbers of events in the single-lepton Signal Regions, and the background expectations from the fit. The inputs to the fit are also shown; these consist of the data-driven multijet background estimate and the nominal expectations from simulation (MC), normalized to theoretical cross sections. The errors shown are the statistical plus systematic uncertainties.

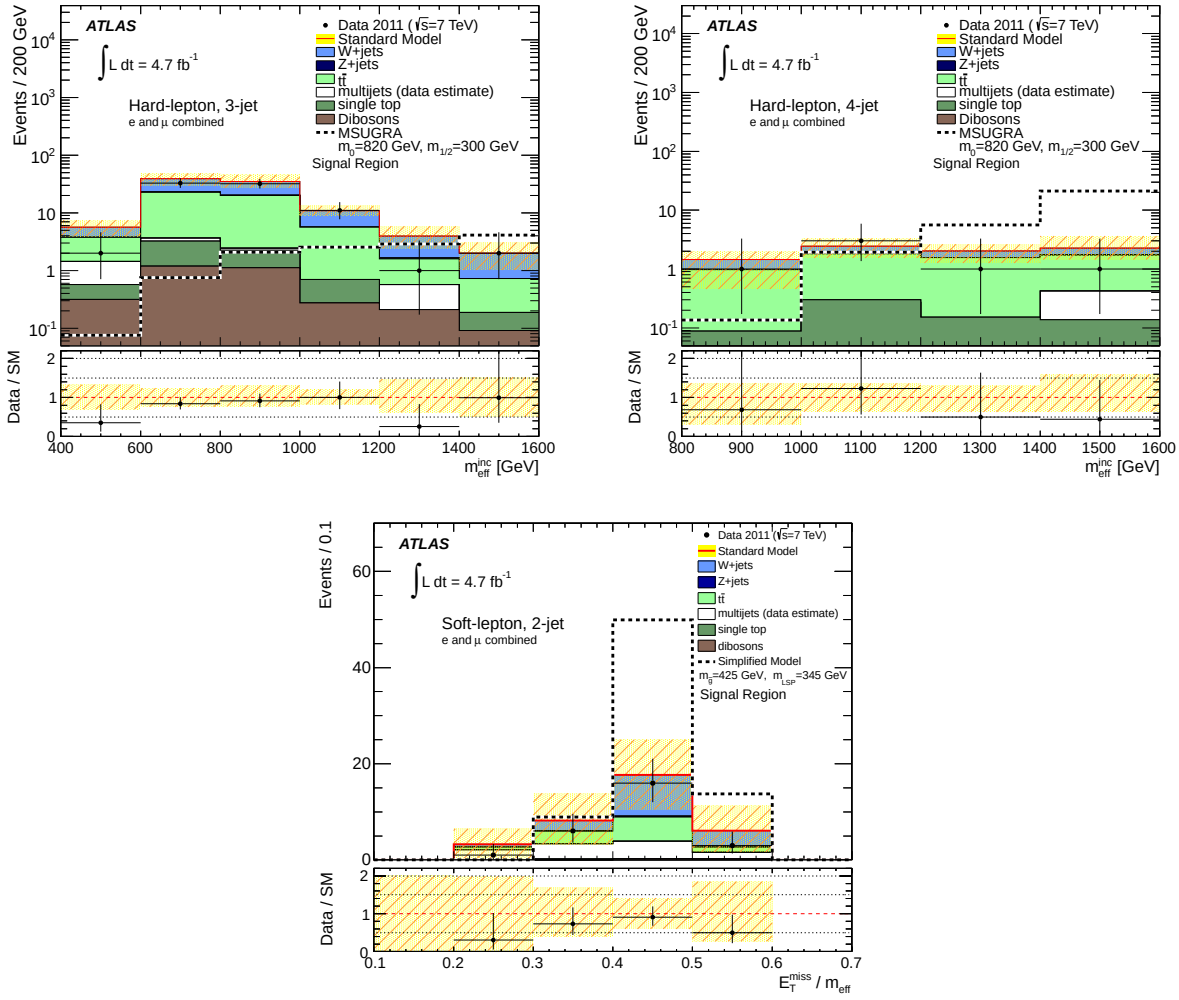

Figure 112: Top: Distribution of $m_{\text{eff}}^{\text{inc}}$ in the 3-jet (left) and 4-jet (right) hard-lepton Signal Regions after all selection requirements except for that on the inclusive effective mass. Bottom: The $E_T^{\text{miss}}/m_{\text{eff}}$ distribution in the soft-lepton Signal Region after all selection requirements except for that on $E_T^{\text{miss}}/m_{\text{eff}}$. The last $m_{\text{eff}}^{\text{inc}}$ bin includes all overflows. The different lepton flavors have been combined for ease of presentation. The "Data/SM" plots show the ratio between data and the total Standard Model expectation. The Standard Model expectation shown here is the input to the final fit, and is derived from simulation only, normalized to the theoretical cross sections. The uncertainty band around the Standard Model expectation combines the statistical uncertainty on the simulated event samples with the systematic uncertainties on the jet energy scale, b-tagging, data-driven multijet background, and luminosity. The systematic uncertainties are largely correlated from bin to bin. An example of the distribution for a simulated signal is also shown (not stacked).

F.3. Validation Regions

Tables 33 and 34 show the fit results in the hard one electron and hard one muon Validation Regions as defined in chapter 11.2, while Table 35 contains the results for the soft one lepton Validation Regions.

F.3.1. Hard One Lepton

hard one electron channel	**High-m_T VR**	**W VR**	**$t\bar{t}$ VR**
Observed events	7698	1068	499
Fitted bkg events	7618.1 ± 553.9	1017.8 ± 42.9	501.6 ± 16.7
Fitted top events	3014.6 ± 113.3	213.5 ± 16.9	410.6 ± 17.5
Fitted WZ events	3936.4 ± 162.7	778.1 ± 39.5	58.2 ± 9.7
Fitted other BGs events	231.2 ± 46.3	26.2 ± 5.7	32.8 ± 6.6
Fitted QCD & fake lepton events	435.9 ± 525.6	0.0 ± 0.0	0.0 ± 0.0
MC exp. SM events	8054.7	1160.3	561.7
MC exp. top events	3382.1	281.0	447.7
MC exp. WZ events	3987.6	842.3	72.7
MC exp. other BGs events	249.1	37.0	41.3
Data-driven QCD & fake lepton events	435.9	0.0	0.0

Table 33: Background fit results for the hard one electron Validation Regions. Nominal MC expectations (normalized to MC cross sections) are given for comparison. The errors shown are the statistical plus systematic uncertainties.

hard one muon channel	**High-m_T VR**	**W VR**	**$t\bar{t}$ VR**
Observed events	7088	1020	428
Fitted bkg events	7298.0 ± 152.8	1038.0 ± 37.7	474.9 ± 11.6
Fitted top events	2884.0 ± 111.9	192.1 ± 14.5	371.1 ± 14.8
Fitted WZ events	4148.8 ± 143.5	816.9 ± 34.0	74.6 ± 9.5
Fitted other BGs events	229.6 ± 45.8	24.1 ± 5.1	26.1 ± 5.3
Fitted QCD & fake lepton events	35.7 ± 85.0	5.0 ± 11.5	3.2 ± 5.2
MC exp. SM events	7503.2	1120.9	493.5
MC exp. top events	3213.3	243.2	386.8
MC exp. WZ events	3998.6	840.7	74.7
MC exp. other BGs events	255.7	32.0	28.8
Data-driven QCD & fake lepton events	35.7	5.0	3.2

Table 34: Background fit results for hard one muon Validation Regions. Nominal MC expectations (normalized to MC cross sections) are given for comparison. The errors shown are the statistical plus systematic uncertainties.

F.3.2. Soft One Lepton

channel	soft electron	soft muon
Observed events	295	463
Fitted bkg events	329.0 ± 17.6	478.1 ± 22.9
Fitted top events	60.2 ± 3.6	71.2 ± 3.3
Fitted WZ events	245.1 ± 10.5	374.5 ± 13.7
Fitted other BGs events	10.3 ± 2.1	14.9 ± 3.0
Fitted QCD & fake lepton events	13.4 ± 11.7	17.5 ± 18.2
MC exp. SM events	342.4	479.1
MC exp. top events	69.5	80.9
MC exp. WZ events	247.1	363.7
MC exp. other BGs events	12.4	17.1
Data-driven QCD & fake lepton events	13.4	17.5

Table 35: Background fit results for the soft lepton Validation Regions. Nominal MC expectations (normalized to MC cross sections) are given for comparison. The errors shown are the statistical plus systematic uncertainties.

F.4. Model-independent Upper Limits

Table 36 contains the model-independent upper limits for the hard and soft one lepton Signal Regions as discussed in chapter 12.2.

Signal channel	$\langle \epsilon\sigma \rangle^{95}_{\text{obs}}$[fb]	S^{95}_{obs}	S^{95}_{exp}	CL_B
hard electron, 3-jet	0.94	4.4	$4.3^{+2.0}_{-0.8}$	0.54
hard muon, 3-jet	0.75	3.6	$4.2^{+2.0}_{-0.7}$	0.27
hard electron, 4-jet	1.22	5.8	$5.3^{+2.6}_{-1.3}$	0.63
hard muon, 4-jet	0.95	4.5	$3.8^{+1.3}_{-0.7}$	0.75
soft electron	1.82	8.6	$10.4^{+4.2}_{-3.1}$	0.28
soft muon	1.92	9.0	$12.5^{+5.4}_{-3.8}$	0.21

Table 36: Left to right: 95% CL upper limits on the visible cross section ($\langle \epsilon\sigma \rangle^{95}_{\text{obs}}$) in the various Signal Regions, and on the number of signal events (S^{95}_{obs}). The third column (S^{95}_{exp}) shows the 95% CL upper limit on the number of signal events, given the expected number (and $\pm 1\sigma$ uncertainty on the expectation) of background events. The last column indicates the CL_B value, i.e. the observed confidence level for the background-only hypothesis.

References

[1] **UA1 Collaboration**, "Experimental Observation of Isolated Large Transverse Energy Electrons with Associated Missing Energy at $\sqrt{s} = 540$ GeV", *Phys. Lett.* **B122** (1983) 103–116.

[2] **UA1 Collaboration**, "Further Evidence for Charged Intermediate Vector Bosons at the SPS Collider", *Phys. Lett.* **B129** (1983) 273.

[3] **UA2 Collaboration**, "Observation of Single Isolated Electrons of High Transverse Momentum in Events with Missing Transverse Energy at the CERN anti-p p Collider", *Phys. Lett.* **B122** (1983) 476–485.

[4] **CDF Collaboration**, "Observation of top quark production in $\bar{p}p$ collisions", *Phys. Rev. Lett.* **74** (1995) 2626–2631, arXiv:hep-ex/9503002 [hep-ex].

[5] **DØ Collaboration**, "Observation of the top quark", *Phys. Rev. Lett.* **74** (1995) 2632–2637, arXiv:hep-ex/9503003 [hep-ex].

[6] **LEP and Tevatron Electroweak Working Group**, "Winter 2012 update." http://lepewwg.web.cern.ch/LEPEWWG/plots/winter2012/.

[7] **ALEPH Collaboration, DELPHI Collaboration, L3 Collaboration, OPAL Collaboration, SLD Collaboration, LEP Electroweak Working Group, SLD Electroweak Group, SLD Heavy Flavour Group**, "Precision electroweak measurements on the Z resonance", *Phys. Rept.* **427** (2006) 257–454, arXiv:hep-ex/0509008 [hep-ex].

[8] G. Jarlskog, P. Rein, "Proceedings of the ECFA Large Hadron Collider Workshop, Aachen, 1990", CERN 90-10, ECFA 90-133, http://cdsweb.cern.ch/record/215298.

[9] **ATLAS Collaboration**, "ATLAS: Technical proposal for a general-purpose p p experiment at the Large Hadron Collider at CERN", CERN-LHCC-94-43, 1994, http://cdsweb.cern.ch/record/290968.

[10] **CMS Collaboration**, "CMS, the Compact Muon Solenoid: Technical proposal", CERN-LHCC-94-38, 1994, http://cdsweb.cern.ch/record/290969.

[11] F. del Aguila and L. Ametller, "On the detectability of sleptons at large hadron colliders", *Phys. Lett.* **B261** (1991) 326–333.

[12] H. Baer, C. Chen, F. Paige and X. Tata, "Signals for minimal supergravity at the CERN large hadron collider: Multi - jet plus missing energy channel", *Phys. Rev.* **D52** (1995) 2746–2759, arXiv:hep-ph/9503271 [hep-ph].

[13] H. Baer, C. Chen, F. Paige and X. Tata, "Signals for minimal supergravity at the CERN large hadron collider. 2: Multi - lepton channels", *Phys. Rev.* **D53** (1996) 6241–6264, arXiv:hep-ph/9512383 [hep-ph].

[14] M. Lungwitz, "Suche nach Supersymmetrie in dileptonischen Endzuständen mit dem ATLAS-Experiment", Diplomarbeit, Rheinische Friedrich-Wilhelms-Universität Bonn, 2009.

[15] **ATLAS Collaboration**, "Early supersymmetry searches with jets, missing transverse momentum and one or more leptons with the ATLAS Detector", ATLAS-CONF-2010-066, Jul 2010, https://cds.cern.ch/record/1281341.

[16] **ATLAS Collaboration**, "Search for supersymmetric particles in events with lepton pairs and large missing transverse momentum in $\sqrt{s} = 7$ TeV proton-proton collisions with the ATLAS experiment", *Eur. Phys. J.* **C71** (2011) 1682, arXiv:1103.6214 [hep-ex].

[17] **ATLAS Collaboration**, "Searches for supersymmetry with the ATLAS detector using final states with two leptons and missing transverse momentum in $\sqrt{s} = 7$ TeV proton-proton collisions", *Phys. Lett.* **B709** (2012) 137–157, arXiv:1110.6189 [hep-ex].

[18] **ATLAS Collaboration**, "Constraining the gauge-mediated Supersymmetry breaking model in final states with two leptons, jets and missing transverse momentum with the ATLAS experiment at $\sqrt(s) = 7$ TeV", ATLAS-CONF-2011-156, Nov 2011, http://cds.cern.ch/record/1398247.

[19] **ATLAS Collaboration**, "Further search for supersymmetry at $\sqrt{s} = 7$ TeV in final states with jets, missing transverse momentum and isolated leptons with the ATLAS detector", *Phys. Rev.* **D86** (2012) 092002, arXiv:1208.4688 [hep-ex].

[20] G. 't Hooft and M. J. G. Veltman, "Regularization and Renormalization of Gauge Fields", *Nucl. Phys.* **B44** (1972) 189–213.

[21] D. I. Kazakov, "Beyond the standard model (in search of supersymmetry)", arXiv:hep-ph/0012288.

[22] P. Langacker, "Introduction to the Standard Model and Electroweak Physics", arXiv:0901.0241 [hep-ph].

[23] S. F. Novaes, "Standard model: An Introduction", arXiv:hep-ph/0001283.

[24] F. Halzen und A. Martin, "Quarks and Leptons: An Introductory Course in Modern Particle Physics", John Wiley & Sons Inc., 1984.

[25] G. Fogli, E. Lisi, A. Marrone, D. Montanino, A. Palazzo *et al.*, "Global analysis of neutrino masses, mixings and phases: entering the era of leptonic CP violation searches", *Phys. Rev.* **D86** (2012) 013012, arXiv:1205.5254 [hep-ph].

[26] **WMAP Collaboration**, "Seven-Year Wilkinson Microwave Anisotropy Probe (WMAP) Observations: Cosmological Interpretation", *Astrophys. J. Suppl.* **192** (2011) 18, arXiv:1001.4538 [astro-ph.CO].

[27] A. Strumia and F. Vissani, "Neutrino masses and mixings and...", arXiv:hep-ph/0606054 [hep-ph].

[28] K. Abazajian, M. Acero, S. Agarwalla, A. Aguilar-Arevalo, C. Albright *et al.*, "Light Sterile Neutrinos: A White Paper", arXiv:1204.5379 [hep-ph].

[29] W. Rodejohann, "Neutrino-less Double Beta Decay and Particle Physics", *Int. J. Mod. Phys.* **E20** (2011) 1833–1930, arXiv:1106.1334 [hep-ph].

[30] **Particle Data Group**, "Review of Particle Physics", *Phys. Rev.* **D86** (2012) 010001.

[31] **ALEPH Collaboration, DELPHI Collaboration, L3 Collaboration, OPAL Collaboration, LEP Electroweak Working Group**, "A Combination of preliminary electroweak measurements and constraints on the standard model", arXiv:hep-ex/0612034 [hep-ex].

[32] **CDF Collaboration, DØ Collaboration, Tevatron Electroweak Working Group**, "2012 Update of the Combination of CDF and DØ Results for the Mass of the W Boson", arXiv:1204.0042 [hep-ex].

[33] **ATLAS Collaboration**, "Observation of a new particle in the search for the Standard Model Higgs boson with the ATLAS detector at the LHC", *Phys. Lett.* **B716** (2012) 1–29, arXiv:1207.7214 [hep-ex].

[34] **CMS Collaboration**, "Observation of a new boson at a mass of 125 GeV with the CMS experiment at the LHC", *Phys. Lett.* **B716** (2012) 30–61, arXiv:1207.7235 [hep-ex].

[35] **ATLAS Collaboration**, "Combined measurements of the mass and signal strength of the Higgs-like boson with the ATLAS detector using up to 25 fb^{-1} of proton-proton collision data", ATLAS-CONF-2013-014, Mar 2013, https://cds.cern.ch/record/1523727.

[36] "Combination of standard model Higgs boson searches and measurements of the properties of the new boson with a mass near 125 GeV", CMS-PAS-HIG-13-005, 2013, https://cds.cern.ch/record/1542387.

[37] **ATLAS Collaboration**, "An update of combined measurements of the new Higgs-like boson with high mass resolution channels", ATLAS-CONF-2012-170, Dec 2012, https://cds.cern.ch/record/1499629.

[38] **CMS Collaboration**, "Combination of standard model Higgs boson searches and measurements of the properties of the new boson with a mass near 125 GeV", CMS-PAS-HIG-12-045, Dec 2012, https://cds.cern.ch/record/1494149.

[39] **ATLAS Collaboration**, "Coupling properties of the new Higgs-like boson observed with the ATLAS detector at the LHC", ATLAS-CONF-2012-127, Sep 2012, https://cds.cern.ch/record/1476765.

[40] F. Goertz, A. Papaefstathiou, L. L. Yang and J. Zurita, "Higgs Boson self-coupling measurements using ratios of cross sections", arXiv:1301.3492 [hep-ph].

[41] S. R. Coleman and J. Mandula, "All possible symmetries of the S-matrix", *Phys. Rev.* **159** (1967) 1251–1256.

[42] O. Pelc and L. Horwitz, "Generalization of the Coleman-Mandula theorem to higher dimension", *J. Math. Phys.* **38** (1997) 139–172, arXiv:hep-th/9605147 [hep-th].

[43] R. Haag, J. T. Lopuszanski and M. Sohnius, "All Possible Generators of Supersymmetries of the s Matrix", *Nucl. Phys.* **B88** (1975) 257.

[44] H. Miyazawa, "Baryon Number Changing Currents", *Prog. Theor. Phys.* **36 (6)** (1966) 1266.

[45] P. Ramond, "Dual Theory for Free Fermions", *Phys. Rev.* **D3** (1971) 2415.

[46] Y. A. Golfand and E. P. Likhtman, "Extension of the Algebra of Poincare Group Generators and Violation of p Invariance", *JETP Lett.* **13** (1971) 323.

[47] A. Neveu and J. H. Schwarz, "Factorizable dual model of pions", *Nucl. Phys.* **B31** (1971) 86.

[48] A. Neveu and J. H. Schwarz, "Quark Model of Dual Pions", *Phys. Rev.* **D4** (1971) 1109.

[49] J. Gervais and B. Sakita, "Field theory interpretation of supergauges in dual models", *Nucl. Phys.* **B34** (1971) 632.

[50] D. V. Volkov and V. P. Akulov, "Is the Neutrino a Goldstone Particle?", *Phys. Lett.* **B46** (1973) 109.

[51] J. Wess and B. Zumino, "A Lagrangian Model Invariant Under Supergauge Transformations", *Phys. Lett.* **B49** (1974) 52.

[52] J. Wess and B. Zumino, "Supergauge Transformations in Four-Dimensions", *Nucl. Phys.* **B70** (1974) 39.

[53] P. Fayet, "Supersymmetry and Weak, Electromagnetic and Strong Interactions", *Phys. Lett.* **B64** (1976) 159.

[54] P. Fayet, "Spontaneously Broken Supersymmetric Theories of Weak, Electromagnetic and Strong Interactions", *Phys. Lett.* **B69** (1977) 489.

[55] G. R. Farrar and P. Fayet, "Phenomenology of the Production, Decay, and Detection of New Hadronic States Associated with Supersymmetry", *Phys. Lett.* **B76** (1978) 575.

[56] P. Fayet, "Relations Between the Masses of the Superpartners of Leptons and Quarks, the Goldstino Couplings and the Neutral Currents", *Phys. Lett.* **B84** (1979) 416.

[57] S. Dimopoulos and H. Georgi, "Softly Broken Supersymmetry and SU(5)", *Nucl. Phys.* **B193** (1981) 150.

[58] U. Ellwanger, C. Hugonie and A. M. Teixeira, "The Next-to-Minimal Supersymmetric Standard Model", *Phys. Rept.* **496** (2010) 1–77, `arXiv:0910.1785 [hep-ph]`.

[59] M. Maniatis, "The Next-to-Minimal Supersymmetric extension of the Standard Model reviewed", *Int. J. Mod. Phys.* **A25** (2010) 3505–3602, `arXiv:0906.0777 [hep-ph]`.

[60] J. E. Kim and H. P. Nilles, "The mu Problem and the Strong CP Problem", *Phys. Lett.* **B138** (1984) 150.

[61] S. P. Martin, "A Supersymmetry primer", `arXiv:hep-ph/9709356 [hep-ph]`.

[62] P. Langacker, "Grand Unified Theories and Proton Decay", *Phys. Rept.* **72** (1981) 185.

[63] **SNO Collaboration**, "Constraints on nucleon decay via 'invisible' modes from the Sudbury Neutrino Observatory", *Phys. Rev. Lett.* **92** (2004) 102004, `arXiv:hep-ex/0310030 [hep-ex]`.

[64] H. K. Dreiner, "An Introduction to explicit R-parity violation", `arXiv:hep-ph/9707435 [hep-ph]`.

[65] R. Barbier, C. Berat, M. Besancon, M. Chemtob, A. Deandrea *et al.*, "R-parity violating supersymmetry", *Phys. Rept.* **420** (2005) 1–202, `arXiv:hep-ph/0406039 [hep-ph]`.

[66] C. W. Misner, K. Thorne and J. Wheeler, "Gravitation", W. H. Freeman; 1st edition, 1974.

[67] P. Van Nieuwenhuizen, "Supergravity", *Phys. Rept.* **68** (1981) 189–398.

[68] H. P. Nilles, "Supersymmetry, Supergravity and Particle Physics", *Phys. Rept.* **110** (1984) 1–162.

[69] E. Witten, "Dynamical Breaking of Supersymmetry", *Nucl. Phys.* **B188** (1981) 513.

[70] N. Sakai, "Naturalness in Supersymmetric Guts", *Z. Phys.* **C11** (1981) 153.

[71] R. K. Kaul and P. Majumdar, "Cancellation Of Quadratically Divergent Mass Corrections In Globally Supersymmetric Spontaneously Broken Gauge Theories", *Nucl. Phys.* **B199** (1982) 36.

[72] J. Ellis, J. Espinosa, G. Giudice, A. Hoecker and A. Riotto, "The Probable Fate of the Standard Model", *Phys. Lett.* **B679** (2009) 369–375, arXiv:0906.0954 [hep-ph].

[73] K. Inoue, A. Kakuto, H. Komatsu and S. Takeshita, "Low-Energy Parameters and Particle Masses in a Supersymmetric Grand Unified Model", *Prog.Theor.Phys.* **67** (1982) 1889.

[74] R. A. Flores and M. Sher, "Higgs Masses in the Standard, Multi-Higgs and Supersymmetric Models", *Annals Phys.* **148** (1983) 95.

[75] O. Buchmueller, R. Cavanaugh, A. De Roeck, M. Dolan, J. Ellis *et al.*, "Higgs and Supersymmetry", *Eur. Phys. J.* **C72** (2012) 2020, arXiv:1112.3564 [hep-ph].

[76] M. W. Cahill-Rowley, J. L. Hewett, A. Ismail and T. G. Rizzo, "The Higgs Sector and Fine-Tuning in the pMSSM", arXiv:1206.5800 [hep-ph].

[77] P. Bechtle, S. Heinemeyer, O. Stål, T. Stefaniak, G. Weiglein *et al.*, "MSSM Interpretations of the LHC Discovery: Light or Heavy Higgs?", arXiv:1211.1955 [hep-ph].

[78] S. S. AbdusSalam and D. Choudhury, "Higgs boson discovery versus sparticles prediction: Impact on the pMSSM's posterior samples from a Bayesian global fit", arXiv:1210.3331 [hep-ph].

[79] F. Mahmoudi, A. Arbey, M. Battaglia and A. Djouadi, "Implications of LHC Higgs and SUSY searches for MSSM", arXiv:1211.2794 [hep-ph].

[80] M. Ibe, S. Matsumoto, T. T. Yanagida and N. Yokozaki, "Heavy Squarks and Light Sleptons in Gauge Mediation From the viewpoint of 125 GeV Higgs Boson and Muon g-2 ", arXiv:1210.3122 [hep-ph].

[81] A. Arbey, M. Battaglia, A. Djouadi and F. Mahmoudi, "An update on the constraints on the phenomenological MSSM from the new LHC Higgs results", arXiv:1211.4004 [hep-ph].

[82] K. Kowalska, S. Munir, L. Roszkowski, E. M. Sessolo, S. Trojanowski *et al.*, "The Constrained NMSSM with a 125 GeV Higgs boson – A global analysis", arXiv:1211.1693 [hep-ph].

[83] V. Sahni, "Dark matter and dark energy", *Lect. Notes Phys.* **653** (2004) 141–180, arXiv:astro-ph/0403324 [astro-ph].

[84] L. Bergstrom, "Nonbaryonic dark matter: Observational evidence and detection methods", *Rept. Prog. Phys.* **63** (2000) 793, arXiv:hep-ph/0002126 [hep-ph].

[85] D. Clowe, M. Bradac, A. H. Gonzalez, M. Markevitch, S. W. Randall *et al.*, "A direct empirical proof of the existence of dark matter", *Astrophys. J.* **648** (2006) L109–L113, arXiv:astro-ph/0608407 [astro-ph].

[86] N. Jarosik, C. Bennett, J. Dunkley, B. Gold, M. Greason *et al.*, "Seven-Year Wilkinson Microwave Anisotropy Probe (WMAP) Observations: Sky Maps, Systematic Errors, and Basic Results", *Astrophys. J. Suppl.* **192** (2011) 14, arXiv:1001.4744 [astro-ph.CO].

[87] D. Larson, J. Dunkley, G. Hinshaw, E. Komatsu, M. Nolta *et al.*, "Seven-Year Wilkinson Microwave Anisotropy Probe (WMAP) Observations: Power Spectra and WMAP-Derived Parameters", *Astrophys. J. Suppl.* **192** (2011) 16, arXiv:1001.4635 [astro-ph.CO].

[88] C. Bennett, R. Hill, G. Hinshaw, D. Larson, K. Smith *et al.*, "Seven-Year Wilkinson Microwave Anisotropy Probe (WMAP) Observations: Are There Cosmic Microwave Background Anomalies?", *Astrophys. J. Suppl.* **192** (2011) 17, arXiv:1001.4758 [astro-ph.CO].

[89] J. D. Bekenstein, "Relativistic gravitation theory for the MOND paradigm", *Phys. Rev.* **D70** (2004) 083509, arXiv:astro-ph/0403694 [astro-ph].

[90] N. Arkani-Hamed, D. P. Finkbeiner, T. R. Slatyer and N. Weiner, "A Theory of Dark Matter", *Phys. Rev.* **D79** (2009) 015014, arXiv:0810.0713 [hep-ph].

[91] S. Weinberg, "A New Light Boson?", *Phys. Rev. Lett.* **40** (1978) 223–226.

[92] N. Arkani-Hamed, S. Dimopoulos and G. Dvali, "Phenomenology, astrophysics and cosmology of theories with submillimeter dimensions and TeV scale quantum gravity", *Phys. Rev.* **D59** (1999) 086004, arXiv:hep-ph/9807344 [hep-ph].

[93] **XENON100 Collaboration**, "First Dark Matter Results from the XENON100 Experiment", *Phys. Rev. Lett.* **105** (2010) 131302, arXiv:1005.0380 [astro-ph.CO].

[94] **XENON100 Collaboration**, "The XENON100 Dark Matter Experiment", *Astropart. Phys.* **35** (2012) 573–590, arXiv:1107.2155 [astro-ph.IM].

[95] **CDMS Collaboration, EDELWEISS Collaboration**, "Combined Limits on WIMPs from the CDMS and EDELWEISS Experiments", *Phys. Rev.* **D84** (2011) 011102, arXiv:1105.3377 [astro-ph.CO].

[96] **DAMA Collaboration**, "First results from DAMA/LIBRA and the combined results with DAMA/NaI", *Eur. Phys. J.* **C56** (2008) 333–355, arXiv:0804.2741 [astro-ph].

[97] C. Savage, G. Gelmini, P. Gondolo and K. Freese, "Compatibility of DAMA/LIBRA dark matter detection with other searches", *JCAP* **0904** (2009) 010, arXiv:0808.3607 [astro-ph].

[98] **CoGeNT collaboration**, "Results from a Search for Light-Mass Dark Matter with a P-type Point Contact Germanium Detector", *Phys. Rev. Lett.* **106** (2011) 131301, arXiv:1002.4703 [astro-ph.CO].

[99] G. Jungman, M. Kamionkowski and K. Griest, "Supersymmetric dark matter", *Phys. Rept.* **267** (1996) 195–373, arXiv:hep-ph/9506380 [hep-ph].

[100] G. Bertone, D. Hooper and J. Silk, "Particle dark matter: Evidence, candidates and constraints", *Phys. Rept.* **405** (2005) 279–390, arXiv:hep-ph/0404175 [hep-ph].

[101] P. Fayet and J. Iliopoulos, "Spontaneously Broken Supergauge Symmetries and Goldstone Spinors", *Phys. Lett.* **B51** (1974) 461–464.

[102] L. O'Raifeartaigh, "Spontaneous Symmetry Breaking for Chiral Scalar Superfields", *Nucl. Phys.* **B96** (1975) 331.

[103] K. Choi and H. P. Nilles, "The Gaugino code", *JHEP* **0704** (2007) 006, arXiv:hep-ph/0702146 [hep-ph].

[104] L. Alvarez-Gaume, J. Polchinski and M. B. Wise, "Minimal Low-Energy Supergravity", *Nucl. Phys.* **B221** (1983) 495.

[105] L. E. Ibanez, "Locally Supersymmetric SU(5) Grand Unification", *Phys. Lett.* **B118** (1982) 73.

[106] J. R. Ellis, D. V. Nanopoulos and K. Tamvakis, "Grand Unification in Simple Supergravity", *Phys. Lett.* **B121** (1983) 123.

[107] K. Inoue, A. Kakuto, H. Komatsu and S. Takeshita, "Aspects of Grand Unified Models with Softly Broken Supersymmetry", *Prog. Theor. Phys.* **68** (1982) 927.

[108] A. H. Chamseddine, R. L. Arnowitt and P. Nath, "Locally Supersymmetric Grand Unification", *Phys. Rev. Lett.* **49** (1982) 970.

[109] R. Barbieri, S. Ferrara and C. A. Savoy, "Gauge Models with Spontaneously Broken Local Supersymmetry", *Phys. Lett.* **B119** (1982) 343.

[110] L. J. Hall, J. D. Lykken and S. Weinberg, "Supergravity as the Messenger of Supersymmetry Breaking", *Phys. Rev.* **D27** (1983) 2359–2378.

[111] N. Ohta, "Grand unified theories based on local supersymmetry", *Prog. Theor. Phys.* **70** (1983) 542.

[112] G. L. Kane, C. F. Kolda, L. Roszkowski and J. D. Wells, "Study of constrained minimal supersymmetry", *Phys. Rev.* **D49** (1994) 6173–6210, `arXiv:hep-ph/9312272 [hep-ph]`.

[113] L. Alvarez-Gaume, M. Claudson and M. B. Wise, "Low-Energy Supersymmetry", *Nucl. Phys.* **B207** (1982) 96.

[114] M. Dine, W. Fischler and M. Srednicki, "Supersymmetric Technicolor", *Nucl. Phys.* **B189** (1981) 575–593.

[115] S. Dimopoulos and S. Raby, "Supercolor", *Nucl. Phys.* **B192** (1981) 353.

[116] C. R. Nappi and B. A. Ovrut, "Supersymmetric Extension of the SU(3) x SU(2) x U(1) Model", *Phys. Lett.* **B113** (1982) 175.

[117] M. Dine and A. E. Nelson, "Dynamical supersymmetry breaking at low-energies", *Phys. Rev.* **D48** (1993) 1277–1287, `arXiv:hep-ph/9303230 [hep-ph]`.

[118] M. Dine, A. E. Nelson and Y. Shirman, "Low-energy dynamical supersymmetry breaking simplified", *Phys. Rev.* **D51** (1995) 1362–1370, `arXiv:hep-ph/9408384 [hep-ph]`.

[119] M. Dine, A. E. Nelson, Y. Nir and Y. Shirman, "New tools for low-energy dynamical supersymmetry breaking", *Phys. Rev.* **D53** (1996) 2658–2669, `arXiv:hep-ph/9507378 [hep-ph]`.

[120] P. Meade, N. Seiberg and D. Shih, "General Gauge Mediation", *Prog. Theor. Phys. Suppl.* **177** (2009) 143–158, `arXiv:0801.3278 [hep-ph]`.

[121] M. Buican, P. Meade, N. Seiberg and D. Shih, "Exploring General Gauge Mediation", *JHEP* **0903** (2009) 016, `arXiv:0812.3668 [hep-ph]`.

[122] L. M. Carpenter, M. Dine, G. Festuccia and J. D. Mason, "Implementing General Gauge Mediation", *Phys. Rev.* **D79** (2009) 035002, `arXiv:0805.2944 [hep-ph]`.

[123] G. Giudice and R. Rattazzi, "Theories with gauge mediated supersymmetry breaking", *Phys. Rept.* **322** (1999) 419–499, arXiv:hep-ph/9801271 [hep-ph].

[124] **DELPHI Collaboration**, "Searches for supersymmetric particles in e+ e- collisions up to 208 GeV and interpretation of the results within the MSSM", *Eur. Phys. J.* **C31** (2003) 421–479, arXiv:hep-ex/0311019 [hep-ex].

[125] **LEP SUSY Working Group**, **ALEPH**, **DELPHI**, **L3** and **OPAL** experiments, "Interpretation in Constrained MSSM and limit on the LSP mass", LEPSUSYWG/02-06.2,, http://lepsusy.web.cern.ch.

[126] **DØ Collaboration**, "Search for squarks and gluinos in events with jets and missing transverse energy using 2.1 fb^{-1} of $p\bar{p}$ collision data at $\sqrt{s} = 1.96$ TeV", *Phys. Lett.* **B660** (2008) 449–457, arXiv:0712.3805 [hep-ex].

[127] **DØ Collaboration**, "Search for associated production of charginos and neutralinos in the trilepton final state using 2.3 fb^{-1} of data", *Phys. Lett.* **B680** (2009) 34–43, arXiv:0901.0646 [hep-ex].

[128] **LEP SUSY Working Group**, **ALEPH**, **DELPHI**, **L3** and **OPAL** experiments, "Combined LEP Selectron/Smuon/Stau Results, 183-208 GeV", LEPSUSYWG/04-01.1,, http://lepsusy.web.cern.ch.

[129] **OPAL Collaboration**, "Searches for gauge-mediated supersymmetry breaking topologies in e+ e- collisions at LEP2", *Eur. Phys. J.* **C46** (2006) 307, arXiv:hep-ex/0507048 [hep-ex].

[130] **LEP SUSY Working Group**, **ALEPH**, **DELPHI**, **L3** and **OPAL** experiments, "Combined LEP GMSB Stau/Smuon/Selectron Results, 189-208 GeV", LEPSUSYWG/02-09.2,, http://lepsusy.web.cern.ch.

[131] **D0 Collaboration**, "Search for diphoton events with large missing transverse energy in 6.3 fb^{-1} of $\mathbf{p\bar{p}}$ collisions at $\sqrt{\mathbf{s}} = \mathbf{1.96}$ TeV", *Phys.Rev.Lett.* **105** (2010) 221802, arXiv:1008.2133 [hep-ex].

[132] G. Belanger, F. Boudjema, A. Cottrant, A. Pukhov and S. Rosier-Lees, "Lower limit on the neutralino mass in the general MSSM", *JHEP* **0403** (2004) 012, arXiv:hep-ph/0310037 [hep-ph].

[133] F. Borzumati, "The Decay $b \to s\gamma$ in the MSSM revisited", *Z. Phys.* **C63** (1994) 291–308, arXiv:hep-ph/9310212 [hep-ph].

[134] F. Mahmoudi, "New constraints on supersymmetric models from $b \to s\gamma$", *JHEP* **0712** (2007) 026, arXiv:0710.3791 [hep-ph].

[135] O. Buchmueller, R. Cavanaugh, A. De Roeck, J. Ellis, H. Flacher *et al.*, "Predictions for m(t) and M(W) in Minimal Supersymmetric Models", *Phys. Rev.* **D81** (2010) 035009, arXiv:0912.1036 [hep-ph].

[136] J. C. Collins, D. E. Soper and G. F. Sterman, "Factorization for Short Distance Hadron - Hadron Scattering", *Nucl. Phys.* **B261** (1985) 104.

[137] V. Gribov and L. Lipatov, "Deep inelastic e p scattering in perturbation theory", *Sov. J. Nucl. Phys.* **15** (1972) 438–450.

[138] G. Altarelli and G. Parisi, "Asymptotic Freedom in Parton Language", *Nucl. Phys.* **B126** (1977) 298.

[139] Y. L. Dokshitzer, "Calculation of the Structure Functions for Deep Inelastic Scattering and e+ e- Annihilation by Perturbation Theory in Quantum Chromodynamics.", *Sov. Phys. JETP* **46** (1977) 641–653.

[140] C. Quigg, "LHC Physics Potential versus Energy", arXiv:0908.3660 [hep-ph].

[141] **ATLAS Collaboration**, "Search for direct production of charginos and neutralinos in events with three leptons and missing transverse momentum in $\sqrt{s} = 7$ TeV pp collisions with the ATLAS detector", arXiv:1208.3144 [hep-ex].

[142] **ATLAS Collaboration**, "Search for direct slepton and gaugino production in final states with two leptons and missing transverse momentum with the ATLAS detector in pp collisions at $\sqrt{s} = 7$ TeV", arXiv:1208.2884 [hep-ex].

[143] **ATLAS Collaboration**, "Expected performance of the ATLAS detector in GMSB models with tau final states", ATL-PHYS-PUB-2009-089, Nov 2009, https://cds.cern.ch/record/1222126.

[144] A. Buckley, "PySLHA: a Pythonic interface to SUSY Les Houches Accord data", arXiv:1305.4194 [hep-ph].

[145] L. Theussl, D. Binosi, C. Kaufhold and J. Collins, "JaxoDraw 2.0-1." http://jaxodraw.sourceforge.net.

[146] W. Beenakker, R. Hopker, M. Spira and P. Zerwas, "Squark and gluino production at hadron colliders", *Nucl. Phys.* **B492** (1997) 51–103, arXiv:hep-ph/9610490 [hep-ph].

[147] A. Kulesza and L. Motyka, "Threshold resummation for squark-antisquark and gluino-pair production at the LHC", *Phys. Rev. Lett.* **102** (2009) 111802, arXiv:0807.2405 [hep-ph].

[148] A. Kulesza and L. Motyka, "Soft gluon resummation for the production of gluino-gluino and squark-antisquark pairs at the LHC", *Phys. Rev.* **D80** (2009) 095004, arXiv:0905.4749 [hep-ph].

[149] W. Beenakker, S. Brensing, M. Kramer, A. Kulesza, E. Laenen *et al.*, "Soft-gluon resummation for squark and gluino hadroproduction", *JHEP* **0912** (2009) 041, arXiv:0909.4418 [hep-ph].

[150] W. Beenakker, S. Brensing, M. Kramer, A. Kulesza, E. Laenen *et al.*, "Squark and gluino hadroproduction", *Int. J. Mod. Phys.* **A26** (2011) 2637–2664, arXiv:1105.1110 [hep-ph].

[151] W. Beenakker, M. Klasen, M. Kramer, T. Plehn, M. Spira *et al.*, "The Production of charginos / neutralinos and sleptons at hadron colliders", *Phys. Rev. Lett.* **83** (1999) 3780–3783, arXiv:hep-ph/9906298 [hep-ph].

[152] M. Spira, "Higgs and SUSY particle production at hadron colliders", arXiv:hep-ph/0211145 [hep-ph].

[153] T. Plehn, "Measuring the MSSM Lagrangean", *Czech. J. Phys.* **55** (2005) B213–B220, arXiv:hep-ph/0410063 [hep-ph].

[154] M. Kramer, A. Kulesza, R. van der Leeuw, M. Mangano, S. Padhi *et al.*, "Supersymmetry production cross sections in pp collisions at $\sqrt{s} = 7$ TeV", arXiv:1206.2892 [hep-ph].

[155] **ATLAS Collaboration**, "Search for Supersymmetry in Events with Large Missing Transverse Momentum, Jets, and at Least One Tau Lepton in 7 TeV Proton-Proton Collision Data with the ATLAS Detector", arXiv:1210.1314 [hep-ex].

[156] **ATLAS Collaboration**, "Search for supersymmetry with jets, missing transverse momentum and at least one hadronically decaying τ lepton in proton-proton collisions at $\sqrt{s} = 7$ TeV with the ATLAS detector", *Phys. Lett.* **B714** (2012) 197–214, arXiv:1204.3852 [hep-ex].

[157] **ATLAS Collaboration**, "Search for events with large missing transverse momentum, jets, and at least two tau leptons in 7 TeV proton-proton collision data with the ATLAS detector", *Phys. Lett.* **B714** (2012) 180–196, arXiv:1203.6580 [hep-ex].

[158] T. Hupf, "Suche nach Supersymmetrie in multileptonischen Endzuständen am Experiment ATLAS am LHC in pp-Kollisionen bei $\sqrt{s} = 7$ TeV", Diplomarbeit, Johannes-Gutenberg-Universität Mainz, 2012.

[159] P. Bechtle, K. Desch, M. Uhlenbrock and P. Wienemann, "Constraining SUSY models with Fittino using measurements before, with and beyond the LHC", *Eur. Phys. J.* **C66** (2010) 215–259, arXiv:0907.2589 [hep-ph].

[160] O. Buchmueller, R. Cavanaugh, A. De Roeck, S. Heinemeyer, G. Isidori *et al.*, "Prediction for the Lightest Higgs Boson Mass in the CMSSM using Indirect Experimental Constraints", *Phys. Lett.* **B657** (2007) 87–94, arXiv:0707.3447 [hep-ph].

[161] O. Buchmueller, R. Cavanaugh, A. De Roeck, J. Ellis, H. Flacher *et al.*, "Predictions for Supersymmetric Particle Masses using Indirect Experimental and Cosmological Constraints", *JHEP* **0809** (2008) 117, arXiv:0808.4128 [hep-ph].

[162] O. Buchmueller, R. Cavanaugh, D. Colling, A. De Roeck, M. Dolan *et al.*, "Frequentist Analysis of the Parameter Space of Minimal Supergravity", *Eur. Phys. J.* **C71** (2011) 1583, arXiv:1011.6118 [hep-ph].

[163] S. Asai, M. Baak, M. Backes, M. Becker, M. Bianco *et al.*, "Search for Supersymmetry with jets and missing transverse momentum and one or more leptons at $\sqrt{s} = 7$ TeV (supporting INT note)", ATL-PHYS-INT-2012-082, Oct 2012, https://cds.cern.ch/record/1488897.

[164] J. Alwall, P. Schuster and N. Toro, "Simplified Models for a First Characterization of New Physics at the LHC", *Phys. Rev.* **D79** (2009) 075020, arXiv:0810.3921 [hep-ph].

[165] **LHC New Physics Working Group**, "Simplified Models for LHC New Physics Searches", *J. Phys.* **G39** (2012) 105005, arXiv:1105.2838 [hep-ph].

[166] C. Gutschow and Z. Marshall, "Setting limits on supersymmetry using simplified models", arXiv:1202.2662 [hep-ex].

[167] J. M. Campbell, J. Huston and W. Stirling, "Hard Interactions of Quarks and Gluons: A Primer for LHC Physics", *Rept. Prog. Phys.* **70** (2007) 89, arXiv:hep-ph/0611148 [hep-ph].

[168] M.-A. Pleier, "Review of Top Quark Properties Measurements at the Tevatron", arXiv:0810.5226 [hep-ex].

[169] Christiane Lefèvre, "The CERN accelerator complex", Dec 2008. http://cdsweb.cern.ch/record/1260465.

[170] **LHC Study Group**, "Design study of the large hadron collider (LHC): A Multiparticle collider in the LEP tunnel", CERN-91-03, 1991, http://cdsweb.cern.ch/record/220493.

[171] **LHC Study Group**, "The Large Hadron Collider: Conceptual design", CERN-AC-95-05-LHC, 1995, http://cdsweb.cern.ch/record/291782.

[172] O. S. Bruning, P. Collier, P. Lebrun, S. Myers, R. Ostojic *et al.*, "LHC Design Report. 1. The LHC Main Ring", CERN-2004-003-V-1, 2004, http://cds.cern.ch/record/782076.

[173] M. Bajko, F. Bertinelli, N. Catalan-Lasheras, S. Claudet, P. Cruikshank *et al.*, "Report of the Task Force on the Incident of 19th September 2008 at the LHC", LHC-PROJECT-REPORT-1168, Mar 2009, https://cds.cern.ch/record/1168025.

[174] F. Formenti, Z. Charifoulline, G. J. Coelingh, K. Dahlerup-Petersen, R. Denz *et al.*, "Upgrade of the Quench Protection Systems for the Superconducting Circuits of the LHC Machine at CERN: From Concept and Design to the First Operational Experience", CERN-ATS-2010-129, Jun 2010, https://cds.cern.ch/record/1277645.

[175] M. Lamont, "The LHC from Commissioning to Operation", *Conf. Proc.* **C110904** (2011) 11–15.

[176] **ATLAS Collaboration**, "Luminosity Public Results." https://twiki.cern.ch/twiki/bin/view/AtlasPublic/LuminosityPublicResults.

[177] K. Foraz, "LS1 general planning and strategy for the LHC, LHC injectors", 2012. http://cdsweb.cern.ch/record/1492974.

[178] **ATLAS Collaboration**, "Letter of Intent for the Phase-I Upgrade of the ATLAS Experiment", CERN-LHCC-2011-012. LHCC-I-020, Nov 2011, http://cds.cern.ch/record/1402470.

[179] C. Buttar and D. della Volpe, "Letter of Intent for the Phase-II Upgrade of the ATLAS Experiment", ATL-COM-UPGRADE-2012-040, Oct 2012, https://cds.cern.ch/record/1491186.

[180] **ATLAS Collaboration**, "Physics at a High-Luminosity LHC with ATLAS (Update)", ATL-PHYS-PUB-2012-004, Oct 2012, http://cds.cern.ch/record/1484890.

[181] J. Pequenao, "Computer generated image of the whole ATLAS detector", Mar 2008. http://cdsweb.cern.ch/record/1095924.

[182] **ATLAS Collaboration**, "ATLAS detector and physics performance: Technical Design Report, 1", CERN, 1999. http://cdsweb.cern.ch/record/391176.

[183] **ATLAS Collaboration**, "Expected Performance of the ATLAS Experiment - Detector, Trigger and Physics", arXiv:0901.0512 [hep-ex].

[184] F. Huegging, "The atlas pixel detector", *IEEE Trans. Nucl. Sci.* **53** (2006) 1732–1736, arXiv:physics/0412138 [physics].

[185] J. Pequenao, "Computer generated image of the ATLAS Muons subsystem", Mar 2008. http://cdsweb.cern.ch/record/1095929.

[186] S. van der Meer, "Calibration of the effective beam height in the ISR.", CERN-ISR-PO-68-31. ISR-PO-68-31, 1968, http://cdsweb.cern.ch/record/296752.

[187] J. Soukup, "Lucid: technical design report", CERN EDMS, ATL-UL-ES-0001, Mar 2005, https://edms.cern.ch/document/574724/1.

[188] V. Cindro, D. Dobos, I. Dolenc, H. Frais-Kolbl, H. Frais-Koelbl *et al.*, "The ATLAS beam conditions monitor", *JINST* **3** (2008) P02004.

[189] K. Kordas, M. Abolins, I. Alexandrov, A. Amorim, I. Aracena *et al.*, "The ATLAS Data Acquisition and Trigger: Concept, design and status", *Nucl. Phys. Proc. Suppl.* **172** (2007) 178–182. http://cdsweb.cern.ch/record/1035150.

[190] **ATLAS TDAQ Collaboration**, "ATLAS trigger and data acquisition: Capabilities and commissioning", *Nucl. Instrum. Meth.* **A617** (2010) 306–309.

[191] A. Ebling, B. Bauss, V. Büscher, R. Degele, W. Ji *et al.*, "An FPGA based demonstrator for a topological processor in the future ATLAS L1-Calo trigger 'GOLD'", *JINST* **7** (2012) C01067.

[192] **ATLAS Collaboration**, "ATLAS computing: Technical design report", CERN-LHCC-2005-022, ATLAS-TRD-017, 2005, http://cds.cern.ch/record/837738.

[193] I. Bird, K. Bos, N. Brook, D. Duellmann, C. Eck *et al.*, "LHC computing Grid. Technical design report", CERN-LHCC-2005-024, 2005, http://cds.cern.ch/record/840543.

[194] **GEANT4 Collaboration**, "GEANT4: A Simulation toolkit", *Nucl. Instrum. Meth.* **A506** (2003) 250–303.

[195] **ATLAS Collaboration**, "The ATLAS Simulation Infrastructure", *Eur. Phys. J.* **C70** (2010) 823–874, arXiv:1005.4568 [physics.ins-det].

[196] **ATLAS Collaboration**, "Tracking Results and Comparison to Monte Carlo simulation at $\sqrt{s} = 900$ GeV", ATLAS-CONF-2010-011, Jul 2010, http://cds.cern.ch/record/1276323.

[197] **ATLAS Collaboration**, "Charged-particle multiplicities in pp interactions measured with the ATLAS detector at the LHC", *New J. Phys.* **13** (2011) 053033, arXiv:1012.5104 [hep-ex].

[198] **ATLAS Collaboration**, "Performance of the ATLAS Inner Detector Track and Vertex Reconstruction in the High Pile-Up LHC Environment", ATLAS-CONF-2012-042, Mar 2012, http://cds.cern.ch/record/1435196.

[199] **ATLAS Collaboration**, "Performance of primary vertex reconstruction in proton-proton collisions at $\sqrt{s}$ =7 TeV in the ATLAS experiment", ATLAS-CONF-2010-069, Jul 2010, http://cds.cern.ch/record/1281344.

[200] A. Wildauer, K. Prokofiev and S. Pagan Griso, "Update of primary vertex plots on 7 TeV data from 2011", ATL-COM-PHYS-2011-571, May 2011, http://cds.cern.ch/record/1353244.

[201] F. Meloni, A. Milov, S. Pagan-Griso, K. Prokofiev and A. Wildauer, "Vertexing Performance Data vs MC comparison for LPCC", ATL-COM-PHYS-2011-1312, Sep 2011, http://cds.cern.ch/record/1386234.

[202] W. Lampl, S. Laplace, D. Lelas, P. Loch, H. Ma, S. Menke, S. Rajagopalan, D. Rousseau, S. Snyder and G. Unal, "Calorimeter Clustering Algorithms: Description and Performance",

ATL-LARG-PUB-2008-002. ATL-COM-LARG-2008-003, Apr 2008, https://cds.cern.ch/record/1099735?ln=de.

[203] **ATLAS Collaboration**, "Expected electron performance in the ATLAS experiment", ATL-PHYS-PUB-2011-006, Apr 2011, http://cds.cern.ch/record/1345327.

[204] J. Colas, L. Di Ciaccio, M. Gouanere, R. Lafaye, S. Laplace *et al.*, "Response Uniformity of the ATLAS Liquid Argon Electromagnetic Calorimeter", *Nucl. Instrum. Meth.* **A582** (2007) 429–455, arXiv:0709.1094 [physics.ins-det].

[205] **ATLAS Electromagnetic Liquid Argon Calorimeter Group**, "Performance of the ATLAS electromagnetic calorimeter end-cap module 0", *Nucl. Instrum. Meth.* **A500** (2003) .

[206] **ATLAS Collaboration**, "Electron performance measurements with the ATLAS detector using the 2010 LHC proton-proton collision data", *Eur. Phys. J.* **C72** (2012) 1909, arXiv:1110.3174 [hep-ex].

[207] **ATLAS Collaboration**, "Improved electron reconstruction in ATLAS using the Gaussian Sum Filter-based model for bremsstrahlung", ATLAS-CONF-2012-047, May 2012, http://cds.cern.ch/record/1449796.

[208] **ATLAS Collaboration**, "Identification efficiency measurement for electrons with transverse energy between 7 and 50 GeV", ATL-COM-PHYS-2011-1669, Dec 2011, http://cds.cern.ch/record/1405412.

[209] **ATLAS Collaboration**, "Electron identification efficiency dependence on pileup", ATL-COM-PHYS-2011-1636, Dec 2011, http://cds.cern.ch/record/1403067.

[210] M. Pivk and F. R. Le Diberder, "sPlot: a statistical tool to unfold data distributions", *Nucl. Instrum. Meth.* **A555** (2005) 356–369, arXiv:physics/0402083 [physics].

[211] **CDF Collaboration**, "First measurements of inclusive W and Z cross sections from Run II of the Tevatron collider", *Phys. Rev. Lett.* **94** (2005) 091803, arXiv:hep-ex/0406078 [hep-ex].

[212] **DØ Collaboration**, "Measurement of the shape of the boson rapidity distribution for $p\bar{p} \to Z/\gamma^* \to e^+e^- + X$ events produced at $\sqrt{s}$ of 1.96 TeV", *Phys. Rev.* **D76** (2007) 012003, arXiv:hep-ex/0702025 [hep-ex].

[213] L. Serin and M. Donega, "Updated preliminary egamma plots with collision data", ATL-COM-PHYS-2009-656, Dec 2009, https://cds.cern.ch/record/1228555.

[214] M. Oreglia, "A Study of the reactions $\psi' \to \gamma\gamma\psi$", PhD thesis, Stanford University, 1980.

[215] J. Gaiser, "Charmonium spectroscopy from radiative decays of the J/ψ and ψ'", PhD thesis, Stanford University, 1982.

[216] T. Vu Anh, "Data-driven measurement of low-pT electron efficiency using J/Ψ to ee", Presented at the ATLAS egamma meeting, 06.11.08. https://indico.cern.ch/contributionDisplay.py?contribId=10&confId=39297.

[217] M. Schott, "Common Approach to ATLAS Performance Determination in Data", ATL-SOFT-PUB-2009-003. ATL-COM-SOFT-2008-013, Oct 2008, https://cds.cern.ch/record/1133612.

[218] **ATLAS Collaboration**, "The ATLAS InsituPerformance Packages." https://twiki.cern.ch/twiki/bin/viewauth/AtlasProtected/InsituPerformance.

[219] **ATLAS Collaboration**, "Electron performance of the ATLAS detector using the $J/\Psi \to e^+e^-$ decays", ATL-COM-PHYS-2010-518, July 2010, https://cds.cern.ch/record/1277921.

[220] **ATLAS Collaboration**, "ATLAS muon spectrometer: Technical Design Report", 1997. https://cdsweb.cern.ch/record/331068. CERN/LHCC/97-22.

[221] F. Bauer, L. Chevalier, J. Ernwein, A. Formica, P.-F. Giraud *et al.*, "ATLAS 2004 Combined Test Beam results: Muon Chamber Alignment and Muon Reconstruction", ATL-MUON-PUB-2007-003. ATL-COM-MUON-2006-012, Apr 2006, https://cds.cern.ch/record/942276.

[222] R. Nicolaidou, L. Chevalier, S. Hassani, J. Laporte, E. Le Menedeu *et al.*, "Muon identification procedure for the ATLAS detector at the LHC using Muonboy reconstruction package and tests of its performance using cosmic rays and single beam data", *J. Phys. Conf. Ser.* **219** (2010) 032052.

[223] **ATLAS Collaboration**, "A measurement of the ATLAS muon reconstruction and trigger efficiency using J/Ψ decays", ATLAS-CONF-2011-021, Mar 2011, https://cds.cern.ch/record/1336750.

[224] **ATLAS Collaboration**, "Muon reconstruction efficiency in reprocessed 2010 LHC proton-proton collision data recorded with the ATLAS detector", ATLAS-CONF-2011-063, Apr 2011, https://cds.cern.ch/record/1345743.

[225] "Pile-up Depedence of the ATLAS Muon Performance", ATL-COM-PHYS-2011-1640, April 2011, https://cds.cern.ch/record/1403080.

[226] M. Cacciari, G. P. Salam and G. Soyez, "The Anti-k(t) jet clustering algorithm", *JHEP* **0804** (2008) 063, arXiv:0802.1189 [hep-ph].

[227] M. Cacciari and G. P. Salam, "Dispelling the N^3 myth for the k_t jet-finder", *Phys. Lett.* **B641** (2006) 57–61, arXiv:hep-ph/0512210 [hep-ph].

[228] **ATLAS Collaboration**, "Jet energy measurement with the ATLAS detector in proton-proton collisions at $\sqrt{s} = 7$ TeV", arXiv:1112.6426 [hep-ex].

[229] **ATLAS Collaboration**, "Pile-up corrections for jets from proton-proton collisions at $\sqrt{s} = 7$ TeV in ATLAS in 2011", ATLAS-CONF-2012-064, Jul 2012, https://cds.cern.ch/record/1459529.

[230] **DØ Collaboration**, "Measurement of the $p\bar{p} \to t\bar{t}$ production cross section at $\sqrt{s} =$ 1.96-TeV in the fully hadronic decay channel.", *Phys. Rev.* **D76** (2007) 072007, arXiv:hep-ex/0612040 [hep-ex].

[231] D. W. Miller, A. Schwartzman and D. Su, "Pile-up jet energy scale corrections using the jet-vertex fraction method", ATL-PHYS-INT-2009-090, Sep 2009, https://cds.cern.ch/record/1206864.

[232] D. W. Miller, A. Schwartzman and D. Su, "Jet-Vertex Association Algorithm", ATL-COM-PHYS-2008-008, Jan 2008, https://cds.cern.ch/record/1082880.

[233] **Heavy Flavor Averaging Group**, "Averages of b-hadron, c-hadron, and tau-lepton properties as of early 2012", arXiv:1207.1158 [hep-ex].

[234] **ATLAS Collaboration**, "Commissioning of the ATLAS high-performance b-tagging algorithms in the 7 TeV collision data", ATLAS-CONF-2011-102, Jul 2011, https://cds.cern.ch/record/1369219.

[235] G. Piacquadio and C. Weiser, "A new inclusive secondary vertex algorithm for b-jet tagging in ATLAS", *J. Phys. Conf. Ser.* **119** (2008) 032032.

[236] **ATLAS Collaboration**, "Measuring the b-tag efficiency in a top-pair sample with 4.7 $fb^{-}1$ of data from the ATLAS detector", ATLAS-CONF-2012-097, Jul 2012, https://cds.cern.ch/record/1460443.

[237] **ATLAS Collaboration**, "Performance of Missing Transverse Momentum Reconstruction in Proton-Proton Collisions at 7 TeV with ATLAS", *Eur. Phys. J.* **C72** (2012) 1844, arXiv:1108.5602 [hep-ex].

[238] **ATLAS Collaboration**, "Performance of Missing Transverse Momentum Reconstruction in ATLAS with 2011 Proton-Proton Collisions at $\sqrt{s} = 7$ TeV", ATLAS-CONF-2012-101, Jul 2012, https://cds.cern.ch/record/14639150.

[239] **ATLAS Collaboration**, "Search for gluinos in events with two same-sign leptons, jets and missing transverse momentum with the ATLAS detector in pp collisions at $\sqrt{s} = 7$ TeV", *Phys. Rev. Lett.* **108** (2012) 241802, arXiv:1203.5763 [hep-ex].

[240] **ATLAS Collaboration**, "Luminosity Determination in pp Collisions at $\sqrt{s} = 7$ TeV Using the ATLAS Detector at the LHC", *Eur. Phys. J.* **C71** (2011) 1630, arXiv:1101.2185 [hep-ex].

[241] **ATLAS Collaboration**, "Luminosity Determination in pp Collisions at $\sqrt{s} = 7$ TeV using the ATLAS Detector in 2011", ATLAS-CONF-2011-116, Aug 2011, https://cds.cern.ch/record/1376384.

[242] **ATLAS Collaboration**, "Search for Supersymmetry with jets and missing transverse momentum and one lepton at $\sqrt{s} = 7$ TeV", ATL-PHYS-INT-2011-056, Jun 2011, https://cds.cern.ch/record/1358865.

[243] **ATLAS Collaboration**, "Performance of the ATLAS Electron and Photon Trigger in p-p Collisions at $\sqrt{s} = 7$ TeV in 2011", ATLAS-CONF-2012-048, May 2012, https://cds.cern.ch/record/1450089.

[244] **ATLAS Collaboration**, "Performance of the ATLAS muon trigger in 2011", ATLAS-CONF-2012-099, Jul 2012, https://cds.cern.ch/record/1462601.

[245] ATLAS SUSY Working Group, "SUSYTools package." https://svnweb.cern.ch/cern/wsvn/atlasoff/PhysicsAnalysis/SUSYPhys/SUSYTools/tags/SUSYTools-00-00-61/.

[246] ATLAS EGamma Combined Performance Group, "LAr Cleaning And Object Quality." https://twiki.cern.ch/twiki/bin/view/AtlasProtected/LArCleaningAndObjectQuality.

[247] **ATLAS Collaboration**, "Data-Quality Requirements and Event Cleaning for Jets and Missing Transverse Energy Reconstruction with the ATLAS Detector in Proton-Proton

Collisions at a Center-of-Mass Energy of $\sqrt{s} = 7$ TeV", ATLAS-CONF-2010-038, Jul 2010, https://cds.cern.ch/record/1277678.

[248] ATLAS Jet/Etmiss Group, "Recommendations for jet cleaning for data 2011." https://twiki.cern.ch/twiki/bin/viewauth/AtlasProtected/HowToCleanJets2011.

[249] ATLAS EGamma Combined Performance Group, "EGamma Object Quality package." https://svnweb.cern.ch/cern/wsvn/atlasgrp/CombPerf/EGamma/EGammaOQ/EGammaOQ_2011/tags/EGammaOQ_2011-00-00-04.

[250] S. Asai, M. Baak, S. Beale, S. Becker, M. Bianco *et al.*, "Search for Supersymmetry with jets and missing transverse momentum and one lepton at $\sqrt{s} = 7$ TeV", ATL-PHYS-INT-2011-082, Oct 2011, https://cds.cern.ch/record/1387044.

[251] M. L. Mangano, M. Moretti, F. Piccinini, R. Pittau and A. D. Polosa, "ALPGEN, a generator for hard multiparton processes in hadronic collisions", *JHEP* **0307** (2003) 001, arXiv:hep-ph/0206293 [hep-ph].

[252] S. Frixione and B. R. Webber, "Matching NLO QCD computations and parton shower simulations", *JHEP* **0206** (2002) 029, arXiv:hep-ph/0204244 [hep-ph].

[253] G. Corcella, I. Knowles, G. Marchesini, S. Moretti, K. Odagiri *et al.*, "HERWIG 6: An Event generator for hadron emission reactions with interfering gluons (including supersymmetric processes)", *JHEP* **0101** (2001) 010, arXiv:hep-ph/0011363 [hep-ph].

[254] J. Butterworth, J. R. Forshaw and M. Seymour, "Multiparton interactions in photoproduction at HERA", *Z. Phys.* **C72** (1996) 637, arXiv:hep-ph/9601371 [hep-ph].

[255] **ATLAS Collaboration**, "ATLAS tunes of PYTHIA6 and PYTHIA8 for MC11", ATL-PHYS-PUB-2011-009, 2011, https://cdsweb.cern.ch/record/1363300.

[256] ATLAS Top Working Group, "Heavy Flavor Overlap Removal Tool." https://twiki.cern.ch/twiki/bin/viewauth/AtlasProtected/HforTool.

[257] J. Pumplin, D. Stump, J. Huston, H. Lai, P. M. Nadolsky *et al.*, "New generation of parton distributions with uncertainties from global QCD analysis", *JHEP* **0207** (2002) 012, arXiv:hep-ph/0201195 [hep-ph].

[258] A. Martin, W. Stirling, R. Thorne and G. Watt, "Update of parton distributions at NNLO", *Phys. Lett.* **B652** (2007) 292, arXiv:0706.0459 [hep-ph].

[259] M. Aliev, H. Lacker, U. Langenfeld, S. Moch, P. Uwer *et al.*, "HATHOR: HAdronic Top and Heavy quarks crOss section calculatoR", *Comput. Phys. Commun.* **182** (2011) 1034, arXiv:1007.1327 [hep-ph].

[260] K. Melnikov and F. Petriello, "Electroweak gauge boson production at hadron colliders through O(alpha(s)**2)", *Phys. Rev.* **D74** (2006) 114017, arXiv:hep-ph/0609070 [hep-ph].

[261] H.-L. Lai, M. Guzzi, J. Huston, Z. Li, P. M. Nadolsky *et al.*, "New parton distributions for collider physics", *Phys. Rev.* **D82** (2010) 074024, arXiv:1007.2241 [hep-ph].

[262] N. Kidonakis, "Next-to-next-to-leading-order collinear and soft gluon corrections for t-channel single top quark production", *Phys. Rev.* **D83** (2011) 091503, arXiv:1103.2792 [hep-ph].

[263] N. Kidonakis, "NNLL resummation for s-channel single top quark production", *Phys. Rev.* **D81** (2010) 054028, arXiv:1001.5034 [hep-ph].

[264] N. Kidonakis, "Two-loop soft anomalous dimensions for single top quark associated production with a W- or H-", *Phys. Rev.* **D82** (2010) 054018, arXiv:1005.4451 [hep-ph].

[265] A. Sherstnev and R. Thorne, "Different PDF approximations useful for LO Monte Carlo generators", arXiv:0807.2132 [hep-ph].

[266] J. M. Campbell, R. Ellis and D. L. Rainwater, "Next-to-leading order QCD predictions for W + 2 jet and Z + 2 jet production at the CERN LHC", *Phys. Rev.* **D68** (2003) 094021, arXiv:hep-ph/0308195 [hep-ph].

[267] F. E. Paige, S. D. Protopopescu, H. Baer and X. Tata, "ISAJET 7.69: A Monte Carlo event generator for pp, anti-p p, and e+e- reactions", arXiv:hep-ph/0312045 [hep-ph].

[268] H. Baer, F. E. Paige, S. D. Protopopescu and X. Tata, "Simulating Supersymmetry with ISAJET 7.0 / ISASUSY 1.0", arXiv:hep-ph/9305342 [hep-ph].

[269] P. Z. Skands, B. Allanach, H. Baer, C. Balazs, G. Belanger *et al.*, "SUSY Les Houches accord: Interfacing SUSY spectrum calculators, decay packages, and event generators", *JHEP* **0407** (2004) 036, arXiv:hep-ph/0311123 [hep-ph].

[270] B. Allanach, C. Balazs, G. Belanger, M. Bernhardt, F. Boudjema *et al.*, "SUSY Les Houches Accord 2", *Comput. Phys. Commun.* **180** (2009) 8–25, arXiv:0801.0045 [hep-ph].

[271] M. Bahr, S. Gieseke, M. Gigg, D. Grellscheid, K. Hamilton *et al.*, "Herwig++ Physics and Manual", *Eur. Phys. J.* **C58** (2008) 639, arXiv:0803.0883 [hep-ph].

[272] A. Sherstnev and R. Thorne, "Parton Distributions for LO Generators", *Eur. Phys. J.* **C55** (2008) 553, arXiv:0711.2473 [hep-ph].

[273] J. Alwall, M. Herquet, F. Maltoni, O. Mattelaer and T. Stelzer, "MadGraph 5 : Going Beyond", *JHEP* **1106** (2011) 128, arXiv:1106.0522 [hep-ph].

[274] T. Sjöstrand, S. Mrenna and P. Skands, "PYTHIA 6.4 physics and manual", *JHEP* **05** (2006) 026.

[275] J. Alwall, S. Hoche, F. Krauss, N. Lavesson, L. Lonnblad *et al.*, "Comparative study of various algorithms for the merging of parton showers and matrix elements in hadronic collisions", *Eur. Phys. J.* **C53** (2008) 473, arXiv:0706.2569 [hep-ph].

[276] "TLimit, Class to compute 95% CL limits." http://root.cern.ch/root/htmldoc/TLimit.html.

[277] T. Junk, "Confidence level computation for combining searches with small statistics", *Nucl. Instrum. Meth.* **434** (1999) 435.

[278] T. Müller, "Suche nach Supersymmetrie im 2-Lepton-Endzustand mit dem ATLAS-Experiment", Diplomarbeit, Johannes-Gutenberg-Universität Mainz, 2010.

[279] A. Loginov, "Strategies of data-driven estimations of ttbar backgrounds in ATLAS", ATL-PHYS-PROC-2010-067, Aug 2010, https://cds.cern.ch/record/1287126.

[280] ATLAS SUSY Working Group, "FakeLeptBkg package." https://svnweb.cern.ch/trac/atlasoff/browser/PhysicsAnalysis/SUSYPhys/FakeLeptBkg.

[281] C. Meyer, "Search for supersymmetry in the one lepton final state with the ATLAS experiment", PhD thesis, Johannes-Gutenberg-Universität Mainz, 2013.

[282] S. Frixione, P. Nason and C. Oleari, "Matching NLO QCD computations with Parton Shower simulations: the POWHEG method", *JHEP* **0711** (2007) 070, arXiv:0709.2092 [hep-ph].

[283] S. Alioli, P. Nason, C. Oleari and E. Re, "A general framework for implementing NLO calculations in shower Monte Carlo programs: the POWHEG BOX", *JHEP* **1006** (2010) 043, arXiv:1002.2581 [hep-ph].

[284] R. Gavin, Y. Li, F. Petriello and S. Quackenbush, "FEWZ 2.0: A code for hadronic Z production at next-to-next-to-leading order", *Comput. Phys. Commun.* **182** (2011) 2388–2403, arXiv:1011.3540 [hep-ph].

[285] M. Hohlfeld, M. Lungwitz, C. Meyer and T. Mueller, "Estimating theory uncertainties in W/Z+jets and ttbar+jets events using the Alpgen generator", ATL-COM-PHYS-2012-070, Jan 2012, https://cds.cern.ch/record/1419198.

[286] S. Asai, M. Baak, M. Bianco, J. Boyd, R. Bruneliere *et al.*, "Search for Supersymmetry with jets and missing transverse momentum and one lepton at $\sqrt{s} = 7$TeV (supporting INT note)", ATL-PHYS-INT-2011-008, Feb 2011, https://cds.cern.ch/record/1327968.

[287] K. Edmonds, "Single Lepton Final State SUSY Searches with the ATLAS Detector", PhD thesis, Johannes-Gutenberg-Universität Mainz, 2010.

[288] C. Berger, Z. Bern, L. J. Dixon, F. Febres Cordero, D. Forde *et al.*, "Next-to-Leading Order QCD Predictions for W+3-Jet Distributions at Hadron Colliders", *Phys. Rev.* **D80** (2009) 074036, arXiv:0907.1984 [hep-ph].

[289] ATLAS EGamma Combined Performance Group, "Electron Trigger scale factors." https://svnweb.cern.ch/cern/wsvn/atlasoff/Reconstruction/egamma/egammaAnalysis/egammaAnalysisUtils/tags/egammaAnalysisUtils-00-02-56.

[290] **ATLAS Collaboration**, "Validating the measurement of jet energies with the ATLAS detector using Z + jet events from proton-proton collisions at $\sqrt{s} = 7$ TeV", ATLAS-CONF-2011-159, Dec 2011, https://cds.cern.ch/record/1403179.

[291] **ATLAS Collaboration**, "Probing the measurement of jet energies with the ATLAS detector using Z+jet events from proton-proton collisions at $\sqrt{s} = 7$ TeV", ATLAS-CONF-2012-053, May 2012, https://cds.cern.ch/record/1452641.

[292] **ATLAS Collaboration**, "Probing the measurement of jet energies with the ATLAS detector using photon+jet events in proton-proton collisions at $\sqrt{s} = 7$ TeV", ATLAS-CONF-2012-063, Jul 2012, https://cds.cern.ch/record/1459528.

[293] ATLAS Jet/Etmiss Group, "JetEnergyResolutionProvider, `JetResolution` package." https://twiki.cern.ch/twiki/bin/viewauth/AtlasProtected/JetEnergyResolutionProvider.

[294] **ATLAS Collaboration**, "Jet energy resolution in proton-proton collisions at $\sqrt{s} = 7$ TeV recorded in 2010 with the ATLAS detector", arXiv:1210.6210 [hep-ex].

[295] ATLAS Jet/Etmiss Group, "JESUncertaintyProvider, `JetUncertainties` package." https://twiki.cern.ch/twiki/bin/viewauth/AtlasProtected/JESUncertaintyProvider.

[296] ATLAS Jet/Etmiss Group, "MultijetJESUncertaintyProvider, `JetUncertainties` package." `https://twiki.cern.ch/twiki/bin/viewauth/AtlasProtected/MultijetJESUncertaintyProvider`.

[297] ATLAS EGamma Combined Performance Group, "EnergyRescaler, `egammaAnalysisUtils` package." `https://twiki.cern.ch/twiki/bin/viewauth/AtlasProtected/EnergyRescaler`.

[298] ATLAS EGamma Combined Performance Group, "egammaSFclass, `egammaAnalysisUtils` package." `https://twiki.cern.ch/twiki/bin/viewauth/AtlasProtected/EfficiencyMeasurements#Electron_efficiencies_2011_Morio`.

[299] ATLAS Muon Combined Performance Group, "`MuonEfficiencyCorrections` package." `https://twiki.cern.ch/twiki/bin/viewauth/AtlasProtected/MCPAnalysisGuidelinesRel17MC11a`.

[300] **ATLAS Collaboration**, "Reconstruction and Calibration of Missing Transverse Energy and Performance in Z and W events in ATLAS Proton-Proton Collisions at $\sqrt{s}$=7 TeV", ATLAS-CONF-2011-080, May 2011, `https://cds.cern.ch/record/1355703`.

[301] ATLAS Jet/Etmiss Group, "MissingEt Utility Package." `https://svnweb.cern.ch/trac/atlasoff/browser/Reconstruction/MissingETUtility/tags/MissingETUtility-00-02-13`.

[302] **ATLAS Collaboration**, "Calibrating the b-Tag Efficiency and Mistag Rate in 35 pb^{-1} of Data with the ATLAS Detector", ATLAS-CONF-2011-089, June 2011, `https://cds.cern.ch/record/1356198`.

[303] **ATLAS Collaboration**, "Measurement of the b-tag Efficiency in a Sample of Jets Containing Muons with 5 fb^{-1} of Data from the ATLAS Detector", ATLAS-CONF-2012-043, March 2012, `https://cds.cern.ch/record/1435197`.

[304] ATLAS Flavour Tagging Group, "BTaggingCalibrationDataInterface." `https://svnweb.cern.ch/trac/PhysicsAnalysis/JetTagging/JetTagPerformanceCalibration/CalibrationDataInterface/tags/CalibrationDataInterface-00-01-02`.

[305] T. Eifert, "Parton-Shower uncertainty in SUSY 1-lep TFs", ATLAS SUSY 1 lepton channel sharepoint, 19.03.12. `https://espace.cern.ch/atlas-susy-etmiss/1leptonchannel/Shared%20Documents/susy_1lep_PSunc.pdf`.

[306] ATLAS SUSY Working Group, "SignalUncertaintiesUtils Package." `https://svnweb.cern.ch/trac/atlasoff/browser/atlasphys/Physics/SUSY/Tools/SignalUncertaintiesUtils/tags/SignalUncertaintiesUtils-00-00-04`.

[307] A. Alonso, S. Brazzale, P. Bechtle, M. Bianco, M. Boehler *et al.*, "Constraining the gauge-mediated Supersymmetry breaking model in final states with two leptons, jets and missing transverse momentum with the ATLAS experiment at $\sqrt{s} = 7$ TeV", ATL-PHYS-INT-2011-096, Nov 2011, `https://cds.cern.ch/record/1402507`.

[308] R. Bruneliere, M. Baak, J. Lundberg, M. C. Rammensee and T. J. Khoo, "Setting exclusion limits in ATLAS supersymmetry searches with a likelihood ratio based method", ATL-PHYS-INT-2011-032, Apr 2011, `https://cds.cern.ch/record/1342545`.

[309] ATLAS SUSY Working Group, "`HistFitter` package." `https://svnweb.cern.ch/trac/atlasphys/browser/Physics/SUSY/Analyses/HistFitter/tags/HistFitter-00-00-10`.

[310] L. Moneta *et al.*, "The RooStats Project", arXiv:1009.1003 [physics.data-an].

[311] K. Cranmer, G. Lewis, L. Moneta, A. Shibata and W. Verkerke, "HistFactory: A tool for creating statistical models for use with RooFit and RooStats", CERN-OPEN-2012-016, Jun 2012.

[312] A. Read, "Presentation of search results: the CLs technique", *J. Phys. G* **28** (2002) no. 10, 2693.

[313] G. Cowan, K. Cranmer, E. Gross and O. Vitells, "Asymptotic formulae for likelihood-based tests of new physics", *Eur. Phys. J.* **C71** (2011) 1554, arXiv:1007.1727 [physics.data-an].

[314] **ATLAS Collaboration**, **CMS Collaboration** and **LHC Higgs Combination Group**, "Procedure for the LHC Higgs boson search combination in summer 2011", ATL-PHYS-PUB-2011-011, CMS NOTE-2011/005, Aug 2011, https://cds.cern.ch/record/1375842.

[315] S. Wilks, "The large-sample distribution of the likelihood ratio for testing composite hypotheses", *Ann. Math. Statist.* **9** (1938) 60–62.

[316] G. Casella and R. L. Berger, "Statistical Inference", Duxbury Press; 2nd edition, 2001.

[317] A. Wald, "Tests of Statistical Hypotheses Concerning Several Parameters When the Number of Observations is Large", *Trans. Amer. Math. Soc.* **54** (1943) 426–482.

[318] G. Cowan, K. Cranmer, E. Gross and O. Vitells, "Power-Constrained Limits", arXiv:1105.3166 [physics.data-an].

[319] ATLAS SUSY Working Group, "SUSY Limit Plotting." https://twiki.cern.ch/twiki/bin/viewauth/AtlasProtected/SUSYLimitPlotting.

[320] B. Delaunay, "Sur la sphère vide", *Bull. Acad. Sci. URSS* **7** (1934) 793–800.

[321] K. Cranmer, "The ATLAS+CMS Higgs Combination: where physics and statistics meet", Presented at the ATLAS/CMS statistics forum meeting, 06.07.10. https://indico.cern.ch/contributionDisplay.py?contribId=2&confId=100458.

[322] **ATLAS Collaboration**, "Search for squarks and gluinos with the ATLAS detector in final states with jets and missing transverse momentum using 4.7 fb^{-1} of $\sqrt{s} = 7$ TeV proton-proton collision data", *Phys.Rev.* **D87** (2013) 012008, arXiv:1208.0949 [hep-ex].

[323] **ATLAS Collaboration**, "Hunt for new phenomena using large jet multiplicities and missing transverse momentum with ATLAS in 4.7 fb^{-1} of $\sqrt{s} = 7$ TeV proton-proton collisions", *JHEP* **1207** (2012) 167, arXiv:1206.1760 [hep-ex].

[324] **CMS Collaboration**, "Search for supersymmetry in pp collisions at $\sqrt{s} = 7$ TeV in events with a single lepton, jets, and missing transverse momentum", *Eur. Phys. J. C* **73** (2013) 2404, arXiv:1212.6428 [hep-ex].

[325] **CMS Collaboration**, "Search for new physics in events with opposite-sign leptons, jets, and missing transverse energy in pp collisions at $\sqrt{s} = 7$ TeV", *Phys.Lett.* **B718** (2013) 815–840, arXiv:1206.3949 [hep-ex].

[326] **CMS Collaboration**, "Search for supersymmetry in events with opposite-sign dileptons and missing transverse energy using an artificial neural network", *Phys.Rev.* **D87** (2013) 072001, arXiv:1301.0916 [hep-ex].

[327] **ATLAS Collaboration**, "Search for supersymmetry in final states with jets, missing transverse momentum and one isolated lepton in $\sqrt{s} = 7$ TeV pp collisions using 1 fb^{-1} of ATLAS data", *Phys. Rev.* **D85** (2012) 012006, arXiv:1109.6606 [hep-ex].

[328] **LEP SUSY Working Group**, **ALEPH**, **DELPHI**, **L3** and **OPAL** experiments, "Combined LEP Chargino Results, up to 208 GeV for large m0", LEPSUSYWG/01-03.1,, http://lepsusy.web.cern.ch.

[329] **CMS Collaboration**, "Interpretation of searches for supersymmetry with simplified models", arXiv:1301.2175 [hep-ex].

[330] **ATLAS Collaboration**, "Search for supersymmetry at $\sqrt{s} = 8$ TeV in final states with jets, missing transverse momentum and one isolated lepton", ATLAS-CONF-2012-104, Aug 2012, https://cds.cern.ch/record/1472673.

[331] **XENON100 Collaboration**, "Dark Matter Results from 225 Live Days of XENON100 Data", *Phys.Rev.Lett.* **109** (2012) 181301, arXiv:1207.5988 [astro-ph.CO].

[332] **LHCb Collaboration**, "Strong constraints on the rare decays $B_s \to \mu^+\mu^-$ and $B^0 \to \mu^+\mu^-$", *Phys.Rev.Lett.* **108** (2012) 231801, arXiv:1203.4493 [hep-ex].

[333] O. Buchmueller, R. Cavanaugh, M. Citron, A. De Roeck, M. Dolan *et al.*, "The CMSSM and NUHM1 in Light of 7 TeV LHC, $B_s \to \mu^+\mu^-$ and XENON100 Data", *Eur.Phys.J.* **C72** (2012) 2243, arXiv:1207.7315 [hep-ph].

[334] T. Eifert, M. D'Onofrio, A. Hoecker, T. Lari, Y. Nakahama, S. Pataraia and I. Vivarelli, "SUSY direct stop search summaries for Moriond QCD 2013", ATL-COM-PHYS-2013-264, Mar 2013, https://cds.cern.ch/record/1522438.

[335] **ATLAS Collaboration**, "Physics at a High-Luminosity LHC with ATLAS", ATL-PHYS-PUB-2012-001, Aug 2012, https://cds.cern.ch/record/1472518.

[336] ATLAS SUSY Working Group, "SUSYD3PDMaker package." https://svnweb.cern.ch/cern/wsvn/atlasoff/PhysicsAnalysis/D3PDMaker/SUSYD3PDMaker/tags/SUSYD3PDMaker-00-11-18.